Tampere University

MIKA TAKALA

Asteroid Tomography

by Utilizing Nanosatellites

Tampere University Dissertations 291

Tampere University Dissertations 291

MIKA TAKALA

Asteroid Tomography

by Utilizing Nanosatellites

ACADEMIC DISSERTATION
To be presented, with the permission of
the Faculty of Information Technology and Communication Sciences
of Tampere University,
for public discussion at Tampere University,
on 28 August 2020, at 16 o'clock.

ACADEMIC DISSERTATION
Tampere University, Faculty of Information Technology and Communication Sciences
Finland

Responsible supervisor and Custos	Associate Professor Sampsa Pursiainen Tampere University Finland	
Supervisor	Professor Timo D. Hämäläinen Tampere University Finland	
Pre-examiners	Professor Alain Herique Université Grenoble Alpes, IPAG France	Professor Dirk Plettemeier Technische Universität Dresden Germany
Opponent	Professor Erik Asphaug University of Arizona United States of America	

The originality of this thesis has been checked using the Turnitin OriginalityCheck service.

Cover design: Roihu Inc.

ISBN 978-952-03-1650-1 (print)
ISBN 978-952-03-1651-8 (pdf)
ISSN 2489-9860 (print)
ISSN 2490-0028 (pdf)
http://urn.fi/URN:ISBN:978-952-03-1651-8

PunaMusta Oy – Yliopistopaino
Vantaa 2020

Dedicated to those that made the dreams possible.

PREFACE

I would like to begin my thesis by giving thanks to my supervisor, Assoc. Prof. Sampsa Pursiainen for encouraging me to start this work as a PhD student in 2016. My background in embedded electronics and software had me quite a bit of catching up to do in mathematics and scientific work, and his way of finding the essential things for me to learn, and at the same time, bringing my existing knowledge to our group's work got us on a level we didn't think could be achieved during this short time.

This research was conducted in the Laboratory of Mathematics at Tampere University of Technology. The laboratory and our Inverse Problems research group is now part of the Faculty of Information Technology and Communication Sciences at Tampere University. I'd like to thank Academy of Finland for funding the research via the Academy of Finland Key Project 305055 and by the Academy of Finland Centre of Excellence in Inverse Modelling and Imaging 2018-2025.

I wish to thank all my coworkers at Tampere University. I also thank those that did the same exercises in the PhD related courses, from whom I learned a lot from. I would also like to thank Professor Timo D. Hämäläinen for giving me guidance and interesting research ideas. Most interesting of them couldn't be investigated during the time of this thesis project!

Finally, I thank my friends and family. Friends in real life, at the University, at work, and those online in various hobby communities are essential and without them this work could not have been completed. I cannot thank my family enough of encouraging me and giving me opportunity to embark on this interesting adventure. I love you all.

Tampere, May 5th, 2020
Mika Takala

ABSTRACT

In the last 10 years, utilization of nanosatellites has gained popularity in Low Earth Orbit (LEO) applications via the CubeSat standard. They have been an important part of so called new space economy, where larger and larger objectives in space can be achieved with low-cost, off-the-shelf electronics. While CubeSats have remained for research and technology development purposes, the science-oriented space missions have utilized larger spacecraft. One such mission was the European Space Agency's (ESA's) Rosetta mission, which reached comet 67P/Churyumov–Gerasimenko in August 2014. An integral part of the mission was to attempt a radio tomography experiment, where the interior structure of the comet would have been mapped via radar signals. This thesis considers utilization of CubeSat-scale spacecraft to attempt to recover the interior structure of a small Near-Earth Asteroid (NEA). This has not been attempted before. During this thesis project, ESA selected CubeSats to fly on the Hera mission to asteroid Didymos. One of these CubeSats will include a radar instrument based on the one on Rosetta and its lander, Philae.

This thesis extends the previous work of the Inverse Problems research group in Tampere University in simulating radio wave propagation within the asteroid via Finite-Difference Time Domain (FDTD) method as well as using the full wave measurement data in state of the art mathematical inversion strategies to recover the interior structure of the asteroid. Here, the focus is on investigating the effects of the measurement strategy and noise to the inversion results, improving the speed and accuracy of the method by using a multiresolution approach, and extending the modeling domain to make it possible to perform the simulations when the transmitting and receiving spacecraft are in far field, outside the finite element mesh based simulation domain. Important aspect of the work includes utilization of state-of-the-art Graphics Processing Units (GPUs) which make it possible to accelerate the simulations both locally and in a calculation cluster.

A CubeSat feasibility study called Deep Interior Scanning CubeSat (DISCUS)

was performed during the thesis project with the project collaborators. The goal of DISCUS is to fly a CubeSat to a NEA and perform the measurements, store the data and send the data back to Earth. The study includes analysis of currently available CubeSat hardware with realistic performance parameters, analysis of the mission parameters and the potential target asteroids, and realistic orbital parameters to perform the measurements on-site. DISCUS concept was later extended for a space mission called Asteroid In-situ Interior Investigation - 3way (Ai3), which was proposed for ESA's F-class mission call in summer of 2018. While Ai3 was not selected, it was one of the six proposals on the second round of the process. The general interest towards studies of NEAs indicate that NEAs remain important for science, planetary protection purposes, as well as commercial companies, which motivates further studies in the topic.

TIIVISTELMÄ

Viimeisen kymmenen vuoden aikana pienten ns. nanosatelliittien hyödyntäminen matalalla Maan kiertoradalla on kasvattanut suosiotaan CubeSat-standardin ansiosta. Nämä nanosatelliitit ovat olleet tärkeä osa ns. uutta avaruusteollisuutta, jossa toinen toistaan suuremmat tavoitteet on mahdollista saavuttaa halvempaa tekniikkaa hyödyntäen. Nanosatelliitteja on käytetty toistaiseksi pääasiassa tutkimus- ja teknologiankehitystarkoituksiin, ja varsinaiset tieteelliset avaruusmissiot on tehty suurempia avaruuslaitteita käyttäen. Yksi tällaisista missioista oli Euroopan avaruusjärjestö ESA:n Rosetta-missio, joka kohtasi komeetta 67P/Churyumov-Gerasimenkon elokuussa 2014. Lennon yhtenä peruselementtinä oli kokeilla radiotomografiakoetta, jossa komeetan sisustan rakenne olisi kartoitettu tutkasignaaleilla. Tämä väitöskirja tutkii nanosatelliittien käyttöä pienten Maan lähiasteroidien sisustan kartoitukseen. Tätä ei ole yritetty aikaisemmin. Väitöskirjatutkimuksen aikana ESA valitsi nanosatelliitteja Didymos-asteroidille lentävälle Hera-missiolleen. Yksi valituista nanosatelliiteista sisältää radiotomografiainstrumentin, joka pohjautuu aikaisemmassa Rosetta-missiossa ja sen Philae-laskeutujassa käytettyyn tekniikkaan.

Tämä väitöstutkimus laajentaa Tampereen yliopiston inversio-ongelmien tutkimusryhmän aikaisempaa työtä. Tutkimuksessa on simuloitu radioaaltojen etenemistä asteroidin sisällä elementtimenetelmällä, sekä koko vastaanotetun aaltodatan käyttämistä huippuluokan matemaattisilla inversiomenetelmillä siten, että asteroidin sisä-rakenne saadaan kuvannettua. Painopiste työssä on mittausmenetelmän ja kohinan vaikutuksessa kuvannustulokseen sekä mallinnuksen parantamiseen siten, että elementtimenetelmää voidaan käyttää, vaikka mittausta suorittavat avaruusalukset olisivat simulaatiossa käytetyn elementtiverkon ulkopuolella. Tärkeä osa työtä on myös viimeisimpien grafiikkaprosessoreiden (GPU) hyödyntäminen, koska niiden avulla simulaatioiden suoritusaikaa pystytään nopeuttamaan sekä lokaaleilla työasemilla että laskentaklustereissa.

Nanosatelliitin käyttämisestä tässä tarkoituksessa tehtiin Deep Interior Scanning

CubeSat (DISCUS) -niminen soveltuvuustutkimus yhdessä projektikumppaneiden kanssa. DISCUS-konseptin tavoitteena oli lennättää nanosatelliitti Maan lähiasteroidille ja tehdä tarvittavat mittaukset, tallentaa data ja lähettää data Maahan. Tutkimus sisältää analyysin tällä hetkellä saatavilla olevista nanosatelliitien komponenteista, niiden realistisista suoritusarvoista, lennon parametrien analyysin sekä mahdolliset kohdeasteroidit. DISCUS-konseptia laajennettiin myöhemmin avaruusmissioksi nimeltä Asteroid In-situ Interior Investigation - 3way (Ai3), joka oli ehdolla ESA:n F-tyypin missiohaussa kesällä 2018. Vaikka Ai3:a ei valittu, se oli yksi kuudesta ehdotuksesta haun toisella kierroksella. Yleinen kiinnostus Maan lähiasteroidien tutkimukseen osoittaa, että ne ovat tärkeitä tieteen, maapallon puolustuksen sekä myös kaupallisten toimijoiden näkökulmista, mikä motivoi asteroidien kuvantamisen tekniikan jatkotutkimuksia.

CONTENTS

List of Figures

List of Tables

ABBREVIATIONS

CDF	Concurrent Design Facility
CONSERT	Comet Nucleus Sounding Experiment by Radiowave Transmission
COTS	Commercial Off-The-Shelf (hardware)
CT	Computed Tomography
DISCUS	Deep Interior Scanning CubeSat
ESA	European Space Agency
FETD	Finite Element Time Domain
FFT	Fast Fourier Transform
GPU	Graphics Processing Unit
JAXA	Japan Aerospace Exploration Agency
LEO	Low Earth Orbit
M-ARGO	Miniaturised-Asteroid Remote Geophysical Observer, ESA's deep space CubeSat and mission concept
MARCO	Mars Cube One, NASA's CubeSat on Insight mission.
NASA	National Aeronautics and Space Administration
NEA	Near-Earth Asteroid
SNR	Signal-to-Noise Ratio
TV	Total Variation Technique

ORIGINAL PUBLICATIONS

Publication I — M. Takala, T. D. Hämäläinen and S. Pursiainen. The Effect of Hardware-Computed Travel Time on Localization Accuracy in the Inversion of Experimental (Acoustic) Waveform Data. *IEEE Transactions on Computational Imaging* 3.2 (June 2017), 344–354. ISSN: 2333-9403. DOI: 10.1109/TCI.2017.2686698.

Publication II — M. Takala, D. Us and S. Pursiainen. Multigrid-Based Inversion for Volumetric Radar Imaging With Asteroid Interior Reconstruction as a Potential Application. *IEEE Transactions on Computational Imaging* 4.2 (June 2018), 228–240. ISSN: 2333-9403. DOI: 10.1109/TCI.2018.2811908.

Publication III — M. Takala, P. Bambach, J. Deller, E. Vilenius, M. Wittig, H. Lentz, H. M. Braun, M. Kaasalainen and S. Pursiainen. Far-Field Inversion for the Deep Interior Scanning CubeSat. *IEEE Transactions on Aerospace and Electronic Systems* 55.4 (Aug. 2019), 1683–1697. ISSN: 0018-9251. DOI: 10.1109/TAES.2018.2874755.

Publication IV — P. Bambach, J. Deller, E. Vilenius, S. Pursiainen, M. Takala, H. M. Braun, H. Lentz and M. Wittig. DISCUS – The Deep Interior Scanning CubeSat mission to a rubble pile near-Earth asteroid. *Advances in Space Research* 62.12 (2018). Advances in Technologies, Missions and Applications of Small Satellites, 3357–3368. ISSN: 0273-1177. DOI: 10.1016/j.asr.2018.06.016.

Author's contribution

Publication I — The main results and methods from the author's master of science thesis were refined and presented. The goal was to investigate the hardware aspects of the inverse imaging applications of wave propagation with a special focus on the tomography of small solar system bodies. In the study, acoustic waveform data were first recorded using an experimental setup. Then the data were processed using different assumptions on the hardware performance using a high-level synthesis approach. After processing, the wave velocity field was reconstructed via a tomographic approach to investigate the effect of the processing in the inversion stage. Author disseminated the study results and wrote the majority of the publication.

Publication II — This study is a joint project between the participants of the Academy of Finland Key Project in High and Low Frequency Inverse Imaging with Signal Sparsity (AoF 305055). The study introduced and tested in 2D a mathematical multiresolution approach. The author's contribution is in the implementation and geophysical application of the presented mathematical methodology, article writing, and serving as the contributing author.

Publication III — This article is a part of the Key Project in High and Low Frequency Inverse Imaging with Signal Sparsity which included international research collaboration. A far-field model to complement the mathematical multigrid approach established in the previous 2D study was developed and tested. A local network of workstations was established to enable performing computations in 3D with Graphics Computing Unit (GPU) acceleration. The final computations were run in the Narvi cluster of Tampere University which includes high-performance GPU-segment. The author's contribution is in cluster computing and management, article writing, and serving as the contributing author.

Publication IV Together with collaborators, the Deep Interior Scanning CubeSat (DISCUS) concept for performing full-wave radar measurements in-situ and to record data which could be inverted through the mathematical tomography approach developed in the earlier studies was developed and published. The concept was, later on, a part of a space mission proposal Asteroid In-situ Interior Investigation - 3way (AI3) which was among the six mission proposals selected for the second round of European Space Association's (ESA's) F-class mission call. As a specialist of embedded systems and hardware engineering the author was a key member in the team as well as a major contributor to the final design and in writing the article.

1 INTRODUCTION

Asteroids are, in their most common explanation, rocks that fly in space. The interior structure of asteroids is largely unknown. Obtaining some information of them is important to many different fields of research. These include developing models of the solar system, especially to understand its formation and evolution. The commercial utilization of asteroids is a prospect that is emerging as a realizable venture. For the planet Earth, methods and knowledge about the effectiveness of planetary protection would be important. The content of the work in this thesis includes mathematical representation of the tomography computation methodology to recover the interior structure of a Near-Earth Asteroid (NEA), simulation results, and a mission concept design that has been used as a basis of a real space mission plan. This chapter contains important background information of these different research topics. There is also a short list of previous missions that have been flown to asteroids as well as a short introduction to tomography and its applications. Chapter 2 outlines the utilization of a radar in a mission concept that could be implemented to perform asteroid tomography. In Chapter 3, tomography methods and inversion methodologies used in the publications are outlined and in Chapter 4 the computing advances that makes it possible to perform the wave propagation simulations required for the tomography simulations are discussed. Chapter 5 outlines the results of the research and the final chapter is the summary.

1.1 Tomography applications and methods

Tomography is an imaging method that can be used to acquire typically 3-dimensional information about the inner contents of an object by measuring a physical change induced to the signal by the target when it is illuminated, disturbed or penetrated by a signal. The signals can be either light, acoustic waves, radio waves, quasi-static electromagnetic fields, gravity fields, radioactive particles, neutrons or a combina-

tion of these [27, 58, 121, 126]. In Computed Tomography (CT) [87], the target area or 3-dimensional volume is modeled as sections, and by using mathematics and computing, the distribution of the unknown material parameter within the target can be computed via a reconstruction algorithm.

There are various fields of science and engineering that utilize CT. The fields of science closest to the tomography of asteroids in the context of this thesis are the geosciences [37], civil engineering [53, 55, 124] and biomedical applications [90, 110] , that are described briefly in next sections. Tomography is also used in optical applications where reconstructing the parameters by utilizing light intensity and reflections are used. An example of this is the tomography of those biomedical engineering applications where the measurements are on cellular or molecular level, and the structures to be measured are thin enough to be permeable by light. This is the case in, for example, Optical Projection Tomography (OPT) [111]

1.1.1 Civil engineering applications

Travel-time tomography originates from seismic tomography which was envisioned in the 1760s [48]. More recent advances have concentrated on achieving a 3-dimensional data from received signals [74, 134]. Even more localized tomography can be used in several applications such as reconstructing underground structures for tunneling or mapping of oil fields [75, 135]. In addition, developing measurement instruments and strategies for concrete structures is important, as the infrastructure in many developed parts of the world is aging and needs maintenance in the future [83].

Common to the civil engineering applications is that the data cannot typically be measured from every direction. Most clear example of this is the case of tomography of a soil surface where the measurement can only be performed from the top. This case is most relevant for the scope of this thesis as an asteroid can only be realistically measured from the top of the surface or from orbit. Typical of this case is that the signal used to perform the tomography must be suitable to penetrate the soil to be measured, and also that the reflections and echoes from the subsurface features must reach the receiver on the surface. For acoustic measurements especially in the vacuum of space, this leads to the requirement that the transmitters and receivers have a physical contact to the surface. For radio wave-based measurements, the resulting

signal frequency to be able to penetrate the soil imposes hardware challenges, as low frequencies requiring a large antenna are required [63].

1.1.2 Modern biomedical engineering applications

X-ray Computed Tomography has been most used and developed in the field of biomedical engineering. Recently these imaging methods which do not use x-rays or other radioactive substances have been more used. These methods include Magnetic Resonance Imaging (MRI) and ultrasonic tomography [46, 102]. They allow reducing the radiation dose given to the subject and, in case of ultrasonic tomography, more economic measuring devices. The current computational resources can be adapted to take into account the complex wave propagation effects especially in ultrasonic tomography [13]. Specifically, tomography of the breast (mammography) by ultrasonic tomography has been researched and an accurate 3D image of the breast can be recovered [117]. It is also used for other medical applications [35].

1.1.3 Analogy to asteroid tomography

One of the central motivations for the present work is that the mathematical methods of the above described applications are very similar to those needed in potential asteroid subsurface investigations in Publications II-III and in [99]. Tomography of asteroids, i.e., finding out their interior structure or heterogeneities, can be attempted based on, e.g., gravity field measurements or penetrating radar signals. In space, the measurements can be performed from multiple different directions which, in principle, motivates reconstructing the global interior structure. However, the in-situ measurements involve several restrictions due to which obtaining a full signal coverage is difficult. These include, for example, the strict payload limits which prevent using heavy instrumentation in the measurements. For small solar system bodies, however, even a small spacecraft can be sufficient, since on one hand, the weak gravity field does not necessitate high propulsion power, and on the other hand, the mineral composition of small solar system bodies is highly porous and has, therefore, a relatively low permittivity and is penetrable by a low-power (e.g. 1 W) radar signal [63]. Another challenge is set by the orbitography, that is, the orientation of the orbit or the trajectory of the spacecraft in relation to the asteroid spin axis.

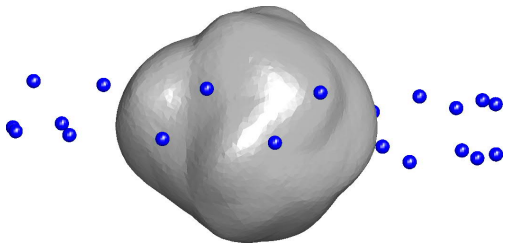

Figure 1.1 A schematic (non-scaled) illustration showing a set of possible measurement points from a limited-angle orbit configuration. This orbitography results in a pronounced aperture around the polar regions of the target asteroid.

Namely, if the target asteroid has a spin perpendicular to the orbiting direction, a full measurement point coverage can be obtained even by a single spacecraft, but other spin-orbit combinations enable only limited-angle measurements. That is, there will be an aperture around poles of the asteroid which is not visited by the spacecraft as illustrated in Figure 1.1.

The ground-based gravity and radar inversion applications are analogous to asteroid tomography. Inverting the gravity field for a bounded target is also closely related to other quasi-static inverse applications such as the Electro-/Magnetoencephalography (EEG/MEG) or Electrical Impedance Tomography (EIT) of the human brain and the head, which is also one of the research foci of our research team. Similarly, the tomographic radar imaging can be associated with microwave tomography of the brain [110] or specifically that of the breast [117], whose permittivity is close to the level occurring in an asteroid, e.g., the relative dielectric permittivity ϵ of 4.

The mathematical methods used in tomography in biomedical applications are very similar to those being developed for asteroid tomography. One example of such imaging method and application is neonatal EEG. In EEG the electrical activity in brain can only be measured by a limited number of electrodes attached to the human head, and the directions that can be acquired are also limited as the electrodes cannot be installed inside the head. This results in a sparse measurement data set as in asteroid tomography. The ongoing research of our team [100] has focused on the improvement of the electrode model used in this application.

1.2 Asteroids and other small solar system bodies

Asteroids are typically described as rocks flying in the solar system in various types of orbits around the Sun [16]. They have been observed via telescopic measurements that show the asteroids in different types of orbits, that is, they are in different parts of the solar system. Spectroscopy observations show that the reflected light spectra of asteroids differ from one another [23]. This allows for the only direct method to observe the asteroids from Earth. Large number of observations has resulted in classification of asteroids into many different categories that are referred as taxonomies by the planetary scientists [18]. Most commonly the taxonomies divide the asteroids into few main groups based on observations of reflected spectra and by their location in the solar system. There are the C-type asteroids, which are dark and have carbon in their spectra, S-type which have silicate in their spectra and are usually described as stony, and M-type which have metals in their spectra. However, M-type asteroid does not always mean metallic composition, as for example asteroid Lutetia turned out to be very different when observed more closely by a visiting spacecraft [93]. There are also other types that do not belong to the first three groups. This taxonomy grouping presented here is very simplified, and it follows the Tholen classification [21]. Existing taxonomies are being improved and new taxonomies are developed based on new observations and the needs of the scientists.

To understand why asteroids are in different types of orbits around the Sun, it is vital to describe some details about the evolution of the solar system and how the evolution is modelled. In addition, there are also other challenging mathematical issues related to asteroids, such as population analysis [16] and light curve imaging [107].

1.3 Asteroid composition as a point of interest

At least the following three different fields of science, economy or engineering are interested in asteroids, and in particular, their interiors. The motivation for each of them is however different.

1.3.1 Scientific interests

The formation and evolution of the solar system has been studied since as least the 17th century. French mathematician Rene Descartes first proposed a model of the formation of the solar system, but his proposed model of the evolution was primitive and it could not explain everything [112]. Since then, the models have been improved and new hypotheses have been developed and tested.

Currently developed model of the early solar system formation is called the Nice model [28, 44]. The development was done at the Observatoire de la Cote d'Azur in Nice, and the model was released in 2005. The basis of the model is the hypothesis that the initial protoplanetary disk first formed the giant planets quite near the Sun. The giant planets then migrated to their current positions relatively far away from the Sun. This explains many aspects of the observed solar system conditions in their present state, including the Kuiper belt objects at the outermost part of the solar system, and trans-Neptunian objects which are the small dwarf planets outside the orbit of Neptune, such as Pluto. The model has already been improved and extended since the initial release as the scientific research and modelling has progressed. These changes do not affect the initial conditions and hypotheses in the model, and it is still seen as solid foundation to build new theories and to motivate further studies.

Many aspects in the Nice model are still left without direct proof. One of them is the evolution and distribution of those fragments of the protoplanetary disk that did not end up forming the present planets during the earliest evolution. This is described by the Grand Tack model [84], which is a refinement of the Nice model suggesting that Jupiter first approached the Sun before obtaining its position further away. The models suggest that the fragments are not direct leftovers of the original formation and that they are collisionally evolved through the evolution of the solar system. This happened through a process called Late Heavy Bombardment[45] and a resonance condition in the orbits of Jupiter and Saturn [73]. These explain, at least partially, the current state of the outer solar systems, the existence of the asteroid belt and the orbital features of many of the asteroid classes. If the small solar system bodies are collisionally evolved, they are most likely not monolithic due to fragmentation in the impacts. This collisional evolution of the solar system would be most evident in those asteroids that have not been evolved in recent history of the solar system. This has motivated impact simulations [31] and direct compar-

isons of the effects of the simulated impacts to real-world observations of features on asteroids [26]. These observations are obtained via ground-based telescopes and on-site visits or flybys of space missions. Among the most interesting asteroids are the Near-Earth Asteroids (NEAs) for their close distance to the Earth. Their orbits are close to the orbit of Earth and they are not disturbed by the gravity of the giant planets of the outer solar system. Some of them are in highly inclined orbits, which make them difficult to detect and new ones are being found all the time [17].

The scientific interest in asteroids is, among other things, directly related to trying to find out if the asteroids are, in general, monolithic rocks or collisionally evolved rubble piles. There is indirect evidence that points to these asteroids being non-monolithic [127]. These indirect observations include simulating asteroids impacting each other and trying to figure out how the asteroids would look like after this type of evolution [31] and then comparing these results with images of real asteroids. Other indirect observation method is the measurement of the bulk density or the mass of the asteroid through observations of its orbit in fly-bys of other, better known objects. The direct evidence and on-site observation of the interior of these asteroids is one of the most important missing links. However, in recent years, more data of NEAs has been collected through on-site visits by space missions (see following chapters), but no direct observations of the interior configuration of such targets through radar measurements have been done.

Another important point is valid for smaller than $\sim$40 km diameter asteroids. NEAs fall into this size distribution. Some asteroids smaller than 250 m in diameter seem to rotate fast [97] and there are practically no larger fast rotators larger than that. Small bodies are generally limited to comparably slow rates if they would be bound together merely by gravitational forces. That is, faster rotating bodies would break apart due to rotation-induced forces overcoming the gravitational forces. This they seem to be non-monolithic gravitationally bound rubble pile asteroids [98, 125].

1.3.2 Planetary protection

Space agencies such as National Aeronautics and Space Adminstration (NASA)[1] and the European Space Agency (ESA)[2] are motivated to study Near-Earth Asteroids. They are also, in part, politically mandated to do so. One of the most important reasons for the agencies is to gain insight on the asteroids to more accurately simulate different ways to deflect those asteroids that might threaten the Earth. Several methods of deflection have been studied. There are several ways on how to alter asteroids trajectory, some of which are presented in Figure 1.2.

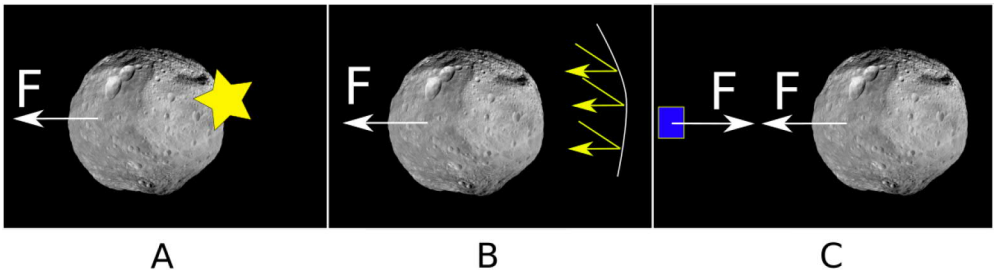

Figure 1.2 Three methods of asteroid deflection. Each one of these applies a force F to the asteroid, which will affect the direction and magnitude of the velocity vector (not drawn). A) Explosive propulsion. B) Propulsion via focused solar radiation and outgassing C) Deflection via gravitational effect. Image not to scale. Options A and B as presented are simplified and do not account for the Yarkovsky effect [15]. Original Vesta image: NASA/JPL-Caltech/UCAL/MPS/DLR/IDA

Most obvious way to deflect an asteroid is to affect it by detonating an explosive near or on it, and one possible device to achieve this is a nuclear detonation. This method has some difficulties with international legislation, namely, the Outer Space Treaty of 1967 prevents placing any weapons of mass destruction into outer space [3], but might be required if there is a quickly emerging threat to Earth. However, in recent years the United Nations has set up an agreement on planetary defence to have a coordinated, international strategy and action plan for planetary defence matters [62]. For some targets and required amounts of deflection, a kinetic impactor is a possibility. However, the effect of these approaches depends on the composition of

[1]The space agency of the USA. `http://www.nasa.gov/`.

[2]European Space Agency. `http://www.esa.int/`.

[3]Outer Space Treaty of 1967. `https://history.nasa.gov/1967treaty.html`. Accessed 5.7.2019.

the target. What remains after the explosion or the impact is mainly unknown, as the interior structure of the asteroid is unknown. For these methods of planetary protection, it is vital to gain insight of the interior structure to be certain about the effects of the deflection attempt, and to ensure that the remaining parts of the asteroid are sufficiently small so that they will not cause a global catastrophe upon hitting the Earth. This type of mission has been recently studied in NASA's HAMMER mission study [9].

Second way of altering the trajectory of the asteroid via propulsive means has been extensively studied. These methods are largely based on focusing some type of energy to the asteroid surface, which causes either propulsive effect directly [30] or indirectly through heating and outgassing. The latter can be done via focusing the energy radiating from the Sun to the surface of the asteroid with mirrors and other similar reflective surfaces. The surfaces of several asteroids have been studied *in-situ* and spectroscopy measurements can be performed via optical means from Earth or via Earth-orbiting space telescopes. However, these effects can also influence the Yarkowski effect [15]. This effect is a force that acts on a rotating body in space due to the warming of the surface having a phase delay in relation to the Sun's direction. Altering the direction of this force could be possible by altering the surface heat of the object.

Other ways of deflection include gravitationally pulling the asteroid by flying multiple heavy spacecrafts in a parallel trajectory with the asteroid to alter its orbit around the Sun in such a way that the collision threat is eliminated [76]. For these methods to work, the mass and other characteristics of the asteroid must be determined with some accuracy. It is unlikely that a mission to directly measure the mass could be implemented before flying the actual deflection mission. Studies regarding characterization missions to gain this knowledge have been conducted, such as [42].

1.3.3 Commercial interests

Asteroid mining has been a popular term during the recent decade. There have been recent technological advances and scientific efforts [6] to make it real rather than science fiction. These include less expensive rocket launches to space with cheaper, reusable launch vehicles such as ones produced by Space Exploration Technologies

Inc. (SpaceX)[4]. Also there is a so-called newspace boom especially in the United States, with several small startups developing new technologies. The newspace economy refers to a concept in which countries and commercial companies of all sizes can participate in evolving space technology and missions, for example, through affordable small spacecraft. That is why also Finland has an ongoing newspace economy program [5]. Asteroid mining, which is a dream of some of these startups, can be thought as a puzzle. There are many pieces that must be in place for it to become realistic possibility.

Commercial interests are focused on several different types of asteroid utilization. Firstly, *in-situ* utilization of asteroids as raw materials is the focus for Near-Earth asteroids. If the asteroid contains water or hydrogenated minerals, it can be processed on-site to separate it to oxygen and hydrogen which can then be utilized as fuel for rocket engines. Water can also be just stored to be utilized for human consumption on manned missions. Usage of electrolysis to use water as thermally stable propellant has been studied recently [33]. In addition, the raw rock material could be used as building material.

Another type of utilization is more far-fetched. X-group asteroids include some asteroid types that can contain precious metals, such as platinum. This has been proven via spectral observations [24]. The main commercial interest is to utilize the metals for production *in-situ* [61]. Another idea is to have the metallic fragment sent to a collision course with Earth, as the fragment would survive the re-entry into the atmosphere and the material could then be collected from the bottom of the ocean. If the valuable metals are common inside many M-asteroids, then it would benefit the commercial companies to try to localize them via tomographic measurements before the expensive and time-consuming on-site mining process.

Typical focus of the asteroid mining startups is either to develop some small parts in the big puzzle, such as asteroid capture and water recovery (Ad Astra[6]) or a new propulsion system (Deep Space Industries, DSI)[7]). Some of these companies appear to have a far-reaching vision related utilization of materials in space, building space stations, colonization of outer space and other such things. Of the first asteroid

[4]SpaceX.`http://www.spacex.com/`. Accessed January 1st, 2019.

[5]Business Finland: New Space Economy. `https://www.businessfinland.fi/suomalaisille-asiakkaille/palvelut/ohjelmat/new-space-economy/`. Accessed 10.7.2019.

[6]Ad Astra Rocket Company. `http://www.adastrarocket.com/aarc/`. Accessed January 1st, 2019.

[7]Deep Space Industries. `http://deepspaceindustries.com/`. Accessed January 2nd, 2019.

mining startups, DSI and Planetary Resources[8] were the most prominent. They had to start from small parts of the puzzle. DSI started with propulsion system that can utilize water, and Planetary Resources with spectroscopy-based systems that can detect the water and other hydrated minerals on Earth from Low Earth Orbit, with a view from utilizing this technology in asteroid prospection in the future. In 2018, both of these companies were acquired by other companies. DSI was acquired by Bradford Space, Inc.[9], which is a technology company that develops propulsion and attitude control systems for various types of satellites. Planetary Resources was bought by ConsenSys[10], which is a blockchain technology company. ConsenSys is potentially interested in Planetary Resources' model of commercial transactions with regards to buying, processing, and selling resources in outer space. With these company acquisitions, it can be said that the first asteroid mining boom is over and next startups will focus on yet new things to solve, such as developing a low-cost spacecraft[11] capable to perform a deep space mission or to visit a small solar system body.

1.4 Spacecraft and missions

Many missions to asteroids have been proposed previously. In the context of this introduction, it is relevant to introduce the most relevant missions and their features. These missions include interesting new concepts, such as tomography or radar instruments, a landing, or a new technology that is being utilized.

1.4.1 Previous missions

One of the original ideas, the Deep Interior mission concept, to try to reconstruct the interior of an asteroid was proposed by Asphaug in 2003 [3, 4]. This mission concept included a spacecraft together with an initial instrument suite. It is unclear how much detailed analysis was performed for this concept, but it stands out as one of the first proposals to try to accomplish the interior imaging by utilizing radio

[8]Planetary Resources. `https://www.planetaryresources.com/`. Accessed Feb 2nd, 2019.

[9]Bradford Space Inc. `http://bradford-space.com/`. Accessed January 2nd, 2019.

[10]ConsenSys. `http://bradford-space.com/`. Accessed January 3rd, 2019

[11]Bradford Space: Explorer `http://bradford-space.com/products-xplorer.php`. Accessed 1.8.2019.

waves, in this case, radio reflectance (monostatic) imaging where the reflected radio signals are analyzed. It can be assumed that tomography-based approach would have been possible.

In the early 2000s, ESA studied an asteroid rendezvous mission called ISHTAR [29]. It was a mission study centered around a radar tomography instrument that would probe a small asteroid up to 200 m depth. The study involved European industry participants and was selected for further studies. However, Don Quijote mission was chosen for further analysis and development [41], and the ISHTAR mission was not developed further. The Don Quijote mission in itself continued evolving.

Missions that have visited asteroids, such as NASA's NEAR-Shoemaker and Deep Impact, China's Chang'e 2, Japanese Hayabusa [1] and Hayabusa 2 [116] have not included a radio science instrument. Scientists proposed a mission named Marco Polo [11] in many mission calls. The mission proposal did include a tomographic radar instrument within the optional lander package [12, 79, 95]. However, in the 2013 ESA Cosmic Vision call, the mission was not selected for implementation[12].

The most relevant mission in regard to the radio tomography is the Rosetta mission by ESA [43]. It was a follow-up on numerous other previous missions to comets, and was originally meant to be as shared project with NASA. However, NASA cancelled the mission and ESA was left to design a mission of its own. The original target of Rosetta was the comet 46P/Wirtanen, but the launch window was missed due to technical difficulties, and the eventual mission was flown to comet 67P/Churyumov-Gerasimenko. During the course of the flight to the target comet, Rosetta made several flybys of Near-Earth Asteroids and used spectroscopy instruments to gain data about the asteroids. Rosetta included a lander that was named Philae, and onboard both the lander and the orbiter was a radio tomography instrument called CONSERT [10, 64]. It was designed to transmit a signal through the body of the comet and the Rosetta spacecraft had signal reception and recording hardware. The plan was to try to achieve tomographic reconstruction of the comet interiors, but due to partially failed landing of Philae, the very limited amount of data recorded made this very challenging [65]. This mission set a reference point for tomography modeling and radar imaging of small solar system bodies. A large amount of fundamental research [10, 64, 65] and technical studies [88, 94] were done in preparation and during the mission.

[12]ESA selects Planet-hunting Plato mission `https://sci.esa.int/web/plato/-/53707-esa-selects-planet-hunting-plato-mission`. Accessed 1.3.2020.

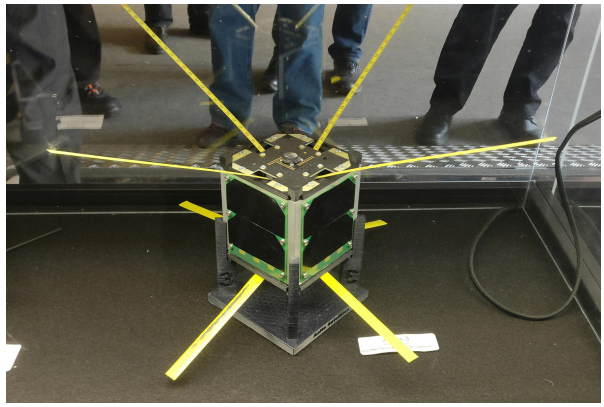

Figure 1.3 A model of the Finnish Aalto-3 CubeSat on display on an educational tour around Finland.

1.4.2 Small spacecrafts and CubeSats

In recent years, small nanosatellites, CubeSats, have gained popularity. They are nanosatellites that follow standardized shape and size, and they utilize a standard release mechanism from a standard deployment device, which is installed on a space launch vehicle's upper stage [123]. These types of nanosatellites have proven to be an inexpensive way to develop and test new techniques by utilizing cost effective commercial off-the-shelf (COTS) electronics on a Low Earth Orbit (LEO). They have especially proved useful in university-based projects, such as in the Finnish Aalto CubeSats (Figure 1.3). The CubeSats are typically flown on limited length (1-2 years) missions on low orbits inside the Van Allen's radiation belts [128], so the harmful effects from solar radiation is not a big issue.

Both ESA and NASA have made advances in developing the CubeSats to be used in outer space. NASA has already utilized two Mars Cube One (MarCO) CubeSats with the InSight lander mission [13]. The task of these CubeSats was to relay detailed telemetry from the InSight spacecraft during its landing to Mars. ESA has developed the Miniaturized-Asteroid Remote Geophysical Observer (M-ARGO) mission concept, which is a stand-alone deep space CubeSat to a NEA. The actual spacecraft is now being designed[14] and many aspects of the hardware and mission concept have

[13]Mars Cube One. `https://www.jpl.nasa.gov/cubesat/missions/marco.php`. Accessed 3.1.2019

[14]ESA and GomSpace sign contract for implementation of the Juventas CubeSat in support of the Hera mission. `https://gomspace.com/news/esa-and-gomspace-sign-contract-for-implementa.aspx`. Accessed 10.8.2020.

been studied [78]. The trend towards the nanosatellite and other small spacecraft utilization is a change from the ISHTAR concept, in which the spacecraft mass was 313.5 kg [29].

1.4.3 On-going and future missions

The Japanese Space Exploration Agency (JAXA) has flown its Hayabusa-2 mission [129] to asteroid 162173 Ryugu. The spacecraft approached its target in 2018 and made a successful landing on it in 2019. Notable detail of this mission is the utilization of small spacecrafts in addition to the main spacecraft. Hayabusa-2 included the European Mobile Asteroid Surface Scout (MASCOT) lander and two Minerva-II rovers. The rovers feature a novel method of hopping on the surface of the asteroid.

NASA launched the OSIRIS-REx mission to asteroid 101955 Bennu in 2016 [14]. Like Hayabusa missions, OSIRIS-REx is a sample return mission. This mission deserves to be mentioned as the first of many NASA missions to asteroids. NASA has selected two more missions (Lucy and Psyche) to asteroids to be launched before 2023 [47]. Neither of these missions particularly focuses in the interior of the asteroid targets, but the Psyche mission will attempt to deduce the interior structure of the asteroid by measuring its gravity field by measuring tiny changes to the spacecraft orbit via radio measurements [89].

The most recent rejected ESA mission proposal was the Asteroid Impact Mission (AIM), in which the AIM spacecraft would have released two or more CubeSats, and a lander called Mascot-2 [80]. This lander would have included a radar instrument. The AIM mission would have been the European contribution to NASA's Asteroid Impact & Deflection Assessment mission (AIDA) [81]. AIDA was, in turn, a later development of the Don Quijote mission[15], and the project was deep in development when it decided not to be funded in 2016 [16]. AIM would have included two radars: a low frequency radar for deep interior investigation, and a high frequency radar to investigate the surface regolith [49, 50, 52]. After the funding decision, AIM continued as a technology development project and was renamed Hera [81],

[15]The story so far. ESA. `https://www.esa.int/Safety_Security/Hera/The_story_so_far`. Accessed 15.3.2020.

[16]Jeff Foust, The Space Review. `http://www.thespacereview.com/article/3124/1`. Accessed 20.3.2019.

which was accepted for implementation at the end of 2019[17]. It will demonstrate autonomous operations and other technologies for CubeSat utilization in deep space. These will be valuable in order to implement more ambitious missions using CubeSats. ESA selected two CubeSats called ASPECT and JUVENTAS for this mission. With JUVENTAS CubeSat, Hera includes a radar tomography instrument based on CONSERT heritage hardware [51, 60].

During the course of this thesis study, ESA performed a Concurrent Design Facility study [18] for different types of missions to a Near-Earth Asteroid or to the asteroid belt. In this study, a radar instrument with a tomographic analysis approach that was developed in this PhD project in Publication IV was analyzed and deemed to be a mission enabling technology. The radar instrument was onboard one or more CubeSats which the mission's mothership spacecraft would fly to the target asteroid. Based on this study, a new ESA mission class called F-class was introduced [19]. An F-class mission would be an opportunity to perform a more complex multi-spacecraft mission based on experiences from Hera.

1.5 Research outline

The scientific need to get more information of the rubble pile Near-Earth asteroids is clear. There are also other parties that are interested in utilizing the technology that enables this. The research target is to combine all three aspects described in this introduction: Science case, small spacecraft utilization as a part of a larger mission or on its own mission, and the existing tomography applications.

The things to be analyzed include computational, modelling and physical mission design and hardware aspects. Computationally the simulation runs related to the tomography must be able to be run in a sensible time to enable efficient development of algorithms and methodology. Also, the modelling errors must be kept sufficiently low. For physical hardware, the main challenge is related to small nanosatellite-sized spacecraft's autonomy in harsh radiation environment, while utilizing COTS electronics. In addition, packaging a long, deployable dipole antenna into a CubeSat is

[17] ESA ministers commit to biggest ever budget. ESA 2019. http://www.esa.int/About_Us/Corporate_news/ESA_ministers_commit_to_biggest_ever_budget. Accessed 2.3.2020

[18] ESA Small Planetary Probes CDF Study Report: http://sci.esa.int/jump.cfm?oid=60411. Accessed 23.2.2019

[19] ESA F-class call.http://sci.esa.int/jump.cfm?oid=60498. Accessed 20.8.2019

challenging.

In this context, the research began with analysis of the tomography method in Publication I and the nature of the signals and how much the signals could be compressed onboard the spacecraft to their minimum information content. This was to get a feel of the nature of data in the worst case, and to study how the existing methodology could be converted to real hardware on a spacecraft. There was also a need to develop the radar and tomography modeling methods to be implementable on a real space mission with realistic parameters. This required further development of the simulation methods so that the method development and analysis was possible to be performed. Furthermore, it was required to analyze the feasibility of a real mission to see if all the possible parameters both in simulations and model development as well as physical parameters would agree, in principle, with the real-life conditions on such a mission to a rubble-pile NEA.

2 METHODS ENABLING TOMOGRAPHIC IMAGING OF A NEAR-EARTH ASTEROID

For the tomography of an asteroid to be possible, it is necessary to study different radar methods and the parameters that affect the signal propagation in the asteroid. It is expected that the asteroid will be of certain size and that it will have a certain dielectric permittivity. These will be the limiting parameters to the required penetration depth of the radar signal. Furthermore, it is required to analyze a realistic mission configuration and identify its effect on the result.

For this thesis project, a way to utilize Stepped Frequency Radar (SFR) technology was studied. SFR records so called frequency lines consisting of received signal amplitude and phase shift data. Using this data, and combining multiple frequencies at one measurement position, makes it possible to shift the data from the frequency domain to time domain by using inverse Fast Fourier Transform (IFFT) methods. The expected tomography inversion results by using this type of radar implemented on a small CubeSat was analyzed in Publication III. Furthermore, a mission concept study was made and published in Publication IV.

2.1 Principles of penetrating wave measurement

A radar works by transmitting an electromagnetic wave through a medium. In the case of asteroid tomography by utilizing one or more orbiting spacecraft, this medium consists of empty space and the target asteroid itself. When an electromagnetic wave meets up a boundary between different dielectric permittivities caused by the surface of the asteroid or by interior details, it can get reflected, diffracted, or transmitted through. These transmission modalities are present at the same time. A 3-dimensional mathematical presentation of this process is presented in Chapter 3.

The signals can be received at any position around the asteroid, but in the as-

teroid tomography application, the positions are sparse and limited by the number of spacecraft and the number of possible measurements around the asteroid during the limited lifetime of the mission. The latter limitation is also due to the physical limitations that come from the achievable orbit configuration, as well as due to the limited memory onboard the CubeSat-type spacecrafts.

Recording of such signals can be done in several ways. In Publication I, an analysis was performed on studying the travel time of the transmitted signals. By examining the travel time of the power of the signal, a potentially promising way to reduce the amount of data required to a minimum was discovered. However, travel-time tomography is one of less sophisticated ways to implement tomographic imaging, and due to several constraints, it will be beneficial to use more advanced radar scheme.

2.2 Limiting factors for signal transmission and reception

The target of this thesis study is to utilize several CubeSats or other small spacecraft with radar units, instead of a single large spacecraft with a powerful radar. This imposes several limits on the radar properties. The first main limitation is the amount of power available for signal transmission. A small spacecraft can only have a small solar panel for electricity production. An energy store (battery) helps, as using stored energy can enable the peak power usage to be larger than the electricity produced by the solar panels. However, the size of the spacecraft also imposes a limit in electronics cooling capability, as the available external surface for radiative cooling will be limited.

A CubeSat might have a solar panel having deployed dimensions of 0.2 m x 0.3 m, resulting in an area of 0.06 m^2. Assuming a solar radiation flow[1] of 1370 W/m^2 and a rather optimistic energy conversion efficiency $\eta = 0.30$, the maximum electrical power available is in the region of 25 W. It can be assumed, that a battery is used, and that spacecraft cannot fly in an ideal orientation with regards to the Sun. Also, the solar panels will degrade due to radiation effects. and the other systems onboard the spacecraft consume some of this power. Therefore, a radar unit power consumption of 40 W to 50 W when transmitting with a very low duty cycle of less than 1 % is a reasonable maximum estimate.

[1]This solar radiation flow is shown as the average flow on 1 AU distance from the Sun in multiple literature sources, and is called solar constant.

In bistatic radar, where there are separate receivers and transmitters, the basic relationship between radar signal transmission range, antenna efficiency and transmitted and received signal power levels is given by the bistatic radar equation

$$P_r = \frac{P_t G_t G_r \lambda^2 \sigma}{(4\pi)^3 R_{tx}^2 R_{rx}^2}, \tag{2.1}$$

where P_r is the received signal power, P_t is the transmitted power, G_t is the effective gain of transmitting antenna, G_r is the gain of receiving antenna and λ is the wavelength of the signal [130]. The σ is the radar cross section of the target. Terms R_{tx} and R_{rx} denote the radar range, i.e. the range of the target from the transmitter and receiver, respectively. In the equation, the received signal power benefits from larger wavelength and higher transmitted signal power. However, this equation is based on propagation in free space, i.e. it does not include any attenuation effects due to signal traveling inside the target, or scattering effects when the signal is being affected by the target material. Therefore, this equation is not valid for tomography and finding a relationship between the resolution of the recovered permittivity distribution, radar parameters and the tomography calculations is required.

The size of the potential target asteroids for tomography is in the region of 100 m - 1 km. Therefore, as low frequency as possible is optimal, as the penetration depth to the material has a relationship to the used wavelength [63]. For wavelength consideration, a simplest antenna type that can be used is a dipole antenna, which can consist of a single wire. In space, the antenna material and structure must be carefully considered for it to stay in its dipole form, i.e. straight and rigid. Dipole antennas can have a length of, e.g., 2λ, λ, $\lambda/2$, $\lambda/4$ and according to [67] the half dipole offers balanced gain and is the most used type. Considering a radar frequency of 20 MHz, the wavelength given by $\lambda = C/f$ where C is the wave propagation speed (the speed of light, 299 792 458 m/s) would be 14.99 m and thus the half dipole antenna length would be 7.49 m. This is on the upper limit of what can be installed and flown in a small CubeSat-sized satellite when divided in two sections. The configuration would be as presented in Figure 5.5, i.e., the $\lambda/2$ dipole would be formed by opening the sections in two opposite directions from the main spacecraft body.

For the received signal power, it would be optimal if the transmitting and receiving dipole antennas would be accurately pointed so that most of the transmitted signal power would be directed towards the target. However, a 45 degree error in the

antenna orientation will result in only 1 dB power loss in the received signal, so the antenna and thus the spacecraft does not need to be very accurately pointed.

Considering Equation 2.1, using even lower frequency would be beneficial on the received signal power, but the target is to gather data on the interior structure of the target, lower frequency would result in diminished detail in the reconstruction. Considering a stepped frequency radar, the relationship the range resolution ΔR and the radar bandwidth B is given by $\Delta R = C/2B$ where B is the bandwidth of the modulated radar signal [101]. In the case of an asteroid, the radar cross section of the asteroid is dependent on the radar frequency that is being utilized, thus the parameters λ, B and σ have complex relationship. Scattering effects can be assumed to dominate over λ due to the complex shape of the target and the radar cross section can vary significantly with different frequencies. Radar bandwidth must be at a certain level to resolve details in the target. Optimizing these parameters requires detailed investigations with the target and results vary significantly with different targets. This is due to having to optimize the parameters for the expected dielectric properties. Recently this type of modelling has been done in [49] for the Hera mission.

2.3 Radar imaging strategies

There exist several ways to utilize radio wave transmissions in a radar application [101]. Radar wave can be continuously transmitted wave with a certain frequency f or several frequencies, where typically a signal is modulated on a lower-frequency carrier wave. A receiver can then listen to this signal and record the amplitude of the received signal. If the receiving antenna is the same as the transmitting antenna, which can be the case on mass restricted systems in space missions, the transmitted signal must be pulsed, i.e., it can transmit for a time period and then listen the radio wave that gets reflected and affected by the target domain. From this received signal, one can measure travel time, signal amplitudes and the phase difference to the original signal if an adequate synchronization inside the radar electronics can be maintained for this time period.

In Publication I we studied effectiveness of travel time tomography when the signal is arguably very low quality and showed that if a rigorous enough mathematical modeling is used, even it can give interesting data about the target domain. How-

ever, to get maximum amount of data for radar modeling, the signal should be able to be recorded in time domain, which is a challenge in a real radar electronics unit. One possible radar methodology is the stepped frequency radar, where the radar electronics, including the antenna, is designed to operate on base frequency f, and many frequency steps Δf around this base frequency are measured. The result is a measurement set of frequency lines consisting of amplitude and phase shift measurements. Using inverse FFT methods [40], this data can then be converted back to time domain, enabling full wave tomography which required the time-domain data.

For any bistatic or multistatic radar measurement, the signal transmission from the transmitting spacecraft and reception from the other spacecraft must be synchronized. Some radar imaging strategies require more stricter synchronization than others. One of benefits of the stepped frequency radar is that the frequency lines can be measured even when the synchronization is less accurate, and the inverse FFT can still result in a acceptable time domain representation of the measurement. The critical issue is in the radar electronics which requires the oscillators to be synchronized with the incoming signal. In general, space-grade atomic clocks are in development by the space agencies [38, 69]. The parameters such as power consumption, radiation tolerance and physical size of commercially available, less accurate chip-size atomic clocks are within implementable parameters for even the small spacecraft. However, for stepped frequency radar, there are some other challenges for the radar hardware itself, that are briefly described in [101].

2.4 Mission concept and design

Utilization of small satellites has become popular in Low Earth Orbit (LEO) missions through the CubeSats. CubeSats are semi-standardized nanosatellites, typically consisting of 10 cm x 10 cm x 10 cm cube-shaped units. One unit is denoted as 1U. Designs with 1U, 3U and 6U sizes have become popular for LEO applications, as they can be either small technology demonstrations (1U-3U) or larger scale platforms (6U or more). The other aspect of the CubeSat revolution is the semi-standard deployment mechanism, that enables the CubeSats to be integrated to the launch vehicle and released in such a way that they do not pose any additional risk to the main missions. This way, they typically utilize the available extra performance in the launch vehicle.

In recent years, the space agencies have had increased interest to utilizing small satellites as additional elements in science missions. In science point of view, they are attractive as they enable multipoint measurements at the target. This will be potentially very important in the future Hera and F-class-type missions. Multi-point measurements can be used for radar, enabling bistatic or multistatic measurements. They can also be used to measure the target's gravity field using either direct measurements of the gravity gradient or indirectly by precisely measuring the movement of the spacecrafts within the gravity field. The former method is unlikely to be successful in a small spacecraft, as the accurate measurement of the gravity gradient is based on measuring the movement of a small weight on a spring when that weight is sufficiently far away from the center of mass of the spacecraft. For a nanosatellite, this would require a separate deployable boom where in the instrument would be installed, and that could lead to control issues or additional risk from the deployment of the boom. The latter method of measuring the movement can be done via doppler measurements if the radio frequency is sufficiently high to reveal the movement. 22-25 GHz radio signals (Ka-band) is shown to be sufficiently high for this, and there are existing radio solutions that can be integrated on CubeSat designs.

The trend to utilize small satellites is not going away, as more missions with extra performance is flown out of Low Earth orbit, and even to outer space. The most prominent example of such is NASA's new human-rated Space Launch System (SLS). It will have extra performance on almost every mission, thus yielding many new opportunities for small-scale scientific missions.

2.5 Current missions and developments

In 2018, the Mars Insight lander successfully landed on Mars. The mission included two Mars Cube One (MarCO) CubeSats as a technology demonstration. They were not performing scientific measurements, but they successfully demonstrated deep space communications by a CubeSat platform, autonomous operations, and radiation protection. The main purpose for the MarCO CubeSats was to relay telemetry from the InSight lander directly to the Earth receiving stations. This had to be done, as the spacecraft entering the atmosphere of Mars was ionizing the atmosphere around the spacecraft. That forms a barrier for data communications, and the relay satellites could receive these weak signals to relay the data.

ESA has a long-running M-Argo CubeSat design study, that was analyzed in the ESTEC Concurrent Design Facility in 2017 [78]. With M-Argo, ESA is identifying the required development paths so that the CubeSat technology can be utilized in deep space in the future. The technical developments include integrated electrical propulsion, flat array antenna for sufficient radio signal strength, and an X-band transponder that would enable ranging and navigation by utilizing the signal measurements done from Earth. Except for the first, these are very similar developments to the NASA's MarCO project.

JAXA's Hayabusa-2 mission differs in concept from the MarCO and M-Argo missions. Haybusa-2 utilizes small spacecraft to perform additional science with low technical risk, but it does not utilize CubeSat deployment system nor the CubeSat size standards. Hayabusa-2 includes a German Mobile Asteroid Surface Scout (MASCOT) lander, which is quite small (circa 30 cm x 27 cm x 20 cm) unit. MASCOT landed on the asteroid and performed scientific measurements with its spectrometer, magnetometer, and infrared radiometer. It used non-rechargeable batteries which lasted for around 17 hours. Hayabusa-2 also includes two so-called MINERVA rovers, that are very small cylindrical landers with approx. 18 cm diameter and 7 cm height. They can move on the asteroid surface by performing hops using a mechanical actuator. They remained operational for an extended period time on the asteroid surface, and included thermometers, stereo and wide-angle cameras. There is also a Rover-2 on the mission, which includes an additional accelerometer and might add to the scientific outcome of the mission by measuring the gravity field of the asteroid. [129]

For missions in deep space, advancing the CubeSat technology is important to increase their utilization. When taking a mission to a low gravity field target such as an asteroid or comet into consideration, there are a few key technologies, partly out-of-scope for this thesis project, to consider. One of them is the need for a new low-velocity CubeSat deployment system. Typically, the deployment systems used on LEO impart a sufficiently high impulse to the CubeSat to cause it to fly it out from the target asteroid's gravity field very fast. One or two orders of magnitude lower impulse deployer must be developed.

Other focus of the technology development is to find a reliable commercial off-the-shelf (COTS) computer platform that can be flown to outer space. The challenge is to make the utilization of such platform repeatable for several projects. During this

PhD project, it has been noticed that there are a few difficulties related to COTS systems. A CubeSat gets designed a long time before the mission is finally flown, and by the launch date, the technology that gets put on a CubeSat could be obsolete. This slows down the adoption of CubeSats for these missions, as the technology development and computer platforms need to be re-designed and reimplemented again for every mission. Recently, utilization of hardware originally meant for automotive purposes - that is, electronics in cars - has been seen promising and could help in developing technically stable CubeSat platforms for the deep space missions [68, 72]. This is due to safety and reliability being a major motivator in automotive industry.

2.6 DISCUS mission case study

To analyze the currently available CubeSat technology and suitability for a deep space mission to a small rubble pile Near-Earth Asteroid, we studied a standalone mission to such asteroid. As there was not direct funding for the mission, we performed the study as a feasibility study to identify the major issues. The basic concept of the mission is to perform low frequency radar measurements of an asteroid from 5 km distance, or closer. The spacecraft could be launched either as a standalone mission, or as extra payload on a mission that aims to get to the Moon. The mission shall consider using commercial off-the shelf electronics for the main computer, but we were not restricted to any computer platform. However, some comparisons and suitability of different platforms were evaluated. We identified four different areas that will need focusing on if this type of mission is designed: Radar antenna deployment, Autonomous control systems, Radiation protection and communications to Earth. Furthermore, the radar antenna orientation has implications on the orbit and orientation configuration at the asteroid. The Publication IV includes the main points that we studied, and the following section appends that by the parts we did not manage to include within the publication.

2.6.1 Radiation protection

CubeSats in deep space are exposed to radiation from various sources. These are radiation from the Sun, galactic cosmic rays, and in some cases, radiation from planets such as Jupiter. For the DISCUS study, some preliminary simulations on the

radiation dose on a typical mission to NEA were performed. Due to publication constrains, the results were left out, but they are included here for completeness. The simulations were performed by the team at Max Planck Institute of Solar System Research, Göttingen, Germany.

The flight time parameter used in the simulation was two year's worth of flight in deep space, which would be enough to reach at least some of the potential target asteroids. The amount of aluminium shielding on the outer surface of the spacecraft to protect the electronics was assumed to be in the range of 1-2 mm. The simulations were made by ESA's SPENVIS tool [2], and the effect of the particle radiation from the Sun was modeled with the Rosenqvist model [103]. The resulting radiation dose of 6 krad (1 mm) or 2 krad (3 mm) can be compared to published radiation dose tolerance of popular microcontrollers used in CubeSats [5]. The results point out that while the radiation dose will be high, the COTS electronics should survive a deep space mission with this type of protection. In addition, if the DISCUS CubeSat gets a ride to the target as a part of a larger mission, this radiation protection issue due to the accumulated dose will be reduced further as the CubeSat will be partially shielded by the host spacecraft during transit. Focusing on having protection despite of that is however beneficial to avoid other solar radiation related issues, such as single event upsets [36].

2.6.2 Orbit configuration

There are several orbit configurations that could be used to orbit an asteroid. For tomography measurements, some technical limitations apply. A dipole antenna is the least sensitive to noise when it is pointed at the noise source. In the case of Near-Earth asteroid, the strongest noise source is then Sun. Therefore, the antenna must be oriented so that the noise signal reception is minimized. For dipole antenna, this means that the long axis of antenna boom must point towards the noise source, i.e. the Sun. Other noise sources include planet Jupiter, which emits noise near the proposed 20-25 MHz band [22]. Depending on the target asteroid's location in relation to Jupiter, this radio noise must be further analyzed. Another limitation is the battery capacity on a CubeSat. This necessitates flying in an orbit that avoids

[2]SPace ENVironment Information System. `https://www.spenvis.oma.be/`. Accessed 10.9.2019.

extended periods of flying in the asteroid's shadow.

The radar measurements and suggested positioning accuracy (in Publication IV and in [66, 106]) present another requirement for the control systems. For every radar measurement, the orientation accuracy of 3 degrees should be sufficient and in the study process related to the Publication IV we analyzed the accuracy of readily available star trackers and concluded that sufficient accuracy can be achieved by using them. In addition, the DISCUS spacecraft is equipped with a laser altimeter, which enables accurate measure the distance from the surface of the asteroid.

2.6.3 Control systems and autonomy

Recently, the focus of both ESA and NASA regarding deep space CubeSats has been to demonstrate autonomous operations. In a spacecraft, these typically include both the scientific measurements or technical operations that serve the real purpose of the satellite, as well as automatic detection and recovery from any faults. The latter is is markedly more important when flying in deep space, where there are no fixed reference points, such as the infrared-radiating Earth surface nearby. Often the Sun can be found from the sky, and a star tracker can be used to identify the position accurately. Losing the time, i.e. computer clock reset, can be a huge issue. For the Earth-orbiting CubeSats, the most common way to recover from this is to put the spacecraft into safe mode and to await further commands. For deep space applications, this could be an issue, as the communication windows from the Earth can be difficult and sparse. Therefore, the computer must be redundant, and the clock must be specially protected from possible resets.

For DISCUS, the scientific goal requires to orbit the target asteroid in roughly stable distance and at a certain orientation with regards to the Sun. In the study, we concluded that it is often not possible to remain at a stable orbit for a very long time due to solar wind and radiation pressure having a proportionally significant effect compared to gravity of the asteroid. Due to this the minimum safe distance to approach could be as high as 5 kilometers. The realistic orbits are not circular, but elliptical, spiraling or so-called synthetic orbits. In synthetic orbit, the spacecraft flies between pre-determined points around the asteroid by utilizing its thrusters periodically to change the direction of the velocity, and in arched parabolas during other times. For example the Rosetta spacecraft used this type of trajectory [122]. These

orbit characteristics mean that control of the spacecraft could be easily lost without continuous autonomy. If the fault situation is prolonged, the spacecraft might eventually be just blown away from the asteroid by solar radiation pressure or impact it. However, this issue is mitigated by the low overall relative velocities. These dynamic situations are new to CubeSats and demonstrating these types of operations in deep space would be new for CubeSats. In addition, formation flying for multiple CubeSats - if DISCUS is launched in a bistatic or multistatic radar enabling spacecraft configuration - is still quite new [82, 96, 133]. It appears that ESA is currently doing exactly this research within the M-Argo CubeSat concept study as well as in implementing the CubeSats for the Hera mission. However, the point to make here is to suggest the teams to ensure that the lessons learned and the technology that is developed will not suffer from the obsolescence issue described in the previous chapter. This can be avoided if the control systems are developed in software or synthetized on hardware in such a way that they can be reused as the underlying technology changes.

2.6.4 Communications

If DISCUS was to be realized as a free-flying spacecraft, it would need a direct method to communicate with the Earth. The other deep space CubeSats M-Argo and MarCo use Earth-based receivers for the scientific data. In Publication IV we propose to utilize COTS satellite television (DVB-S2) radio components that operate in the 31.8 to 32.3 GHz frequency band. The suitable antenna must be able to be deployed from the spacecraft structure, and it must be rigid enough to hold the its form when deployed. The estimated data back to Earth from the radar measurements, the camera and the laser altimeter will be less than 2 GB in total. Preliminary calculations performed for the publication indicate that this amount of data could be transmitted back to Earth in less than 7 hours. This is advantageous as the onboard storage capacity requirements on the spacecraft can be reduced as the data can be transmitted periodically. The suggested communications strategy using COTS components could be implemented to the existing ESA ground stations, without the need of the largest dish antennas. This would reduce the operational cost, as the deep space communications can be an expensive operational overhead and utilization of the largest antennas is high, and available time is highly competed. This is due to limited com-

munication windows that result from the Earth's rotation and due to many different interplanetary missions using the same assets.

2.7 Ai3 mission proposal

After the DISCUS mission concept was published and ESA had published the results of the CDF study mentioned previously, ESA opened a new type of mission call. This mission call was named F-class, where in the letter F would mean a fast development cycle. Basic premise of the mission is to have hardware ready to launch for a mission in 2026 on one of the first Ariane 6 space launch vehicles. The main payload of the mission is the ARIEL spacecraft [92] (Atmospheric Remote-sensing Infrared Exoplanet Large-survey) and the remaining capacity of the launch is available for a F-class mission. Based on the DISCUS mission concept, we gathered an international team to develop a mission concept that utilizes multiple measurement modalities and multiple spacecraft, and called our proposal Ai3 - Asteroid In-situ Interior Investigation - 3way (Ai3) [7, 32]. The mission concept included two DISCUS CubeSats to perform the tomography experiment and JAXA's Small Carry-On Impactor (SCSCI) like that on Hayabusa 2 mission [129]. Added to the DISCUS concept in this version is the gravimeter, which could have provided useful additional information for tomography.

3 FULL-WAVE TOMOGRAPHY

This research started with existing wave propagation model used in [99]. At the start of the research, it was noted that there are other ways to simulate wave propagation, such as [77]. However, building on the previous work was a good starting point. To make it possible to simulate the wave propagating through an asteroid in a realistic scenario, the existing model had to be improved. The improvements done within this work extend the model of previous works, which have used the Finite Element Time Domain (FETD) method [19, 109]. As the main improvement the model of [99] was equipped with a far-field part to enable using realistic orbit distances in the numerical simulation. Moreover, in the 2D simulation of [99] the polarization effect was neglected due to a transverse electric wave propagation mode within a plane. The scalar wave propagation omitting the polarization provides a rough estimate also in the 3D case, and it has been used recently, e.g., in [104]. However, in the Publication III the polarization effect is taken into account and it is presented as an additional term due to the strong scattering effects on the surface of the asteroid which might result in significant changes in the polarization.

In addition, the calculation domain was restricted via a surface -based boundary to make it possible to simulate the system numerically in a GPU-equipped calculation cluster or even a high-end desktop computer. The size of the calculation domain, which would include the transmitting sources and receivers and the target itself, increases drastically when the sources and receivers are far away from the target surface (asteroid). The mathematical presentation in this chapter follows the one in Publication III by extending the description, and on the other hand, simplifying it slightly.

Table 3.1 Formulas for scaling between the unitless and SI-unit expressions. Here, s is a scaling factor and c is the speed of light in vacuum, 299 792 458 m/s^2

Item	Unitless	SI-units
Dielectric permittitivity	ε_r	ε_r
Electrical conductivity	σ	$(\mu_0/\varepsilon_0)^{-1/2}s^{-1}\sigma$
Position	$\vec{x}$	$s\vec{x}$
Time	t	$(\varepsilon_0\mu_0)^{1/2}st$
Frequency	t^{-1}	$(\varepsilon_0\mu_0)^{-1/2}s^{-1}t^{-1}$
Velocity ($\mathrm{c}=\varepsilon_r$)	c	$(\varepsilon_0\mu_0)^{-1/2}\mathrm{c}$

3.1 Mathematical formulation of the wave equation

The present wave equation and its weak form can be derived from the (unitless) Maxwell's equations

$$\nabla\cdot\varepsilon_r\vec{E} = 0 \tag{3.1}$$

$$\nabla\cdot\vec{B} = 0 \tag{3.2}$$

$$\nabla\times\vec{E} = -\frac{\partial\vec{B}}{\partial t} \tag{3.3}$$

$$\nabla\times\vec{B} = \vec{J}+\varepsilon_r\frac{\partial\vec{E}}{\partial t} \tag{3.4}$$

in which $\vec{E}$ and $\vec{B}$ denote the electric and magnetic field, respectively, and $\vec{J}=\sigma\vec{E}+\vec{f}$ is the total current density with $\vec{f}$ denoting the current density of the antenna. These formulas are in unitless form, and they can be converted to SI units by using the formulas in Table 3.1. The permittivity and magnetic permeability of the vacuum are given by $\varepsilon_0 = 8.85\cdot10^{-12}$ F/m, and $\mu_0 = 4\pi\cdot10^{-7}$ H/m, respectively, and s (meters) denotes the spatial scaling factor. By substituting the equations 3.1-3.3 directly, it follows that the curl of the 3.3 can be written as

$$\nabla\times\nabla\times\vec{E} = \nabla(\nabla\cdot\vec{E})-\nabla^2\vec{E} = -\sigma\frac{\partial\vec{E}}{\partial t}-\varepsilon_r\frac{\partial^2\vec{E}}{\partial t^2}-\frac{\partial\vec{f}}{\partial t}. \tag{3.5}$$

In equation 3.5 the first term affects the signal polarization change in the inter-

face between two dielectric (non-conducting) material. There are no free current sources, thus, no current, in the dielectric material. For this reason, the term in the parenthesis vanishes in other parts except the interface. When an electromagnetic wave propagates through an interface, there are current sources in the interface due to the changing dielectric permittivity. This happens if the dielectric permittivity is different between the materials. On the material boundaries inside and between the empty space and the target (asteroid), this term is non-zero and affects the polarity of the wave. In component form, this means that the component parallel to the surface normal is altered. In situation where the electric field is perpendicular to the surface normal, the polarization is unchanged which is always true for the component in that direction. A situation where electric field is always perpendicular is called transverse electric (TE) mode which is a relevant situation in 2D geometries and implicitly assumed in Publication II.

The second term is Laplace operator, which together with the terms on the right side of the formula forms a classical dampened wave equation in scalar form. The first term is the first-order derivative, and its multiplier $-\sigma$ (conductivity) causes absorption. The relative permittivity ε_r is the term that affects the velocity of the wave, and it is the unknown parameter in this inverse problem. Expressing the electric field and the position vector in the component-wise form, i.e., $\vec{E} = (E_1, E_2, E_3)$ and $\vec{x} = (x_1, x_2, x_3)$, respectively, one obtains the following general form of the present wave propagation model

$$\varepsilon_r \frac{\partial^2 E_i}{\partial t^2} + \sigma \frac{\partial E_i}{\partial t} - \sum_{j=1}^{3} \frac{\partial^2 E_i}{\partial x_j^2} + \frac{\partial}{\partial x_i} \sum_{j=1}^{3} \frac{\partial E_j}{\partial x_j} = -\frac{\partial f_i}{\partial t}. \tag{3.6}$$

3.6 is essentially the same equation as 3.5 but presented in a component wise form. The first-order partial differential formulation of this equation is given by

$$\frac{\partial g_j^{(i)}}{\partial t} - \frac{\partial E_i}{\partial x_j} = 0, \tag{3.7}$$

$$\varepsilon_r \frac{\partial E_i}{\partial t} + \sigma E_i - \sum_{j=1}^{3} \frac{\partial g_j^{(i)}}{\partial x_j} + \frac{\partial}{\partial x_i} \sum_{j=1}^{3} g_j^{(j)} = -f_i, \tag{3.8}$$

in which the first equation holds for $i = 1, 2, 3$ and the second one for $i, j = 1, 2, 3$.

The entries of the vectors $\vec{g}^{(1)}, \vec{g}^{(2)}$ and $\vec{g}^{(3)}$ are given by $g_j^{(i)} = \int_0^t \frac{\partial E_i}{\partial x_j}(\tau, \vec{x})\, d\tau$ for $j = 1,2,3$. The first and the second equation of (3.7) are multiplied by the test functions $\vec{w}^{(i)} \in [L_2(\Omega)]^3$ and $v_i \in H^1(\Omega)$, respectively. These test functions are locally supported functions which belong to the same space with the solution and whose superposition is the numerical solution of wave propagation equation. Integrating the result of this multiplication by parts yields the system

$$\begin{aligned} 0 = &\frac{\partial}{\partial t} \sum_{j=1}^{3} \int_\Omega g_j^{(i)} w_j^{(i)} \,\mathrm{d}V \\ &- \sum_{j=1}^{3} \int_\Omega w_j^{(i)} \frac{\partial E_i}{\partial x_j} \,\mathrm{d}V, \end{aligned} \tag{3.9}$$

$$\begin{aligned} -\int_\Omega f_i v_i \,\mathrm{d}V = &\frac{\partial}{\partial t} \int_\Omega \varepsilon_r E_i v_i \,\mathrm{d}V + \int_\Omega \sigma E_i v_i \,\mathrm{d}V \\ &+ \sum_{j=1}^{3} \int_\Omega g_j^{(i)} \frac{\partial v_i}{\partial x_j} \,\mathrm{d}V \\ &- \sum_{j=1}^{3} \int_\Omega g_j^{(j)} \frac{\partial v_i}{\partial x_i} \,\mathrm{d}V. \end{aligned} \tag{3.10}$$

This formulation is generally called as variation formulation or weak form of the original equation, which allows for less regular (smooth) solution than the original one. Therefore, the problem can be approached using simple piecewise linear test function basis when seeking for the numerical solution. The extension of the system into the component-wise form was done in Publication III. This system can be discretized via the approach presented in the two-dimensional study [99]. Using the notation of [99], the last right-hand side term affecting the polarization of the wave, absent in the 2D case, is of the form $-\mathbf{B}^{(i)T} \sum_{j=1}^{3} \mathbf{q}_k^{(k)}$, where $\mathbf{q}_j^{(i)}$ denotes the coordinate vector of $g_i^{(j)}$.

The signal transmission at point $\vec{p}$ is modeled as a point source of the form

$$\frac{\partial \vec{f}}{\partial t}(t, \vec{x}) = \frac{\partial \vec{h}}{\partial t}(t)\, \delta(\vec{x} - \vec{p}) \quad \text{with} \quad h(0) = \frac{\partial \vec{h}}{\partial t}(0) = 0, \tag{3.11}$$

where $\vec{h}$ denotes the dependence of $\vec{f}$ on time and $\delta(\vec{x} - \vec{p})$ is the Dirac's delta function satisfying $\int q(\vec{x}) \delta(\vec{x} - \vec{p})\, dV = q(\vec{p})$ for any sufficiently regular function

q. Physically the orientation and magnitude of vector $\vec{(h)}$ are determined by the antenna specifications and its amplitude and waveform of the feeding current.

Following from equations 3.9 and 3.10 the i-th component $E = E_i$ electric field $\vec{E} = E_i$ evoked by $\vec{f}$ satisfies the following bilinear expression of the weak form:

$$a(E, \mathbf{g}; \mathbf{w}; \Omega) = 0, \tag{3.12}$$

$$b(E, \mathbf{g}; v; \Omega) = -\langle f, v; \Omega \rangle \tag{3.13}$$

where $\mathbf{g} = (\vec{g}^{(1)}, \vec{g}^{(2)}, \vec{g}^{(3)})$ with $\vec{g}(j) = \int_0^t \nabla E_i(\tau, \vec{x})\, d\tau$ for $j = 1, 2, 3$ and $\langle f, v; \Omega \rangle = \int_\Omega f v \, dV$. The bilinear forms a and b correspond to the right-hand sides of the equations (3.9) and (3.10), respectively, and $v \in H^1(\Omega)$, $\mathbf{w} = (\vec{w}^{(1)}, \vec{w}^{(2)}, \vec{w}^{(3)})$ with $\vec{w}^{(i)} \in [L_2(\Omega)]^3$ are test functions. The system as formulated in (3.12) and (3.13) is used to simplify the definition of the simulation. Under regular enough initial conditions this weak form [99] has a unique solution $E : [0, T] \to H^1(\Omega)$ [39].

3.1.1 Incident and Scattered Field

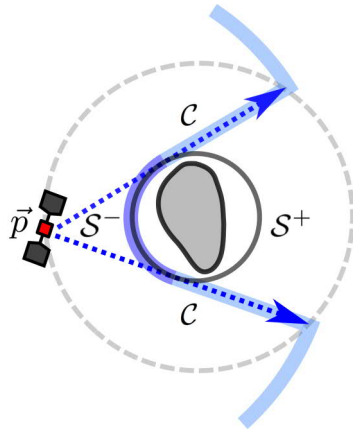

Figure 3.1 A visualization of the domain decomposition utilized in the numerical simulations. The far-field of the signal is obtained as a surface integral evaluated on the spherical surface $\mathscr{S}$ which is divided into two parts (+/-) by the cone whose tip is at the point of the signal transmission and mantle is tangential to the sphere. The simulation is performed on the part (-) closer to the transmission point.

As a result of the potential mission configuration, it is required to simulate a wave propagation in a domain that is much larger than the domain that contains the

target object (asteroid) and its immediate surroundings. This would result in very large domain with possible accumulated modeling errors in simulation. Therefore, to avoid having to discretize the whole domain, it is necessary to divide the domain via some way.

For modeling the far-field, we assume that the domain Ω (Figure 3.1) consists of two sub-domains: an outer part Ω_1 and an enclosed ball Ω_2 containing the target asteroid. The spherical inner boundary is denoted with $\mathscr{S} = \Omega_1 \cap \Omega_2$. The spacecraft position $\vec{p}$ is assumed to be located outside Ω. This is done in Publication III as follows. A surface $\mathscr{S}$ (Figure 3.1) is defined to accomplish this. $\mathscr{S}$ is defined as a spherical surface, which defines a boundary condition. The total field E is expressed as the sum of the incident and scattered field, i.e., $E = E_{\mathrm{I}} + E_{\mathrm{S}}$, where the incident field E_{I} emanates from the source and vanishes in the interior of Ω_2, that is, in $\Omega_2 \setminus \mathscr{S}$. The scattered field E_{S} is the total field in Ω_2, and its restriction to the surface $\mathscr{S}$ is utilized in calculating the measured far-field. The incident field E_{I} satisfies the following modified weak form which can be evaluated with respect to the surface $\mathscr{S}$ which holds in the larger domain Ω_1:

$$a(E_{\mathrm{I}}, \mathbf{g}_{\mathrm{I}}; \mathbf{w}; \Omega_1) = 0, \tag{3.14}$$

$$b(E_{\mathrm{I}}, \mathbf{g}_{\mathrm{I}}; v; \Omega_1) = -\langle f, v; \Omega_1 \rangle + \langle \mathbf{g}_{\mathrm{I}}, v; \mathscr{S} \rangle, \tag{3.15}$$

in which

$$\langle \mathbf{g}_{\mathrm{I}}, v; \mathscr{S} \rangle = \int_{\mathrm{S}} (\vec{g}_{\mathrm{I}} \cdot \vec{n}) v \, \mathrm{d}S \tag{3.16}$$

with $\vec{g}_{\mathrm{I}} = \int_0^t \nabla E_{\mathrm{I}}(\tau, \vec{x}) \, d\tau$. The inner product $\langle \mathbf{g}_{\mathrm{I}}, v; \mathscr{S} \rangle$ corresponds to the nonzero surface term in the integral

$$\int_{\Omega_i} (\nabla \cdot \vec{g}_{\mathrm{I}}) \, v \, dV = (-1)^j \int_{\mathrm{S}} (\vec{g}_{\mathrm{I}} \cdot \vec{n}) v \, \mathrm{d}S - \int_{\Omega_i} \vec{g}_{\mathrm{I}} \cdot \nabla v \, \mathrm{d}V, \tag{3.17}$$

where $\vec{n}$ denotes the outward unit normal of $\mathscr{S}$ and $j = 1, 2$. For the scattered field E_{S}, it holds $E_{\mathrm{S}} = E - E_{\mathrm{I}}$. Thus, its weak form in Ω_i for $i = 1, 2$ can be obtained by subtracting both sides of (3.14), (3.15) from (3.12), (3.13) written for Ω_1 and Ω_2, respectively, taking into account that $\langle f, v; \Omega_2 \rangle_2 = 0$ and that the incident field vanishes in $\Omega_2 \setminus \mathscr{S}$. It follows that a weak form which can be solved separately for the subdomains and thereby allows restricting computations to the smaller domain Ω_2

can be defined:

$$a(E_{\mathrm{S}}, \mathbf{g}_{\mathrm{S}}; \mathbf{w}; \Omega_i) = 0, \tag{3.18}$$

$$b(E_{\mathrm{S}}, \mathbf{g}_{\mathrm{S}}; v; \Omega_i) = -\langle \mathbf{g}_{\mathrm{I}}, v; \mathscr{S} \rangle \tag{3.19}$$

for $i = 1, 2$. Summing both sides of (3.18), (3.19) for Ω_1 and Ω_2 together leads to the following full domain weak form for the scattered field:

$$a(E_{\mathrm{S}}, \mathbf{g}_{\mathrm{S}}; \mathbf{w}; \Omega) = 0, \tag{3.20}$$

$$b(E_{\mathrm{S}}, \mathbf{g}_{\mathrm{S}}; v; \Omega) = -2 \langle \mathbf{g}_{\mathrm{I}}, v; \mathscr{S} \rangle. \tag{3.21}$$

This formulation is otherwise similar to (3.12)–(3.13), but instead of a single point, the source function $\mathbf{g}_{\mathrm{I}}$ is evaluated on the sphere $\mathscr{S}$.

3.2 Incident Far-Field

To enable evaluating $\mathbf{g}_{\mathrm{I}}$ on the spherical surface $\mathscr{S}$ the wave propagation in the empty space has to be inspected analytically which is possible using classical Green's function based solutions [34]. In empty space ($\varepsilon_r = 1$ and $\sigma = 0$), the incident field for a monopolar (isotropic) point source (3.11) placed at $\vec{p}$ can be expressed as the following convolution:

$$E_{\mathrm{I}} = -\mathscr{G} *_\tau \frac{\partial h}{\partial t} = -\frac{1}{4\pi|\vec{x} - \vec{p}|} \left[\frac{\partial h}{\partial t} \right], \tag{3.22}$$

This formulation is required to calculate the boundary condition $\mathbf{g}_{\mathrm{I}}$ numerically. In 3.22 $h *_\tau k(t, \vec{x}) = \int_0^\infty h(t - \tau, \vec{x}) k(\tau, \vec{x}) \, d\tau$, $[\partial h / \partial t]$ is a retarded signal evaluated at $t - |\vec{x} - \vec{p}|$ and $\mathscr{G} = \delta(t - |\vec{x} - \vec{p}|)/(4\pi|\vec{x} - \vec{p}|)$ is a Green's function with δ denoting the Dirac's delta function defined with respect to time. That is, $h(t, \vec{x}) = \int_0^\infty h(t - \tau, \vec{x}) \delta(\tau) \, d\tau$ for any sufficiently regular h. It follows from (3.22) through a straightforward calculation that

$$\nabla E_{\mathrm{I}} = \frac{(\vec{x} - \vec{p})}{4\pi|\vec{x} - \vec{p}|^3} \left[\frac{\partial h}{\partial t} \right] + \frac{(\vec{x} - \vec{p})}{4\pi|\vec{x} - \vec{p}|^2} \left[\frac{\partial^2 h}{\partial t^2} \right] \tag{3.23}$$

$$\vec{g}_{\mathrm{I}} = \int_0^t \nabla E_{\mathrm{I}} \, d\tau = \frac{\vec{x} - \vec{p}}{4\pi|\vec{x} - \vec{p}|^3} [h] + \frac{\vec{x} - \vec{p}}{4\pi|\vec{x} - \vec{p}|^2} \left[\frac{\partial h}{\partial t} \right]. \tag{3.24}$$

The incident field E_{I} needs to be evaluated only on its first arrival at $\mathscr{S}$, that is, in the subset $\mathscr{S}^- = \{\vec{x} \in \mathscr{S} \,|\, (\vec{x} - \vec{p}) \cdot \vec{n} < 0\}$ (Figure 3.1). In the remaining part $\mathscr{S}^+ = \mathscr{S} \setminus \mathscr{S}^-$, E_{I} is set to be zero. Hence, it follows that $\langle \vec{g}_{\mathrm{I}}, v; \mathscr{S}^- \rangle = \langle \vec{g}_{\mathrm{I}}, v; \mathscr{S} \rangle$ with

$$\langle \vec{g}_{\mathrm{I}}, v; \mathscr{S}^- \rangle = \int_{\mathscr{S}^-} \left(\frac{(\vec{x} - \vec{p}) \cdot \vec{n}}{4\pi |\vec{x} - \vec{p}|^3} [h] + \frac{(\vec{x} - \vec{p}) \cdot \vec{n}}{4\pi |\vec{x} - \vec{p}|^2} \left[\frac{\partial h}{\partial t} \right] \right) v \, \mathrm{d}S. \tag{3.25}$$

This can be verified by extending the surface $\mathscr{S}^-$ with the tangent cone of $\mathscr{S}$ which intersects $\vec{p}$, and further with a $\vec{p}$-centric sphere with a radius larger than T. For the resulting surface $\mathscr{C}$, it holds that $\langle \vec{g}_{\mathrm{I}}, v; \mathscr{C} \rangle = \langle \vec{g}_{\mathrm{I}}, v; \mathscr{S}^- \rangle$. Namely, the integrand in (3.25) is zero on the tangent cone and within the distance $> T$ from $\vec{p}$ the incident wave is zero for $t \in [0, T]$.

3.3 Simulation method

To simulate the system as described in previous sections, the domain Ω_2 is discretized through a finite element mesh $\mathscr{T} = T_1, T_2, \ldots, T_n$. The mesh is equipped with normalized finite element basis functions $\varphi_1, \varphi_2, \ldots, \varphi_n \in H^1(\Omega)$. The discretized solution is assumed to be of the form $u = \sum_{j=1}^{n} p_j \varphi_j$ and $\vec{g} = \sum_{k=1}^{d} g^{(k)} \vec{e}_k$. Here $g^{(k)} = \sum_{i=1}^{m} q_i^{(k)} \chi_i$ is the sum of the element indicator functions $\chi_1, \chi_2, \ldots, \chi_m \in L_2(\Omega)$. Indicator function is a function that outputs either 0 or 1 depending on the input values. Parameter d is the number of spatial dimensions; usually it is 2 or 3.

Restricting the test functions for v and $\vec{g}$ results to a following Ritz-Galerkin -type matrix [20] version of the weak form formula 3.12. It is presented here in its 2D form, for simplicity.

$$\frac{\partial}{\partial t} \mathbf{A}\mathbf{q}^{(k)} - \mathbf{B}^{(k)}\mathbf{p} + \mathbf{T}^{(k)}\mathbf{q}^{(k)} = 0, \quad \text{for} \quad k = 1, \ldots, d, \tag{3.26}$$

$$\frac{\partial}{\partial t} \mathbf{C}\mathbf{p} + \mathbf{R}\mathbf{p} + \mathbf{S}\mathbf{p} + \sum_{k=1}^{d} \mathbf{B}^{(k)^T} \mathbf{q}^{(k)} = \mathbf{f}, \tag{3.27}$$

where $\mathbf{p} = (p_1, p_2, \ldots, p_m)$, $\mathbf{q}^{(k)} = (q_1^{(k)}, q_2^{(k)}, \ldots, q_n^{(k)})$ and

$$A_{i,i} = \int_{T_i} d\Omega, \qquad A_{i,j} = 0 \quad \text{if} \quad i \neq j, \tag{3.28}$$

$$B_{i,j}^{(k)} = \int_{T_i} \vec{e}_k \cdot \nabla \varphi_j \, d\Omega, \quad \text{for} \quad k = 1, \ldots, d \tag{3.29}$$

$$C_{i,j} = \int_{\Omega} \varepsilon \, \varphi_i \varphi_j \, d\Omega, \quad R_{i,j} = \int_{\Omega} \sigma \, \varphi_i \varphi_j \, d\Omega, \quad S_{i,j} = \int_{\Omega} \xi \, \varphi_i \varphi_j \, d\Omega, \tag{3.30}$$

$$T_{i,j}^{(k)} = \int_{\Omega} \zeta^{(k)} \, \varphi_i \varphi_j \, d\Omega, \quad f_i = -\int_{\Omega} f \, \varphi_i \, d\Omega. \tag{3.31}$$

Numerically, the matrix $C_{i,j}$ is a mass matrix, which is straightforward to invert. Notice, that for simplicity, we have assumed here a transverse electric (TE) propagation mode, in which the last term of the second equation is zero, meaning that the divergence of the electric field is zero everywhere. This is true in the TE mode and in 2D geometry where the material boundaries and the electric field are perpendicular, and the polarization effects are absent in the model. In general case, the last term of the second equation is of the form:

$$-\mathbf{B}^{(i)^T} \sum_{j=1}^{3} \mathbf{q}_k^{(k)} \tag{3.32}$$

where $\mathbf{q}_j^{(i)}$ denotes the coordinate vector of $g_i^{(j)}$.

Partial derivatives over time for equations 3.26 and 3.27 can be approximated with finite difference method with Δt time steps with N points of time. This results in leap-frog time integration formulas as follows:

$$\mathbf{q}^{(k)}{}_{\ell+1/2} = \mathbf{q}_{\ell-1/2}^{(k)} + \Delta t \, \mathbf{A}^{-1} \left(\mathbf{B}^{(k)} \mathbf{p}_\ell - \mathbf{T}^{(k)} \mathbf{q}_{\ell-1/2}^{(k)} \right), \quad \text{for} \quad k = 1, \ldots, d, \tag{3.33}$$

$$\mathbf{p}_{\ell+1} = \mathbf{p}_\ell + \Delta t \, \mathbf{C}^{-1} \left(\mathbf{f} - \mathbf{R}\mathbf{p}_\ell - \mathbf{S}\mathbf{p}_\ell - \sum_{k=1}^{d} \mathbf{B}^{(k)^T} \mathbf{q}^{(k)}{}_{\ell+1/2} \right). \tag{3.34}$$

Thus, using leap-frog integration method [132], a signal propagating in Ω_1 can be simulated. This leap-frog method is known as the Finite Element Time Domain (FETD) method, which is used to propagate a wave equation in simulation [109].

In short, FDTD generally works by first solving electric field u at given time step. After that the magnetic field is solved at the same space or volume at the next time step. The step-by-step process is repeated until the wave has propagated completely or the system has otherwise achieved a steady state.

In the case of electromagnetic waves, the unknown parameter of the Ω_1 is the dielectric permittivity ε. It affects the speed of the wave propagating in a medium. The permittivity is handled as a sum of a fixed background permittivity ε_{bg} distribution and variable perturbation $\varepsilon_r^{(p)} = \sum_{j=1}^{n} c_j \chi_j'$ which were composed by indicator functions χ_j' over the $\Omega_0 \cup \Omega_1$. The simulation is linearized around background permittivity through a Jacobian matrix $\mathbf{L}$, which can also be interpreted as the first-degree Born approximation of the wave scattering process [56]. It is a list of all first order partial derivatives of a vector-valued function. It is formed by differentiating formulas 3.33 and 3.34 over suitable time steps as follows:

$$\frac{\partial \mathbf{q}^{(k)}{}_{\ell+1/2}}{\partial c_j} = \frac{\partial \mathbf{q}^{(k)}_{\ell-1/2}}{\partial c_j} + \Delta t \mathbf{A}^{-1} \left(\mathbf{B}^{(k)} \frac{\partial \mathbf{p}}{\partial c_j} - \mathbf{T}^{(k)} \frac{\mathbf{q}^{(k)}_{\ell-1/2}}{\partial c_j} \right) \tag{3.35}$$

$$\text{for } k = 1, \ldots, d,$$

$$\frac{\partial \mathbf{p}_{\ell+1}}{\partial c_j} = \frac{\partial \mathbf{p}_\ell}{\partial c_j} - \Delta t \mathbf{C}^{-1} \left(\mathbf{R} \frac{\partial \mathbf{p}_\ell}{\partial c_j} + \mathbf{S} \frac{\partial \mathbf{p}_\ell}{\partial c_j} + \sum_{k=1}^{d} \mathbf{B}^{k\,T} \frac{\partial \mathbf{q}^{(k)}_{\ell+1/2}}{\partial c_j} \right)$$

$$- \Delta t \frac{\partial \mathbf{C}^{-1}}{\partial c_j} \left(\mathbf{R}\mathbf{p}_\ell + \mathbf{S}\mathbf{p}_\ell + \sum_{k=1}^{d} \mathbf{B}^{k\,T} \mathbf{q}^{(k)}_{\ell+1/2} \right) \tag{3.36}$$

The governing matrix setting affecting the speed of the iteration is the inverse matrix C^{-1}. This means that on each step one must solve one solution for the linear equation system. We apply an iterative solver based on property that the finite velocity of the wave limits the perturbation to the previous solution on each leap-frog step in a bounded environment. Size of this environment is determined by the velocity of the wave times the time step length. An iterative solver operates in this well-localized set and thus numerical solution is found quickly with few iterations on each time step. Furthermore, it is essential to optimize the speed of the iterative solver to minimize the total forward simulation time. Therefore, we apply a GPU accelerated iteration as a GPU provides an effective platform to parallelize a product

between a sparse matrix and a vector. For this reason, the GPU acceleration is an efficient technique in wave modeling and simulations which is further discussed in the next chapter.

3.4 Matrices

PDE System	Eq. 1	$\frac{\partial g_j^{(i)}}{\partial t}$	$\frac{\partial E_i}{\partial x_j}$
	Eq. 2 ($\vec{E}$)	$\varepsilon_r \frac{\partial E_i}{\partial t}$	σE_i
	Eq. 2 (**g**)	$\sum_{j=1}^{3} \frac{\partial g_j^{(i)}}{\partial x_j}$	$\frac{\partial}{\partial x_i} \sum_{j=1}^{3} g_j^{(j)}$
	Source	$-f_i$	
Weak form	Eq. 1	$\frac{\partial}{\partial t} \sum_{j=1}^{3} \int_\Omega \vec{g}_j^{(i)} w_j^{(i)} \, \mathrm{d}V$	$-\sum_{j=1}^{3} \int_\Omega w_j^{(i)} \frac{\partial E_i}{\partial x_j} \, \mathrm{d}V$
	Eq. 2 (E_i)	$\frac{\partial}{\partial t} \int_\Omega \varepsilon_r E_i \, v_i \, \mathrm{d}V$	$\int_\Omega \sigma E_i \, v_i \, \mathrm{d}V$
	Eq. 2 (**g**)	$\sum_{j=1}^{3} \int_\Omega g_j^{(i)} \frac{\partial v_i}{\partial x_j} \, \mathrm{d}V$	$-\sum_{j=1}^{3} \int_\Omega g_j^{(j)} \frac{\partial v_i}{\partial x_i} \, \mathrm{d}V$
	Source	$-\int_\Omega f_i v_i \, \mathrm{d}V$	
Matrix	Eq. 1	$\frac{\partial}{\partial t} \mathbf{A}\mathbf{q}^{(k)}$	$\mathbf{B}^{(k)}\mathbf{p}$
	Eq. 2. (E_i)	$\frac{\partial}{\partial t} \mathbf{C}\mathbf{p}$	$\mathbf{R}\mathbf{p}$
	Eq. 2. (**g**)	$\sum_{k=1}^{d} \mathbf{B}^{(k)^T} \mathbf{q}^{(k)}$	$-\mathbf{B}^{(i)^T} \sum_{j=1}^{3} \mathbf{q}_k^{(k)}$
	Source	$\mathbf{f}$	

Table 3.2 The system matrices (bottom line) that result from the corresponding parts of the wave equations (top lines).

In previous sections 3.1-3.3 a system of equations was formulated. These result in a list of matrices. Table 3.2 expresses that system in a form that attempts to show a top to bottom approach on how the equations result in matrices that are used in

numerical simulations.

3.5 Inverse problem approach

Following from the wave equation, the dependence of the radar measurement data denoted here by $\mathbf{y}$ and the permittivity distribution ε_r is highly non-linear and some permittivity features are not necessarily visible in the data, e.g., due to attenuation and scattering effects taking place in the wave propagation. Consequently, reconstructing ε_r given $\mathbf{y}$ is an ill-posed and ill-conditioned non-linear inverse problem, meaning that the solution is non-unique and even a slight amount of noise in the data can cause substantial effects to the final reconstruction. To solve the inverse problem in the general case would require a mathematical approach taking all these aspects into account. However, to simplify the inversion goal, this work concentrates on finding relatively small perturbations of the permittivity structure, such as boulders, voids, cracks, and surface layers. Therefore the inverse problem is approached in its linearized form, meaning that dependence between $\mathbf{y}$ and unknown $\mathbf{x} = (c_1, c_2, \ldots, c_n)$, i.e., the coordinate vector of a discretized permittivity perturbation $\varepsilon_r^{(p)} = \sum_{j=1}^{n} c_j \chi_j'$ is given by the linear formula

$$\mathbf{y} - \mathbf{y}_0 = \mathbf{L}(\mathbf{x} - \mathbf{x}_0) + \mathbf{n}, \tag{3.37}$$

where $\mathbf{y}$ is the actual data vector, $\mathbf{y}_0$ and $\mathbf{L}$ denote the simulated data $\mathbf{p}[\mathbf{x}_0]$ and Jacobian matrix $\mathbf{J}[\mathbf{x}_0]$ for a constant *a priori* guess $\mathbf{x}_0$, and $\mathbf{n}$ is a noise vector containing both modeling and measurement errors. Solving this equation necessitates forming the matrix $\mathbf{L}$ and applying a mathematical inverse algorithm to obtain an estimate for $\mathbf{x}$ given $\mathbf{y}$. This section briefly reviews the methodology related to these steps.

3.5.1 Regularized deconvolution

The leap-frog formulae can be linearized as shown in Section 3.3. The linearized system (3.35)–(3.36) is of identical form with original leap-frog system (3.33)–(3.34) if source vector in the original one is replaced by the following by defining the fol-

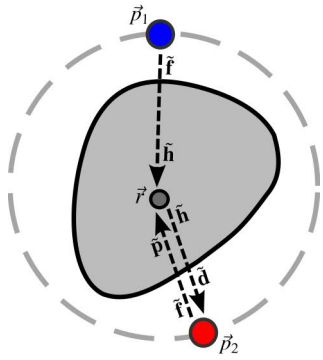

Figure 3.2 A schematic picture visualizing the regularized deconvolution-based multiresolution solution. **(1)** Place the source $\tilde{\mathbf{f}}$ at the point $\vec{p}_1$ and solve the system (3.33)–(3.34) using the leap-frog iteration. Based on the solution, calculate and store $\tilde{\mathbf{h}}$ of the form (3.38) for a given node $\vec{r}$ and element T of the mesh $\mathscr{T}'$. **(2)** Place $\tilde{\mathbf{f}}$ at $\vec{p}_2$. Solve (3.33)–(3.34) and store $\tilde{\mathbf{p}}$ of the form (3.33) at $\vec{r}$. **(3)** Estimate the Green's function $\tilde{\mathbf{g}}$ satisfying $\tilde{\mathbf{p}} = \tilde{\mathbf{g}} * \tilde{\mathbf{f}}$ using Tikhonov regularized deconvolution with a suitably chosen regularization parameter δ [57]. **(4)** Based on the estimated $\tilde{\mathbf{g}}$ and the reciprocity of the signal wave [2], approximate $\tilde{\mathbf{d}}$, the solution of an auxiliary system at $\vec{p}_2$, through the convolution of auxiliary $\tilde{\mathbf{d}} = \tilde{\mathbf{g}} * \tilde{\mathbf{h}}$ as described in Publication **II**.

lowing linearization-point-specific auxiliary source vector:

$$\mathbf{h}_\ell^{(i,j)} = \frac{\partial \mathbf{C}}{\partial c_j} \mathbf{Q}^{(i)} \mathbf{b}_\ell, \tag{3.38}$$

where $\mathbf{b}_\ell = \mathbf{C}^{-1}(\mathbf{R}\mathbf{p}_\ell + \mathbf{S}\mathbf{p}_\ell + \sum_{k=1}^{\mathrm{d}} \mathbf{B}^{(k)^T} \mathbf{q}_{\ell+\frac{1}{2}}^{(k)})$, the matrix $\mathbf{Q}^{(i)} \in \mathbb{R}^{n \times n}$ has one nonzero entry $\mathrm{Q}_{i,i}^{(i)} = 1$, and $(\partial \mathbf{C}/\partial c_j)_{i_1,i_2} = \int_{\mathrm{T}'_j} \varphi_{i_1} \varphi_{i_2} \, \mathrm{d}\Omega$ is nonzero if the j-th element includes nodes i_1 and i_2. Consequently, forming the Jakobian matrix via the leap-frog iteration would require propagating as many complete waves as there are linearization points in the domain Ω. This would lead to an extremely slow process without any additional speedup. Regularized deconvolution allows to approximate the Jakobian matrix by relying on the reciprocity of the wave, which is possible if wave has been propagated for each signal transmission and measurement point separately. Below, this process is explained by denoting point-wise time evolution of the wavefield and source functions with an additional symbol $\sim$ on top of each variable.

The algorithm proceeds as follows:

(1) Place the source $\tilde{\mathbf{f}}$ at the transmission point $\vec{p}_1$ and solve the system (3.33)–(3.34) using the leap-frog iteration. Based on the solution, calculate and store the auxiliary source (wave) $\tilde{\mathbf{h}}$ of the form (3.38) for a given node $\vec{r}$ and element T of the mesh $\mathscr{T}'$.

(2) Place $\tilde{\mathbf{f}}$ at measurement point $\vec{p}_2$. Solve (3.33)–(3.34) and store the wave $\tilde{\mathbf{p}}$ of the form (3.34) at $\vec{r}$.

(3) Estimate the Green's function $\tilde{\mathbf{g}}$ satisfying $\tilde{\mathbf{p}} = \tilde{\mathbf{g}} * \tilde{\mathbf{f}}$ using Tikhonov regularized deconvolution with a suitably chosen regularization parameter δ [57].

(4) Based on the estimated $\tilde{\mathbf{g}}$ and the reciprocity of the signal wave [2], approximate $\tilde{\mathbf{d}}$, the solution of (3.36) at $\vec{p}_2$, through the convolution $\tilde{\mathbf{d}} = \tilde{\mathbf{g}} * \tilde{\mathbf{h}}$.

Note, that backscattering data will be obtained, if $\vec{p}_1 = \vec{p}_2$.

3.5.2 Inversion procedure

In this study, a regularized solution of $\mathbf{x}$ is obtained via total variation regularized iteration

$$\mathbf{x}_{\ell+1} = \mathbf{x}_0 + (\mathbf{L}^T\mathbf{L} + \alpha\mathbf{D}\boldsymbol{\Gamma}_\ell\mathbf{D})^{-1}\mathbf{L}^T(\mathbf{y} - \mathbf{y}_0) \tag{3.39}$$

in which $\boldsymbol{\Gamma}_\ell$ is a weighting matrix satisfying $\boldsymbol{\Gamma}_0 = \mathbf{I}$ and $\boldsymbol{\Gamma}_\ell = \mathrm{diag}(|\mathbf{D}[\mathbf{x}_\ell - \mathbf{x}_0]|)^{-1}$ for $\ell \geq 1$, and $\mathbf{D}$ denotes a diagonally conditioned total variation regularization matrix of the form

$$D_{i,j} = \beta\delta_{i,j} + \frac{(2\delta_{i,j} - 1)\int_{\mathrm{T}'_i \cap \mathrm{T}'_j} \mathrm{d}s}{\max_{i,j}\int_{\mathrm{T}'_i \cap \mathrm{T}'_j} \mathrm{d}s}, \quad \delta_{i,j} = \begin{cases} 1, & \text{if } j = i, \\ 0, & \text{otherwise.} \end{cases} \tag{3.40}$$

The first regularization term limits the magnitude of $\mathbf{x}$ and the second one penalizes the jumps over the edges of $\mathscr{T}'$. The iteration (3.39) can be shown [99] to minimize $F(\mathbf{x}) = ||\mathbf{L}(\mathbf{x} - \mathbf{x}_0) - (\mathbf{y} - \mathbf{y}_0)||_2^2 + 2\sqrt{\alpha}||\mathbf{D}(\mathbf{x} - \mathbf{x}_0)||_1$ in which the second term equals to the total variation of $\mathbf{x}$, if $\beta = 0$ [25, 57, 108, 115]. Here, the total variation regularization strategy produces distributions with large connected subsets close to constant, which helps to avoid noise in the reconstructions.

4 COMPUTED TOMOGRAPHY

In this chapter, general methods of scientific computing are presented. The focus of this part of the thesis project has been to take advantage of previously existing computation scripts and routines to improve them. At the same time, there was an opportunity to take advantage of modern Graphics Processing Units (GPUs), as they are known to accelerate calculations.

4.1 Parallelization of computing by using GPUs

In scientific computing, many computation tasks or operations are performed several times. Typically, the same calculation is done for multiple data. In this case, the calculation runs are not dependent on the results of the previous calculation, i. e., the calculations can be performed in parallel. This parallelism can be found on many levels of abstraction. A whole computation task can be parallelized in this way, but a task can also contain parallelism within itself. For example, task A, which can include multiple operations, can include fundamental calculations such as multiplication or addition, that is performed on many inputs at the same point in the algorithm. These levels of parallelization are called task parallelism and data parallelism.

Modern graphical processing units have been designed with the data parallelism in mind. In computer graphics a graphics processor needs to perform the same calculation to multiple data. Example of this can be any lighting calculation to a *scene* that is being rendered for viewing. In microprocessor architecture, this is called Single Instruction, Multiple Data (SIMD). The microprocessors in GPUs have been designed to perform this type of operations fast, and they have a substantially large number of processing units, *cores*, which are typically on a single silicon die.

These cores can be programmed to run arbitary code, i. e., the data is not required to be graphics data. The software (code) that runs on GPU is a program that

is specifically compiled to run on the GPU. This program does not include any of the usual high-level interfaces that are usually found in the programs that run on computers. These high-level interfaces include interfaces with the computer's operating system, file system etc. For this reason, the program that runs on a GPU is called a *kernel*. It contains only the very fundamental code that is required to interface the task with the GPU and of course the calculation routine that is being run.

In recent years, utilization of GPUs for scientific computing has become popular. GPU vendors, including nVidia[1] and AMD[2], have built software libraries that can be used to compile kernels to run on the GPU's. Widely used open solution for writing code is OpenCL[3], which includes support for nVidia, AMD and many others. On the other hand, nVidia has its own proprietary implementation called CUDA[4] It supports many programming languages, such as Fortran, C and C++. In scientific computing, CUDA has become more popular of these, as it is directly supported by the hardware manufacturer and thus it can be better optimized for the hardware. In academic research, OpenCL has gained a foothold as it is a vendor-independent solution.

General purpose computing platforms such as Matlab[5], SciLab[6] and Octave[7] support GPU computing. In Matlab, this is realized via a separate Parallel Computing Toolbox add-on, SciLab has only basic support via a 3rd-party module, and Octave has GPU vendor provided add-ons. From these, the Matlab version is the most versatile when using nVidia GPUs. In Parallel Computing Toolbox, there are special functions to transfer data into the internal memory of the GPU and to read the data back to the memory of the PC. In this way, the interface to the GPU computing is user friendly and compatible with existing Matlab code. User friendliness comes from the code compatibility with already existing Matlab code: once an elementary calculation is performed for the data that is placed in the GPU memory, Matlab automatically calls for the CUDA implementation for this calculation. In Matlab, there are CUDA implementations for almost all fundamental operations for many types of data, and is possible to implement one's own CUDA kernels and call them

[1] NVidia corporation. `https://www.nvidia.com`. Accessed 13.3.2020.

[2] Advanced Micro Devices, Inc. `https://www.amd.com`. Accessed 13.3.2020

[3] OpenCL. The Khronos Group Inc. `https://www.khronos.org`. Accessed 13.3.2020.

[4] Compute Unified Device Architecture. NVidia. `https://developer.nvidia.com/cuda-zone`. Accessed 13.3.2020.

[5] MATLAB. MathWorks Inc. `https://www.mathworks.com`. Accessed 14.3.2020.

[6] Scilab. `https://www.scilab.org`. Accessed 14.3.2020.

[7] GNU Octave. `https://www.gnu.org/software/octave/`. Accessed 14.3.2020

from Matlab via a well-documented interface.

The platform used in this work is Matlab and its GPU processing interface provided by the Parallel Computing Toolbox. However, there are also other types of software that can be used, that are not general purpose math-related computing platforms. Astra Tomography Toolbox [8] is developed specifically for tomography calculations and parts of it take advantage of GPUs. It has an interface for Matlab and Python, allowing easy integration for existing code. For some tomography projection operations, could offer even easier integration to Matlab compared to the Parallel Computing Toolbox. In addition, there are existing studies that focus on further optimization of a wavefront propagation such as [54]. Detailed analysis and optimization can make the simulations faster in the future.

4.2 GPU computing limitations

Currently, there are limitations in the utilization of GPUs. These are a result of the limited amount of memory on a single GPU and the limited bandwidth of the data transfer between different GPU units. In asteroid tomography, the amount of memory directly influences the size of the asteroid that can be processed with purely GPU based approach. This is because a cube-shaped finite element mesh is being utilized to discretize the calculation domain. The relationship is roughly as follows:

$$D = s_\Omega * n^3 \tag{4.1}$$

where D is the amount of total data resulting from n number of elements that have size s_Ω with respect to the side of the modelling domain. This means doubling the computational domain dimension size, i.e. making the side of the domain twice as big, making it possible to accommodate twice as big asteroid, the amount of data volume required will be multiplied to the power of 3. As an example, in Publication III around 9.4 GB of data was held at the memory for a cube-shaped domain with a side length of 160 m. This fits into memory of readily available desktop PC GPU models. If the length of the side of the domain was to be doubled, the memory required would clearly not fit on a readily available desktop GPU memory[9]. Trying to

[8] The ASTRA Toolbox. `https://www.astra-toolbox.com/`. Accessed 5.6.2019.

[9] At the time of writing, the largest desktop GPUs have 32 GB of memory.

make the domain larger, however, has direct implications on the required frequency for penetrating measurement signal [91].

To make it possible to calculate larger domains with GPU, some type of GPU memory sharing without too much overhead would be needed. So far, this has not been the case as the GPU units are driven by graphics processing needs, and typically those only utilize one GPU and its memory. This means that the memory on a typical GPU unit is tightly coupled to only that GPU via dedicated memory bus, and access to all external devices is via much slower bus. Therefore, sharing memory would be a large overhead from memory transfer delays. The very advances with high-bandwidth memory has produced a 512GB datacenter GPU with a shared memory for 16 GPUs. However, that unit costs in excess of 400.000 USD[10]. This means that the calculation task should fit into one desktop GPU for most cost-efficient GPU-based simulations, and if not, then a traditional CPU or GPU based computing cluster must be used.

4.3 Finite Element and other stencil approaches

To optimize the memory consumption, the approach chosen for the simulations of this work have used an adapted finite element mesh, where the mesh has been pre-generated to be more dense for the volume that covers the target, and less dense elsewhere. Figure 4.1 illustrates this configuration. Using this mesh optimization allows one to more accurately simulate the wave propagation inside the target body where the the material will affect the wave. The mesh is pre-generated manually and not automatically adapted for any shape, as there is typically only one mesh required for any given computing run. There are existing automatic mesh adaptation and optimization strategies that could be taken advantage of [71, 131].

The finite element mesh approach has some disadvantages compared to implementations in a regular stencil grid. There is a requirement for careful selection of the time step length in the simulations to keep the simulation stable. Namely, the Courant-Friedrichs-Levy condition [70] states that the time step must be less than the time for the wave to travel to adjacent grid points. For a finite element mesh this is determined by the shortest edge which might be shorter than in a regular stencil, meaning that a finite element solver might involve more time steps than a

[10]Nvidia DGX-2, `https://www.nvidia.com/en-us/data-center/dgx-2/`. Accessed 18.6.2019.

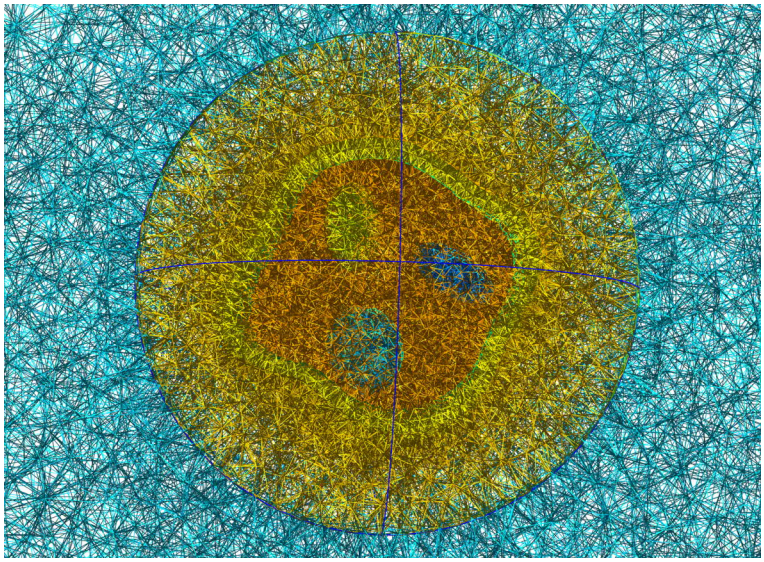

Figure 4.1 Slice of a finite element mesh for Asteroid Ky. The volume containing the asteroid (red) and its internal voids (blue) has a tighter mesh than the surrounding space (yellow), and the free space (turquoise).

stencil-based implementation. In the case of the finite element mesh, the gradient and divergence evaluation is also computationally more expensive than in a stencil grid. This is important as another avenue for optimization is to minimize the number of matrices on the GPU. The gradients can be used to replace the large matrices.

More simplified mesh that could be perhaps more naturally adapted to any computer code, GPU data structures and stencil code would be a grid-style (orthogonal) mesh. With this simplified mesh, it would be much easier to evaluate gradients and the mesh regularity would be uniform. Also, the data structures would be more optimized for GPU stencils, as the structures inside a memory are naturally more like orthogonal grids. Therefore, it would be possible to optimize the data structure layouts in the GPU memory for optimal speed and to take optimal advantage of special features on modern GPUs. The finite element mesh, however, has a superior adaptability compared to a stencil, which is also a key feature regarding GPU memory and performance optimization. Thus, a future work on comparing the performance of these two approaches in the present application would be well-motivated.

As the Matlab software includes the pre-existing CUDA-enabled operations for the matrix operations, the work in this thesis does not include experimentation on

optimization of the code that runs inside these pre-existing implementations. Therefore, future work would include experimenting with such optimizations on CUDA or similar GPU-oriented parallel computing platform to see how efficient the pre-existing implementations are. Implementing more optimized solutions would allow to achieve the most optimal memory efficiency and calculation time.

4.4 Clusters

Calculation cluster is a network of connected computers that have many processors (nodes) available for scientific computing. The number of processor cores is larger than desktop-based PCs, and typically the available memory for a single node is higher. Modern clusters also have dedicated GPU-equipped nodes installed. Clusters enable user to overcome some of the GPU computing limitations. In the case of tomography, the GPU accelerated computing can be transported to a cluster with GPU's, enabling accelerated calculations with the same code. This allows to perform many more wave propagation simulations simultaneously. However, the amount of GPU memory available in a GPU equipped node is around the same as in a high-end desktop GPU, so the limitation of the calculation domain size still holds. However, utilizing the large amount of CPU's and the larger amount of memory compared to the GPU memory allows to run simulations in larger calculation domains. This is what has to be done also if carrier wave-based simulations are run, as the higher frequency carrier wave signal results in a larger calculation domain size via more dense element mesh.

4.5 Acceleration of tomography simulations

In the present radar simulations, GPU can be used to propagate the wave through the leap-frog iteration. In our case, this means that all the sparse matrices following from the FETD discretization of the weak form of the wave equation are moved into the GPU memory. Since GPU is advantageous for evaluating sparse matrix-vector products this results in an essential acceleration regarding the calculation time. GPU has significantly less memory compared to a typical PC workstation computer which can be used for scientific calculations. For this reason, a memory-saving approach in the practical implementation has to be used. Most importantly, when inverting a

linear system corresponding to the mass matrix C, we have used the preconditioned conjugate iteration with a lumped diagonal preconditioner, i.e., a diagonal matrix with row-sums of the matrix entries on its diagonal. This approach is effective regarding the memory consumption avoiding any off-diagonal filling, i.e., non-zero non-diagonal entries. Even though using a more advanced preconditioner would lead to a stepwise shorter iteration, the high performance of a GPU allows a rapid solution also with a diagonal one. A diagonal preconditioner is also particularly advantageous for inverting a mass matrix, since the condition number of a mass matrix which is, in addition to the system size, the main factor affecting the computational complexity of the preconditioned conjugate gradient (PCG) solver [20], is determined by its diagonal entries [59] in a quasi-uniform mesh, i.e., in a mesh with a finite ratio between the largest and smallest element size. Thus, by conditioning (scaling) the diagonal entries it is, in theory, to approach the optimal performance which is obtained when the condition number is one.

GPU has been also used in the evaluation of the regularized deconvolution process. The actual inversion procedure with total variation regularization is less computationally demanding which is why our current implementation for it does not use GPU-based computing. Since we have used Matlab-based implementations for which sparse matrices are not processed via multi-threading, the CPU and GPU processing times have a significant difference corresponding to a factor of around one hundred.

5 RESULTS

The work consisted of 4 different areas of study. Firstly, basic working of tomography with reduced data quality was studied, and at the same, a novel way of implementing calculation on FPGA hardware was evaluated. The second and third studies concentrated on improving the inverse imaging algorithms and modelling in a realistic, implementable asteroid tomography scenario. The implementation of calculations via GPU-based routines was done, which enabled to achieve quick results and fast development cycle for testing algorithms. Lastly, a study was made to identify the main hardware and mission aspects that could give problems if an asteroid tomography mission were implemented. This was done together with experienced project collaborators.

5.1 Hardware-based effects on reconstruction results

In the first study, we investigated the effect of hardware-level processing to inversion of sparse waveform data. We showed that the bit depth, i.e., number of bits of information in each sample, and the strategy applied to calculate the travel time have a significant effect on the inversion quality, i.e., reconstructed wave velocity distribution. These effects were emphasized in the presence of strong signal attenuation and sparsity of the measurements which are potential scenarios for in-situ measurements in deep space. These results were obtained using an experimental acoustic measurement setup which was built for the experiment. The dataset obtained is available as supplementary data for Publication I. Figure 5.1 shows the basic principle of different types of travel time measurement used in the study. We compared the arrival time of sufficient signal power (Integrated Travel Time, ITT) to a more straightforward thresholded signal level measurement with multiple parameters. Figure 5.2 shows an example of the results of the study. It is seen that the ITT measurement achieves better results than the simpler thresholded travel time measurement espe-

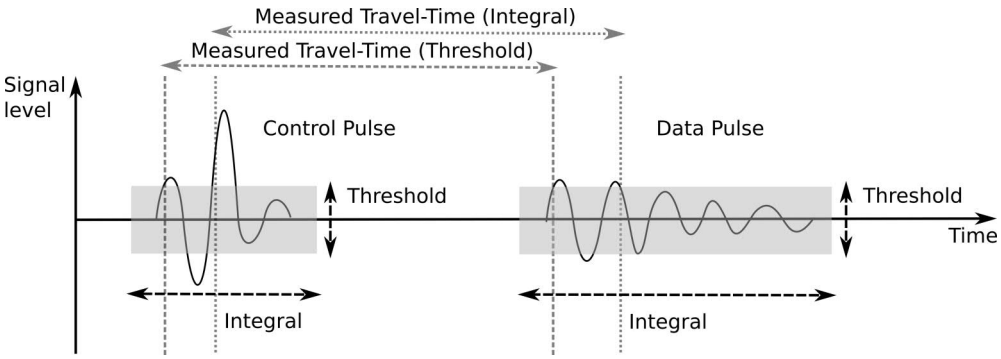

Figure 5.1 Visualisation of travel time calculation strategies. Greyed area represents the time period used for signal integral calculation.

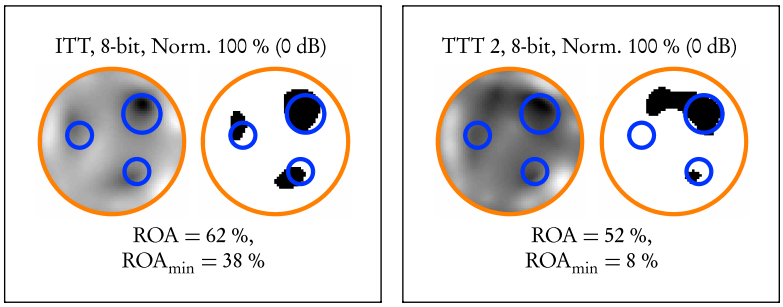

Figure 5.2 Travel-time tomography results with sparse data and reduced signal bit-depth. On the left, result using integrated travel time measurement and on the right result with thresholded travel time. The results suggest using the thresholded travel-time misses some details completely.

cially when the signal quality is decreased and the measurement data is sparse. While the acoustic measurement scenario is not the most relevant to asteroid tomography via radar, it might be relevant in laser vibrometry based measurement scenario as in [105] or via an impact experiment with the measurement instruments deployed on the asteroid surface. The results suggest that successful in-situ investigations might necessitate measuring and storing full-wave information. The further studies have, therefore, concentrated on full-wave inversion.

The hardware-related study in Publication I produced an interesting result. While the high-level synthesis, where higher-level programming language is used to design digital signal processing hardware, was found to be promising, no further study of this area was performed. However, the results motivate further studies, both for fur-

ther reducing the data quality and in designing signal processing hardware optimized for the required type of signal measurements.

5.2 Multiresolution inverse imaging and far-field modeling

In Publication II, a novel way of using full-wave tomography with a coarse-to-fine nested finite element mesh structure was used for the simulation and inversion of the electromagnetic waveform signals. This coarse-to-fine method made the inversion process more robust to noise especially in the situation where the source data is sparse. This will be the case on a space mission. As a secondary benefit of this study, a way to compress the elements in the fine element mesh was tested. Ultimately, in the multiresolution study it is shown that by utilizing the methodology, the signal-to-noise ratios required for a workable inversion and maximum angular positional errors were manageable. As a reference level, 10 dB signal-to-noise ratio (SNR) was suggested. The results are shown in Figure 5.3 for the case where the multistatic measurement configuration is used. Angular sensitivity for the full-wave data increases after 5 degrees but stays within manageable levels and projected data is more sensitive to noise. The projected data in this study is an analog for the travel time data used in the Publication I. Most importantly, with the full-wave data, a superior noise-robustness was achieved, and it showed similarities to the values shown in other studies in the target appliation area [65]. Furthermore, an inverse comparison between a projected and full-wave signal showed the advantage of the full-wave approach compared to projections, e.g., travel-time investigations.

However, the multiresolution study lacked some important real-life limitations. These include the realistic orbiting distance from the target asteroid (5 km), realistic power levels (10 W) from a small spacecraft to be utilized for radar transmissions, and a realistic number of measurement points around the target. Most importantly, comparison of one vs. two spacecraft (monostatic vs. bistatic) measurements was performed. The main results in Publication III are that a finite element mesh-based modeling that contain only the target asteroid and its immediate surrounds can be simulated even if the transmitting spacecraft is outside the mesh. This is important to reduce the amount of memory consumption in the simulation, and it enables the simulations to be run with a GPU based workstation computer or a cluster in a timely manner. The study utilized realistic background noise. Differences between

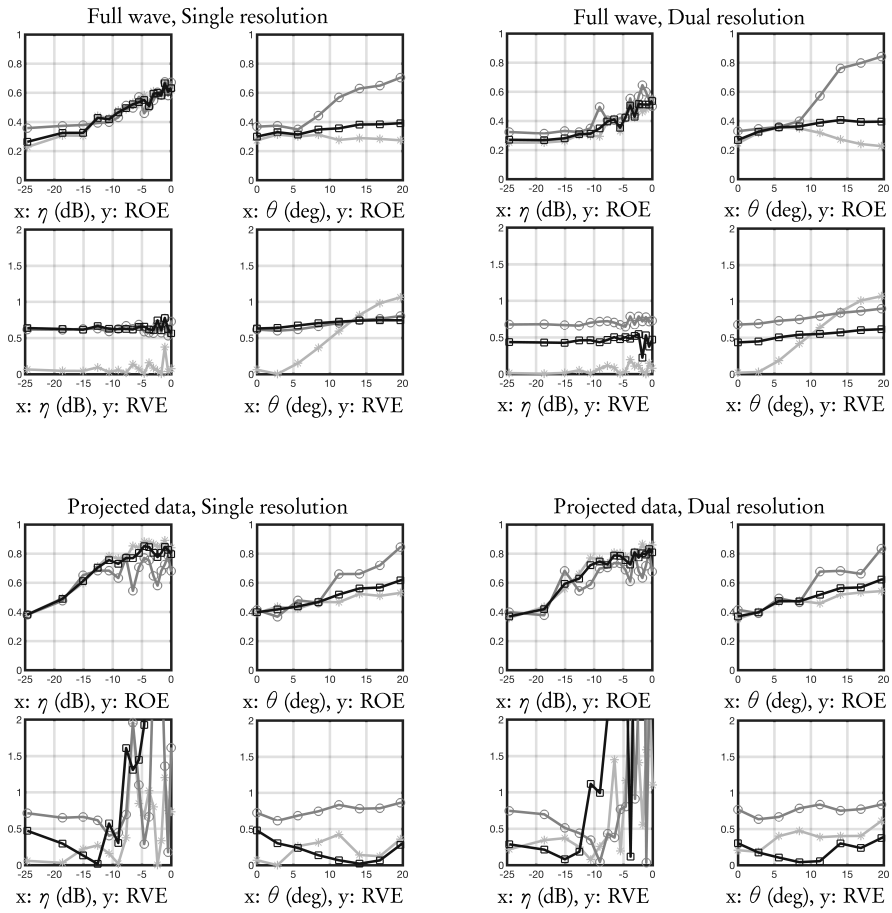

Figure 5.3 Relative Overlap Error (ROE) and Relative Value Error (RVE) results for the bistatic measurement configuration. Legend: Surface layer: light grey line, star marker, Voids: darker grey line, circle marker, Total value: black line, square marker.

monostatic and bistatic measurements were found and the most important ones are shown in Figure 5.4. The relative overlap error (ROE) starts to increase after total noise level of 10 dB and that the monostatic measurement has difficulties with the surface part of the asteroid when the measurement angle is limited. While monostatic measurement showed a better reconstruction in some cases, the additional performance of bistatic measurements was shown to be an advantage that shows in the overall relative measurement error.

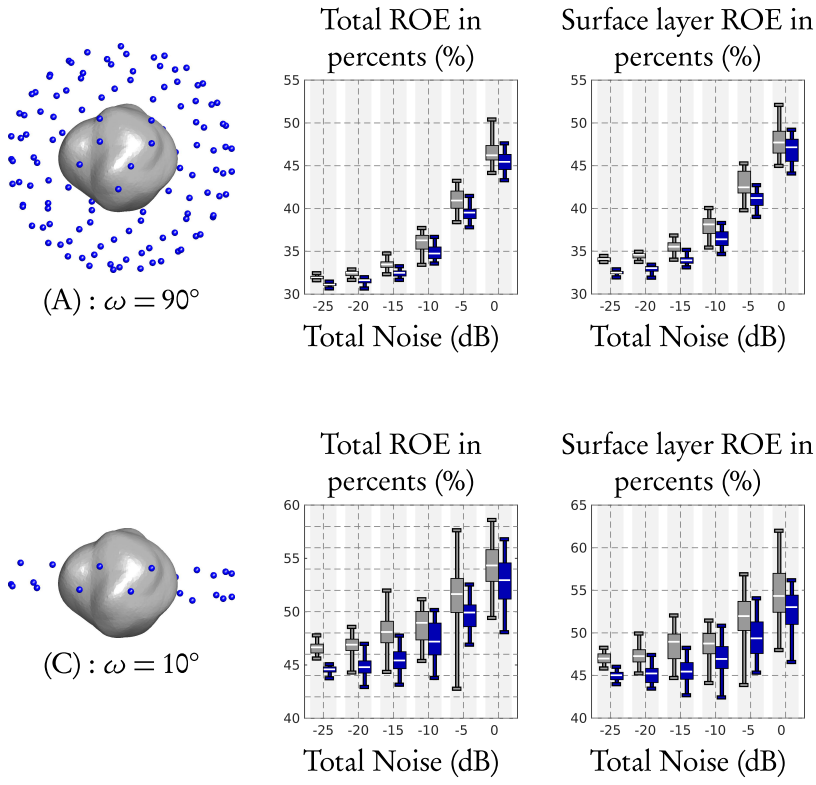

Figure 5.4 Left: A schematic (non-scaled) illustration showing the sparse full-angle configuration (A) of 128 measurement points (top) and a sparse limited-angle configurations (C) of 24 (bottom) points, respectively. The angle ω between the orbiting plane normal and the asteroid spin is 90 and 10 degrees. The limited-angle configurations results in a pronounced aperture around the polar regions in (C). The results for the monostatic and bistatic data correspond to the light grey and dark blue box plot bars, respectively.

5.3 GPU acceleration results

The GPU acceleration of the existing Matlab scripts enabled performing the tomography simulations for Publications I-III. The work included utilization of Matlab's existing functionalities to make several parallel calculations run on GPUs. The work is published as part of the separate Geoceles [1] and Zeffiro [2] software suites. As such,

[1]Geoceles - Geoimaging tool for small celestial bodies. `https://github.com/sampsapursiainen/Geoceles`. Accessed 1.7.2019.

[2]Zeffiro - Interface for using finite elements in electromagnetic brain imaging. `https://github.com/sampsapursiainen/zeffiro_interface`. Accessed 1.7.2019.

the methods used are not groundbreaking, but this work formed a very important part of this thesis project.

For optimization of the simulation parameters, that is, parameters related to wave propagation time step and element mesh, is vital as the simulations can produce invalid results when incompatible parameters are used. The parameters were first adjusted on a GPU-equipped local desktop computer before sending a batch of large amount of wave propagation simulation calculations jobs to the likewise GPU-equipped cluster. This was vital to achieve the results as the cluster has several users and the calculation jobs are placed in a queue. By using a local GPU-equipped computer, the iterative process of finding suitable calculation parameters was achieved in a sensible time. One wave simulation for a single source position took about 71 and 184 minutes in the case of the background (without voids) and exact (with test voids) data, respectively, on a local desktop computer. This meant that multiple parameter iterations were able to be performed in a day.

As a main result of this work, limitations in the GPU memory is the main observation. To scale the simulations to a larger target object while still having the simulations running on GPUs, there would need to be advances in the memory of the GPU units on workstation computers as well as on clusters. Lately, it has been seen that GPU units with larger memories have become available, but the development is slow. Sharing of memory between separate GPU units is prohibitively slow, and advances should be made in architecture of such multiple GPU configurations to overcome the observed limitations.

5.4 CubeSat design and hardware

The DISCUS CubeSat study published in Publication IV was performed to analyze a potential configuration for a standalone mission utilizing one or multiple similar CubeSats. While the design work didn't get very far in the scope of this project, main limitations of utilizing these cost-effective COTS hardware were found and studied. In actual hardware problems, packaging of the large dipole antenna on the spacecraft and deploying it in space was studied and lab-tested by the project collaborators.

One of the main obstacles for the actual computer hardware design is the relative maturity of the CubeSat technology. The small spacecraft that are launched into space are based on recent technology developments and the development cy-

cles are, in relative sense, fast for space missions. During the thesis project, ESA's F-class mission call was opened, closed, analyzed, and a mission to be flown was selected by ESA. While the DISCUS-based mission was not selected, the timetables for this fast mission shows that the CubeSats must be based on mature technology but they are to be launched in 8-9 years at the earliest. Having hardware manufacturer support, including spare parts, production lines, engineering resources and other related aspects for this long time makes the COTS electronics less attractive for these types of missions compared to more common LEO-based CubeSat projects which are implemented in shorter time. Several companies are now developing suitable CubeSat-based platforms for utilization in Deep Space, which can help to realize the independent, privately funded missions. A separate hardware-independent platform for developing on-board software could be helpful in the future. One of such methods was studied in Publication I where a signal processing algorithm was converted to FPGA hardware description, which would then be implementable on a more supported platform in timely manner when the actual hardware assembly phase begins.

5.5 Real missions

The results of this work were used to propose a mission in the ESA F-class mission call in 2018. The proposed mission was called the Asteroid In-situ Interior Investigation - 3way. While the Discus CubeSat was a key element in the proposal, it included many other elements including contribution from JAXA and a mothership spacecraft supplied by ESA, which made the communications systems on Discus proposal easier to implement.

The recent research are also be utilized in the Hera mission proposal. The funding and implementation of this mission is subject to a decision by the meeting of the ESA ministers in November 2019. ESA selected the CubeSats for this mission at the end of 2018. The mission includes Juventas CubeSat (Figure 5.5), which includes a low frequency radar that is going to be built based on the CONSERT experiment heritage. The modelling advances in Publications II and III are applicable to these upcoming real measurements to recover the final dielectric permittivity distribution result.

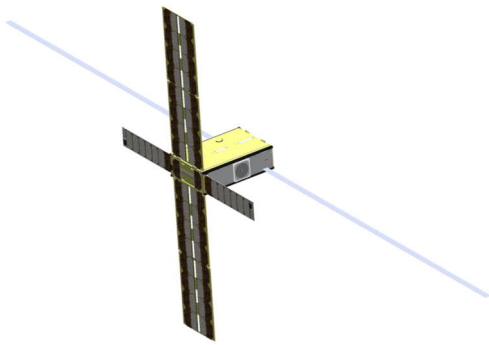

Figure 5.5 Juventas CubeSat for the ESA's Hera mission featuring a half-wave dipole antenna (light blue) for low-frequency radar. Copyright GomSpace, 2018. Used here with permission.

5.6 Open questions and further work

During the study, many open questions have arisen that are already being solved or further analyzed in a peer reviewed article or are to be studied later. Firstly, these studies did not use a realistic asteroid model. In a new publication [114] a novel way of generating a more realistic asteroid interior model is presented, and even more realistic models can be tried in the future. Inspired by the ESA F-class mission proposal, a way to combine many data modalities in the inversion results is being studied and developed, and initial work towards this goal has already been published in [113]. These modalities include radar-based data as in this work but adds tomographic modeling and analysis of gravity gradient data. The work presents a potentially workable method for improving the radar tomography results by having a better a-priori estimate of the relative permittivity distribution.

For radar modeling, implementing the wave model in a carrier wave-based scenario might be required to perform the wave propagation in as realistic way as possible. This would also cause to have a better look on how the cluster-based tomography calculations would be able to utilize GPU-equipped nodes via reducing the amount of communication required between the GPUs. Some work and architecture design for this has been done, such as [85]. However, to find the optimal solution based on the calculation software developed and utilized in this work will require some architectural rework of the software.

The tomography calculations, even with the released software, requires signifi-

cant expertise. The general arrangement of workflow from real radar data to tomography software and the way results are presented and compared, requires further work. If a real mission is flown, then this type of workflow or pipeline should be developed. Such pipeline has been developed for biomedical sciences for head CT scans in [86], but it appears that there does not exist a de-facto standard in that field of science either. In order to make the pipeline as user friendly as possible, converting the Matlab-based code to more open platform would be essential as there are popular alternatives. Namely, Python[3] has become very popular in scientific computing, so implementing the code with that could advance information sharing within the tomography science community.

[3]Python programming language. `https://www.python.org/`. Accessed 24.10.2019.

6 CONCLUSION

Over the last few years, interest towards the inner contents of asteroids has been increasing. There have been commercial companies that have attempted asteroid mining and the national space agencies are showing continued interest. There are no signs of decreasing number of small space missions using small CubeSat-based spacecraft and their utilization on deep space missions. Namely, during this study, the ESA-based F-class mission call gathered many proposals.

Theoretical modeling of asteroid tomography has taken advances in recent years, and this thesis, in Publications II and III the existing tomography methodology was advanced via a coarse-to-fine multiresolution approach in inversion of the data and a novel way to use finite element time domain wave propagation simulations in where the target wave source was in far field, i.e., outside the finite element mesh. These additions proved to be essential as the tomography simulations were, for the first time, performed with realistic parameters such as noise sources and noise levels, radar transmitting signal power and radar frequency. Also, the physical limitations on a space mission, such as realistic orbiting distance and the number of spacecrafts used, was important to consider. The results show how the simulated monostatic (single spacecraft) measurements compare with the bistatic (two spacecrafts) measurements. Main result is that from even a single spacecraft's measurements where backscattering is used, can produce relevant inversion results. The GPU-based acceleration of simulations was important as the results that were published required multiple iterations in fine tuning the parameters used and getting preliminary results was important before committing to cluster-based calculation jobs. A conceptual spacecraft and mission design DISCUS was introduced in Publication IV. In the publication, a realistic mission concept was analyzed and shown to be implementable. In the thesis, several issues related to utilization of CubeSats in deep space missions, especially those built by space agencies, was identified.

For further work, studies in tomography modeling are already being performed

and the work is still ongoing. These studies include a simulation-based study with realistic asteroid interior models, utilization of multi-modal data such as gravity gradient measurements to fine tune the tomography simulations, and carrier wave-based simulations. For some of the future simulations, especially those with carrier wave, to be performed in timely fashion, it would be beneficial to advance the GPU acceleration to work with larger amount of data at a time, in a cluster-based environment with the latest cluster-based GPU units. It would also help if GPU units on a single workstation would work more directly together. However, this could need further analysis from the mathematics and modeling viewpoint as well.

If a real space mission to perform the actual tomography of a small solar system object is going to proceed, the thesis project and working with collaborators showed that a well-defined modeling and simulation software with excellent documentation and support for free software would be required. Interface with the actual radar hardware and the format of the simulation input and output data would have to be compatible with several interfaces. This would bring the small asteroid tomography community together and advance the different modeling approaches.

REFERENCES

[1] S. Abe, T. Mukai, N. Hirata, O. S. Barnouin-Jha, A. F. Cheng, H. Demura, R. W. Gaskell, T. Hashimoto, K. Hiraoka, T. Honda, T. Kubota, M. Matsuoka, T. Mizuno, R. Nakamura, D. J. Scheeres and M. Yoshikawa. Mass and Local Topography Measurements of Itokawa by Hayabusa. *Science* 312.5778 (2006), 1344–1347. DOI: 10.1126/science.1126272.

[2] C. Altman and K. Suchy. *Reciprocity, Spatial Mapping and Time Reversal in Electromagnetics*. Developments in Electromagnetic Theory and Applications. Springer Netherlands, 1991. ISBN: 9780792313397.

[3] E. Asphaug, M. J. S. Belton and R. Y. Kakuda. Geophysical Exploration of Asteroids: The Deep Interior Mission Concept. *Lunar and Planetary Science Conference*. Lunar and Planetary Science Conference. Mar. 2001, 1867.

[4] E. Asphaug, M. Belton, A. Cangahuala, L. Keith, K. Klaasen, L. McFadden, G. Neumann, S. Ostro, R. Reinert, A. Safaeinili et al. Exploring asteroid interiors: The Deep Interior mission concept. *Lunar and Planetary Science Conference*. Vol. 34. 2003.

[5] K. Avery, J. Finchel, J. Mee, W. Kemp, R. Netzer, D. Elkins, B. Zufelt and D. Alexander. Total Dose Test Results for CubeSat Electronics. *2011 IEEE Radiation Effects Data Workshop*. 2011, 1–8.

[6] V. Badescu. *Asteroids: Prospective energy and material resources*. Springer Science & Business Media, 2013.

[7] P. Bambach, J. Deller, E. Vilenius, O. Karatekin, F. da Silva Pais Cabral, S. Pursiainen, L.-I. Sorsa, K. Wada, T. Kohout, H. Goldberg and P. Tortora. ESA F-Class mission candidate AI3: A mothership/daughters concept to deliver CubeSats to an asteroid. *iCubeSat 2019, Milan, Italy*. 2019, Abstract 2019.A.3.5.

[8] P. Bambach, J. Deller, E. Vilenius, S. Pursiainen, M. Takala, H. M. Braun, H. Lentz and M. Wittig. DISCUS – The Deep Interior Scanning CubeSat mission to a rubble pile near-Earth asteroid. *Advances in Space Research* 62.12 (2018). Advances in Technologies, Missions and Applications of Small Satellites, 3357–3368. ISSN: 0273-1177. DOI: 10.1016/j.asr.2018.06.016.

[9] B. W. Barbee, M. B. Syal, D. Dearborn, G. Gisler, K. Greenaugh, K. M. Howley, R. Leung, J. Lyzhoft, P. L. Miller, J. A. Nuth, C. Plesko, B. D. Seery, J. Wasem, R. P. Weaver and M. Zebenay. Options and uncertainties in planetary defense: Mission planning and vehicle design for flexible response. *Acta Astronautica* 143 (2018), 37–61. ISSN: 0094-5765. DOI: 10.1016/j.actaastro.2017.10.021.

[10] J.-P. Barriot, W. Kofman, A. Herique, S. Leblanc and A. Portal. A two dimensional simulation of the CONSERT experiment (Radio tomography of comet Wirtanen). *Advances in Space Research* 24.9 (1999), 1127–1138.

[11] M. A. Barucci, M. Yoshikawa, P. Michel, J. Kawagushi, H. Yano, J. R. Brucato, I. A. Franchi, E. Dotto, M. Fulchignoni, S. Ulamec and Marco Polo Science Team. MARCO POLO: Near Earth object sample return mission. *Experimental Astronomy* 23.3 (Mar. 2009), 785–808. ISSN: 1572-9508. DOI: 10.1007/s10686-008-9087-8.

[12] M. A. Barucci, A. Cheng, P. Michel, L. Benner, R. Binzel, P. Bland, H. Böhnhardt, J. Brucato, A. C. Bagatin, P. Cerroni et al. MarcoPolo-R near earth asteroid sample return mission. *Experimental Astronomy* 33.2-3 (2012), 645–684.

[13] S. Bernard, V. Monteiller, D. Komatitsch and P. Lasaygues. Ultrasonic computed tomography based on full-waveform inversion for bone quantitative imaging. *Physics in Medicine & Biology* 62.17 (Aug. 2017), 7011–7035. DOI: 10.1088/1361-6560/aa7e5a.

[14] E. Beshore, D. Lauretta, W. Boynton, C. Shinohara, B. Sutter, D. Everett, J. Gal-Edd, R. Mink, M. Moreau and J. Dworkin. The OSIRIS-REx asteroid sample return mission. *2015 IEEE Aerospace Conference*. IEEE. 2015, 1–14.

[15] W. F. Bottke Jr, D. Vokrouhlicky, D. P. Rubincam and D. Nesvorny. The Yarkovsky and YORP effects: Implications for asteroid dynamics. *Annu. Rev. Earth Planet. Sci.* 34 (2006), 157–191.

[16] W. Bottke. *Asteroids III*. University of Arizona space science series. University of Arizona Press, 2002. ISBN: 9780816522811.

[17] W. F. Bottke, R. Jedicke, A. Morbidelli, J.-M. Petit and B. Gladman. Understanding the distribution of near-Earth asteroids. *Science* 288.5474 (2000), 2190–2194.

[18] E. Bowell, C. R. Chapman, J. C. Gradie, D. Morrison and B. Zellner. Taxonomy of asteroids. *Icarus* 35.3 (1978), 313–335. ISSN: 0019-1035. DOI: 10.1016/0019-1035(78)90085-4.

[19] D. Braess. *Finite Elements*. Cambridge: Cambridge University Press, 2001.

[20] D. Braess. *Finite Elements: Theory, Fast Solvers, and Applications in Solid Mechanics*. Cambridge University Press, 2007. ISBN: 9781139461467.

[21] T. H. Burbine. *Asteroids*. Vol. 17. Cambridge University Press, 2016.

[22] B. F. Burke and K. Franklin. Observations of a variable radio source associated with the planet Jupiter. *Journal of Geophysical Research* 60.2 (1955), 213–217.

[23] S. J. Bus, F. Vilas and M. A. Barucci. Visible-Wavelength Spectroscopy of Asteroids. *Asteroids III*. Ed. by W. F. Bottke Jr., A. Cellino, P. Paolicchi and R. P. Binzel. 2002, 169–182.

[24] S. J. Bus and R. P. Binzel. Phase II of the Small Main-Belt Asteroid Spectroscopic Survey: A Feature-Based Taxonomy. *Icarus* 158.1 (2002), 146–177. ISSN: 0019-1035. DOI: 10.1006/icar.2002.6856.

[25] A. Chambolle. An algorithm for total variation minimization and applications. *Journal of Mathematical imaging and vision* 20.1 (2004), 89–97.

[26] C. R. Chapman. Cratering on Asteroids from Galileo and NEAR Shoemaker. *Asteroids III*. Ed. by W. F. Bottke Jr., A. Cellino, P. Paolicchi and R. P. Binzel. 2002, 315–329.

[27] D. Colton and R. Kress. *Inverse Acoustic and Electromagnetic Scattering Theory*. Applied Mathematical Sciences. Springer Berlin Heidelberg, 2013. ISBN: 9783662035375.

[28] A. Crida. Solar System Formation. *Reviews in Modern Astronomy*. John Wiley & Sons, Ltd, 2010, 215–227. ISBN: 9783527629190. DOI: 10.1002/9783527629190.ch12.

[29] P. D'Arrigo, M. A. Barucci and C.-I. Lagerkvist. The ISHTAR mission. *Asteroids, Comets, and Meteors: ACM 2002*. Ed. by B. Warmbein. Vol. 500. ESA Special Publication. Nov. 2002, 95–98.

[30] A. J. DeCicco and C. M. Hartzell. System-level design considerations for asteroid despin via neutral beam emitting spacecraft. *2016 IEEE Aerospace Conference*. Mar. 2016, 1–8. DOI: 10.1109/AERO.2016.7500595.

[31] J. Deller. Hyper-Velocity Impacts on Rubble Pile Asteroids. PhD thesis. University of Kent, International Max Planck Research School for Solar System Science, July 2015. URL: https://kar.kent.ac.uk/54352/.

[32] J. Deller, O. Karatekin, S. Pursiainen, K. Carroll, K. Wada, M. Jutzi, T. Kohout, B. Ritter, J. Agarwal, G. Becker, M. Takala, E. Vilenius, H. M. Braun, F. da Silva Pais Cabral, H. Goldberg, K. Schilling, F. Sjoberg, O. Roders and P. Bambach. AI3: The Asteroid In-Situ Investigation – 3Ways to measure the interior of asteroid Apophis. *Planetary Protection Conference 2019 (PDC2019), Washington DC, USA*. 2019, Abstract IAA-PDC-19-03–07.

[33] K. Doyle. Water Electrolysis Propulsion: Systems Architecture and Technology Development. PhD thesis. Cornell University, 2019.

[34] D. Duffy. *Green's Functions with Applications*. Applied Mathematics. CRC Press, 2001. ISBN: 9781420034790.

[35] N. Duric, B. Byram and S. (Society). *Medical Imaging 2018: Ultrasonic Imaging and Tomography: 13-15 February 2018, Houston, Texas, United States*. Proceedings of SPIE. 5200-. SPIE. ISBN: 9781510616493.

[36] C. Dyer. Radiation effects on spacecraft & aircraft. *Solspa 2001, Proceedings of the Second Solar Cycle and Space Weather Euroconference*. Ed. by H. Sawaya-Lacoste. Vol. 477. ESA Special Publication. Mar. 2002, 505–512.

[37] D. Eisenburger, Y. Krellmann, H. Lentz and G. Triltzsch. Stepped-Frequency Radar System in Gating Mode: An Experiment as a New Helicopter-Borne GPR System for Geological Applications. *IGARSS 2008 - 2008 IEEE International Geoscience and Remote Sensing Symposium*. Vol. 1. July 2008, I-153-I–156. DOI: 10.1109/IGARSS.2008.4778816.

[38] T. A. Ely, E. A. Burt, J. D. Prestage, J. M. Seubert and R. L. Tjoelker. Using the Deep Space Atomic Clock for Navigation and Science. *IEEE Transactions on Ultrasonics, Ferroelectrics, and Frequency Control* 65.6 (June 2018), 950–961. ISSN: 0885-3010. DOI: 10.1109/TUFFC.2018.2808269.

[39] L. Evans. *Partial Differential Equations*. Graduate studies in mathematics. American Mathematical Society, 2010. ISBN: 9780821849743.

[40] G. Folland. *Fourier Analysis and Its Applications*. Pure and applied undergraduate texts. American Mathematical Society, 2009. ISBN: 9780821847909.

[41] A. Gálvez and I. Carnelli. ESA studies on the Don Quijote NEO mission: dealing with impact uncertainties. (Jan. 2005).

[42] A. Gálvez and I. Carnelli. ESA's Don Quijote Mission: an opportunity for the investigation of an artificial impact crater on an asteroid. *25th International Symposium on Space Technology and Science*. 2006.

[43] K.-H. Glassmeier, H. Boehnhardt, D. Koschny, E. Kührt and I. Richter. The Rosetta mission: flying towards the origin of the solar system. *Space Science Reviews* 128.1-4 (2007), 1–21.

[44] R. Gomes, H. F. Levison, K. Tsiganis and A. Morbidelli. Origin of the cataclysmic Late Heavy Bombardment period of the terrestrial planets. *Nature* 435 (2005), 466–469. DOI: 10.1038/nature03676.

[45] R. Gomes, H. F. Levison, K. Tsiganis and A. Morbidelli. Origin of the cataclysmic Late Heavy Bombardment period of the terrestrial planets. *Nature* 435.7041 (2005), 466–469.

[46] A. V. Goncharsky, S. Y. Romanov and S. Y. Seryozhnikov. Low-frequency three-dimensional ultrasonic tomography. *Doklady Physics* 61.5 (May 2016), 211–214. ISSN: 1562-6903. DOI: 10.1134/S1028335816050086.

[47] J. Green and D. Daou. NASA's Planetary Science Missions Present and Future Plans. *42nd COSPAR Scientific Assembly*. Vol. 42. 2018.

[48] C. L. Hardin. The scientific work of the Reverend John Michell. *Annals of Science* 22.1 (1966), 27–47.

[49] A. Herique, B. Agnus, E. Asphaug, A. Barucci, P. Beck, J. Bellerose, J. Biele, L. Bonal, P. Bousquet, L. Bruzzone, C. Buck, I. Carnelli, A. Cheng, V. Ciarletti, M. Delbo, J. Du, X. Du, C. Eyraud, W. Fa, J. G. Fernandez, O. Gassot, R. Granados-Alfaro, S. Green, B. Grieger, J. Grundmann, J. Grygorczuk, R. Hahnel, E. Heggy, T.-M. Ho, O. Karatekin, Y. Kasaba, T. Kobayashi, W. Kofman, C. Krause, A. Kumamoto, M. Küppers, M. Laabs, C. Lange, J. Lasue, A. Levasseur-Regourd, A. Mallet, P. Michel, S. Mottola, N. Murdoch, M. Mütze, J. Oberst, R. Orosei, D. Plettemeier, S. Rochat, R. RodriguezSuquet, Y. Rogez, P. Schaffer, C. Snodgrass, J.-C. Souyris, M. Tokarz, S. Ulamec, J.-E. Wahlund and S. Zine. Direct observations of asteroid interior and regolith structure: Science measurement requirements. *Advances in Space Research* 62.8 (2018), 2141–2162. ISSN: 0273-1177. DOI: 10.1016/j.asr.2017.10.020.

[50] A. Herique, V. Ciarletti, D. Plettemeier and J. Grygorczuk. a Direct Observation of the Asteroid's Structure from Deep Interior to Regolith: Two Radars on the Aim Mission. *AGU Fall Meeting Abstracts*. Dec. 2016, P43B–2109.

[51] A. Herique, D. Plettemeier, W. Kofman, Y. Rogez, C. Buck and H. Goldberg. A Low Frequency Radar to Fathom Asteroids from Juventas Cubesat on HERA. *EPSC-DPS Joint Meeting 2019*. Vol. 2019. Sept. 2019, EPSC-DPS2019–807.

[52] A. Herique, D. Plettemeier, C. Lange, J. T. Grundmann, V. Ciarletti, T.-M. Ho, W. Kofman, B. Agnus, J. Du, W. Fa, O. Gassot, R. Granados-Alfaro, J. Grygorczuk, R. Hahnel, C. Hoarau, M. Laabs, C. L. Gac, M. Mütze, S. Rochat, Y. Rogez, M. Tokarz, P. Schaffer, A.-J. Vieau, J. Biele, C. Buck, J. G. Fernandez, C. Krause, R. R. Suquet and S. Ulamec. A radar package for asteroid subsurface investigations: Implications of implementing and integration into the MASCOT nanoscale landing platform from science requirements to baseline design. *Acta Astronautica* 156 (2019), 317–329. ISSN: 0094-5765. DOI: 10.1016/j.actaastro.2018.03.058.

[53] K. Hoegh, L. Khazanovich and H. T. Yu. Ultrasonic tomography for evaluation of concrete pavements. *Transportation Research Record* 2232.1 (2011), 85–94.

[54] K. Hou, H. Wang, W. Feng, J. S. Vetter and S. Lee. Highly Efficient Compensation-Based Parallelism for Wavefront Loops on GPUs. *2018 IEEE International Parallel and Distributed Processing Symposium (IPDPS)*. 2018, 276–285.

[55] J. Hugenschmidt, A. Kalogeropoulos, F. Soldovieri and G. Prisco. Processing strategies for high-resolution GPR concrete inspections. *NDT & E International* 43.4 (2010), 334–342.

[56] J. D. Jackson. *Classical electrodynamics*. 3rd ed. New York, NY: Wiley, 1999. ISBN: 9780471309321.

[57] J. P. Kaipio and E. Somersalo. *Statistical and Computational Methods for Inverse Problems*. Berlin: Springer, 2004.

[58] J. Kaipio and E. Somersalo. *Statistical and Computational Inverse Problems*. Applied Mathematical Sciences. Springer New York, 2006.

[59] L. Kamenski, W. Huang and H. Xu. Conditioning of finite element equations with arbitrary anisotropic meshes. *Mathematics of Computation* 83.289 (2014), 2187–2211. DOI: 10.1090/S0025-5718-2014-02822-6.

[60] Ö. Karatekin and H. Goldberg. Juventas CubeSat. *Hera community workshop 15-16 November 2018*. https://www.cosmos.esa.int/documents/1786001/1846091/7.+juventas-overview_v3.pdf/b548e67a-9243-9263-96d7-60d643f8f8e1. Nov. 2018.

[61] J. S. Kargel. Metalliferous asteroids as potential sources of precious metals. *Journal of Geophysical Research: Planets* 99.E10 (1994), 21129–21141. DOI: 10.1029/94JE02141.

[62] R. Kofler, G. Drolshagen, L. Drube, A. Haddaji, L. Johnson, D. Koschny and R. Landis. International coordination on planetary defence: The work of the IAWN and the SMPAG. *Acta Astronautica* 156 (2019), 409–415. ISSN: 0094-5765. DOI: 10.1016/j.actaastro.2018.07.023.

[63] W. Kofman. Radar techniques to study subsurfaces and interiors of the solar system objects. *2012 19th International Conference on Microwaves, Radar Wireless Communications*. Vol. 2. May 2012, 409–412. DOI: 10.1109/MIKON.2012.6233605.

[64] W. Kofman, Y. Barbin, J. Klinger, A.-C. Levasseur-Regourd, J.-P. Barriot, A. Herique, T. Hagfors, E. Nielsen, E. Grün, P. Edenhofer, H. Kochan, G. Picardi, R. Seu, J. van Zyl, C. Elachi, J. Melosh, J. Veverka, P. Weissman, L. Svedhem, S. Hamran and I. Williams. Comet nucleus sounding experiment by radiowave transmission. *Advances in Space Research* 21.11 (1998), 1589–1598. ISSN: 0273-1177. DOI: 10.1016/S0273-1177(97)00952-6.

[65] W. Kofman, A. Herique, Y. Barbin, J.-P. Barriot, V. Ciarletti, S. Clifford, P. Edenhofer, C. Elachi, C. Eyraud, J.-P. Goutail, E. Heggy, L. Jorda, J. Lasue, A.-C. Levasseur-Regourd, E. Nielsen, P. Pasquero, F. Preusker, P. Puget, D. Plettemeier, Y. Rogez, H. Sierks, C. Statz, H. Svedhem, I. Williams, S. Zine and J. Van Zyl. Properties of the 67P/Churyumov-Gerasimenko interior revealed by CONSERT radar. *Science* 349.6247 (2015). DOI: 10.1126/science.aab0639.

[66] T. Kohout, A. Näsilä, T. Tikka, M. Granvik, A. Kestilä, A. Penttilä, J. Kuhno, K. Muinonen, K. Viherkanto and E. Kallio. Feasibility of asteroid exploration using CubeSats—ASPECT case study. *Advances in Space Research* 62.8 (2018), 2239–2244.

[67] J. Kraus. *Antennas, 2nd Edition*. Electrical Engineering Series. McGraw-Hill, 1988. ISBN: 9780070354227.

[68] K. A. LaBel. The NASA Electronic Parts and Packaging (NEPP) Program-Automotive Electronics. (2014).

[69] P. Laurent, D. Massonnet, L. Cacciapuoti and C. Salomon. The ACES/PHARAO space mission. *Comptes Rendus Physique* 16.5 (2015). The measurement of time / La mesure du temps, 540–552. ISSN: 1631-0705. DOI: 10.1016/j.crhy.2015.05.002.

[70] P. D. Lax. Stability of Difference Schemes. *The Courant–Friedrichs–Lewy (CFL) Condition: 80 Years After Its Discovery*. Ed. by C. A. de Moura and C. S. Kubrusly. Boston: Birkhäuser Boston, 2013, 1–7. ISBN: 978-0-8176-8394-8. DOI: 10.1007/978-0-8176-8394-8_1.

[71] K. Ho-Le. Finite element mesh generation methods: a review and classification. *Computer-aided design* 20.1 (1988), 27–38.

[72] H. Leppinen, A. Kestilä, P. Pihajoki, J. Jokelainen and T. Haunia. On-board data handling for ambitious nanosatellite missions using automotive-grade lock-step microcontrollers. *Small Satellites Systems and Services-The 4S Symposium*. 1. 2014, 1–10.

[73] H. F. Levison, A. Morbidelli, C. Van Laerhoven, R. Gomes and K. Tsiganis. Origin of the structure of the Kuiper belt during a dynamical instability in the orbits of Uranus and Neptune. *Icarus* 196 (July 2008), 258–273. DOI: 10.1016/j.icarus.2007.11.035.

[74] Q. Liu and Y. Gu. Seismic imaging: From classical to adjoint tomography. *Tectonophysics* 566-567 (2012), 31–66. ISSN: 0040-1951. DOI: 10.1016/j.tecto.2012.07.006.

[75] L. Lo Monte, D. Erricolo, F. Soldovieri and M. C. Wicks. Radio Frequency Tomography for Tunnel Detection. *IEEE Transactions on Geoscience and Remote Sensing* 48.3 (Mar. 2010), 1128–1137. ISSN: 0196-2892. DOI: 10.1109/TGRS.2009.2029341.

[76] E. T. Lu and S. G. Love. Gravitational tractor for towing asteroids. *Nature* 438.7065 (2005), 177.

[77] T. Lu, W. Cai and P. Zhang. Discontinuous Galerkin time-domain method for GPR simulation in dispersive media. *Geoscience and Remote Sensing, IEEE Transactions on* 43.1 (2005), 72–80. ISSN: 0196-2892. DOI: 10.1109/TGRS.2004.838350.

[78] A. Mereta and D. Izzo. Target selection for a small low-thrust mission to near-Earth asteroids. *Astrodynamics* 2 (Feb. 2018). DOI: 10.1007/s42064-018-0024-y.

[79] P. Michel, M. Barucci, A. Cheng, H. Böhnhardt, J. Brucato, E. Dotto, P. Ehrenfreund, I. Franchi, S. Green, L.-M. Lara et al. MarcoPolo-R: Near-Earth Asteroid sample return mission selected for the assessment study phase of the ESA program cosmic vision. *Acta Astronautica* 93 (2014), 530–538.

[80] P. Michel, M. Kueppers, I. Carnelli, A. Galvez, K. Mellab and A. Cheng. Asteroid Impact Mission (AIM): the European component of the AIDA space project. *Lunar and Planetary Science Conference*. Vol. 47. 2016, 1204.

[81] P. Michel, M. Kueppers, H. Sierks, I. Carnelli, A. Cheng, K. Mellab, M. Granvik, A. Kestilä, T. Kohout, K. Muinonen, A. Näsilä, A. Penttila, T. Tikka, P. Tortora, V. Ciarletti, A. Hérique, N. Murdoch, E. Asphaug, A. Rivkin, O. Barnouin, A. Bagatin, P. Pravec, D. Richardson, S. Schwartz, K. Tsiganis, S. Ulamec and O. Karatekin. European component of the AIDA mission to a binary asteroid: Characterization and interpretation of the impact of the DART mission. English (US). *Advances in Space Research* (Jan. 2017). ISSN: 0273-1177. DOI: 10.1016/j.asr.2017.12.020.

[82] D. Miller, A. Saenz-Otero, J. Wertz, A. Chen, G. Berkowski, C. Brodel, S. Carlson, D. Carpenter, S. Chen and S. Cheng. SPHERES: A Testbed for Long Duration Satellite Formation Flying in Micro-Gravity Conditions. *ADVANCES IN THE ASTRONAUTICAL SCIENCES* 105 (2000), 167–180.

[83] N. Mita and T. Takiguchi. Principle of ultrasonic tomography for concrete structures and non-destructive inspection of concrete cover for reinforcement. *Pacific Journal of Mathematics for Industry* 10.1 (Sept. 2018), 6. ISSN: 2198-4115. DOI: 10.1186/s40736-018-0040-0.

[84] A. Morbidelli, K. J. Walsh, D. P. O'Brien, D. A. Minton and W. F. Bottke. The Dynamical Evolution of the Asteroid Belt. *Asteroids IV*. Ed. by P. Michel et al. Univ. of Arizona, Tucson, 2015, 493–507.

[86] J. Muschelli. Recommendations for Processing Head CT Data. *Frontiers in Neuroinformatics* 13 (2019), 61. ISSN: 1662-5196. DOI: 10.3389/fninf.2019.00061.

[87] F. Natterer. *The mathematics of computerized tomography*. SIAM, 2001.

[88] E. Nielsen, W. Engelhardt, B. Chares, L. Bemmann, M. Richards, F. Backwinkel, D. Plettemeier, P. Edenhofer, Y. Barbin, J. Goutail, W. Kofman and L. Svedhem. Antennas for sounding of a cometary nucleus in the Rosetta mission. English. *Eleventh International Conference on Antennas and Propagation, Vols 1 and 2*. IEE Conference Publications 480. 379 THORNALL ST, EDISON, NJ 08837 USA: Inst Electrical Engineers Inspec INC, 2001, 436–441. ISBN: 0-85296-733-0.

[89] D. Y. Oh, S. Collins, D. Goebel, B. Hart, G. Lantoine, S. Snyder, G. Whiffen, L. Elkins-Tanton, P. Lord, Z. Pirkl et al. Development of the Psyche Mission for NASA's Discovery Program. 2017.

[90] K. J. Opielinski and T. Gudra. Multi-parameter ultrasound transmission tomography of biological media. *Ultrasonics* 44 (2006), e295–e302.

[91] L. Orlando. Object dimension Vs antenna frequency. *Ground Penetrating Radar (GPR), 2010 13th International Conference on*. 2010, 1–5. DOI: 10.1109/ICGPR.2010.5550258.

[92] E. Pascale, P. Eccleston and G. Tinetti. The ARIEL space mission. *2018 5th IEEE International Workshop on Metrology for AeroSpace (MetroAeroSpace)*. IEEE. 2018, 31–34.

[93] M. Pätzold, T. P. Andert, S. W. Asmar, J. D. Anderson, J.-P. Barriot, M. K. Bird, B. Häusler, M. Hahn, S. Tellmann, H. Sierks, P. Lamy and B. P. Weiss. Asteroid 21 Lutetia: Low Mass, High Density. *Science* 334.6055 (2011), 491–492. DOI: 10.1126/science.1209389.

[94] D. Plettemeier, S. Balling, D. Landmann and K.-H. Gonschorek. Use of Genetic Algorithms to Solve Inverse Scattering Problems a Contribution to the Experiment CONSERT onboard the Spacecraft Rosetta. *Electromagnetic Compatibility, 2007. EMC 2007. IEEE International Symposium on*. July 2007, 1–6. DOI: 10.1109/ISEMC.2007.155.

[95] D. Plettemeier and A. Herique. FANTINA instrument suite: A payload proposed to measure the asteroid's structure from deep interior to regolith. *AGU Fall Meeting Abstracts*. Vol. 2013. Dec. 2013, P23A–1752.

[96] R. Pongvthithum, S. M. Veres, S. B. Gabriel and E. Rogers. Universal adaptive control of satellite formation flying. *International Journal of Control* 78 (1 2005), 45–52.

[97] P. Pravec and A. W. Harris. Fast and Slow Rotation of Asteroids. *Icarus* 148 (Nov. 2000), 12–20. DOI: 10.1006/icar.2000.6482.

[98] P. Pravec, A. W. Harris and T. Michalowski. Asteroid rotations. *Asteroids III* 113 (2002).

[99] S. Pursiainen and M. Kaasalainen. Orbiter-to-orbiter Tomography: A Potential Approach for Small Solar System Body. *IEEE Transactions on Aerospace and Electronic Systems*. Vol. 52. 2016, 2747–2759. DOI: 10.1109/TAES.2016.150638.

[100] S. Pursiainen, S. Lew and C. Wolters. Forward and Inverse Effects of the Complete Electrode Model in Neonatal EEG. English. *Journal of Neurophysiology* 117.3 (Mar. 2017), 876–884. ISSN: 0022-3077. DOI: 10.1152/jn.00427.2016.

[101] M. A. Richards. *Fundamentals of radar signal processing*. Tata McGraw-Hill Education, 2005.

[102] R. A. Robb. 3-D visualization in biomedical applications. *Annual review of biomedical engineering* 1.1 (1999), 377–399.

[103] L. Rosenqvist, A. Hilgers, H. Evans, E. Daly, M. Hapgood, R. Stamper, R. Zwickl, S. Bourdarie and D. Boscher. Toolkit for updating interplanetary proton cumulated fluence models. *Journal of spacecraft and rockets* 42.6 (2005), 1077–1090.

[104] P. Sava and E. Asphaug. 3D radar wavefield tomography of comet interiors. English (US). *Advances in Space Research* (Jan. 2018). ISSN: 0273-1177. DOI: 10.1016/j.asr.2018.01.040.

[105] P. Sava and E. Asphaug. Seismology on small planetary bodies by orbital laser Doppler vibrometry. *Advances in Space Research* 64.2 (July 2019), 527–544. DOI: 10.1016/j.asr.2019.04.017.

[106] D. Scheeres. Orbital mechanics about small bodies. *Acta Astronautica* 72 (2012), 1–14. ISSN: 0094-5765. DOI: 10.1016/j.actaastro.2011.10.021.

[107] P. Scheirich and P. Pravec. Modeling of lightcurves of binary asteroids. *Icarus* 200.2 (2009), 531–547. ISSN: 0019-1035. DOI: 10.1016/j.icarus.2008.12.001.

[108] O. Scherzer, M. Grasmair, H. Grossauer, M. Haltmeier and F. Lenzen. *Variational Methods in Imaging*. Applied Mathematical Sciences. Springer New York, 2008. ISBN: 9780387309316.

[109] J. B. Schneider. *Understanding the FDTD Method*. John B. Schneider, 2016. URL: http://www.eecs.wsu.edu/~schneidj/ufdtd/.

[110] S. Y. Semenov and D. R. Corfield. Microwave tomography for brain imaging: Feasibility assessment for stroke detection. *International Journal of Antennas and Propagation* 2008 (2008).

[111] J. Sharpe, U. Ahlgren, P. Perry, B. Hill, A. Ross, J. Hecksher-Sørensen, R. Baldock and D. Davidson. Optical projection tomography as a tool for 3D microscopy and gene expression studies. *Science* 296.5567 (2002), 541–545.

[112] E. Slowik. Descartes' Physics. *The Stanford Encyclopedia of Philosophy*. Ed. by E. N. Zalta. Fall 2017. Metaphysics Research Lab, Stanford University, 2017.

[113] L.-I. Sorsa, M. Takala, P. Bambach, J. Deller, E. Vilenius, J. Agarwal, K. A. Carroll, Ö. Karatekin and S. Pursiainen. Tomographic inversion of gravity gradient field for a synthetic Itokawa model. *Icarus* 336 (2020), 113425. ISSN: 0019-1035. DOI: 10.1016/j.icarus.2019.113425.

[114] L.-I. Sorsa, M. Takala, P. Bambach, J. Deller, E. Vilenius and S. Pursiainen. Bistatic Full-wave Radar Tomography Detects Deep Interior Voids, Cracks, and Boulders in a Rubble-pile Asteroid Model. *The Astrophysical Journal* 872.1 (Feb. 2019), 44. DOI: 10.3847/1538-4357/aafba2.

[115] W. Stefan. *Total Variation Regularization for Linear Ill-posed Inverse Problems: Extensions and Applications*. Arizona State University, 2008.

[116] System design of the Hayabusa 2—Asteroid sample return mission to 1999 JU3. *Acta Astronautica* 91 (2013), 356–362. ISSN: 0094-5765. DOI: 10.1016/j.actaastro.2013.06.028.

[117] A. S. Tagliafico, M. Calabrese, G. Mariscotti, M. Durando, S. Tosto, F. Monetti, S. Airaldi, B. Bignotti, J. Nori, A. Bagni et al. Adjunct screening with tomosynthesis or ultrasound in women with mammography-negative dense breasts: interim report of a prospective comparative trial. *J Clin Oncol* 34.16 (2016), 1882–1888.

[118] M. Takala, P. Bambach, J. Deller, E. Vilenius, M. Wittig, H. Lentz, H. M. Braun, M. Kaasalainen and S. Pursiainen. Far-Field Inversion for the Deep Interior Scanning CubeSat. *IEEE Transactions on Aerospace and Electronic Systems* 55.4 (Aug. 2019), 1683–1697. ISSN: 0018-9251. DOI: 10.1109/TAES.2018.2874755.

[119] M. Takala, T. D. Hämäläinen and S. Pursiainen. The Effect of Hardware-Computed Travel Time on Localization Accuracy in the Inversion of Experimental (Acoustic) Waveform Data. *IEEE Transactions on Computational Imaging* 3.2 (June 2017), 344–354. ISSN: 2333-9403. DOI: 10.1109/TCI.2017.2686698.

[120] M. Takala, D. Us and S. Pursiainen. Multigrid-Based Inversion for Volumetric Radar Imaging With Asteroid Interior Reconstruction as a Potential Application. *IEEE Transactions on Computational Imaging* 4.2 (June 2018), 228–240. ISSN: 2333-9403. DOI: 10.1109/TCI.2018.2811908.

[121] A. Tarantola. *Inverse Problem Theory and Methods for Model Parameter Estimation*. Other titles in applied mathematics. Society for Industrial and Applied Mathematics, 2005. ISBN: 9780898715729.

[123] A. Toorian, K. Diaz and S. Lee. The CubeSat Approach to Space Access. *2008 IEEE Aerospace Conference*. Mar. 2008, 1–14. DOI: 10.1109/AERO.2008.4526293.

[124] L. Topczewski, F. M. Fernandes, P. J. Cruz and P. B. Lourenço. Practical implications of GPR investigation using 3D data reconstruction and transmission tomography. *Journal of Building Appraisal* 3.1 (2007), 59–76.

[125] D. E. Trilling, F. Valdes, L. Allen, D. James, C. Fuentes, D. Herrera, T. Axelrod and J. Rajagopal. The Size Distribution of Near-Earth Objects Larger Than 10 m. *Astronomical Journal* 154, 170 (Oct. 2017), 170. DOI: 10.3847/1538-3881/aa8036.

[126] G. Uhlmann. *Inside out: inverse problems and applications*. Vol. 47. Cambridge University Press, 2003.

[122] C. Vallat, N. Altobelli, B. Geiger, B. Grieger, M. Kueppers, C. Muñoz Crego, R. Moissl, M. G. Taylor, C. Alexander, B. Buratti and M. Choukroun. The science planning process on the Rosetta mission. *Acta Astronautica* 133 (2017), 244–257. ISSN: 0094-5765. DOI: 10.1016/j.actaastro.2017.01.018.

[127] K. J. Walsh. Rubble Pile Asteroids. *Annual Review of Astronomy and Astrophysics* 56.1 (2018), 593–624. DOI: 10.1146/annurev-astro-081817-052013.

[128] M. Walt. *Introduction to geomagnetically trapped radiation*. Cambridge University Press, 2005.

[129] S.-i. Watanabe, Y. Tsuda, M. Yoshikawa, S. Tanaka, T. Saiki and S. Nakazawa. Hayabusa2 mission overview. *Space Science Reviews* 208.1-4 (2017), 3–16.

[130] N. Willis. Bistatic radar. In Radar Handbook. *Radar Handbook*. Ed. by M. I. Skolnik. McGraw-Hill Professional, New York, 2008.

[131] L. Xiao, Q. Xue and H. Wang. Finite element mesh optimisation for improvement of the sensitivity matrix in electrical resistance tomography. *IET Science, Measurement Technology* 9.7 (2015), 792–799.

[132] K. S. Yee. Numerical solution of initial boundary value problems involving Maxwells equations in isotropic media. *IEEE Trans. Antennas and Propagation* (1966), 302–307.

[133] H.-H. Yeh and A. Sparks. Geometry and control of satellite formations. *American Control Conference, 2000. Proceedings of the 2000*. Vol. 1. 6. Sept. 2000, 384–388 vol.1. DOI: 10.1109/ACC.2000.878926.

[134] Ö. Yilmaz and S. Doherty. *Seismic Data Analysis: Processing, Inversion, and Interpretation of Seismic Data*. Investigations in Geophysics Series nid. 1. Society of Exploration Geophysicists, 2001. ISBN: 9781560800989.

[135] R. P. Young and S. C. Maxwell. Seismic characterization of a highly stressed rock mass using tomographic imaging and induced seismicity. *Journal of Geophysical Research: Solid Earth* 97.B9 (1992), 12361–12373. DOI: 10.1029/92JB00678.

[85] J. Zhou, Y. Cui, E. Poyraz, D. J. Choi and C. C. Guest. Multi-GPU Implementation of a 3D Finite Difference Time Domain Earthquake Code on Heterogeneous Supercomputers. *Procedia Computer Science* 18 (2013). 2013 International Conference on Computational Science, 1255–1264. ISSN: 1877-0509. DOI: 10.1016/j.procs.2013.05.292.

PUBLICATIONS

PUBLICATION

I

The Effect of Hardware-Computed Travel Time on Localization Accuracy in the Inversion of Experimental (Acoustic) Waveform Data

M. Takala, T. D. Hämäläinen and S. Pursiainen

IEEE Transactions on Computational Imaging 3.2 (2017), 344–354
DOI: 10.1109/TCI.2017.2686698

The effect of hardware-computed travel-time on localization accuracy in the inversion of experimental (acoustic) waveform data

Mika Takala, Timo D. Hämäläinen, Sampsa Pursiainen

***Abstract*—This study aims to advance hardware-level computations for travel-time tomography applications in which the wavelength is close to the diameter of the information that has to be recovered. Such can be the case, for example, in the imaging applications of (1) biomedical physics, (2) astro-geophysics and (3) civil engineering. Our aim is to shed light on the effect of that preprocessing the digital waveform signal has on the inversion results and to find computational solutions that guarantee robust inversion when there are incomplete and/or noisy measurements. We describe a hardware-level implementation for integrated and thresholded travel-time computation (ITT and TTT). We compare the ITT and TTT approaches in inversion analysis with experimental acoustic travel-time data recorded using a ring geometry for the transmission and measurement points. The results obtained suggest that ITT is essential for maintaining the robustness of the inversion with imperfect signal digitization and sparsity. In order to ensure the relevance of the results, the specifications of the test setup were related to those of applications (1)–(3).**

***Index Terms*—Inverse Imaging, Waveform Tomography, Travel-Time Measurements, Field Programmable Gate Array (FPGA), High-Level Synthesis.**

I. Introduction

This paper concerns waveform tomography in which either an acoustic or electromagnetic wave travels through a target object and, based on the external measurements of the wave, the task is to estimate the distribution(s) of a given parameter within the target [1] such as the velocity of the wave or the absorbtion parameter. Tomographic imaging based on wave propagation requires computationally heavy mathematical inversion of the data in order to retrieve the relevant result set, such as an image or three-dimensional model of the test subject.

In this paper, we explore the problem of determining the travel-time of the signal [2], [3] and its relation to accuracy of the the inverse localization. In particular, we focus on the effect of hardware-level computations in applications where the signal wavelength may be expected to be close to the diameter of the details that are to be recovered. Such can be the case, for example, in biomedical microwave or ultrasonic tomography [4]–[11], in astro-geophysical subsurface imaging [12]–[16] and in non-destructive testing of civil engineering materials and structures [17]–[20]. Our aim is determine what effect the preprocessing of digital waveform signal has on the inversion results and in that context to find computational solutions that guarantee robust inversion even with incomplete and noisy measurements. We use travel-time data, as it is known to yield robust information of the unknown parameter [21], and also because it requires minimal data transfer between the hardware and the inversion routines. Data preprocessing performed on embedded hardware has its limitations, and therefore, we aim to find out how the hardware-level evaluation of the travel-time is related to the tomography results. To perform the preprocessing operations, a field programmable gate array (FPGA) [22] chip on a development board is used as a platform for the design. In order to make the implementation fast and flexible, the hardware on the FPGA was implemented by adapting Matlab scripts [23] to C code [24] and then utilizing Catapult C hardware synthesis [25] to generate the hardware from the adapted C code.

FPGA-based processing of tomographic travel-time data is utilized in all above-mentioned application fields. As specific examples we consider (**1**) the microwave and ultrasonic computed tomography (MCT and UCT) of the breast [4]–[9], (**2**) tomography of small solar system bodies (SSSBs), e.g., the COmet Nucleus Sounding Experiment by Radiowave Transmission (CONSERT) [12], [13], [15], [16], and (**3**) the acoustic/electromagnetic imaging and testing of concrete structures [10], [11], [17]–[20]. An M/UCT breast scan (Figure 1) can be performed by utilizing a 2D sensor ring [4], [8], [26] which records data slices sharing the direction of the plane normal with the ring. MCT and UCT have recently been shown to have the potential to detect and classify breast lesionsat least as reliably as other imaging methods, such as computed X-ray tomography (CT) and magnetic resonance imaging (MRI) [8], [27], [28]. Other recently studied methods for breast cancer diagnosis include, e.g., optical tomography [29], [30]. The CONSERT experiment took place as a part of the European Space Agency's *Rosetta* mission. The objective of CONSERT was to recover the internal structure of the nucleus of the comet 67P/Churyumov-Gerasimenko based on sparse lander-to-orbiter signal transfer between the Rosetta spacecraft and a single comet lander *Philae* (Figure 1). Space technology also involves also the challenging space environment as a limitation [31], [32], leading, e.g., to sparse measurements. In concrete testing [17]–[20], the task can be for example to detect interior defects within a concrete element (Figure 1) in a similar way to, e.g. the way voids are localized in geoscientific applications.

In the numerical experiments, we compared integrated and thresholded travel-time (ITT and TTT) approaches via inversion analysis utilizing experimental acoustic waveform data. A 16-bit and 8-bit analog-to-digital (A/D) conversions were tested together with two different threshold criteria and normalization levels. The results obtained suggest that ITT is essential for maintaining the robustness of the inversion if the A/D conversion is incomplete. In order to ensure the relevance of the results, the specifications of the test setup were related to those of applications (**1**)–(**3**).

This paper is organized as follows. Section 2 describes the materials and methods, including the mathematical forward modeling and inversion techniques, the test setup, the equipment and the FPGA implementation. Section 3 presents the inversion results. Section 4 sums up the findings of this work and discusses the results and the potential direction of future work.

M. Takala and S. Pursiainen (corresponding author) are with the Laboratory of Mathematics, Tampere University of Technology, Finland.

M. Takala and T. D. Hämäläinen are with Laboratory of Pervasive Computing, Tampere University of Technology, Finland.

This paper has supplementary downloadable material available at http://ieeexplore.ieee.org., provided by the author. The material includes a set of audio wave measurement data files, a readme file and a Matlab plot scrip. Contact sampsa.pursiainen@tut.fi for further questions about this work.

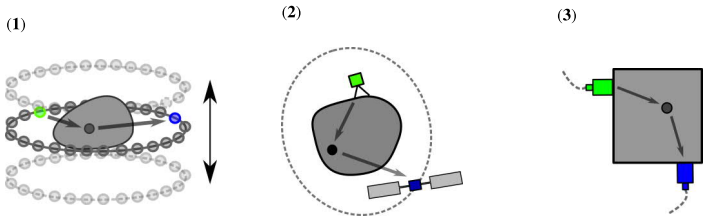

Fig. 1. A schematic picture of the travel-time measurement in the applications (**1**)–(**3**). The signal path between the transmitter (green) and receiver (blue) is refracted by a perturbation (circle) in the wave speed distribution. **Left:** A movable sensor ring that can be used to scan a 3D target object of M/UCT in slices [4], [8], [26]. **Center:** The CONSERT experiment in which the objective was to recover the internal structure of the nucleus of the comet 67P/Churyumov-Gerasimenko based on sparse lander-to-orbiter signal transfer between the Rosetta spacecraft and a single comet lander Philae [13]. **Right:** Ultrasonic detection of defects within a concrete block via two transducers and a semi-direct transmission [10].

II. Materials and Methods

A. Forward modeling

1) Signal wave: In this study, a waveform signal is modeled as a scalar field u representing an electromagnetic or acoustic wave. The computational domain Ω is assumed to contain the target object of the tomography together with its immediate surroundings. During the measurements, that is, when $t \in [t_1, t_2]$, the transmitters and receivers can be either fixed or moving or touching the surface or remote from it. In $(t, \vec{x}) \in [t_1, t_2] \times \Omega$, the scalar field u is assumed to obey the following second-order wave equation system:

$$\frac{1}{\mathtt{c}^2}\frac{\partial^2 u}{\partial t^2} - \Delta_{\vec{x}} u = f(t)\,\delta(\vec{x} - \vec{x}^{(0)}), \tag{1}$$

$$u(0, \vec{x}) = \frac{\partial u}{\partial t}(0, \vec{x}) = 0, \tag{2}$$

where $\mathtt{c}$ denotes the signal velocity in Ω, $f(t)$ is the time dependence of the signal transmission, $\vec{x}^{(0)}$ is the point (spatial location) of the transmission, and $\delta(\vec{x} - \vec{x}^{(0)})$ is a Dirichlet delta function, i.e., it is zero everywhere except at $\vec{x} = \vec{x}^{(0)}$ and satisfies the integral identity $\int_\Omega \delta(\vec{x} - \vec{x}^{(0)})\, d\Omega = 1$. The left-hand side of Equation (1) is the standard hyperbolic operator of the wave equation [33], and the right-hand side represents a point source transmitting an isotropic signal pulse. The isotropic radiation pattern is altered, if the source is placed in front of a reflector (with $\mathtt{c} = 0$). In this study, a loudspeaker profile is used as a reflector. Additionally, it is assumed that only the set of points belonging to Ω can transmit a signal and that there are no other signal sources present. Defining a new variable $\vec{g}(t, \vec{x}) = \int_0^t \nabla u(\tau, \vec{x})\, d\tau$ and $h(t) = \int_0^t f(\tau)\, d\tau$, the resulting system is of the following first-order form:

$$\frac{1}{\mathtt{c}^2}\frac{\partial u}{\partial t} - \nabla \cdot \vec{g} = h(t)\,\delta(\vec{x} - \vec{x}^{(0)}), \tag{3}$$

$$\frac{\partial \vec{g}}{\partial t} - \nabla u = 0. \tag{4}$$

This system can be discretized spatially using the finite element method (FEM) [34] and temporally via the finite-difference time-domain (FDTD) method [35] leading to so-called leap-frog formulae which enable the simulation of the complete wave [15].

2) Measurement model: In this study, we aim at localizing perturbations in the inverse of the velocity distribution $\mathtt{n} = 1/\mathtt{c}$ based on the travel-time T of the signal, as this is known to provide robust information about the velocity [2], [21]. The wave $u_m(t, \vec{x})$ measured at $\vec{x}$ is a sum of the propagating wave $u(t, \vec{x})$ and a random noise term $\varepsilon(t, \vec{x})$, i.e.,

$$u_m(t, \vec{x}) = u(t, \vec{x}) + \varepsilon(t, \vec{x}). \tag{5}$$

The noise can include both modeling and measurement errors. In order to minimize the effect of the noise, *a priori* information should be used, for example, to determine the most relevant time interval for each measurement point. However, deriving a complete statistical model for $\varepsilon(t, \vec{x})$ can be difficult due to potential but unknown error sources, such as reflections, refractions and absorption. There is also no unique way to obtain T based on the waveform measurement u_m [2].

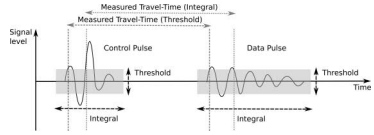

(a) Measured travel-time calculation.

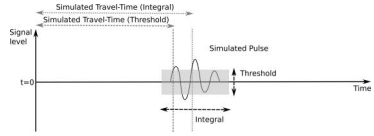

(b) Simulated travel-time calculation.

Fig. 2. Visualisation of travel time calculation types. The greyed out areas represent the integrated signal. The (b) image highlights how the methods must also be used in a simulation.

3) Integrated and thresholded travel-time estimates: In this paper, we study integration and thresholding as two alternative techniques for estimating T. Given the measured wave u_m, the integrated travel-time (ITT) estimate for a signal received at $\vec{x}$ within the time interval $[t_1, t_2]$ can be defined via the formula [36]

$$T(\vec{x}) = \frac{\int_{t_1}^{t_2} t\, u_m(t, \vec{x})^2 dt}{\int_{t_1}^{t_2} u_m(t, \vec{x})^2 dt}. \tag{6}$$

To interface the mathematic model and real signals, some decisions have to be made. These include how to decide the time interval $[t_1, t_2]$ and whether to use the ITT or an alternative strategy, e.g., the thresholded travel-time (TTT) estimate. ITT and TTT were calculated as follows:

1) Detect the time value t_0 (TTT) where the amplitude reaches a pre-selected threshold value.
2) Set $t_1 = t_0 - \tau_1$ and $t_2 = t_0 + \tau_2$, where τ_1 and τ_2 are auxiliary *a priori* parameters ensuring that the essential part of the signal pulse will be contained in $[t_1, t_2]$. Then, obtain ITT through Equation (6).

Here, τ_1 extends the inspected time interval in the reverse direction, that is, (before) the signal detection point t_0. Parameter τ_2 cuts the signal based on the *a priori* information of the pulse length in order

to prevent noise due to reflections. Figure 2 visualizes the calculation of ITT and TTT for measurement and simulated data. Figure shows that in the measurements, the travel-time can only be calculated if the starting point (control pulse) is also measured. The measured travel-time can be compared to the simulated case (Figure 2(b)) where the starting point (zero-point) is defined exactly.

Based on the measurements, exactly one travel-time value T is calculated for each transmitter-receiver position pair within the measurement configuration. The resulting set of values is referred to as the measurement data. The simulated signal refers to the wave that can be obtained via the FDTD method [15] using an initial (constant) estimate for the unknown parameter.

4) Path integrals and ray-tracing: In addition to FEM/FDTD computations, a forward simulation for the travel-time can be obtained via an integral of the form

$$T = \int_{\mathcal{C}} \mathtt{n}\, ds, \tag{7}$$

where $\mathcal{C}$ is the signal path [21]. In this approach, the prediction for $\mathcal{C}$ has a central role. This can be done, e.g., based on Snell's law of reflection and reftraction [37]. We use the approximation (7) in order to find a reconstruction of $\mathtt{n}$. We assume that the signal paths $\mathcal{C}_1, \mathcal{C}_2, \ldots, \mathcal{C}_M$ are straight line segments and that $\mathtt{n}$ is of the form $\mathtt{n} = \mathtt{n}_p + \mathtt{n}_0$, where $\mathtt{n}_0$ is an *a priori* known constant background distribution and $\mathtt{n}_p$ is an unknown perturbation. A discretized version of (7) can be obtained by subdividing the computational domain into pixels $P_1, P_2, \ldots, P_N$ and estimating $\mathtt{n}_p$ with a pixelwise constant distribution. Using $\mathbf{x}$ to denote the vector of pixel values, the equation (7) can be written in the discretized form

$$\mathbf{y} = \mathbf{L}\mathbf{x} + \mathbf{y}_0, \tag{8}$$

where $L_{i,j} = \int_{\mathcal{C}_i \cap P_j} ds$ and y_0 is a simulated vector estimated from the travel-time data corresponding to $\mathtt{n}_0$.

B. Inversion procedure

To invert the data, we use a classical total variation based regularization technique, which aims at minimizing (Appendix) the regularized objective funcion $\Psi(\mathbf{x}) = \|\mathbf{y} - \mathbf{y}_0 - \mathbf{L}\mathbf{x}\|_2 + \alpha\|\mathbf{D}\mathbf{x}\|_1$ via the iterative recursion procedure

$$\mathbf{x}^{(k)} = \left(\mathbf{L}^T\mathbf{L} + \alpha\mathbf{D}\mathbf{\Gamma}^{(k)}\mathbf{D}\right)^{-1}\mathbf{L}^T(\mathbf{y} - \mathbf{y}_0), \tag{9}$$

where $\mathbf{\Gamma}^{(k)}$ is a diagonal weighting matrix defined as $\mathbf{\Gamma}^{(k)} = \text{diag}\left(\|\mathbf{D}\mathbf{x}^{(k)}\|\right)^{-1}$ and $\mathbf{D}$ is a regularization matrix whose entries satisfy

$$D_{i,j} = \beta\delta_{i,j} + \frac{\int_{P_i\cap P_j}(2\delta_{i,j} - 1)\, ds}{\max_{i,j}\left(\int_{P_i\cap P_j} ds\right)} \tag{10}$$

with $\delta_{i,j} = 1$ if $i = j$, and zero if otherwise. In $\mathbf{D}$, the first term penalizes the norm of $\mathbf{x}$ and the second one the total variation, i.e., the total sum $\sum_{i,j}\int_{P_i\cap P_j}|x_i - x_j|ds$ in which each non-zero term equals to the total jump of $\mathbf{x}$ between two adjacent pixels multiplied by the pixel's side-length [1]. This simple inversion approach usually converges sufficiently in a relatively low number of iteration steps, e.g., five. The value of the parameter β determines the balance between the regularization matrices. A small value for β leads to inverse estimates with low total variation and larger values can be expected to result in well-localized estimates [15], [36], [37].

TABLE I
TRANSMITTERS AND RECEIVERS USED IN RECORDING THE EXPERIMENTAL DATA.

Type	Item	Details
Transmitter	Two-way active speaker	20 Hz – 18 kHz frequency response.
Receiver	Dynamic microphone	Unidirectional 60 Hz – 13 kHz frequency response, -72 dB sensitivity.

TABLE II
THE DIAMETER AND CENTER COORDINATES OF THE DOMAIN Ω AND THE FOAM CYLINDERS **A**–**C**.

Target	x (cm)	y (cm)	Diameter (cm)
A	-11.0	12.0	15.0
B	12.0	10.0	10.0
C	-2.5	-13.0	10.0
Ω	0.0	0.0	59.0

C. Test setup and scenario

1) Domain: An acoustic setup with one speaker and two microphones was utilized to gather the experimental data. The computational domain Ω was a 59 cm diameter disk drawn on a 0.5 cm thick soft foam covering (Figure 3). In the experiment, the locations of three foam cylinders **A**, **B** and **C** with diameters 15, 10 and 10 cm, respectively, were to be detected. These were placed in the disk Ω in the upright position and apart from each other. The perimeter of Ω contained 64 equally spaced control points **1**–**64** for localizing the transmitter and the receiver of the signal. A top-down view of the experiment setup is included in Figure 3. The diameters and positions of Ω and **A**–**C** can be found in Table II.

2) Signal: The signal pulse transmitted (Figure 4) was of the form

$$f(t) = \sin(36t)\exp[-35(t-0.60)^2] \text{ for } t = [0, 1.2] \text{ (milliseconds)}, \tag{11}$$

and $f(t) = 0$, in all other times. The resulting signal with 5.8 kHz center frequency was transmitted from the points **1**, **24** and **43** using an active two-way speaker. Corresponding to each point of transmission, the signal was recorded for the 57 centermost control points opposite the transmitter. Based on the measurements, two travel-time data sets (**I**) and (**II**) (Figure 3) were formed. In (**I**) (dense set), the 47 centermost points were utilized in the final data set consisting of $3 \times 47 = 141$ individual travel-time values, while only every other point of the set (**I**) was included in (**II**) (sparse set) resulting in $3 \times 24 = 72$ travel-time values. The measured waveform data can be found in Figure 5. The simulated data were obtained using the FDTD method using the constant 334 m/s as the signal velocity (the speed of sound in air at 20 °C). Both the measured and simulated data have been included as supplementary material.

3) Equipment: The data recording device was an ordinary laptop computer equipped with an external sound card interface. Two-channel audio data was recorded using the waveform audio file format (WAV), 24 bit resolution and a 48 kHz sample rate. To eliminate any possible hardware or software based delays, a control pulse was recorded by one microphone placed 3.5 cm directly above the speaker. The actual data pulse was recorded with the other microphone positioned on the perimeter of the target area in the radial direction. Figure 3 shows the test setup with both microphones near each other. The technical data of the hardware used in the setup can be found in Table I.

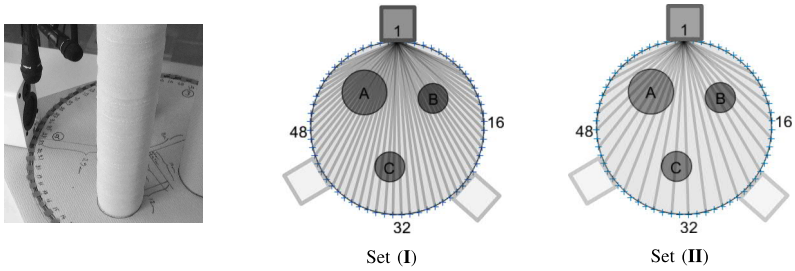

Fig. 3. **Left:** The test setup during the measurement procedure. **Center and Right:** A top-down diagram of the setup. The control points **1–64** are shown as light blue crosses on the perimeter. Four of them are numbered to show the clockwise ordering. Points **1**, **24** and **43** were used as transmitter locations. The dark grey box represents the transmitter (speaker) when positioned at **1** and the light grey boxes show it in the case of **24** and **43** (clockwise). Based on the measurements two travel-time data sets (**I**) and (**II**) were formed. In (**I**) (dense set, center), the centermost 47 points were utilized in the final data set consisting of $3 \times 47 = 141$ individual travel-time values, while only every other point of the set (**I**) was included in (**II**) (sparse set, right) resulting in $3 \times 24 = 72$ travel-time values.

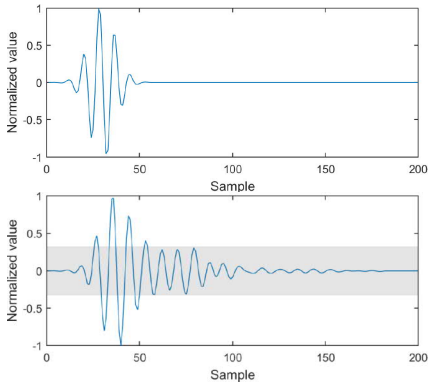

Fig. 4. **Top:** The transmitted signal pulse as given by equation (11). **Bottom:** The signal pulse received at the perimeter of the (empty) test domain Ω without the foam cylinders placed inside. The tail of the received signal contains noise due to echoes and inaccuracies in transmission (ringing). Based on a comparison with the original signal the noise peaks were observed to be mainly 10 dB (grey area) below the main peak.

4) Noise: Figure 4 includes a comparison between the transmitted signal pulse and the one received at the perimeter of the (empty) test domain Ω without the foam cylinders placed inside. The tail of the signal received was observed to contain noise due to echoes and inaccuracies in transmission (ringing). Based on a comparison with the original signal the noise peaks were estimated to be mainly 10 dB (greyed area) below the main peak.

5) Relevance: The relevance of the test setup with respect to a real travel-time tomography application is the following. The transmitter sends a waveform signal pulse at a known position which is then recorded by the receiver in a known position, and the resulting signal recordings are then sent via a communication link. Further processing will consist of compression or some other processing technique, such as calculating travel-time values.

D. Experimental FPGA hardware

The travel-time calculation was implemented using a high-level synthesis of hardware on an FPGA development board (Altera DE2) with the typical performance of an embedded signal acquisition system. FPGA enables fast processing of data which is essential in waveform imaging because of the massive data input needed to record a complete wave. A high-level data flow chart of the implementation has been included in Figure 6.

In this study, we investigated different bit resolution, threshold and normalization levels. These were set in a separate parameters file. A functioning Matlab script was first transformed directly into C code and the result was then further modified to accept parameters. The hardware was generated by using the Mentor Graphics *Catapult* High-Level Synthesis (HLS) tool [38]. HLS is a method where digital hardware is generated from a high level programming language, such as C [39]. The tool takes the modified, algorithmic C code and generates register transfer level (RTL) code, which is synthesized as digital logic on an Field Programmable Gate Array (FPGA) chip [40].

The basic hardware for signed 16-bit input (audio) data was implemented first for ITT and TTT, and then adapted separately for the signed 8-bit input data. The software on computer uses common datatypes [41], but efficient hardware requires accurately defined bit resolutions for all inputs, outputs and intermediate variables [42]. The HLS tool does not offer a way to calculate the maximum bit resolution for an arbitary integer number. An example of this is the divisor in Equation (6), which has the sum of the squares of the numbers for a part of the signal. Knowing the bit resolution of the element and thus the maximum values, the bit resolution for the square could be calculated. The 8-bit and 16-bit versions of the hardware required individual optimizations.

E. Numerical experiments

In the numerical experiments, the initial guess for the signal velocity distribution was set to be $\mathsf{c} = 334$ m/s (the speed of sound in air at 20 $^\circ$ C). The number of inverse iteration steps was set at three and the regularization parameters α and β were both given the value 0.01 which, based on our preliminary tests, is a reasonable approximaitoion of the midpoint of the interval of the workable values. To evaluate the data processing artifacts, bit resolutions of the signed 16 and the signed 8 bits were used as in the A/D conversion units of practical applications [43].

The maximum amplitude in the measurement data set was normalized to a given level ν dB FS (full of the bit scale) and the other signals proportional thereto. The control signal was normalized to 0 dB FS for each individual measurement point. 16-bit preprocessing was evaluated at 100 % ($\nu = 0$ dB FS) normalization and 8-bit at 100 % ($\nu = 0$ dB FS) and 6 % ($\nu = -24$ dB FS) normalization. The 6 % level represents an extreme case where the signal noise is

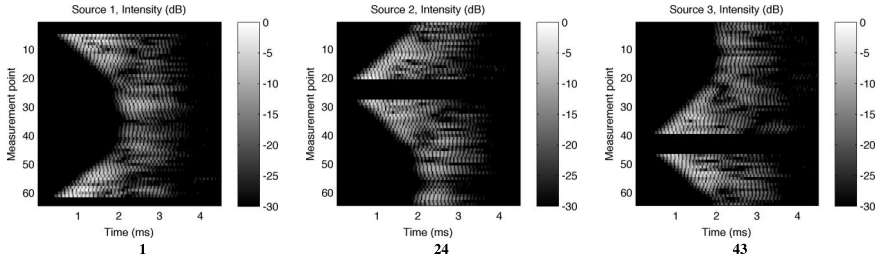

Fig. 5. Measurement data for transmitter locations **1**, **24** and **43** visualized on a decibel (dB) scale.

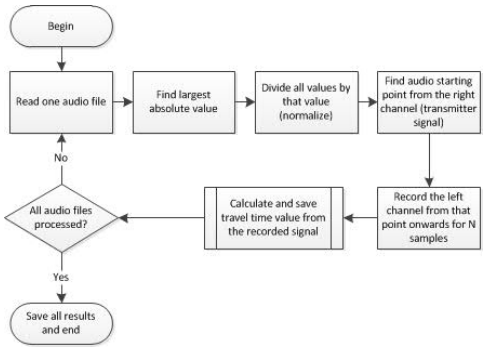

Fig. 6. A simplified high-level flow chart of the travel-time calculation algorithm.

large, thus simulating either a weak reception of transmitted signals or an insensitive receiver. Two different threshold levels 90 % and 70 % for initial signal detection were tested corresponding to around -1 dB FS and -3 dB FS of the maximum value of a normalized signal.

The data vector $\mathbf{y}$ was obtained as the difference between the measurement and simulation based travel-time both of which were computed using either the ITT or TTT approach. The interval of the ITT was determined by $\tau_1 = 5$ and $\tau_2 = 250$ (samples at 48 kHz) resulting in a total length of 256 samples (5.3 ms). TTT was evaluated using two alternative strategies TTT 1 and TTT 2. In the former, ITT was applied to the control pulse and TTT to the data pulse. In the latter, the travel-time of both the control and data pulse was computed via TTT. The motivation for investigating TTT 1, was the potential situation in which the simulated and measured travel-time are obtained via different techniques, e.g., due to different suppliers of computer software and measurement equipment.

The reconstructions were analyzed by measuring the Relative Overlapping Area (ROA) and the minimum relative overlap ROA_{min} between the foam cylinders $\mathcal{S}_{\mathbf{A}}$, $\mathcal{S}_{\mathbf{B}}$, $\mathcal{S}_{\mathbf{C}}$ the set $\mathcal{S}_{\text{rec}}$ in which the value of the reconstruction was less than a fixed limit such that $\text{Area}(\mathcal{S}_{\text{rec}}) = \text{Area}(\mathcal{S}_{\mathbf{A}} \cup \mathcal{S}_{\mathbf{B}} \cup \mathcal{S}_{\mathbf{C}})$. ROA and ROA_{min} were calculated as given by the equations

$$\text{ROA} = \frac{\text{Area}(\mathcal{S}_{\text{rec}} \cap [\mathcal{S}_{\mathbf{A}} \cup \mathcal{S}_{\mathbf{B}} \cup \mathcal{S}_{\mathbf{C}}])}{\text{Area}(\mathcal{S}_{\mathbf{A}} \cup \mathcal{S}_{\mathbf{B}} \cup \mathcal{S}_{\mathbf{C}})} \tag{12}$$

$$\text{ROA}_{\text{min}} = \min\Big(\frac{\text{Area}(\mathcal{S}_{\text{rec}} \cap \mathcal{S}_{\mathbf{A}})}{\text{Area}(\mathcal{S}_{\mathbf{A}})}, \frac{\text{Area}(\mathcal{S}_{\text{rec}} \cap \mathcal{S}_{\mathbf{B}})}{\text{Area}(\mathcal{S}_{\mathbf{B}})}, \frac{\text{Area}(\mathcal{S}_{\text{rec}} \cap \mathcal{S}_{\mathbf{C}})}{\text{Area}(\mathcal{S}_{\mathbf{C}})}\Big). \tag{13}$$

The reconstructions were computed using a laptop computer equipped with the 2.8 GHz Intel Core i7 processor 2640M and 8 GB of RAM. Computing a single reconstruction took 9 seconds of CPU time.

III. Inversion results

Figures 7-10 show the test area recovery (inversion) results. These figures consist of image pairs. The outlines of the three foam cylinders are superimposed on the top of the images. For each image the left side image is the actual result image. From that image, an area with strongest values is collected so that it has the same area as that of the foam cylinders. The right side image shows only the solid black areas.

ITT was found to yield robust results with respect to the A/D conversion bit resolution, signal normalization, threshold, and sparsity of the measurements. The highest ROA (ROA_{min}) obtained with ITT was 64 % (56 %) and the lowest one 54 % (38 %). TTT was observed to be advantageous under optimized conditions with respect to the bit resolution, normalization, threshold, and density of the data. It was also significantly more sensitive than ITT to variations in any of these parameters. For TTT 1, the highest and lowest ROA (ROA_{min}) were 70 (57 %) and 17 % (0 %), respectively. For TTT 2, these values were 71 (68 %) and 25 % (0 %), respectively. The results obtained with TTT 2 were slightly superior to those achieved using TTT 1. The 16-bit signed integer travel-time calculation module produced essentially the same outcome as 64-bit floating point arithmetics.

The HLS method was found to work appropriately in developing the FPGA hardware. A complete prototyping cycle took a few hours, most of which time was spent implementing a new feature in C. It was found that since the algorithmic C-like code is much more maintainable than traditional designs using VHDL, further changes and reuse of the code can be done more easily via HLS. A summary of the synthesis results for the 8-bit and 16-bit designs for the ITT and TTT is presented in Table III. The hardware for ITT was almost as fast as that of TTT, and the difference in chip area between these two methods was not significant.

TABLE III
Synthesis results for the travel-time calculation modules implemented with Catapult C. The percentages given for area is the percentage of available logic elements used on the FPGA chip (EP2C35F672C6N) of the DE2 board.

Mode	Bits	Speed (MHz)	Latency (Cycles)	Area (Logic Elements)
Thresholding	8	106.0	13 594	821 (2.5 %)
Thresholding	16	99.4	13 558	1 075 (3.2 %)
Integrating	8	74.8	13 565	891 (2.7 %)
Integrating	16	82.6	13 581	1 253 (3.8 %)

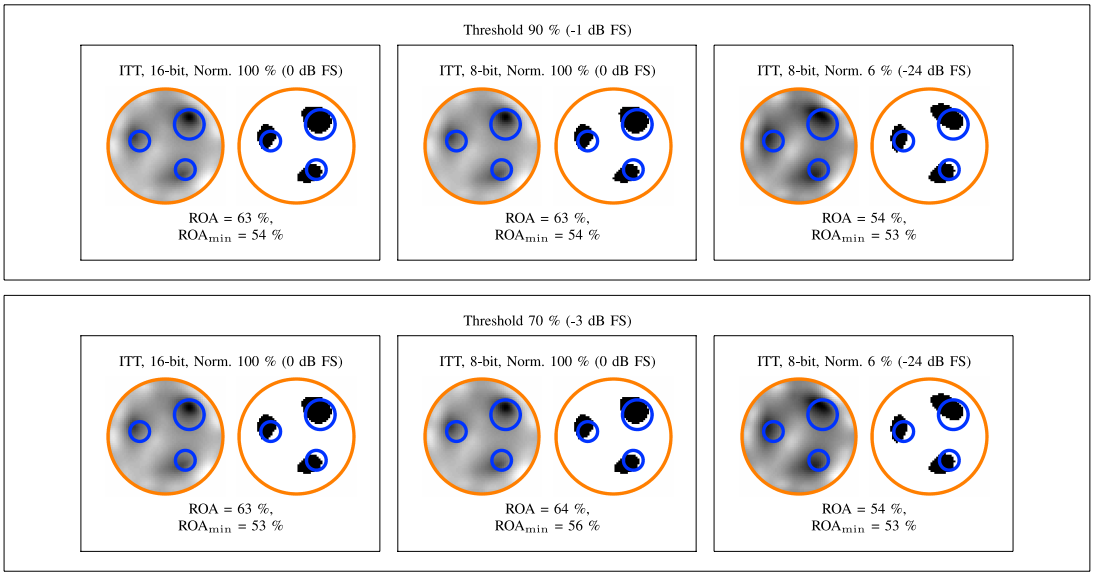

Fig. 7. Results with Integrated travel time (ITT) used for both the control signal and measured signal.

IV. Discussion

This paper focused on developing the processing and inversion of waveform tomography data for applications in which the signal wavelength is close to the diameter of the details that are to be recovered. In particular, FPGA-based hardware was used. We compared the integrated and thresholded travel-time (ITT and TTT) in numerical experiments in which three foam cylinders were to be localized based on an experimental 5.8 kHz acoustic signal. We tested a 16-bit and 8-bit analog-to-digital (A/D) conversion together with two different threshold criterions and normalization levels. As reference applications of this study, we considered (**1**) microwave and ultrasonic computed tomography (MCT and UCT), (**2**) tomography of small solar system bodies (SSSBs), in particular, the CONSERT experiment and (**3**) ultrasonic/microwave detection of concrete defects.

A. Experiments

The recovery of the test object locations on the target area by using the described inversion methods was found to work appropriately. Our results show that ITT is more stable than TTT if the signal quality decreases. This can been seen from the stability of the relative overlapping area (ROA) percentages (53 - 64 %). These percentages are comparable to our previous research on waveform inversion within a 2D domain. In [15] the best ROA percentage 71 % was obtained by using the full wave data. Using TTT the best recovery result was exactly the same 71%. ITT was 7 % less accurate, but more stable when data preprocessing was performed using source data with lesser bit resolution.

The results show that ITT is invariant with respect to source data bit resolution reduction in the time-domain and the level of thresholding used to locate the signal pulse from recorded audio data. ITT was also found to be more reliable than TTT with respect to the normalization of the signal and the sparsity of the measurements. We normalized the 8-bit signal to two different levels, 100 % (0 dB FS) and 6 % (-24 dB FS) amplitude, to simulate weak receivers, i.e., to decrease signal-to-noise ratio (SNR). This is relevant in applications where the signal quality is reduced. For example, in astro-geoscientific applications, the signals can be weak in some directions. This was evident from the CONSERT experiment [13], [44] in which the power and quality of the received signal varied significantly depending on the direction of the measurement [12]. The result concerning the sparsity of the measurements is essential for CONSERT, and other applications in which not all the data can be gathered.

Based on the results, we suggest that ITT can be superior to TTT with respect to the robustness of the inversion. It also seems obvious that TTT might achieve a higher ROA than ITT for a high-quality signal and a well-chosen threshold parameter. Namely, under optimal conditions TTT filters out the noisy tail part of the signal that is present in the computation of the ITT. This advantage is utilized, e.g., in the first-arrival sound speed inversion [3]. The present results suggest that the ITT method does not significantly diminish the inversion quality, and indeed, it can increase the reliability of the results with respect to the uncertainty factors and incompleteness of the data.

B. Applications

Tomography applications differ from each other by the speed and length of the electromagnetic or sound waves. The feature size d that can be detected is dependent on the wave length λ (e.g. $\lambda/2$). In Table IV, the significance of the test setup with respect to the present reference applications (**1**)–(**3**) has been summarized based on d, λ, the diameter of the target domain D and the ratios d/λ and D/λ.

The values d, λ, and D utilized in Table IV can be reasoned as follows. (**1**) In MCT, signal frequencies 1–6 GHz are being used and the diameter of the sensor ring can be, e.g., $D = 15$ cm [4], [26]. At 5 GHz, the wavelength is $\lambda \approx 1.9$ cm corresponding to the relative permittivity of the breast $\varepsilon_r \approx 10$ [45], [46]. Medical UCT utilizes frequencies in the range of 1 - 20 MHz [47]. Using the 1 MHz value

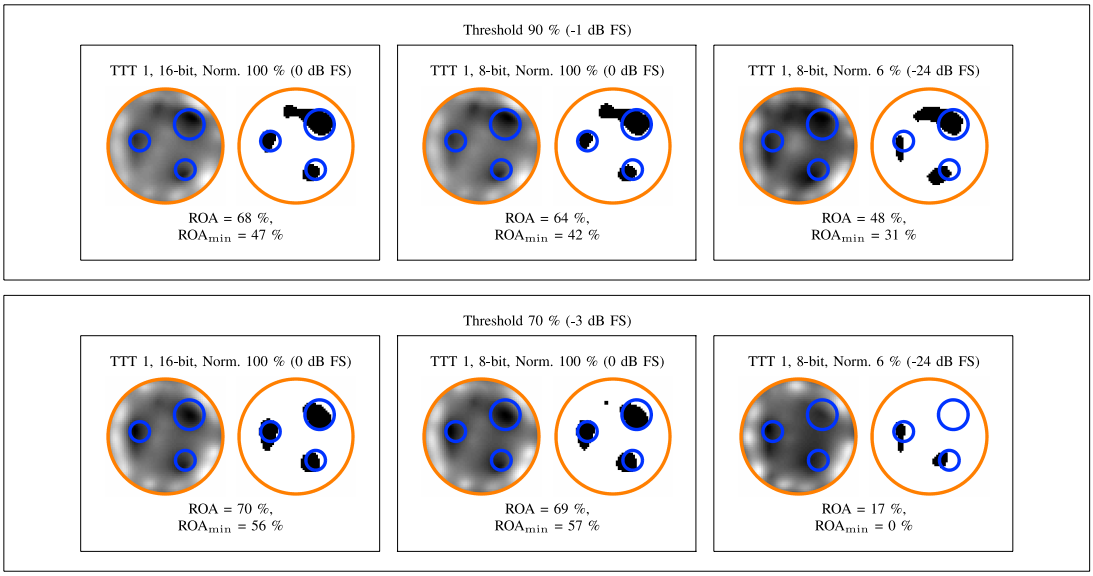

Fig. 8. Results with ITT used for the measured signal. Control signal was thresholded.

and the speed of 1500 m/s for ultrasound propagation in human tissue [48], the wavelength is $\lambda = 1.5$ mm. In UCT and MCT, the feature to be recovered can be, e.g., a small T1 or T1a tumor which can have a maximum diameter of $d = 2$ cm and $d = 0.5$ cm, respectively. (**2**) A signal frequency of 10 MHz has been suggested for the tomography of SSSBs [49] matching roughly with the wavelength $\lambda \approx 15$ m ($\varepsilon_r \approx 4$, e.g., for dunite and kaolinite [50]) which is the estimated resolution of the CONSERT experiment [13], [44]. The diameter of the SSSB can be for example $D = 150$ m. (**3**) In ultrasonic material testing for concrete the velocity of the wave is 3500 m/s [51]. At a typical ultrasound frequency of 100 kHz the wavelength of the signal is $\lambda = v/f = 3.5$ m and the diameter of the concrete beam being tested could be, for example, $D = 30$ cm. A fault or crack inside the beam could be $d = 3$ cm.

Based on Table IV, the present experiment setup can be considered applicable to all application contexts (**1**)–(**3**). In MCT and UCT the best match to the test geometry is obtained with the T1 and T1a tumor size, respectively. Obviously, the difference between ITT and TTT can be less significant in applications, where the wave length is likely to be considerably smaller than the smallest detail to be detected. As an additional comparison, in the tomography of the ionosphere, the speed of the electromagnetic wave is around the speed of light and a typical frequency used in tomography is between 120 MHz and 400 MHz. Using a value of 200 MHz the wavelength is $\lambda = 1.5$ m. The size of the ionosphere is up to $D = 1000$ km from the surface of the Earth and a typical vertical feature to be recovered can be $d = 100$ km, for example [52]. Consequently, d/λ and D/λ can be 100 and 670, respectively. This suggests that our test scenario might be too different from the tomography of the ionosphere to be able to draw inferences from the results.

The noise peaks in the experimental data were estimated to be mainly 10 dB below the maximum peak. This can be considered as appropriate for the applications (**1**)–(**3**). For a MCT imaging system, the relative reconstruction error has been shown to stay under 10 % for amplitude errors down to 10 dB SNR [45]. The total noise peak level of around 20 dB was observed in the CONSERT experiment [12]. In concrete testing, structural noise [53], e.g., echoes from walls, can be significant resulting in noise peaks that can be comparable to the main peak.

C. Hardware

The use of high-level synthesis (HLS) to develop the test hardware was found to be essential, as the specifications for the travel time calculation changed during the implementation phase and so changes to the hardware had to be made quickly. We aimed at a very direct workflow in implementing the hardware, and thus some optimization methods in the design partitioning and in the HLS tool were not utilized. In addition, having the different bit resolution implementations in separate files increased the work when changes had to be made. The resulting digital hardware was synthesized on an FPGA platform for demonstration and to facilitate further development of the data gathering system towards a laboratory instrument.

Many operations in the computation scripts, such as the normalization of values, require divisions. In the ITT calculation formula (6) there is a large-valued divisor that first sums the squares of the travel time and then divides the sum with that value. Catapult generates divisions as combinatorial logic if written directly as it is in typical C code [42]. Combinatorial logic [40] is not synchronized with the hardware clock, which makes it unreliable in use. This gives a false sense of flexibility in the HLS tool and the user has to know what is being generated. Catapult has a math library which has synthesizable, basic algorithmic division operators for integers. Changing all divisions to use division operators offered by this library improved the results, and resulted in a working design for most division operations whereas combinatorial dividers did not.

Travel-time calculation can be seen as an extreme form of compression in time domain. There are more compression methods such as filtering in the frequency domain. Our work used reduced the bit

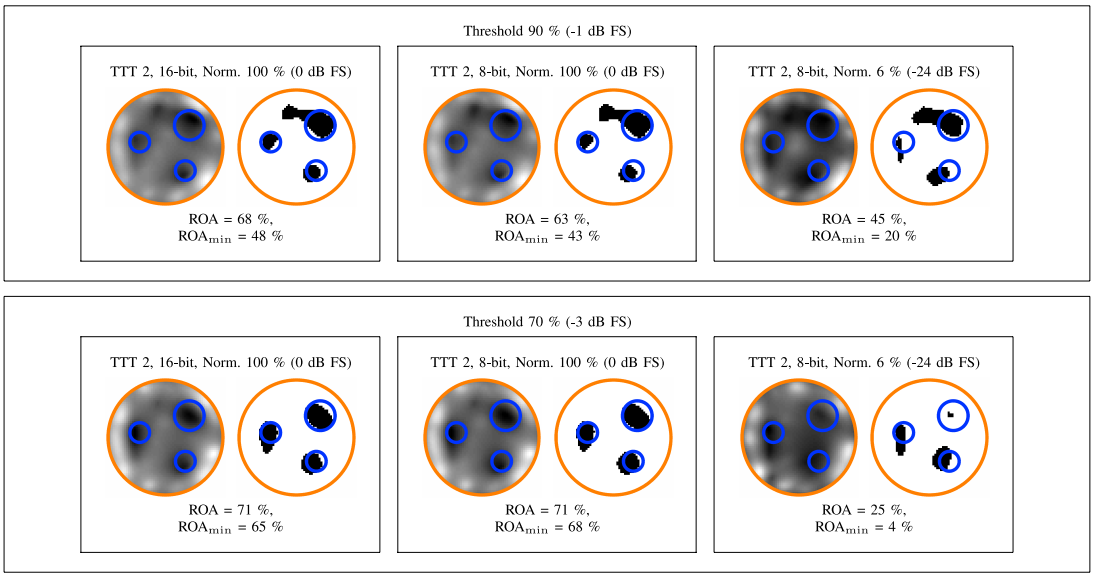

Fig. 9. Results with thresholded travel time used for both the control signal and measured signal.

TABLE IV
THE SIGNIFICANCE OF THE ACOUSTIC TOMOGRAPHY RESULTS BASED ON THE PARAMETERS OF OTHER TOMOGRAPHY APPLICATIONS. SSSB IS A SMALL SOLAR SYSTEM BODY, SUCH AS A COMET OR AN ASTEROID. ([a] SIGNAL FREQUENCY, [b] SIGNAL WAVELENGTH, [c] DIAMETER OF THE TARGET OBJECT, [d] DIAMETER OF THE TARGET OF RECONSTRUCTION)

Application	λ (m)[b]	D (m)[c]	d (m)[d]	D/λ	d/λ	Significance
Test	$59 \cdot 10^{-3}$	0.58	0.10	10	1.0	
MCT (T1)	$19 \cdot 10^{-3}$	0.15	0.02	7.9	1.1	Strong
MCT (T1a)	$19 \cdot 10^{-3}$	0.15	$5.0 \cdot 10^{-3}$	2.0	0.28	Medium
UCT (T1)	$1.5 \cdot 10^{-3}$	0.15	0.02	100	13	Medium
UCT (T1a)	$1.5 \cdot 10^{-3}$	0.15	$5.0 \cdot 10^{-3}$	25	3.3	Strong
SSSBs	15	150	15	10	1.0	Strong
Concrete	$35 \cdot 10^{-3}$	0.3	0.03	10	0.86	Strong
Ionosphere	1.5	$1.0 \cdot 10^{6}$	$0.1 \cdot 10^{6}$	670	100	Weak

resolution for input audio data. Calculation of the travel times was also performed with integer arithmetics. These reduce the accuracy of the results. bit resolution reduction is relevant when using FPGAs in general. This is because vendor-provided hardware multipliers available for use on FPGA chips such as Altera's Cyclone II have limited bit resolutions [54]. For example, a FIR filter can use these hardware multipliers on FPGAs as in [55]. Because the operator is a multiplication that can increase the required bit resolution to store the intermediate results, the original bit resolution of the data has to be reduced. One system [55] has implemented Fast Fourier Transform (FFT) filtering in the frequency domain and inverse FFT (IFFT) signal reconstruction back to the time domain. In currently available FPGA DSP chips, the available bit resolutions for multipliers are much larger [56], but reduction in bit resolution can still be required. This makes the invariance of the source data bit resolution of our ITT method an important point of interest. An example of decreased signal quality is found in Ground Penetrating Radar (GPR) applications. In [43] an instrumentation system with either 8-bit or 16-bit Analog-to-Digital conversion was employed. This shows that bit resolution limitations are also found in instrument hardware.

D. Outlook

Finally, the present results indicate various directions for future work. We will study hardware-level solutions regarding (i) processing and (ii) inverting waveform data. (i) Investigating harware constraints utilizing a more sophisticated statistical travel-time detection model, such as the akaike information criterion [57], would be an interesting goal. The calculation of travel-time values is only one data preprocessing method that can be used, and mathematical methods to accomodate other types of filtering, such as compressing in the frequency domain could be developed. The goal in preprocessing depends on the application: in the space environment minimal data transfer between the sensors and the computation unit is important for the limited communication capacity available, whereas in biomedical and civil engineering the main objective can be to optimize the speed of the procedure in order to allow recording as much data as possible. (ii) We aim to develop inversion approaches utilizing the FPGA environment, so extending the current study of hardware-level constraints to include inversion algorithms is essential.

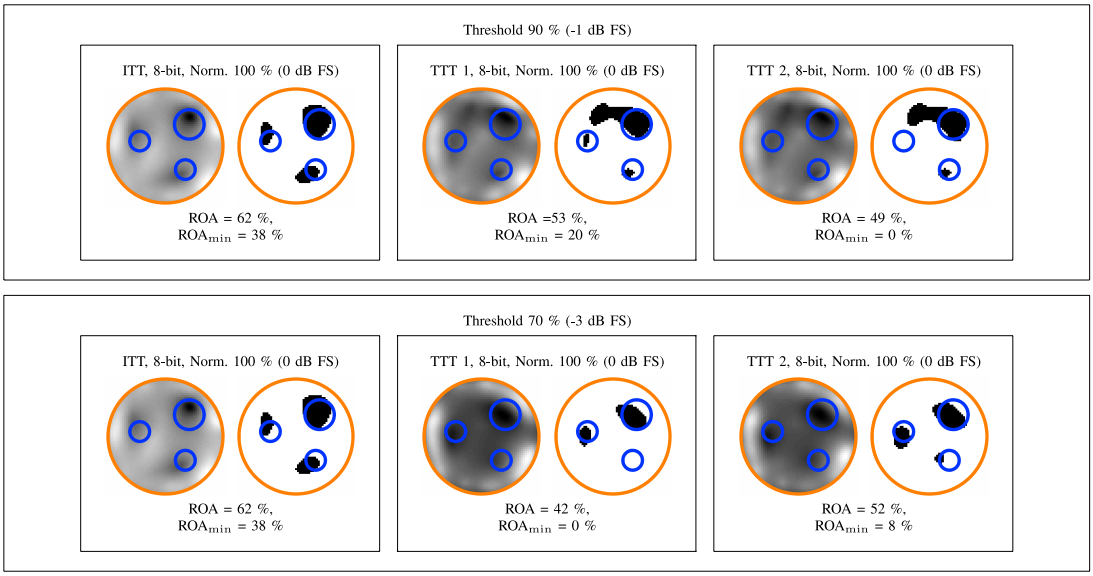

Fig. 10. Result with sparse data. ITT is on the left, TTT 1 in the middle and TTT 2 on the right.

ACKNOWLEDGEMENTS

M.T. and S.P. were supported by the Academy of Finland Key Project 305055 and the Academy of Finland Centre of Excellence in Inverse Problems Research.

E. Appendix

In the inversion procedure (9), the matrix $\mathbf{D}$ is symmetric and can thus be diagonalized. When $\beta > 0$, $\mathbf{D}$ is also positive definite and also invertible. Hence, one can define $\hat{\mathbf{x}} = \mathbf{D}\mathbf{x}$ and $\hat{\mathbf{L}} = \mathbf{L}\mathbf{D}^{-1}$. Substituting $\hat{\mathbf{x}}$ and $\hat{\mathbf{L}}$ into (9) leads to the following form [1], [15], [16]

$$\hat{\mathbf{x}}_{\ell+1} = (\hat{\mathbf{L}}^T\hat{\mathbf{L}} + \alpha\hat{\mathbf{\Gamma}}_\ell)^{-1}\hat{\mathbf{L}}^T\mathbf{y}, \quad \hat{\mathbf{\Gamma}}_\ell = \mathrm{diag}(|\hat{\mathbf{x}}_\ell|)^{-1}, \quad \hat{\mathbf{\Gamma}}_0 = \mathbf{I}. \tag{14}$$

which can be associated with alternating conditional minimization of the function $H(\hat{\mathbf{x}}, \hat{\mathbf{z}}) = \|\hat{\mathbf{L}}\hat{\mathbf{x}} - \mathbf{y}\|_2^2 + \alpha\sum_{j=1}^M \frac{\hat{x}_j^2}{\hat{z}_j} + \alpha\sum_{j=1}^M \hat{z}_j$ in which $z_j > 0$, for $i = 1, 2, \ldots, M$. As $H(\hat{\mathbf{x}}, \hat{\mathbf{z}})$ is quadratic with respect to $\hat{\mathbf{x}}$, the conditional minimizer $\hat{\mathbf{x}}' = \arg\min_{\hat{\mathbf{x}}} H(\hat{\mathbf{x}} \mid \hat{\mathbf{z}})$ is given by the least-squares solution of the form $\hat{\mathbf{x}}' = (\hat{\mathbf{L}}^T\hat{\mathbf{L}} + \alpha\hat{\mathbf{\Gamma}}_{\hat{\mathbf{z}}})^{-1}\hat{\mathbf{L}}^T\mathbf{y}$, $\hat{\mathbf{\Gamma}}_{\hat{\mathbf{z}}} = \mathrm{diag}(\hat{\mathbf{z}})^{-1}$ and $\hat{\mathbf{\Gamma}}_0 = \mathbf{I}$. At the point of the conditional minimizer $\hat{\mathbf{z}}' = \arg\min_{\hat{\mathbf{z}}} H(\hat{\mathbf{z}} \mid \hat{\mathbf{x}})$, the gradient of $H(\hat{\mathbf{z}} \mid \hat{\mathbf{x}})$ vanishes with respect to $\hat{\mathbf{z}}$, i.e.,

$$\frac{\partial H(\hat{\mathbf{x}}, \hat{\mathbf{z}})}{\partial \hat{z}_j}\Big|_{\hat{\mathbf{z}}'} = -\alpha\frac{\hat{x}_j^2}{(\hat{z}_j')^2} + 1 = 0, \quad \text{i.e.} \quad \hat{z}_j' = |\hat{x}_j|\sqrt{\alpha}. \tag{15}$$

Hence, the global minimizer can be estimated via the following alternating iterative algorithm.

1) Set $\hat{\mathbf{z}}_0 = (1, 1, \ldots, 1)$ and $\ell = 1$. For a desired number of iterations repeat the following two iteration steps.
2) Find the conditional minimizer $\hat{\mathbf{x}}_\ell = \arg\min_{\hat{\mathbf{x}}} H(\hat{\mathbf{x}}, \hat{\mathbf{z}}_{\ell-1})$.
3) Find the conditional minimizer $\hat{\mathbf{z}}_\ell = \arg\min_{\hat{\mathbf{z}}} H(\hat{\mathbf{x}}_\ell, \hat{\mathbf{z}})$.

The sequence $\hat{\mathbf{x}}_1, \hat{\mathbf{x}}_2, \ldots$ produced by this algorithm is identical to that of (14) and $\mathbf{x}_\ell = \mathbf{D}^{-1}\hat{\mathbf{x}}_\ell$ equals to the ℓ-th iterate of (9). If for some $\ell < \infty$ the pair $(\hat{\mathbf{x}}_\ell, \hat{\mathbf{z}}_\ell)$ is a global minimizer of $H(\mathbf{x}, \mathbf{z})$, then, since $(\hat{z}_\ell)_j = |(\hat{x}_\ell)_j|$, $j = 1, 2, \ldots, M$, then it is also the minimizer of

$$\begin{aligned}
\hat{\Psi}(\hat{\mathbf{x}}) &= H(\hat{x}_1, \hat{x}_2, \ldots, \hat{x}_M, |\hat{x}_j|, |\hat{x}_j|, \ldots, |\hat{x}_M|) \\
&= \|\hat{\mathbf{L}}\hat{\mathbf{x}} - \mathbf{y}\|_2^2 + \alpha\sum_{j=1}^M \frac{\hat{x}_j^2}{\hat{z}_j} + \sum_{j=1}^M \hat{z}_j \\
&= \|\hat{\mathbf{L}}\hat{\mathbf{x}} - \mathbf{y}\|_2^2 + \alpha\sum_{j=1}^M \frac{\hat{x}_j^2}{|\hat{x}_j|\sqrt{\alpha}} + \sum_{j=1}^M |\hat{x}_j|\sqrt{\alpha} \\
&= \|\hat{\mathbf{L}}\hat{\mathbf{x}} - \mathbf{y}\|_2^2 + 2\sqrt{\alpha}\|\hat{\mathbf{x}}\|_1.
\end{aligned} \tag{16}$$

Consequently, $\mathbf{x}_\ell = \mathbf{D}^{-1}\hat{\mathbf{x}}_\ell$ is the minimizer of $\Psi(\mathbf{x})$, as $\Psi(\mathbf{x}) = \hat{\Psi}(\hat{\mathbf{x}})$. Furthermore, the minimizer of $\hat{\Psi}(\hat{\mathbf{x}})$ is also the 1-norm regularized solution of the linearized inverse problem.

REFERENCES

[1] J. P. Kaipio and E. Somersalo, *Statistical and Computational Methods for Inverse Problems*. Berlin: Springer, 2004.

[2] A. Tarantola, *Inverse Problem Theory and Methods for Model Parameter Estimation*, ser. Other titles in applied mathematics. Society for Industrial and Applied Mathematics, 2005.

[3] F. M. Hooi and P. L. Carson, "First-arrival traveltime sound speed inversion with a priori information," *Medical Physics*, vol. 41, no. 8, 2014.

[4] T. M. Grzegorczyk, P. M. Meaney, P. A. Kaufman, R. M. di Florio-Alexander, and K. D. Paulsen, "Fast 3-D tomographic microwave imaging for breast cancer detection," *Medical Imaging, IEEE Transactions on*, vol. 31, no. 8, pp. 1584–1592, Aug 2012.

[5] P. M. Meaney, M. W. Fanning, R. M. di Florio-Alexander, P. A. Kaufman, S. D. Geimer, T. Zhou, and K. D. Paulsen, "Microwave tomography in the context of complex breast cancer imaging," in *Engineering in Medicine and Biology Society (EMBC), 2010 Annual International Conference of the IEEE*, Aug 2010, pp. 3398–3401.

[6] E. C. Fear, X. Li, S. C. Hagness, and M. A. Stuchly, "Confocal microwave imaging for breast cancer detection: localization of tumors in three dimensions," *Biomedical Engineering, IEEE Transactions on*, vol. 49, no. 8, pp. 812–822, Aug 2002.

[7] N. V. Ruiter, M. Zapf, T. Hopp, R. Dapp, E. Kretzek, M. Birk, B. Kohout, and H. Gemmeke, "3d ultrasound computer tomography of the breast: A new era?" *European Journal of Radiology*, vol. 81, Supplement 1, no. 0, pp. S133 – S134, 2012.

[8] K. J. Opielinski, P. Pruchnicki, T. G. P. Podgorski, T. Krasnicki, J. Kurcz, and M. Sasiadek, "Ultrasound transmission tomography imaging of structure of breast elastography phantom compared to US, CT and MRI," *Archives of Acoustics*, vol. 38, pp. 321–334, 2013.

[9] B. Ranger, P. J. Littrup, N. Duric, P. Chandiwala-Mody, C. Li, S. Schmidt, and J. Lupinacci, "Breast ultrasound tomography versus MRI for clinical display of anatomy and tumor rendering: preliminary results," *AJR Am J Roentgenol*, vol. 198, no. 1, pp. 233–239, 2012.

[10] L. J. Bond, W. F. Kepler, and D. M. Frangopol, "Improved assessment of mass concrete dams using acoustic travel time tomography part I: theory," *Construction and Building Materials*, vol. 14, no. 3, pp. 133–146, 2000.

[11] W. F. Kepler, L. J. Bond, and D. M. Frangopol, "Improved assessment of mass concrete dams using acoustic travel time tomography part II: application," *Construction and Building Materials*, vol. 14, no. 3, pp. 147–156, 2000.

[12] W. Kofman, A. Herique, Y. Barbin, J. Barriot, V. Ciarletti, S. Clifford, P. Edenhofer, C. Elachi, C. Eyraud, J.-P. Goutail, E. Heggy, L. Jorda, J. Lasue, A.-C. Levasseur-Regourd, E. Nielsen, F. Pasquero, P.and Preusker, P. Puget, D. Plettemeier, Y. Rogez, H. Sierks, C. Statz, H. Svedhem, I. Williams, S. Zine, and J. Van Zyl, "Properties of the 67p/churyumov-gerasimenko interior revealed by consert radar," *Science*, vol. 349, no. 6247, 2015.

[13] W. Kofman, A. Herique, J.-P. Goutail, T. Hagfors, I. P. Williams, E. Nielsen, J.-P. Barriot, Y. Barbin, C. Elachi, P. Edenhofer, A.-C. Levasseur-Regourd, D. Plettemeier, G. Picardi, R. Seu, and V. Svedhem, "The comet nucleus sounding experiment by radiowave transmission (CONSERT): A short description of the instrument and of the commissioning stages," *Space Science Reviews*, vol. 128, no. 1-4, pp. 413 – 432, 2007.

[14] H. Su, F. Xu, S. Lu, and Y.-Q. Jin, "Iterative admm for inverse fe–bi problem: A potential solution to radio tomography of asteroids," *Transactions on Geosciences and Remote Sensing*, vol. PP, 2016.

[15] S. Pursiainen and M. Kaasalainen, "Detection of anomalies in radio tomography of asteroids: Source count and forward errors," *Planetary and Space Science*, vol. 99, no. 0, pp. 36 – 47, 2014.

[16] ——, "Sparse source travel-time tomography of a laboratory target: accuracy and robustness of anomaly detection," p. 114016, 2014.

[17] Y. J. Kim, L. Jofre, F. De Flaviis, and M. Feng, "Microwave reflection tomographic array for damage detection of civil structures," *Antennas and Propagation, IEEE Transactions on*, vol. 51, no. 11, pp. 3022–3032, Nov 2003.

[18] H. K. Chai, D. G. Aggelis, S. Momoki, Y. Kobayashi, and T. Shiotani, "Single-side access tomography for evaluating interior defect of concrete," *Construction and Building Materials*, vol. 24, no. 12, pp. 2411 – 2418, 2010.

[19] H. K. Chai, S. Momoki, Y. Kobayashi, D. G. Aggelis, and T. Shiotani, "Tomographic reconstruction for concrete using attenuation of ultrasound," {*NDT*} *& E International*, vol. 44, no. 2, pp. 206 – 215, 2011.

[20] G. Acciani, G. Fornarelli, A. Giaquinto, D. Maiullari, and G. Brunetti, "Non-destructive technique for defect localization in concrete structures based on ultrasonic wave propagation," in *Computational Science and Its Applications – ICCSA 2008*, ser. Lecture Notes in Computer Science, O. Gervasi, B. Murgante, A. Laganà, D. Taniar, Y. Mun, and M. L. Gavrilova, Eds. Springer Berlin Heidelberg, 2008, vol. 5073, pp. 541–554.

[21] J.-P. Barriot, W. Kofman, A. Herique, S. Leblanc, and A. Portal, "A two dimensional simulation of the CONSERT experiment (radio tomography of comet wirtanen)," *Advances in Space Research*, vol. 24, no. 9, pp. 1127 – 1138, 1999.

[22] W. Wolf, *FPGA-Based System Design*. Pearson Education, 2004.

[23] B. Hunt, R. Lipsman, J. Rosenberg, K. Coombes, J. Osborn, and G. Stuck, *A Guide to MATLAB: For Beginners and Experienced Users*. Cambridge University Press, 2006.

[24] S. G. Kochan, *Programming in C*. Pearson Education, 2004.

[25] P. Coussy and A. Morawiec, *High-Level Synthesis: from Algorithm to Digital Circuit*. Springer Netherlands, 2008.

[26] S.-H. Son, H.-J. Kim, K.-J. Lee, J.-Y. Kim, J.-M. Lee, S.-I. Jeon, and H.-D. Choi, "Experimental measurement system for 3–6 GHz microwave breast tomography," *Journal of Electromagnetic Engineering and Science*, vol. 15, no. 4, pp. 250–257, 2015.

[27] K. J. Opielinski, P. Pruchnicki, T. Gudra, P. Podgorski, J. Kurcz, T. Krasnicki, M. Sasiadek, and J. Majewski, "Imaging results of multi-modal ultrasound computerized tomography system designed for breast diagnosis," *Computerized Medical Imaging and Graphics*, vol. 46, Part 2, pp. 83 – 94, 2015, information Technologies in Biomedicine.

[28] P. M. Meaney, M. W. Fanning, T. Raynolds, C. J. Fox, Q. Fang, C. A. Kogel, S. P. Poplack, and K. D. Paulsen, "Initial clinical experience with microwave breast imaging in women with normal mammography," *Academic radiology*, vol. 14, no. 2, pp. 207–218, 2007.

[29] R. Choe, A. Corlu, K. Lee, T. Durduran, S. D. Konecky, M. Grosicka-Koptyra, S. R. Arridge, B. J. Czerniecki, D. L. Fraker, A. DeMichele *et al.*, "Diffuse optical tomography of breast cancer during neoadjuvant chemotherapy: a case study with comparison to mri," *Medical physics*, vol. 32, no. 4, pp. 1128–1139, 2005.

[30] A. Corlu, R. Choe, T. Durduran, M. A. Rosen, M. Schweiger, S. R. Arridge, M. D. Schnall, and A. G. Yodh, "Three-dimensional in vivo fluorescence diffuse optical tomography of breast cancer in humans," *Optics express*, vol. 15, no. 11, pp. 6696–6716, 2007.

[31] P. Fortescue, J. Stark, and G. Swinerd, *Spacecraft Systems Engineering*, 3rd ed. Wiley & Sons, Chichester, England, 2003, 678 p.

[32] V. Agrawal, *Satellite Technology: Principles and Applications*. Wiley, 2014.

[33] L. Evans, *Partial Differential Equations*, ser. Graduate studies in mathematics. American Mathematical Society, 1998.

[34] D. Braess, *Finite Elements: Theory, Fast Solvers, and Applications in Solid Mechanics*. Cambridge University Press, 2007.

[35] J. B. Schneider, *Understanding the FDTD Method*. John B Schneider, 2016. [Online]. Available: http://www.eecs.wsu.edu/ schneidj/ufdtd/

[36] S. Pursiainen and M. Kaasalainen, "Electromagnetic 3D subsurface imaging with source sparsity for a synthetic object," *Inverse Problems*, vol. 31, no. 12, p. 17, 2015.

[37] ——, "Iterative alternating sequential (IAS) method for radio tomography of asteroids in 3D," *Planetary and Space Science*, vol. 78, 2013.

[38] Mentor Graphics, Inc, "High-Level Synthesis and RTL Low-Power," 2016, accessed 12.3.2016. [Online]. Available: https://www.mentor.com/hls-lp/catapult-high-level-synthesis/

[39] P. Coussy, D. D. Gajski, M. Meredith, and A. Takach, "An introduction to high-level synthesis," *IEEE Design Test of Computers*, vol. 26, no. 4, pp. 8–17, July 2009.

[40] I. Grout, *Digital Systems Design with FPGAs and CPLDs*. Elsevier Science, 2011.

[41] MathWorks, Inc, "Numeric types," 2016, Available: http://se.mathworks.com/help/matlab/numeric-types.html Accessed 5.2.2016.

[42] M. Fingeroff, *High-Level Synthesis Blue Book*. Mentor Graphics Corporation, 2010, 272 p.

[43] G. Leucci, "Ground penetrating radar: the electromagnetic signal attenuation and maximum penetration depth," *Scholarly research exchange*, 2008.

[44] W. Kofman, Y. Barbin, J. Klinger, A.-C. Levasseur-Regourd, J.-P. Barriot, A. Herique, T. Hagfors, E. Nielsen, E. Grün, P. Edenhofer, H. Kochan, G. Picardi, R. Seu, J. van Zyl, C. Elachi, J. Melosh, J. Veverka, P. Weissman, L. Svedhem, S. Hamran, and I. Williams, "Comet nucleus sounding experiment by radiowave transmission," *Advances in Space Research*, vol. 21, no. 11, pp. 1589 – 1598, 1998.

[45] X. Zeng, A. Fhager, and M. Persson, "Effects of noise on tomographic breast imaging," in *General Assembly and Scientific Symposium, 2011 XXXth URSI*, Aug 2011, pp. 1–4.

[46] M. Lazebnik, D. Popovic, L. McCartney, C. B. Watkins, M. J. Lindstrom, J. Harter, S. Sewall, T. Ogilvie, A. Magliocco, T. M. Breslin, W. Temple, D. Mew, J. H. Booske, M. Okoniewski, and S. C. Hagness, "A large-scale study of the ultrawideband microwave dielectric properties of normal, benign and malignant breast tissues obtained from cancer surgeries," *Physics in Medicine and Biology*, vol. 52, no. 20, p. 6093, 2007.

[47] V. Chan and A. Perlas, *Atlas of Ultrasound-Guided Procedures in Interventional Pain Management*. New York, NY: Springer New York, 2011, ch. Basics of Ultrasound Imaging, pp. 13–19.

[48] J. Cameron, *Physical Properties of Tissue A Comprehensive Reference Book*, F. A. Duck, Ed. Academic Press, UK, 1991, 336 p.

[49] R. P. Binzel and W. Kofman, "Internal structure of near-earth objects," *Comptes Rendus Physique*, vol. 6, no. 3, pp. 321–326, 2005.

[50] A. Herique, J. Gilchrist, W. Kofman, and J. Klinger, "Dielectric properties of comet analog refractory materials," *Planetary and Space Science*, vol. 50, no. 9, pp. 857–863, AUG 2002.

[51] K Singh, "Speed of sound in some common solids," 2011.

[52] M. M. J. L. van de Kamp, "Medium-scale 4-D ionospheric tomography using a dense GPS network," *Annales Geophysicae*, vol. 31, no. 1, pp. 75–89, 2013.

[53] C. Maierhofer, H. Reinhardt, and G. Dobmann, *Non-Destructive Evaluation of Reinforced Concrete Structures: Non-Destructive Testing Methods*, ser. Woodhead Publishing Series in Civil and Structural Engineering. Elsevier Science, 2010.
[54] Altera Inc, "Cyclone II Device Handbook, Volume 1," 2008.
[55] M. Birk, S. Koehler, M. Balzer, M. Huebner, N. V. Ruiter, and J. Becker, "FPGA-based embedded signal processing for 3-D ultrasound computer tomography," *IEEE Transactions on Nuclear Science*, vol. 58, no. 4, pp. 1647–1651, Aug 2011.
[56] Altera Inc, "Digital Signal Processing Blocks in Stratix Series FPGAs," 2016, Available: https://www.altera.com/products/fpga/features/stx-dsp-block.html.
[57] C. Li, N. Duric, P. Littrup, and L. Huang, "In vivo breast sound-speed imaging with ultrasound tomography," *Ultrasound in Medicine & Biology*, vol. 35, no. 10, pp. 1615 – 1628, 2009.

Mika Takala (M'16) was born in Nurmo, Finland, in 1982. He received the B.Sc. degree in electrical engineering from the Tampere University of Technology (TUT), in 2015, and the M.Sc.(tech.) degree from TUT in 2016. His master's thesis in the field of embedded systems concentrated on implementation of signal preprocessing modules with High-Level Synthesis for waveform inversion applications. In 2016 Mr. Takala started working at the Department of Mathematics, TUT, as a PhD student. He currently works on his PhD research related geophysical inversion strategies and embedded systems. He also works as a software architect in Granite Devices, Inc., Tampere, Finland.

Timo D. Hämäläinen (M'95) received the M.Sc. and Ph.D. degrees from Tampere University of Technology (TUT), Tampere, Finland, in 1993 and 1997, respectively. He has been a Full Professor with TUT since 2001 and is currently the Head of the Laboratory of Pervasive Computing. He has authored over 70 journals and 210 conference publications. He holds several patents. His research interests include design methods and tools for multiprocessor systems-on-a-chip and parallel video codec implementations.

Sampsa Pursiainen received his MSc(Eng) and PhD(Eng) degrees (Mathematics) in the Helsinki University of Technology (Aalto University since 2010), Espoo, Finland, in 2003 and 2009. He focuses on various forward and inversion techniques of applied mathematics. In 2010–11, he stayed at the Department of Mathematics, University of Genova, Italy collaborating also with the Institute for Biomagnetism and Biosignalanalysis (IBB), University of Münster, Germany. In 2012–15, he worked at the Department of Mathematics and Systems Analysis, Aalto University, Finland and also at the Department of Mathematics, Tampere University of Technology, Finland, where he currently holds an Assistant Professor position.

Received xxxx 20xx; revised xxxx 20xx.

PUBLICATION

II

Multigrid-Based Inversion for Volumetric Radar Imaging With Asteroid Interior Reconstruction as a Potential Application

M. Takala, D. Us and S. Pursiainen

IEEE Transactions on Computational Imaging 4.2 (2018), 228–240
DOI: 10.1109/TCI.2018.2811908

Multigrid-based inversion for volumetric radar imaging with asteroid interior reconstruction as a potential application

Mika Takala, Defne Us, Sampsa Pursiainen

***Abstract*—This study concentrates on advancing mathematical and computational methodology for radar tomography imaging in which the unknown volumetric velocity distribution of a wave within a bounded domain is to be reconstructed. Our goal is to enable effective simulation and inversion of a large amount of full-wave data within a realistic 2D or 3D geometry. For propagating and inverting the wave, we present a rigorous multigrid-based forward approach which utilizes the finite-difference time-domain method and a nested finite element grid structure. We also introduce and validate a multigrid-based inversion algorithm which allows regularization of the unknown distribution through a coarse-to-fine inversion scheme. Using this approach, sparse signals can be effectively inverted, as the coarse fluctuations are reconstructed before the finer ones. Furthermore, the number of nonzero entries in the system matrix can be compressed and, thus, the inversion procedure can be speeded up. As the test scenario, we investigate satellite-based asteroid interior reconstruction. We use both full-wave and projected wave data and estimate the accuracy of the inversion under different error sources: noise and positioning inaccuracies. The results suggest that the present inversion technique allows recovering the interior with a single satellite recording backscattering data. Robust results can be achieved, when the peak-to-peak signal-to-noise ratio is above 10 dB. Furthermore, the robustness for the deep interior part can be enhanced if two satellites can be utilized in the measurements.**

***Index Terms*—Multigrid methods, Radio tomography, Microwave tomography, Asteroids, Biomedical imaging**

I. Introduction

Modeling and inverting a full wave in order to estimate an unknown parameter distribution inside a target object [1], [2] is a computationally challenging imaging approach which has a wide range of applications, e.g., in biomedical microwave or ultrasonic tomography [3], [4], [5], [6], [7], [8], non-destructive material testing [9], [10], [11], [12] and astro/geophysical radar imaging [13], [14], [15], [16], [17]. Waveform (radar) imaging is rapidly becoming a standard approach in several fields of science and technology for the constantly increasing computational resources available for an ordinary user. For example, ultrasonic/microwave detection of breast lesions has recently been approaching the reliability of the classical computed X-ray tomography (CT) and magnetic resonance imaging (MRI) [7], [18].

In this study, we evaluate and compare different inversion schemes for a hierarchical (nested) multigrid mesh [19] resulting from the finite element (FE) discretization of the spatial domain. This multigrid mesh structure is also an essential part of the forward simulation process in which geometrically complex interior and boundary structures need to be modeled. The internal relative permittivity of the target object determining the wave speed is reconstructed using a total variation regularized inversion technique [20], [21], [22], [23], [1]. In forward simulation, a combination of the finite element method (FEM) [19] and finite-difference time-domain (FDTD) method [24] is utilized. The multigrid mesh enables effective forward and inverse computations in connection with nested finite element mesh structures. In particular, we introduce and validate a coarse-to-fine reconstruction algorithm that utilizes the multigrid approach to invert a linearized wave equation. In this approach, the coarse-level estimate can be utilized to regularize sparsity-based reconstructions and also to filter out the uninteresting parts of the permittivity distribution to reduce the computational cost for a large computational domain or three-dimensional geometry.

As a potential future application of the presented methodology, we consider reconstructing the interior structure of a small asteroid based on measurements performed by small orbiting spacecraft. The first attempt to reconstruct the interior structure of an small solar system body (SSSB) was made as a part of the Rosetta mission of the European Space Agency (ESA) in 2014. This Comet Nucleus Sounding Experiment by Radio-wave Transmission [17], [16] (CONSERT) aimed at finding out the permittivity of the comet P67/Churyumov-Gerasimenko based on a radio transmission between the mothership Rosetta and its lander Philae. At the moment, future missions are being planned as several organizations aim to explore SSSBs with probes. There is also a growing interest to use small spacecraft as a part of such a mission. In 2018, the Hayabusa-2 probe [25], [26] by Japan Aerospace Exploration Agency (JAXA) will deploy Mascot-1 [27] (German Aerospace Center, DLR) which will land on the asteroid 162173 Ryugu (1999 JU3). The preliminary plans of the ESA's unrealized Asteroid Impact Mission (AIM) [28] to asteroid 65803 Didymos (1996 GT) included at least three small spacecraft: the Mascot-2 asteroid lander by DLR as well as two or more CubeSats, which would be used to record radio-frequency data of the deep interior [15].

Motivated by these plans, we simulate and compare: (1) dense vs. sparse measurements, (2) sparse monostatic and bistatic measurement configuration, (3) full wave vs. projected (compressed) data, and (4) single- and dual-resolution inversion approach. In the numerical experiments, a cover layer and and internal voids of a 135 m diameter two-dimensional target are to be reconstructed utilizing a 10 MHz radio-frequency signal [29] with several different levels of total noise. The accuracy of the inversion results is analyzed via relative overlap and value error (ROE and RVE) measures. The results suggest that the present full-wave approach allows robust reconstruction of both the cover and the voids with a single satellite recording backscattering data (Figure 1), if the peak-to-peak signal-to-noise ratio is above 10 dB. Reconstructing the deep part of the interior can be enhanced, if, instead of one, two or more satellites can be used to gather the measurements. That is, if also the through-going wave can be recorded in addition to the backscattering part. The present tomography approach seems promising for various volumetric waveform imaging contexts. For the generality of the results, we present an alternative scaling of the parameters for 50 MHz radio and 10 GHz microwave frequencies, and give examples of related tomography applications.

This paper is organized as follows. Section 2 describes the math-

M. Takala, D. Us and S. Pursiainen are with Laboratory of Mathematics, Tampere University of Technology, PO Box 553, 33101 Tampere, Finland.

M. Takala is with Laboratory of Pervasive Computing, Tampere University of Technology.

D. Us is with Laboratory of Signal Processing, Tampere University of Technology.

Digital Object Identifier 10.1109/TCI.2018.2811908

Fig. 1. Two small spacecraft exploring the interior of an asteroid. Each one is equipped with a single-rod dipole antenna similar to those utilized in low-frequency georadar surveys.

ematical forward and inverse approaches of this study. Section 3 and 4 describe the numerical experiments and the results obtained, respectively, and Section 5 includes the discussion.

II. Materials and methods

A. Wave equation

In this study, we model the scalar electric potential distribution u in the spatio-temporal set $[0,T]\times\Omega$. This distribution is assumed to satisfy the following hyperbolic wave equation

$$\varepsilon_r \frac{\partial^2 u}{\partial t^2} + \sigma \frac{\partial u}{\partial t} - \Delta_{\vec{x}} u = \frac{\partial f}{\partial t} \quad \text{for all} \quad (t,\vec{x}) \in [0,T]\times\Omega \qquad (1)$$

with a given real-valued relative electric permittivity ε_r, real conductivity distribution σ, and the initial conditions $u|_{t=0} = u_0$ and $(\partial u/\partial t)|_{t=0} = u_1$. The right hand side is a signal source of the form $\partial f(t,\vec{x})/\partial t = \delta_{\vec{p}}(\vec{x})\partial\tilde{f}(t)/\partial t$ transmitted at the point $\vec{p}$. Here, $\tilde{f}(t)$ denotes the time-dependent part of f and $\delta_{\vec{p}}(\vec{x})$ a Dirac's delta function with respect to $\vec{p}$. The governing equation (1) can be formulated as a first-order system of the form

$$\varepsilon_r \frac{\partial u}{\partial t} + \sigma u - \nabla\cdot\vec{g} = f \quad \text{and} \quad \frac{\partial \vec{g}}{\partial t} - \nabla u = 0, \quad \text{in} \quad \Omega\times[0,T], \quad (2)$$

where $\vec{g} = \int_0^t \nabla u(\tau,\vec{x})\,d\tau$, $\vec{g}|_{t=0} = \nabla u_0$ and $u|_{t=0} = u_1$. Integrating (2) multiplied by $v : [0,T] \to H^1(\Omega)$ and $\vec{w} : [0,T] \to L_2(\Omega)$ and applying the rule of partial integration, one can obtain the weak form

$$\frac{\partial}{\partial t}\int_\Omega \vec{g}\cdot\vec{w}\,\mathrm{d}\Omega - \int_\Omega \vec{w}\cdot\nabla u\,\mathrm{d}\Omega = 0, \qquad (3)$$

$$\frac{\partial}{\partial t}\int_\Omega \varepsilon_r\, u\, v\,\mathrm{d}\Omega + \int_\Omega \sigma\, u\, v\,\mathrm{d}\Omega + \int_\Omega \vec{g}\cdot\nabla v\,\mathrm{d}\Omega = \begin{cases}\tilde{f}(t), & \text{if } \vec{x}=\vec{p},\\ 0, & \text{else.}\end{cases} \qquad (4)$$

Here, it is assumed that the domain and the parameters are regular enough, so that the weak form has a unique solution $u : [0,T] \to H^1(\Omega)$ [30].

B. Multigrid forward approach

In order to solve (1) numerically, we cover the d-dimensional ($d = 2$ or 3) spatial domain Ω with a d-simplex mesh $\mathcal{T}$ consisting of m elements $\mathcal{T}_1, \mathcal{T}_2, \ldots, \mathcal{T}_m$. Each element $\mathcal{T}_i$ is associated with an indicator function $\chi_i \in L_2(\Omega)$. The set of n mesh nodes $\vec{r}_1, \vec{r}_2, \ldots, \vec{r}_n$ is identified with piecewise linear (nodal) basis functions $\varphi_1, \varphi_2, \ldots, \varphi_n \in H^1(\Omega)$ [19]. The potential and gradient fields are approximated as the finite sums $u = \sum_{j=1}^n p_j\varphi_j$ and $\vec{g} = \sum_{k=1}^d g^{(k)}\vec{e}_k$ with $g^{(k)} = \sum_{i=1}^m q_i^{(k)}\chi_i$ which are associated with the coordinate vectors $\mathbf{p} = (p_1, p_2, \ldots, p_n)$, $\mathbf{q}^{(k)} = (q_1^{(k)}, q_2^{(k)}, \ldots, q_m^{(k)})$, respectively. The numerical solution of the wave equation yielding $\mathbf{p}$ and $\mathbf{q}^{(k)}$ has been briefly reviewed in Section A (Appendix).

The relative permittivity distribution is reconstructed utilizing an approximation $\varepsilon_r = \sum_{j=1}^M c_j\chi'_j$ which is defined for the coarse and nested d-simplex mesh $\mathcal{T}'$ with M elements $\mathcal{T}'_1, \mathcal{T}'_2, \ldots, \mathcal{T}'_M$ and N nodes $\vec{r}_1, \vec{r}_2, \ldots, \vec{r}_N$ shared by the dense mesh $\mathcal{T}$ ($N < n$). In the reconstruction procedure, the relation between the coordinate vector of the permittivity $\mathbf{x} = (c_1, c_2, \ldots, c_M)$ and discretized potential field $\mathbf{p}$ is approximated via the following linearized forward (data prediction) model

$$\mathbf{p}[\mathbf{x}] = \mathbf{p}[\mathbf{x}_0] + \mathbf{J}[\mathbf{x}_0](\mathbf{x}-\mathbf{x}_0). \qquad (5)$$

Here, $\mathbf{x}_0$ is an initial *a priori* guess for the permittivity and $\mathbf{J}[\mathbf{x}_0]$ is a Jacobian matrix, which consists of partial derivatives of the form $\partial\mathbf{p}_\ell/\partial c_j$ evaluated at $\mathbf{x}_0$. The partial derivative $\partial\mathbf{p}_\ell/\partial c_j$ can be formulated as the sum

$$\frac{\partial\mathbf{p}_\ell}{\partial c_j} = \sum_{\vec{r}_i\in\mathcal{T}'_j,\, i\le n} \mathbf{d}_\ell^{(i,j)} \qquad (6)$$

in which $\mathbf{d}_\ell^{(i,j)}$ can be obtained by solving the auxiliary system of the form (23) and (24) as shown in Appendix A.

The number of the terms in the sum $\partial\mathbf{p}_\ell/\partial c_j = \sum_{\vec{r}_i\in\mathcal{T}'_j,\, i\le n}\mathbf{d}_\ell^{(i,j)}$ depends on the density of the finite element mesh $\mathcal{T}$, that is, the number of nodes $\vec{r}_i \in \mathcal{T}$ belonging to $\mathcal{T}'_j$. In order to lower this number, and thereby also reduce the computational work in forming the model, we redefine (6) with respect to the coarse mesh $\mathcal{T}'$ as follows:

$$\frac{\partial\mathbf{p}_\ell}{\partial c_j} \approx \sum_{\vec{r}_i\in\mathcal{T}'_j,\, i\le N} \mathbf{d}'^{(i,j)}_\ell = \sum_{k=1}^{d+1} \mathbf{d}'^{(i_k,j)}_\ell, \qquad (7)$$

where the number of terms is $d+1$, that is, the number of nodes in $\mathcal{T}'_j$. This estimate is, in this study, regarded as the multigrid approach to forward modeling, as it is based on the nested multigrid mesh structure (Appendix A).

C. Reconstruction procedure

The linearized forward model can be written as the linear system $\mathbf{y}-\mathbf{y}_0 = \mathbf{L}(\mathbf{x}-\mathbf{x}_0)+\mathbf{n}$, where $\mathbf{y}$ is the actual data vector, $\mathbf{y}_0$ and $\mathbf{L}$ denote the simulated data $\mathbf{p}[\mathbf{x}_0]$ and Jacobian matrix $\mathbf{J}[\mathbf{x}_0]$ for a constant *a priori* guess $\mathbf{x}_0$, and $\mathbf{n}$ is a noise vector containing both modeling and measurement errors. In this study, a regularized solution of $\mathbf{x}$ is obtained via the iteration

$$\mathbf{x}_{\ell+1} = \mathbf{x}_0 + (\mathbf{L}^T\mathbf{L} + \alpha\mathbf{D}\boldsymbol{\Gamma}_\ell\mathbf{D})^{-1}\mathbf{L}^T(\mathbf{y}-\mathbf{y}_0) \qquad (8)$$

in which $\boldsymbol{\Gamma}_\ell$ is a weighting matrix satisfying $\boldsymbol{\Gamma}_0 = \mathbf{I}$ and $\boldsymbol{\Gamma}_\ell = \mathrm{diag}(|\mathbf{D}[\mathbf{x}_\ell - \mathbf{x}_0]|)^{-1}$ for $\ell \ge 1$, and $\mathbf{D}$ denotes a regularization matrix of the form

$$D_{i,j} = \beta\delta_{i,j} + \frac{(2\delta_{i,j}-1)\int_{\mathcal{T}'_i\cap\mathcal{T}'_j}\mathrm{d}s}{\max_{i,j}\int_{\mathcal{T}'_i\cap\mathcal{T}'_j}\mathrm{d}s}, \quad \delta_{i,j} = \begin{cases}1, & \text{if } j=i,\\ 0, & \text{otherwise.}\end{cases} \qquad (9)$$

The first regularization term limits the magnitude of $\mathbf{x}$ and the second one penalizes the jumps over the edges of $\mathcal{T}'$. The iteration (8) can be shown [13] to minimize $F(\mathbf{x}) = \|\mathbf{L}(\mathbf{x}-\mathbf{x}_0)-(\mathbf{y}-\mathbf{y}_0)\|_2^2 + 2\sqrt{\alpha}\|\mathbf{D}(\mathbf{x}-\mathbf{x}_0)\|_1$ in which the second term equals to the total variation of $\mathbf{x}$, if $\beta = 0$ [22], [23], [1], [21]. Here, the total variation regularization strategy produces distributions with large connected subsets close to constant, which helps to avoid noise in the reconstructions.

D. Coarse-to-fine approach

Using two triangular nested inversion meshes $\mathcal{T}'$ and $\mathcal{T}''$, one can obtain a coarse-to-fine version of the inversion algorithm (8) in which the coarse details are reconstructed before the finer ones. Here, the split between the two resolution levels is given by the decomposition

$$\mathcal{S}_{\mathcal{T}'} = \mathcal{S}_{\mathcal{T}''} \oplus \mathcal{S}_{\mathcal{T}'\setminus\mathcal{T}''} \qquad (10)$$

in which $\mathcal{S}_{\mathcal{T}'}$ and $\mathcal{S}_{\mathcal{T}''}$ (Figure 2) denote the spaces of all piecewise (trianglewise) constant distributions of $\mathcal{T}'$ and $\mathcal{T}''$ and $\mathcal{S}_{\mathcal{T}'\setminus\mathcal{T}''}$ is the space of those fine fluctuations of $\mathcal{S}_{\mathcal{T}''}$ that do not belong to $\mathcal{S}_{\mathcal{T}''}$. The basis for $\mathcal{S}_{\mathcal{T}'\setminus\mathcal{T}''}$ can be chosen in various ways. In this study, each basis function obtains the constant values 1 and -1 in an adjacent pair of triangles and is zero elsewhere (Figure 2). Consequently, the support is minimal. For a given permittivity distribution and set of basis functions, both coarse and fine fluctuations are uniquely determined by (10).

Denoting by $\mathcal{R}_c$ and $\mathcal{R}_f$ two linear coordinate transforms from $\mathcal{S}_{\mathcal{T}''}$ and $\mathcal{S}_{\mathcal{T}'\setminus\mathcal{T}''}$ to $\mathcal{S}_{\mathcal{T}'}$, respectively, one can define a coarse and fine level matrix $\mathbf{L}_c = \mathbf{L}\mathcal{R}_c$ and $\mathbf{L}_f = \mathbf{L}\mathcal{R}_f$ which determine the forward model for the coarse and fine details. That is, if $\mathbf{x} = \mathcal{R}_c\mathbf{x}^{(c)} + \mathcal{R}_f\mathbf{x}^{(f)}$, where $\mathbf{x}^{(c)}$ and $\mathbf{x}^{(f)}$ are coordinate vectors for functions in $\mathcal{S}_{\mathcal{T}''}$ and $\mathcal{S}_{\mathcal{T}'\setminus\mathcal{T}''}$, respectively, then the forward model can be decomposed as $\mathbf{Lx} = \mathbf{L}_c\mathbf{x}^{(c)} + \mathbf{L}_f\mathbf{x}^{(f)}$.

With these definitions, the proposed coarse-to-fine inversion routine can be written as follows:

(1) Set the initial guess $\mathbf{x}_0 = (0, 0, \ldots, 0)$.

(2) Find a coarse resolution estimate belonging to $\mathcal{S}_{\mathcal{T}''}$ as given by

$$\mathbf{x}^{(c)}_{\ell+1} = \mathbf{x}^{(c)}_0 + (\mathbf{L}_c^T\mathbf{L}_c + \alpha\mathbf{D}_c\mathbf{\Gamma}_\ell\mathbf{D}_c)^{-1}\mathbf{L}_c^T(\mathbf{y} - \mathbf{y}_0) \tag{11}$$

with $\mathbf{\Gamma}_\ell = \mathrm{diag}(|\mathbf{D}_c[\mathbf{x}^{(c)} - \mathbf{x}^{(c)}_0]|)^{-1}$.

(3) Find a fine resolution correction that belongs to $\mathcal{S}_{\mathcal{T}'\setminus\mathcal{T}''}$ as given by

$$\mathbf{x}^{(f)}_{\ell+1} = \mathbf{x}^{(f)}_0 + (\mathbf{L}_f^T\mathbf{L}_f + \alpha\mathbf{D}_f\mathbf{\Gamma}_\ell\mathbf{D}_f)^{-1}\mathbf{L}_f^T(\mathbf{y} - \mathbf{y}_0 - \mathbf{L}_c[\mathbf{x}^{(c)}_{\ell+1} - \mathbf{x}^{(c)}_0]) \tag{12}$$

with $\mathbf{\Gamma}_\ell = \mathrm{diag}(|\mathbf{D}_f[\mathbf{x}^{(f)}_\ell - \mathbf{x}^{(f)}_0]|)^{-1}$.

(4) Set $\mathbf{x}_{\ell+1} = \mathbf{x}^{(c)}_{\ell+1} + \mathbf{x}^{(f)}_{\ell+1}$ and $\ell \to \ell + 1$.

(5) If ℓ is smaller than the desired number of iterations, then repeat the steps **(2)**–**(5)**.

If more than two nested meshes are used, then the correction step **(2)** can go through multiple resolution levels $f_1, f_2, \ldots, f_{n_f}$ via the recursive process:

$$\begin{aligned}\mathbf{x}^{(f_i)}_{\ell+1} \quad = \quad & (\mathbf{L}_{f_i}^T\mathbf{L}_{f_i} + \alpha\mathbf{D}_{f_i}\mathbf{\Gamma}_\ell\mathbf{D}_{f_i})^{-1}\mathbf{L}_{f_i}^T(\mathbf{y} - \mathbf{y}_0 - \mathbf{L}_c[\mathbf{x}^{(c)}_{\ell+1} - \mathbf{x}^{(c)}_0] \\ & - \sum_{k=1}^{i-1}\mathbf{L}_{f_i}[\mathbf{x}^{(f_i)}_{\ell+1} - \mathbf{x}^{(f_i)}_0])\end{aligned} \tag{13}$$

with $\mathbf{\Gamma}_\ell = \mathrm{diag}(|\mathbf{D}_{f_i}[\mathbf{x}^{(f_i)}_\ell - \mathbf{x}^{(f_i)}_0]|)^{-1}$ for $i = 1, 2, \ldots, n_f$.

E. Compression of coefficients

An important aspect in the above coarse-to-fine algorithm is that the size of $\mathbf{L}_f$ is multiple times that of $\mathbf{L}_c$. For the general structure of image information, low- and high-frequency fluctuations are often concentrated on the same image areas. Hence, the coarse scale structures in the image can be used as a basis to filter and compress also the finer details. In particular, the parts in which an image is close to zero can often be recognized based on its coarse structures. In this study, $\mathbf{L}_f$ is compressed on each step of the coarse-to-fine routine: The matrix $\mathcal{R}_f$ and thereby also $\mathbf{L}_f$ are defined with respect to those basis functions of $\mathcal{S}_{\mathcal{T}'\setminus\mathcal{T}''}$ that correspond to the largest third of the coefficients of $|\mathbf{x}^{(c)}_{\ell+1} - \mathbf{x}^{(c)}_0|$. Since in 2D each element of $\mathcal{S}''_{\mathcal{T}}$ covers three basis functions of $\mathcal{S}_{\mathcal{T}'\setminus\mathcal{T}''}$, the compressed size of $\mathbf{L}_f$ is identical to that of $\mathbf{L}_c$. Compressing the system might be necessary for large computational domains and three dimensional geometries.

F. Projected data

Inversion of projected (compressed) data was investigated by defining the following inner products (projections)

$$\langle a, b\rangle_1 = \int_0^T a(t)\,b(t)\,dt \quad \text{and} \quad \langle a, b\rangle_2 = \frac{1}{T}\int_0^T t\,a(t)\,b(t)\,dt \tag{14}$$

and the projected data vectors $\mathbf{y} = (\mathbf{y}^{(1)}, \mathbf{y}^{(2)})$ and $\mathbf{y}_0 = (\mathbf{y}_0^{(1)}, \mathbf{y}_0^{(2)})$ with $y_i^{(j)} = \langle u(t, \vec{p}_i),\, u(t, \vec{p}_i)\rangle_j$ and $y_0^{(j)}{}_i = \langle u(t, \vec{p}_i),\, u_0(t, \vec{p}_i)\rangle_j$, where $\vec{p}_i$ denotes the i-th measurement point, u_m denotes the measured potential field and u_0 the simulated one corresponding to the *a priori* guess for the permittivity distribution. It holds that

$$\frac{y_i^{(2)}}{y_i^{(1)}} = \frac{\int_0^T t\,u(t, \vec{p}_i)^2\,dt}{T\int_0^T u(t, \vec{p}_i)^2\,dt}, \tag{15}$$

that is, the relative integrated travel-time of the signal pulse. The Jacobian matrix for the projected data can be formed through

$$\frac{\partial}{\partial c_\ell}\langle u(t, \vec{p}_i),\, u_0(t, \vec{p}_i)\rangle_j = \langle u(t, \vec{p}_i),\, \frac{\partial}{\partial c_\ell}u_0(t, \vec{p}_i)\rangle_j. \tag{16}$$

The goal in the projected inversion approach is to find a permittivity distribution such that the corresponding data residual is orthogonal to the original data in terms of both $\langle\cdot,\cdot\rangle_1$ and $\langle\cdot,\cdot\rangle_2$.

III. Numerical experiments

The square $\Omega = [-1, 1]\times[-1, 1]$ was utilized as the test domain of the numerical experiments. The parameters t, $\vec{x}$, ε_r, σ and $\mathtt{c} = \varepsilon_r^{-1/2}$ (velocity) of the governing equation (1) can be scaled to SI-units, respectively, via the expressions $(\mu_0\varepsilon_0)^{1/2}st$, $s\vec{x}$, $\varepsilon_0\varepsilon_r$, $(\varepsilon_0/\mu_0)^{1/2}s^{-1}\sigma$, and $(\varepsilon_0\mu_0)^{-1/2}\mathtt{c}$ ($\mathtt{c} = 1$ for $\varepsilon_r = 1$), where $\varepsilon_0 = 8.85\cdot 10^{-12}$ F/m, $\mu_0 = 4\pi\cdot 10^{-7}$ b/m and s is a spatial scaling factor (meters).

The center part of the domain included a tomography target $\mathcal{D}$ (Figure 3) with an irregular shape and approximate diameter of $d \approx 0.28$. The interior of $\mathcal{D}$ included a surface layer with the thickness around 0.02 and three inclusions (voids) with maximum diameter of 0.01–0.09. The relative permittivity values were chosen to be 4, 3 and 1 for the interior part, cover layer and voids, respectively. Outside $\mathcal{D}$, the relative permittivity was set to be one, i.e., that of air or vacuum. In $\mathcal{D}$, the conductivity causing a signal energy loss was assumed to be a nuisance parameter of the form $\sigma = 5\varepsilon_r$. The remaining part of Ω was assumed to be lossless, i.e. $\sigma = 0$. The parameter values for three alternative choices of s (**I**)–(**III**) have been given in Table I. For (**I**), the minimal radar bandwidth needed for lossless signal pulse transmission is 10 MHz, coninciding the bandwidth of the CONSERT instrument [16]; for (**II**), it is 4 MHz, which we consider more relevant regarding small spacecraft applications; and for (**III**), it is 10 GHz, i.e., within range of microwave tomography applications [32].

The signal was assumed to have been transmitted and received at 0.32 diameter circular orbit C centered at the origin using the Blackman-Harris window [33], [34], [35] as the source function $\tilde{f}(t) = 0.359 - 0.488\cos(20\pi t) + 0.141\cos(40\pi t) - 0.012\cos(60\pi t)$ for $t \le 0.1$ (0.67 ns), and $\tilde{f}(t) = 0$, otherwise. The length of the temporal interval was chosen to be $T = 1.3$. The time interval between each data sampling point was set to be 0.01 corresponding to a 1.25 oversampling rate relative to the Nyquist criterion, i.e., the density of sampling points was $2.5 = 2\times 1.25$ times the highest frequency in the signal pulse. The signal specifications scaled according to (**I**)–(**III**) have been included in Table II.

Three different spatial signal configurations (**A**)–(**C**) (Table III) were tested. Configurations (**A**) and (**B**) were monostatic. They modeled a situation in which a single orbiter moving along C records backscattering data. In (**A**) a dense distribution of 128 measurement

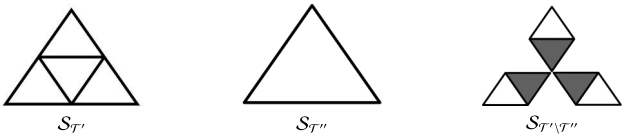

Fig. 2. Each triangle of the coarse mesh $\mathcal{T}''$ contains four nested triangles of the fine one $\mathcal{T}'$. The triangles of $\mathcal{T}'$ and $\mathcal{T}''$ span, respectively, the spaces $\mathcal{S}'_{\mathcal{T}}$ (left) and $\mathcal{S}''_{\mathcal{T}}$ (center), of trianglewise constant basis functions. The space $\mathcal{S}_{\mathcal{T}'\setminus\mathcal{T}''}$ (right) contains those fine fluctuations of $\mathcal{S}'_{\mathcal{T}}$ that do not belong to $\mathcal{S}''_{\mathcal{T}}$. Each basis function of $\mathcal{S}_{\mathcal{T}'\setminus\mathcal{T}''}$ obtains the values 1 and -1 in an adjacent pair of triangles (white and black, respectively) and is zero elsewhere. Consequently, each linear combination of the fine resolution basis functions of $\mathcal{S}'_{\mathcal{T}}$ can be presented as a linear combination of the coarse basis functions of $\mathcal{S}''_{\mathcal{T}}$ those of $\mathcal{S}_{\mathcal{T}'\setminus\mathcal{T}''}$.

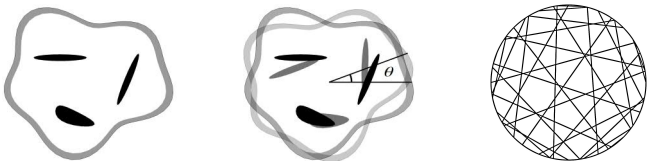

Fig. 3. **Left:** The target $\mathcal{D}$ utilized in the numerical experiments. **Center:** The sensitivity to orientation errors is investigated with different values of the polar angle θ. **Right:** Line segments illustrating the orbiter-to-orbiter signal paths in the bistatic signal configuration (**C**).

TABLE I
THE PROPERTIES OF THE TEST DOMAIN Ω WITH THREE DIFFERENT CHOICES OF THE SCALING PARAMETER s.

Scaling	s		Circle C	Target $\mathcal{D}$	Surface layer	Voids
No scaling	1	Diameter	0.32	0.28	0.02	0.01– 45 m
		ε_r		4	3	1
		σ		20	15	5
(**I**)	500 m	Diameter	160 m	140 m	10 m	5 – 45 m
		ε_r		4	3	1
		σ		1.1E-4 S/m	8.0E-5 S/m	2.7E-5 S/m
(**II**)	1250 m	Diameter	400 m	350 m	25 m	12 – 110 m
		ε_r		4	3	1
		σ		4.4E-5 S/m	3.2E-5 S/m	1.1E-5 S/m
(**III**)	0.5 m	Diameter	16 cm	14 cm	1 cm	0.5 – 4.5 cm
		ε_r		4	3	1
		σ		0.11 S/m	0.80 S/m	0.027 S/m

TABLE II
SIGNAL PROPERTIES FOR THREE DIFFERENT SCALING PARAMETER VALUES. FOR s = 500 M, THE MODEL CAN BE INTERPRETED AS A MONOLITHIC ASTEROID AND, FOR s = 1250 M, AS A RUBBLE PILE, AS ITS DIAMETER IS ABOVE THE RUBBLE PILE SPIN BARRIER [31] AND CONDUCTIVITY IS RELATIVELY LOW (DUE TO A HIGHER POROSITY). FOR s = 0.5 M, THE MODEL HAS A CORRESPONDENCE TO MICROWAVE RANGE APPLICATIONS.

Scaling s	Target	$\mathcal{D}$	Bandwidth[1]	Pulse duration T	Simulated wavelength in $\mathcal{D}$	Class
(**I**)	500 m	Asteroid (monolith)	10 MHz	2.2 μs	15 m	Radio wave
(**II**)	1250 m	Asteroid (rubble pile)	4 MHz	5.5 μs	3–7.5 m	Radio wave
(**III**)	0.5 m	Wood / Fatty tissue Bone marrow	10 GHz	2.2 ns	15 mm	Microwave

[1] The minimum radar bandwidth required for lossless pulse transmission.

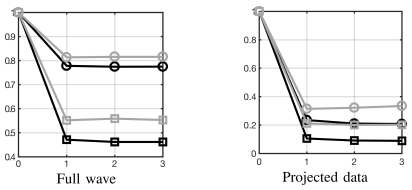

Fig. 4. The 2-norm of the relative residual for the single and dual resolution iteration (black and gray curves, respectively), i.e., $\|\mathbf{L}\mathbf{x}-\mathbf{y}\|_2/\|\mathbf{y}\|_2$ and $\|\mathbf{L}_c\mathbf{x}^{(c)}+\mathbf{L}_f\mathbf{x}^{(f)}-\mathbf{y}\|_2/\|\mathbf{y}\|_2$. The x-axis shows the number of the iteration steps. The curves for the full and projected data have been marked with squares and circles, respectively. The signal configuration is (**A**).

TABLE III
THE SIGNAL CONFIGURATIONS (**A**)–(**C**): THE NUMBER OF MEASUREMENT POINTS, OVERSAMPLING RATE W.R.T. NYQUIST CRITERION, THE NUMBER OF THE ORBITERS, AND THE ORBITING VELOCITY RATIO BETWEEN THE SATELLITES.

Positioning	Meas. points	Oversampling rate	Orbiters	Velocity ratio
(**A**)	128	1.6	1	-
(**B**)	32	0.4	1	-
(**C**)	32	0.4	2	10

points was used corresponding to oversampling by a factor of 1.6 with respect to the Nyquist criterion at C. Configuration (**B**) included 32 points, i.e., undersampling by the factor 0.4. Configuration (**C**) was otherwise similar to (**B**) but bistatic: two orbiters transmitted the signal pulse. The velocity of the second orbiter was assumed to be

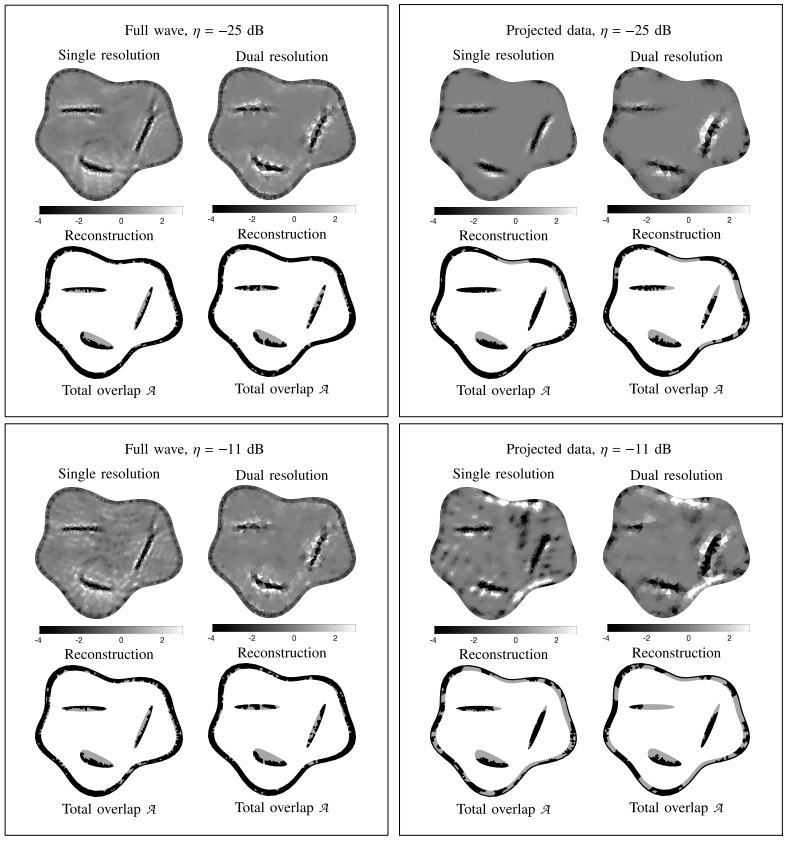

Fig. 5. Single and dual resolution reconstructions obtained with full and projected data at noise levels $\eta = -11$ dB and $\eta = -25$ dB. The color scale shows the difference between the inverse estimate and the initial guess for the relative permittivity, i.e., the constant distribution $\epsilon_r = 4$. Below each reconstruction, the total overlap set $\mathcal{A}$ has been visualized.

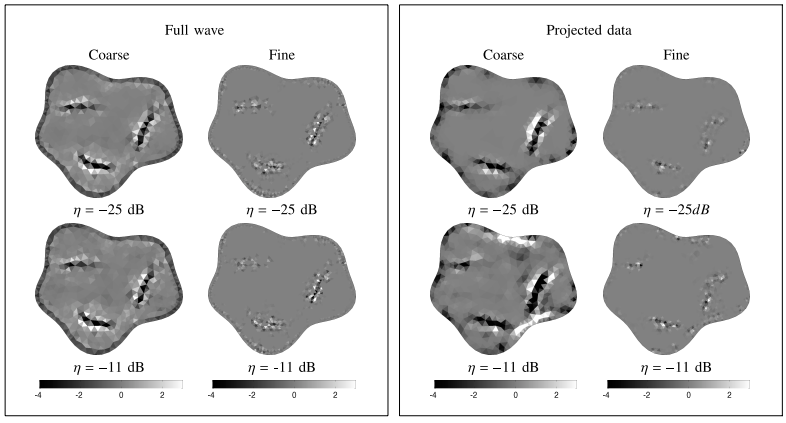

Fig. 6. The coarse and fine level fluctuations of the dual resolution reconstructions for full and projected data at noise levels $\eta = -25$ dB and $\eta = -11$ dB.

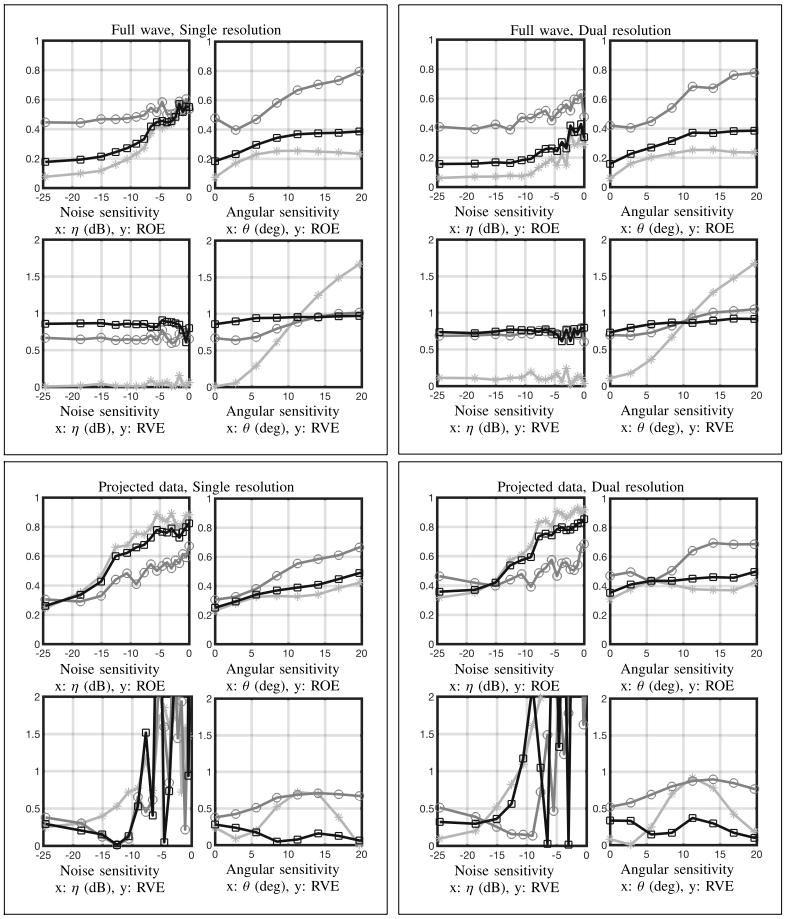

Fig. 7. ROE and RVE results for the signal configuration (**A**). **Surface layer**: light grey line, star marker, **Voids**: darker grey line, circle marker, **Total value**: black line, square marker.

TABLE IV

THE MEAN SQUARED ERROR (MSE) VALUES OBTAINED FOR COARSE, DUAL AND SINGLE RESOLUTION RECONSTRUCTION FOR THE SIGNAL CONFIGURATION (**A**) AT NOISE LEVELS $\eta = -25$ AND $\eta = -11$ (DECIBELS). THE FIRST ONE OF THESE IS THE FINAL COARSE LEVEL ESTIMATE (FIGURE 6) OF THE DUAL RESOLUTION INVERSION SCHEME (SECTION II-D).

		MSE·10^2		
Data	Noise η (dB)	Coarse Res.	Dual Res.	Single Res.
Full	-25	1.41	1.39	1.38
Full	-11	1.40	1.41	1.50
Projected	-25	1.51	1.47	1.15
Projected	-11	1.88	1.86	1.90

TABLE V

SIGNAL CONFIGURATION (**A**): THE SYSTEM MATRICES AND VECTORS, THE NUMBER OF VECTOR ENTRIES, MATRIX SIZES, AND THE INVERSION COMPUTATION TIMES.

Approach	Data	Matrices and vectors	Vector entries	Matrix size (MB)	Comp. time (s)
Single res.	Full	$\mathbf{L}, \mathbf{x}$	3988	494	21.1
Single res.	Proj.	$\mathbf{L}, \mathbf{x}$	3988	8.17	16.2
Dual res.	Full	$\mathbf{L}_c, \mathbf{L}_f, \mathbf{x}^{(c)}, \mathbf{x}^{(f)}$	997	123	12.9
Dual res.	Proj.	$\mathbf{L}_c, \mathbf{L}_f, \mathbf{x}^{(c)}, \mathbf{x}^{(f)}$	997	2.04	10.2

ten times that of the first one, leading to mixing of the line segments between the orbiters. The orbiter-to-orbiter signal paths for (**C**) have been illustrated in Figure 3.

A simulated data vector $\mathbf{y}$ was produced with a finite element mesh of 97517 nodes and 194232 triangular elements. The Jacobian matrix and the data estimate $\mathbf{y}_0$ were obtained using a different mesh $\mathcal{T}$ (99121 nodes, 197440 triangles) in order to avoid overly good inverse estimates [1]. In both cases, the temporal increment of the leap-frog iteration was set to be $\Delta t = 2.5 \cdot 10^{-4}$. In the mesh generation process, an initial mesh $\mathcal{T}''$ was generated first. After that, $\mathcal{T}'$ and finally $\mathcal{T}$ were obtained by using the regular mesh refinement principle recursively, i.e., each element edge was split into two equivalent halves.

Gaussian noise was added to the data. At each measurement point $\vec{p}_i$, the standard deviation ν of the noise was set to be of the form

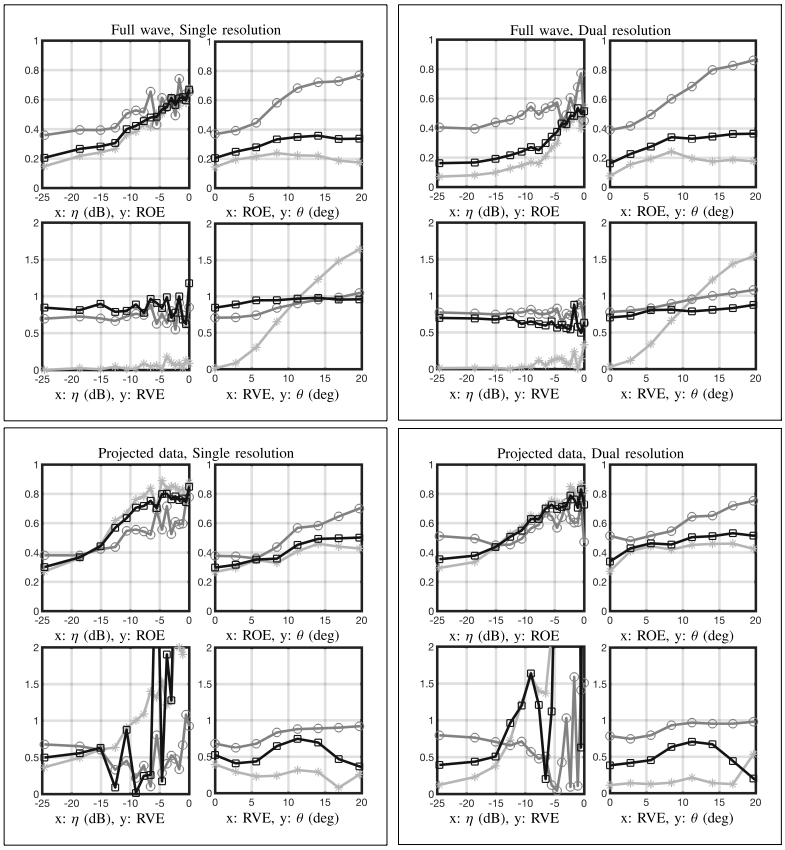

Fig. 8. ROE and RVE results for the signal configuration (**B**). **Surface layer**: light grey line, star marker, **Voids**: darker grey line, circle marker, **Total value**: black line, square marker.

$\nu = 1.645 \cdot 10^{\eta/10} \max_t u(t, \vec{p}_i)$, where η is the desired total noise level in decibels. The absolute value of η was regarded as an estimate for the total peak-to-peak signal to noise ratio. Due to the scaling, approximately 5% of the noise vector entries exceeded the decibel value η with respect to the signal peak $\max_t u(t, \vec{p}_i)$. This noise model was motivated by the noise estimates of [16] in which the peak level is used as the reference. Besides the additive noise, the sensitivity of the inversion to positioning inaccuracies was investigated by rotating the measurement points by (polar) angle θ in between the data simulation and reconstruction phases (Figure 3).

The reconstructions were computed via (1) single and (2) dual scale processing. The number of nested resolution levels was limited to two based on the size of the permittivity fluctuations which was close to the element size in $\mathcal{T}''$. In (1), the reconstruction was found using the mesh $\mathcal{T}'$ and, in (2), both $\mathcal{T}'$ and $\mathcal{T}''$ were used. The *a priori* guess $\mathbf{x}_0$ for the inversion procedure corresponded to a constant $\varepsilon_r = 4$ within $\mathcal{D}$. In the coarse-to-fine iteration, three steps were performed with $\alpha = \beta = 0.01$ for the full data and $\alpha = 10^{-7}$ and $\beta = 1$ for the projected data. These parameter values were approximately in the center of the range of working values based on preliminary numerical tests.

The accuracy of the inversion was examined through the relative overlap and value error (ROE and RVE), i.e., the percentages

$$\mathrm{ROE} = 100\Big(1 - \frac{\mathrm{Area}(\mathcal{A})}{\mathrm{Area}(\mathcal{S})}\Big) \quad \mathrm{RVE} = 100\Big(1 - \frac{\int_{\mathcal{S}} \varepsilon_r^* \, d\mathcal{S}}{\int_{\mathcal{S}} \varepsilon_r \, d\mathcal{S}}\Big). \tag{17}$$

Here ε_r and ε_r^* denote the actual and estimated permittivity, respectively, and $\mathcal{A} = \mathcal{S} \cap \mathcal{R}$ is the overlap between the set $\mathcal{S}$ to be recovered and the set $\mathcal{R}$ in which a given reconstruction is smaller than a limit such that $\mathrm{Area}(\mathcal{R}) = \mathrm{Area}(\mathcal{S})$. ROE and RVE were measured with respect to the noise level η and the angular positioning error θ.

The computations were performed using the Matlab R2017a software and a laptop equipped with a 2,2 GHz Intel Core i7 CPU and 8 GB of 1600 MHz DDR3 RAM. The single thread mode of the CPU was used, i.e., all the processes were run in a single CPU core.

IV. Results

The results of the numerical experiments have been included in Figures 4–9 as well as Tables IV and V. Figure 4 shows the convergence of inverse iteration as a function of iteration steps. Figure 5 visualizes the reconstructions and the overlap sets for configuration (**A**) at noise levels $\eta = -25$ dB and $\eta = -11$ dB. The minimum squared error [36] values for those reconstructions can be found in Table IV. Also the MSE of the coarse level estimate obtained with

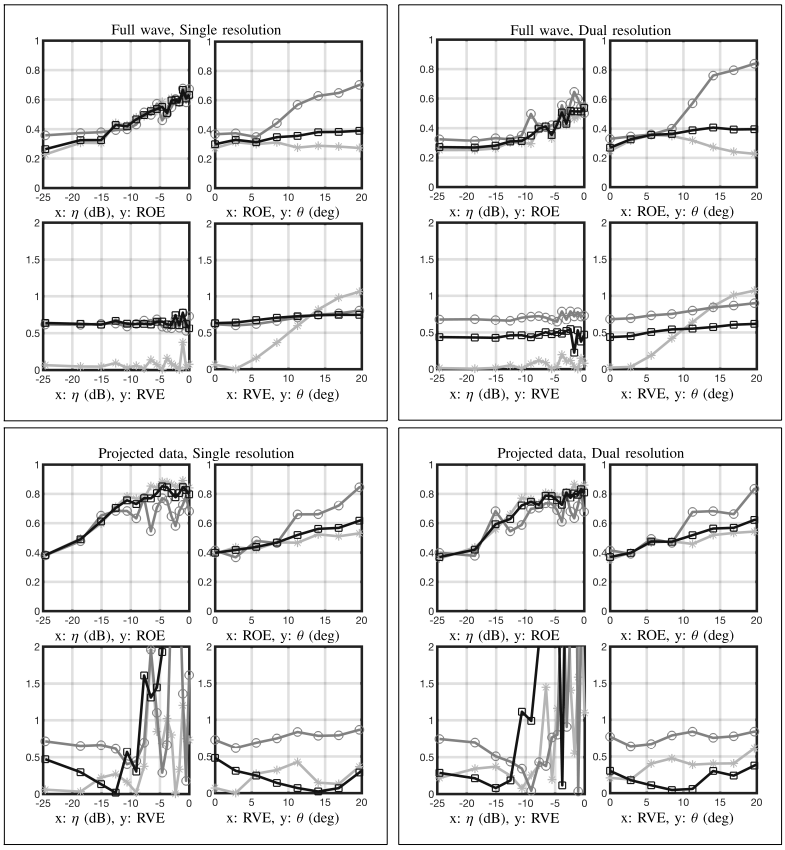

Fig. 9. ROE and RVE results for the signal configuration (**C**). **Surface layer**: light grey line, star marker, **Voids**: darker grey line, circle marker, **Total value**: black line, square marker.

the dual resolution scheme has been evaluated. The coarse and fine level fluctuations of the dual scale reconstruction have been visualized in Figure 6. Those together with the MSE values show that, in the low noise case ($\eta = -25$ dB), the final reconstruction was more accurate than the coarse level estimate. The coarse one was slightly superior, when the higher noise ($\eta = -11$ dB) and full data were used. Based on the MSEs, it is also obvious that the single scale approach is more sensitive to noise than the multigrid technique. Table V includes the vector and matrix sizes as well as the computation times required by the inversion processes, showing that the proposed inversion strategy was, in general, advantageous regarding both the speed and the memory-efficiency of the inversion. The convergence curves for the relative residual norm have been included in Figure V.

Figures 7–9 illustrate the sensitivity of the reconstructions to the total noise level η and to the angular measurement error θ for Configurations (**A**)–(**C**). The dual resolution approach was found to be slightly superior regarding the total ROE and RVE (the black line in Figures 7 – 9), when full wave data were used. With projected data such a difference was not observed. The reconstructions were, in general, more accurate for the surface layer than for the deep part of the interior (voids) with respect to both ROE and RVE.

The results (Figure 8) obtained with the sparse signal configuration (**B**) were close in accuracy to those (Figure 7) obtained with the dense one (**A**). The foremost accuracy for the deep interior part of $\mathcal{D}$ (voids) was achieved with the sparse two-orbiter configuration (**C**). It seemed to drive the balance of the reconstruction towards the deep interior, as (**B**) led to superior results with respect to the surface layer.

The noise level η was observed to affect the reconstruction quality above -15 dB level. When full wave data was used, the dual resolution reconstructions were more tolerant to the noise than those obtained with the single resolution approach: the total ROE and RVE were, in general, less volatile and stayed on a lower level between -15 dB and -10 dB noise in the former case. The clearest difference with respect to the volatility was observed for the sparse configuration (**B**). For projected data, the volatility of RVE was extreme above the -15 dB level with both single and dual resolution approaches. An angular measurement error θ between 0 and 5 degrees was observed to be small regarding the inversion results. An error larger than 5 degrees was led to clearly increased inversion errors in all the analyzed cases. Those seemed to be roughly comparable to above -10 dB noise with respect to the inverse estimates. Of the signal configurations (**A**)–(**C**), the most robust one with respect to noise and angular errors was (**C**) in which the number of signal sources is two.

V. Discussion

This paper concentrated on tomographic multigrid-based [19] inversion of waveform electromagnetic signals within a nested finite element mesh structure. Waveform imaging has a wide range of applications varying from biomedical tomography [3], [4], [5], [6], [7], [8] and non-destructive material testing [9], [10], [11], [12] to astro/geophysical applications. Here, as the foremost application, we considered reconstructing the interior structure of an asteroid [13], [15], [14], [16], [17] using small orbiting spacecraft. Due to the strict limitations of space missions, e.g., the payload weight, it is likely that a sparse set of waveform measurements performed by one or two small satellites will have to be used as data in a real planetary space mission.

A multigrid inverse approach utilizing the total variation regularization [20], [22], [23], [1] was proposed and tested. The primary goal in using more than one scale was to enhance the noise-robustness of the inversion process for sparse data compared to the single level case. The secondary goal was to reduce the system matrix size and the time needed for the inversion process via compression of the fine resolution level coefficients. The proposed technique can be interpreted as an extension of the classical total variation method to multiple resolution levels. It was chosen as it allows reconstructing and regularizing an arbitrary distribution in a similar manner at each level under scarce *a priori* information. In the numerical experiments, the single and dual resolution approaches were compared, three different signal configurations (**A**), (**B**) and (**C**) including dense and sparse measurements were investigated, and both full wave and projected data were used.

A. Results

Reconstructing the interior structure of the target $\mathcal{D}$ was found to be feasible with all the tested inversion approaches, when the noise level η and angular error θ were below -15 dB and 5 degrees, respectively. In the case of projected data, these were found to be the approximate upper limits for workable inversion. With full wave data, appropriate inverse estimates were obtained also above these levels. The results suggest that the proposed dual resolution reconstruction technique is advantageous regarding the total ROE and RVE. In particular, it improves the noise tolerance (robustness) between noise levels -15 dB and -10 dB, especially, for sparse measurements. Of the tested signal configurations, the foremost tolerance for measurement errors was achieved with (**C**), i.e., with two signal sources (orbiters).

B. Application areas

1) Radio tomography: The results obtained are promising from the viewpoint of future planetary missions. Namely, it was documented for CONSERT experiment that the noise peak level measured for the 90 MHz radio signal transmitted through the nucleus of the comet 67P Churyumov-Gerasimenko did not significantly exceed the -20 dB level [16]. Since full wave inversion was found to be feasible without severe artifacts at least up to -15 dB noise peak level, it seems a potential approach for a real mission, strengthening our recent findings [13]. Moreover, the reconstructions obtained can also be considered robust with respect to a couple of degrees angular positioning errors, which will be likely in a real mission.

An additive Gaussian white noise model was utilized. The standard deviation was chosen so that 5% of the generated noise entries exceeded the decibel value η which was used as an estimate for the noise peak level. The motivation to use a generous Gaussian white noise model was the lack of *a priori* knowledge related to the true modeling errors and the resulting noise peaks. Thus, the noise level approximates roughly the total error magnitude. Further analysis of the CONSERT data [16] might help to develop a more sophisticated noise model for future studies. Whether the total variation regularization method is optimal for a real noise distribution will also need to be studied in the future.

The comparison between the sparse signal configurations (**B**) and (**C**) suggests that the robustness of the inversion will improve, if in addition to the backscattering data, through going (orbiter-to-orbiter) signals [13] can be measured. Hence, the most reliable results may be expected, if more than one satellite can be used. In principle, this should be possible as the preliminary plans of the AIM mission [28] already included two small satellites and bistatic radio tomography measurements [15].

The classical low-frequency georadar studies [37] apply a single dipole antenna rod coinciding the model presented in this paper. For this reason and for the simplicity of the configuration, we suggest that a satellite pair utilizing such antennas might be sufficient for reconstructing the interior. A double or triple dipole might increase the reliability of the measurements, since in that case, the signal amplitude could be recorded regardless of the polarization. Equipping a spacecraft, e.g., a small satellite, with a multidirectional antenna might, however, be more difficult and expensive. An antenna attached to a small spacecraft needs to be a relatively simple and light one. We suggest here a half-wavelength dipole design with center frequency between 20–100 MHz (length 1.5–7.5 m), that is, a similar or somewhat lower value compared to the 90 MHz of CONSERT instrument [17], [16] in order to achieve an appropriate signal penetration. We see that emphasizing the signal penetration capability is important, since the relatively high permittivity and the unknown macroporosity structures of asteroid interiors can cause significant signal attenuation via scattering effects. Due to the high permittivity, the 4 MHz bandwidth corresponding to the scaling option (**II**) would yield a range resolution, i.e., the signal velocity divided by two times the bandwidth, close to that of CONSERT (10 MHz bandwidth).

2) Microwave tomography: In addition to radio tomography, the present multigrid methodology is a potential approach also in other fields of waveform tomographic reconstruction, for example, ultrasonic and microwave tomography (MWT). At the 10 GHz microwave frequency, the permittivity and conductivity of the current target domain has a correspondence to fatty tissues [38] and wood (balsam fir) [39] both of which can be inspected via microwave imaging. Similar parameters close to the target's permittivity and conductivity at 10 GHz microwave frequency are fat (σ = 0.58 S/m, ε_r = 4.6), breast fat (σ = 0.74 S/m, ε_r = 3.88) and bone marrow (σ = 0.57 S/m, ε_r = 4.6) as no other part in the body has conductivity lower than 1 S/m and relative permittivity lower than 10 [40].

MWT is useful in biomedical applications when there is high dielectric contrast between the structures, such as bone, soft tissue and fatty tissue. In biological structures, proportional values to the surface/target permittivity ratio given in Table I can be found in certain areas (not necessarily matching conductivity values). For example, in the treatment of fractured bone in extremities, where it is important to be able to differentiate body and soft-tissue elements such as muscle, vessels, nerves and skin, MWT would provide an assessment on the composition of these elements in case of injury [41]. As far as the surface/target permittivity ratio is concerned, MWT could also be used in the detection of blood flow perfusion, which would be helpful in also cardiac and brain imaging. In MWT of a human body torso, the relative permittivity and conductivity changes between different volume compartments at 10 GHz frequency match roughly with those of the current target domain, including skin (σ = 8 S/m, ε_r = 31), blood (σ = 13 S/m, ε_r = 45), heart (σ = 11.8 S/m, ε_r = 42), muscle (σ = 10.6 S/m, ε_r = 42.7), deflated lung (σ = 10.1 S/m, ε_r = 38), and air (σ = 0 S/m, ε_r = 1) [40].

C. Outlook

In the future work, the proposed multigrid approach might be developed and compared to other recent noise-robust approaches [42], [43]. The present forward approach might, for example, be utilized in combination with an alternative inversion strategy. An important future direction regarding radio tomography would be to use a realistic 3D rubble pile asteroid model [44], [45], e.g., to optimize the number of resolution levels and the amount of compression.

In general, further numerical analysis will be necessary regarding, e.g., polarization effects which were not modeled in this study. Also the antenna design is a topic which needs to be addressed in the future research [46]. Finally, the present methodology might be validated using microwave data. This seems a promising topic, as for example, the recent research in microwave breast imaging supports the noise limits discovered in this paper; In [47], the -15 dB has been suggested as a tolerable amplitude error and -11 dB as a turning point above which the inversion artifacts begin to increase.

Acknowledgements

This work was supported by the Academy of Finland Key Project 305055 and the AoF Centre of Excellence in Inverse Problems Research.

Appendix

A. Numerical solution of the wave equation

Defining test functions $v : [0,T] \to \mathcal{V} \subset H^1(\Omega)$ and $\vec{w} : [0,T] \to \mathcal{W} \subset L_2(\Omega)$ with $\mathcal{V} = \text{span}\{\varphi_1, \varphi_2, \ldots, \varphi_n\}$ and $\mathcal{W} = \text{span}\{\chi_1, \chi_2, \ldots, \chi_m\}$ the weak form can be written in the Ritz-Galerkin discretized form [19], that is,

$$\frac{\partial}{\partial t}\mathbf{A}\mathbf{q}^{(k)} - \mathbf{B}^{(k)}\mathbf{p} + \mathbf{T}^{(k)}\mathbf{q}^{(k)} = 0, \tag{18}$$

$$\frac{\partial}{\partial t}\mathbf{C}\mathbf{p} + \mathbf{R}\mathbf{p} + \mathbf{S}\mathbf{p} + \sum_{k=1}^{d} \mathbf{B}^{(k)^T}\mathbf{q}^{(k)} = \mathbf{f}, \tag{19}$$

with $\mathbf{p} = (p_1, p_2, \ldots, p_n)$, $\mathbf{q}^{(k)} = (q_1^{(k)}, q_2^{(k)}, \ldots, q_m^{(k)})$, $\mathbf{f} \in \mathbb{R}^n$, $\mathbf{A} \in \mathbb{R}^{m\times m}$, $\mathbf{B} \in \mathbb{R}^{m\times n}$, $\mathbf{C} \in \mathbb{R}^{n\times n}$, $\mathbf{S} \in \mathbb{R}^{n\times n}$, $\mathbf{T} \in \mathbb{R}^{m\times m}$. Here, $\mathbf{A}$ and $\mathbf{T}^{(k)} = \zeta^{(k)}\mathbf{A}$ are diagonal matrices with non-zero entries determined by $A_{i,i} = \int_{T_i} \mathrm{d}\Omega$. The right-hand side of the second equation is given by $f_i = \int_\Omega f\,\varphi_i\,\mathrm{d}\Omega$. The matrix $\mathbf{B}^{(k)}$ is a projection matrix of the form $B^{(k)}_{i,j} = \int_{T_i} \vec{e}_k \cdot \nabla\varphi_j\,\mathrm{d}\Omega$, and $\mathbf{C}$, $\mathbf{R}$ and $\mathbf{S}$ are mass matrices weighted by ε_r, σ and ξ, respectively, as given by $C_{i,j} = \int_\Omega \varepsilon_r\,\varphi_i\varphi_j\,\mathrm{d}\Omega$, $R_{i,j} = \int_\Omega \sigma\,\varphi_i\varphi_j\,\mathrm{d}\Omega$ and $S_{i,j} = \int_\Omega \xi\,\varphi_i\varphi_j\,\mathrm{d}\Omega$. The matrices $\mathbf{S}$ and $\mathbf{T}^{(k)}$ correspond to a split-field perfectly matched layer (PML), i.e., the set $\{\vec{x} \in \Omega \,|\, \varrho_1 \le \max_k |x_k| \le \varrho_2\}$ which eliminates reflections from the boundary $\partial\Omega$ back to the inner part of Ω [24]. For the PML parameters, $\xi(\vec{x}) = \varsigma$, if $\varrho_1 \le \max_k |x_k| \le \varrho_2$, and $\zeta^{(k)}(\vec{x}) = \varsigma$, if $\varrho_1 \le |x_k| \le \varrho_2$, and $\xi(\vec{x}) = \zeta^{(k)}(\vec{x}) = 0$, otherwise.

To discretize the time interval $[0,T]$, we utilize Δt spaced regular grid of N time points and the standard difference approximations for the time derivative which substituted into equations (18) and (19) lead to the the following system

$$\mathbf{q}^{(k)}_{\ell+\frac{1}{2}} = \mathbf{q}^{(k)}_{\ell-\frac{1}{2}} + \Delta t\mathbf{A}^{-1}\Big(\mathbf{B}^{(k)}\mathbf{p}_\ell - \mathbf{T}^{(k)}\mathbf{q}^{(k)}_{\ell-\frac{1}{2}}\Big), \tag{20}$$

$$\mathbf{p}_{\ell+1} = \mathbf{p}_\ell + \Delta t\mathbf{C}^{-1}\Big(\mathbf{f}_\ell - \mathbf{R}\mathbf{p}_\ell - \mathbf{S}\mathbf{p}_\ell - \sum_{k=1}^{d} \mathbf{B}^{(k)^T}\mathbf{q}^{(k)}_{\ell+\frac{1}{2}}\Big), \tag{21}$$

for $\ell = 1, 2, \ldots, N$. Simulating the signal propagation via (20)–(21) is known as the leap-frog time integration method [24], [48], [49] .

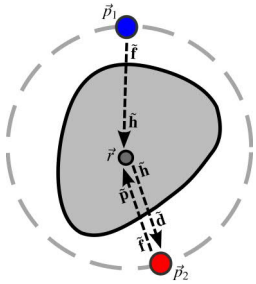

Fig. 10. A schematic picture visualizing the regularized deconvolution-based solution of (23)–(24). **(1)** Place the source $\tilde{\mathbf{f}}$ at the point $\vec{p}_1$ and solve the system (20)–(21) using the leap-frog iteration. Based on the solution, calculate and store $\tilde{\mathbf{h}}$ of the form (22) for a given node $\vec{r}$ and element $\mathcal{T}$ of the mesh $\mathcal{T}'$. **(2)** Place $\tilde{\mathbf{f}}$ at $\vec{p}_2$. Solve (20)–(21) and store $\tilde{\mathbf{p}}$ of the form (20) at $\vec{r}$. **(3)** Estimate the Green's function $\tilde{\mathbf{g}}$ satisfying $\tilde{\mathbf{p}} = \tilde{\mathbf{g}} * \tilde{\mathbf{f}}$ using Tikhonov regularized deconvolution with a suitably chosen regularization parameter δ [1]. **(4)** Based on the estimated $\tilde{\mathbf{g}}$ and the reciprocity of the signal wave [50], approximate $\tilde{\mathbf{d}}$, the solution of (24) at $\vec{p}_2$, through the convolution $\tilde{\mathbf{d}} = \tilde{\mathbf{g}} * \tilde{\mathbf{h}}$.

1) Auxiliary system: In order to obtain the expressions (6) and (7), we define the following auxiliary source vector

$$\mathbf{h}^{(i,j)}_\ell = \frac{\partial \mathbf{C}}{\partial c_j}\mathbf{Q}^{(i)}\,\mathbf{b}_\ell, \tag{22}$$

where $\mathbf{b}_\ell = \mathbf{C}^{-1}(\mathbf{R}\mathbf{p}_\ell + \mathbf{S}\mathbf{p}_\ell + \sum_{k=1}^{d} \mathbf{B}^{(k)^T}\mathbf{q}^{(k)}_{\ell+\frac{1}{2}})$, the matrix $\mathbf{Q}^{(i)} \in \mathbb{R}^{n\times n}$ has one nonzero entry $Q^{(i)}_{i,i} = 1$, and $(\partial\mathbf{C}/\partial c_j)_{i_1,i_2} = \int_{\mathcal{T}'_j} \varphi_{i_1}\varphi_{i_2}\,\mathrm{d}\Omega$ is nonzero if the j-th element includes nodes i_1 and i_2. Furthermore, we define the auxiliary system

$$\mathbf{r}^{(i,j,k)}_{\ell+\frac{1}{2}} = \mathbf{r}^{(i,j,k)}_{\ell-\frac{1}{2}} + \Delta t\mathbf{A}^{-1}\Big(\mathbf{B}^{(k)}\mathbf{d}^{(i,j)}_\ell - \mathbf{T}^{(k)}\mathbf{r}^{(i,j,k)}_{\ell-\frac{1}{2}}\Big), \tag{23}$$

$$\mathbf{d}^{(i,j)}_{\ell+1} = \mathbf{d}^{(i,j)}_\ell + \Delta t\mathbf{C}^{-1}\Big(\mathbf{h}^{(i,j)}_\ell - \mathbf{R}\mathbf{d}^{(i,j)}_\ell - \mathbf{S}\mathbf{d}^{(i,j)}_\ell - \sum_{k=1}^{d} \mathbf{B}^{(k)^T}\mathbf{r}^{(i,j,k)}_{\ell+\frac{1}{2}}\Big). \tag{24}$$

This follows from (20)–(21) simply by substituting $\mathbf{h}^{(i,j)}_\ell$ as the source. Due to the sparse structure of $(\partial\mathbf{C}/\partial c_j)$, the vector $\mathbf{h}^{(i,j)}$ differs from zero only if the i-th node belongs to the element $\mathcal{T}'_j \in \mathcal{T}'$.

2) Regularized deconvolution in forward modeling: For the extensive number of the source vectors $\mathbf{h}^{(i,j)}_\ell$, solving all the system of the form (23)–(24) via the leap-frog iteration would be extremely slow compared to the computation of the systems of the form (20)–(21). A faster way to approach forward modeling is to utilize regularized deconvolution [13] through the following steps (**1**)–(**4**):

(1) Place the source $\tilde{\mathbf{f}}$ at the point $\vec{p}_1$ and solve the system (20)–(21) using the leap-frog iteration. Based on the solution, calculate and store $\tilde{\mathbf{h}}$ of the form (22) for a given node $\vec{r}$ and element $\mathcal{T}$ of the mesh $\mathcal{T}'$.

(2) Place $\tilde{\mathbf{f}}$ at $\vec{p}_2$. Solve (20)–(21) and store $\tilde{\mathbf{p}}$ of the form (20) at $\vec{r}$.

(3) Estimate the Green's function $\tilde{\mathbf{g}}$ satisfying $\tilde{\mathbf{p}} = \tilde{\mathbf{g}} * \tilde{\mathbf{f}}$ using Tikhonov regularized deconvolution with a suitably chosen regularization parameter δ [1].

(4) Based on the estimated $\tilde{\mathbf{g}}$ and the reciprocity of the signal wave [50], approximate $\tilde{\mathbf{d}}$, the solution of (24) at $\vec{p}_2$, through the convolution $\tilde{\mathbf{d}} = \tilde{\mathbf{g}} * \tilde{\mathbf{h}}$.

Here, $\tilde{\mathbf{f}}, \tilde{\mathbf{h}}, \tilde{\mathbf{p}}, \tilde{\mathbf{g}}$, and $\tilde{\mathbf{d}}$ denote vectors whose entries contain the point-wise time evolution of the corresponding variable. Backscattering data will be obtained, if $\vec{p}_1 = \vec{p}_2$. f

3) Multigrid approach to forward modeling: The number of the terms in the sum $\partial \mathbf{p}_\ell / \partial c_j = \sum_{\vec{r}_i \in \mathcal{T}'_j,\, i \le n} \mathbf{d}_\ell^{(i,j)}$ depends on the density of the finite element mesh $\mathcal{T}$, that is, the number of nodes $\vec{r}_i \in \mathcal{T}$ belonging to $\mathcal{T}'_j$. In order to lower this number, and thereby also reduce the computational work in forming the model, we redefine the source (22) with respect to the coarse mesh $\mathcal{T}'$ as

$$\mathbf{h}'^{(i,j)}_\ell = \frac{\partial \mathbf{C}'}{\partial c_j} \mathbf{Q}'^{(i)} \mathbf{b}^{(i)}_\ell. \tag{25}$$

Here, the entries of $\mathbf{C}'$ are of the form $C'_{i,j} = \int_\Omega \varepsilon_r \varphi'_i \varphi'_j \, \mathrm{d}\Omega$ with φ'_i and φ'_j denoting piecewise linear nodal basis functions of $\mathcal{T}'$ and $\mathbf{Q}'^{(i)} \in \mathbb{R}^{N \times n}$ has a single nonzero entry $\mathbf{Q}'^{(i)}_{i,i} = 1$. Denoting by $\mathbf{d}'^{(i,j)}_\ell$ the regularized deconvolution-based solution (Section A2) of (23)–(24) with respect to $\mathbf{h}'^{(i,j)}_\ell = (\partial \mathbf{C}'/\partial c_j)\mathbf{b}'^{(i)}_\ell$, one obtains the estimate (7), that is, the basis of the present multigrid approach.

References

[1] J. P. Kaipio and E. Somersalo, *Statistical and Computational Methods for Inverse Problems*. Berlin: Springer, 2004.

[2] A. Tarantola, "Inverse problem theory and methods for model parameter estimation," 2005.

[3] T. Grzegorczyk, P. Meaney, P. Kaufman, R. di Florio-Alexander, and K. Paulsen, "Fast 3-D tomographic microwave imaging for breast cancer detection," *Medical Imaging, IEEE Transactions on*, vol. 31, no. 8, pp. 1584–1592, Aug 2012.

[4] P. Meaney, M. Fanning, R. di Florio-Alexander, P. Kaufman, S. Geimer, T. Zhou, and K. Paulsen, "Microwave tomography in the context of complex breast cancer imaging," in *Engineering in Medicine and Biology Society (EMBC), 2010 Annual International Conference of the IEEE*, Aug 2010, pp. 3398–3401.

[5] E. Fear, X. Li, S. Hagness, and M. Stuchly, "Confocal microwave imaging for breast cancer detection: Localization of tumors in three dimensions," *Biomedical Engineering, IEEE Transactions on*, vol. 49, no. 8, pp. 812–822, Aug 2002.

[6] N. V. Ruiter, M. Zapf, T. Hopp, R. Dapp, E. Kretzek, M. Birk, B. Kohout, and H. Gemmeke, "3D ultrasound computer tomography of the breast: A new era?" *European Journal of Radiology*, vol. 81, Supplement 1, no. 0, pp. S133 – S134, 2012.

[7] K. J. Opielinski, P. Pruchnicki, T. G. P. Podgorski, T. Krasnicki, J. Kurcz, and M. Sasiadek, "Ultrasound transmission tomography imaging of structure of breast elastography phantom compared to US, CT and MRI," *Archives of Acoustics*, vol. 38, pp. 321–334, 2013.

[8] B. Ranger, P. J. Littrup, N. Duric, P. Chandiwala-Mody, C. Li, S. Schmidt, and J. Lupinacci, "Breast ultrasound tomography versus MRI for clinical display of anatomy and tumor rendering: Preliminary results," *AJR Am J Roentgenol*, vol. 198, no. 1, pp. 233–239, 2012.

[9] Y. J. Kim, L. Jofre, F. De Flaviis, and M. Feng, "Microwave reflection tomographic array for damage detection of civil structures," *Antennas and Propagation, IEEE Transactions on*, vol. 51, no. 11, pp. 3022–3032, Nov 2003.

[10] H. Chai, D. Aggelis, S. Momoki, Y. Kobayashi, and T. Shiotani, "Single-side access tomography for evaluating interior defect of concrete," *Construction and Building Materials*, vol. 24, no. 12, pp. 2411 – 2418, 2010.

[11] H. Chai, S. Momoki, Y. Kobayashi, D. Aggelis, and T. Shiotani, "Tomographic reconstruction for concrete using attenuation of ultrasound," *NDT & E International*, vol. 44, no. 2, pp. 206 – 215, 2011.

[12] G. Acciani, G. Fornarelli, A. Giaquinto, D. Maiullari, and G. Brunetti, "Non-destructive technique for defect localization in concrete structures based on ultrasonic wave propagation," in *Computational Science and Its Applications – ICCSA 2008*, ser. Lecture Notes in Computer Science, O. Gervasi, B. Murgante, A. Laganà, D. Taniar, Y. Mun, and M. L. Gavrilova, Eds. Springer Berlin Heidelberg, 2008, vol. 5073, pp. 541–554.

[13] S. Pursiainen and M. Kaasalainen, "Orbiter-to-orbiter tomography: A potential approach for small solar system body," in *IEEE Transactions on Aerospace and Electronic Systems*, vol. 52, 2016, pp. 2747–2759.

[14] H. Su, F. Xu, S. Lu, and Y.-Q. Jin, "Iterative ADMM for inverse FE–BI problem: A potential solution to radio tomography of asteroids," *IEEE Transactions on Geoscience and Remote Sensing*, vol. 54, no. 9, pp. 5226–5238, 2016.

[15] A. Herique and V. Ciarletti, "A direct observation of the asteroids structure from deep interior to regolith: Two radars on the AIM mission," in *47th Lunar and Planetary Science Conference*, 2016, p. 2096.

[16] W. Kofman, A. Herique, Y. Barbin, J.-P. Barriot, V. Ciarletti, S. Clifford, P. Edenhofer, C. Elachi, C. Eyraud, J.-P. Goutail, E. Heggy, L. Jorda, J. Lasue, A.-C. Levasseur-Regourd, E. Nielsen, P. Pasquero, F. Preusker, P. Puget, D. Plettemeier, Y. Rogez, H. Sierks, C. Statz, H. Svedhem, I. Williams, S. Zine, and J. Van Zyl, "Properties of the 67P/Churyumov-Gerasimenko interior revealed by CONSERT radar," *Science*, vol. 349, no. 6247, 2015. [Online]. Available: http://www.sciencemag.org/content/349/6247/aab0639.abstract

[17] W. Kofman, A. Herique, J.-P. Goutail, T. Hagfors, I. P. Williams, E. Nielsen, J.-P. Barriot, Y. Barbin, C. Elachi, P. Edenhofer, A.-C. Levasseur-Regourd, D. Plettemeier, G. Picardi, R. Seu, and V. Svedhem, "The comet nucleus sounding experiment by radiowave transmission (CONSERT): A short description of the instrument and of the commissioning stages," *Space Science Reviews*, vol. 128, no. 1-4, pp. 413 – 432, 2007.

[18] K. J. Opielinski, P. Pruchnicki, T. Gudra, P. Podgorski, J. Kurcz, T. Krasnicki, M. Sasiadek, and J. Majewski, "Imaging results of multi-modal ultrasound computerized tomography system designed for breast diagnosis," *Computerized Medical Imaging and Graphics*, vol. 46, Part 2, pp. 83 – 94, 2015.

[19] D. Braess, *Finite Elements: Theory, Fast Solvers, and Applications in Solid Mechanics*. Cambridge University Press, 2007.

[20] J. A. Clarkson and C. R. Adams, "On definitions of bounded variation for functions of two variables," *Transactions of the American Mathematical Society*, vol. 35, no. 4, pp. pp. 824–854, 1933.

[21] A. Chambolle, "An algorithm for total variation minimization and applications," *Journal of Mathematical imaging and vision*, vol. 20, no. 1, pp. 89–97, 2004.

[22] O. Scherzer, M. Grasmair, H. Grossauer, M. Haltmeier, and F. Lenzen, *Variational Methods in Imaging*, ser. Applied Mathematical Sciences. Springer New York, 2008.

[23] W. Stefan, *Total Variation Regularization for Linear Ill-posed Inverse Problems: Extensions and Applications*. Arizona State University, 2008.

[24] J. B. Schneider, *Understanding the FDTD Method*. John B. Schneider, 2016. [Online]. Available: http://www.eecs.wsu.edu/~schneidj/ufdtd/

[25] J. Kawaguchi, A. Fujiwara, and T. Uesugi, "Hayabusa — its technology and science accomplishment summary and Hayabusa-2," *Acta Astronautica*, vol. 62, no. 10, pp. 639–647, 2008.

[26] Y. Tsuda, M. Yoshikawa, M. Abe, H. Minamino, and S. Nakazawa, "System design of the Hayabusa 2-asteroid sample return mission to 1999 JU3," *Acta Astronautica*, vol. 91, pp. 356–362, 2013.

[27] C. Lange, J. T. Grundmann, J. Hendrikse, M. Lange, and N. Toth, "Technology and knowledge reuse concepts to enable responsive NEO characterization missions based on the MASCOT lander," in *4th IAA Planetary Defense Conference*, 2015.

[28] P. Michel, M. Kueppers, I. Carnelli, A. Galvez, K. Mellab, and A. Cheng, "Asteroid impact mission (AIM): the european component of the AIDA space project," in *Lunar and Planetary Science Conference*, vol. 47, 2016, p. 1204.

[29] R. P. Binzel and W. Kofman, "Internal structure of near-earth objects," *Comptes Rendus Physique*, vol. 6, no. 3, pp. 321–326, 2005.

[30] L. Evans, *Partial Differential Equations*, ser. Graduate studies in mathematics. American Mathematical Society, 1998.

[31] T. Kwiatkowski, "Photometric survey of the very small near-Earth asteroids with the SALT telescope," *Astronomy and Astrophysics*, vol. 509, p. A95, Jan. 2010.

[32] J. Bourqui, J. Garrett, and E. Fear, "Measurement and analysis of microwave frequency signals transmitted through the breast," *Journal of Biomedical Imaging*, vol. 2012, p. 1, 2012.

[33] J. Irving and R. Knight, "Numerical modeling of ground-penetrating radar in 2-D using MATLAB," *Computers & Geosciences*, vol. 32, no. 9, pp. 1247 – 1258, 2006.

[34] F. J. Harris, "On the use of windows for harmonic analysis with the discrete fourier transform," *Proceedings of the IEEE*, vol. 66, no. 1, pp. 51–83, 1978.

[35] A. H. Nuttall, "Some windows with very good sidelobe behavior," *IEEE Transactions on Acoustics, Speech, Signal Processing*, vol. ASSP-29, no. 1, pp. 84–91, 1981.

[36] E. L. Lehmann and G. Casella, *Theory of point estimation*. Springer Science & Business Media, 2006.

[37] D. J. Daniels, *Ground Penetrating Radar (2nd Edition)*. Stevenage: Institution of Engineering and Technology, 2004.

[38] R. Pethig, "Dielectric properties of body tissues," *Clinical Physics and Physiological Measurement*, vol. 8, no. 4A, p. 5, 1987.

[39] V. Bucur, *Nondestructive Characterization and Imaging of Wood*, ser. Springer Series in Wood Science. Springer Berlin Heidelberg, 2013.
[40] D. Andreuccetti, R. Fossi, and C. Petrucci. (2005) Calculation of the dielectric properties of body tissues. [Online]. Available: http://niremf.ifac.cnr.it/tissprop/htmlclie/htmlclie.php
[41] S. Semenov, "Microwave tomography: review of the progress towards clinical applications," *Philosophical Transactions of the Royal Society of London A: Mathematical, Physical and Engineering Sciences*, vol. 367, no. 1900, pp. 3021–3042, 2009.
[42] B. Wen, S. Ravishankar, and Y. Bresler, "Structured overcomplete sparsifying transform learning with convergence guarantees and applications," *International Journal of Computer Vision*, vol. 114, no. 2-3, pp. 137–167, 2015.
[43] S. Gu, L. Zhang, W. Zuo, and X. Feng, "Weighted nuclear norm minimization with application to image denoising," in *Proceedings of the IEEE Conference on Computer Vision and Pattern Recognition*, 2014, pp. 2862–2869.
[44] J. Deller, "Hyper-velocity impacts on rubble pile asteroids," Ph.D. dissertation, University of Kent and International Max Planck Research School for Solar System Science, 2015.
[45] J. Deller, S. Lowry, C. Snodgrass, M. Price, and H. Sierks, "A new approach to modelling impacts on rubble pile asteroid simulants," *Monthly Notices of the Royal Astronomical Society*, vol. 455, no. 4, pp. 3752–3762, 2016.
[46] E. Nielsen, W. Engelhardt, B. Chares, L. Bemmann, M. Richards, F. Backwinkel, D. Plettemeier, P. Edenhofer, Y. Barbin, J. Goutail, W. Kofman, and L. Svedhem, "Antennas for sounding of a cometary nucleus in the Rosetta mission," in *Eleventh International Conference on Antennas and Propagation, Vols 1 and 2*, ser. IEE Conference Publications, no. 480. Inst Electrical Engineers Inspec INC, 2001, Proceedings Paper, pp. 436–441.
[47] X. Zeng, A. Fhager, and M. Persson, "Effects of noise on tomographic breast imaging," in *2011 XXXth URSI General Assembly and Scientific Symposium*, Aug 2011, pp. 1–4.
[48] A. Bossavit and L. Kettunen, "Yee-like schemes on a tetrahedral mesh, with diagonal lumping," *International Journal of Numerical Modelling: Electronic Networks, Devices and Fields*, vol. 12, no. 1-2, pp. 129–142, 1999.
[49] K. Yee, "Numerical solution of initial boundary value problems involving maxwell's equations in isotropic media," *Antennas and Propagation, IEEE Transactions on*, vol. 14, no. 3, pp. 302–307, 1966.
[50] C. Altman and K. Suchy, *Reciprocity, Spatial Mapping and Time Reversal in Electromagnetics*, ser. Developments in Electromagnetic Theory and Applications. Springer Netherlands, 1991.

Mika Takala received the B.Sc. degree in electrical engineering from the Tampere University of Technology (TUT), Tampere, Finland in 2015, and the M.Sc.(tech.) degree from TUT in 2016. His master's thesis in the field of embedded systems concentrated on implementation of signal preprocessing modules with High-Level Synthesis for waveform inversion applications. In 2016 he started working at the Laboratory of Mathematics, TUT, as a PhD student. He currently works on his PhD research, which is closely related to geophysical inversion strategies witha view towards computing aspects and embedded systems. He also works as a software architect at Granite Devices, Inc., Tampere, Finland.

Defne Us received the B.Sc. degree in electrical and electronics engineering in 2010 from Bilkent University, Ankara, Turkey and M.Sc. degree in biomedical engineering in 2013 from the Tampere University of Technology, Tampere, Finland. She has worked towards Ph.D. degree within the Laboratory of Signal Processing between 2014-2017. She is now continuing her degree with laboratory of Mathematics. Her research interests include metal artifact reduction methods in tomography and medical image reconstruction.

Sampsa Pursiainen received his MSc(Eng) and PhD(Eng) degrees (Mathematics) in the Helsinki University of Technology (Aalto University since 2010), Espoo, Finland, in 2003 and 2009. He focuses on various forward and inversion techniques of applied mathematics. In 2010–11, he stayed at the Department of Mathematics, University of Genova, Italy collaborating also with the Institute for Biomagnetism and Biosignalanalysis (IBB), University of Münster, Germany. In 2012–15, he worked at the Department of Mathetmatics and System Analysis, Aalto University, Finland and also at the Department of Mathematics, Tampere University of Technology, Finland, where he currently continues as an Assistant Professor.

PUBLICATION
III

Far-Field Inversion for the Deep Interior Scanning CubeSat

M. Takala, P. Bambach, J. Deller, E. Vilenius, M. Wittig, H. Lentz, H. M. Braun, M. Kaasalainen and S. Pursiainen

IEEE Transactions on Aerospace and Electronic Systems 55.4 (2019), 1683–1697
DOI: 10.1109/TAES.2018.2874755

Far-Field Inversion for the Deep Interior Scanning CubeSat

M. Takala, P. Bambach, J. Deller, E. Vilenius, M. Wittig, H. Lentz, H. M. Braun, M. Kaasalainen, S. Pursiainen

***Abstract*—This study aims at advancing mathematical and computational techniques for reconstructing the interior structure of a small Solar System body via Computed Radar Tomography (CRT). We introduce a far-field model for full-wave CRT and validate it numerically for an orbiting distance of 5 km using a synthetic 3D target asteroid and sparse limited-angle data. As a potential future application of the proposed method, we consider the Deep Interior Scanning CUbeSat (DISCUS) concept in which the goal is to localize macroporosities inside a rubble pile near-Earth asteroid with two small spacecraft carrying a bistatic radar.**

***Index Terms*—Small Solar System Bodies, Near-Earth Asteroids, Far-Field Measurements, Inverse Imaging, Computed Radar Tomography.**

I. Introduction

The aim of this study is to advance Computed Radar Tomography (CRT) [1], [2] for reconstructing the deep interior structure of a small solar system body (SSSB) [3]–[7]. The first such attempt, the Comet Nucleus Sounding Experiment by Radio-wave Transmission (CONSERT), was made as a part of the ESA's *Rosetta* mission to comet 67P/Churyumov-Gerasimenko. In CONSERT, a tomographic radar signal was transmitted between the orbiter and the *Philae* lander [6], [8]. At the moment, several space organizations aim to rendezvous SSSBs. In 2018, the Osiris-REx by NASA [9], [10] will arrive at the asteroid 101955 Bennu and the Hayabusa-2 [11], [12] mission by Japan Aerospace Exploration Agency (JAXA) has already arrived at asteroid 162173 Ryugu (1999 JU_3. Future CRT experiments have recently been planned for the ESA's proposed Asteroid Impact Mission (AIM) to asteroid 65803 Didymos (1996 GT) [5], [13]. This paper introduces and validates a three-dimensional far-field extension for the full-wave CRT model presented in [3]. We use realistic parameter values, orbiting distance and target scaling in order to support the design of the future planetary missions. In spaceborne CRT, the ability to simulate and invert far-field data is essential, since inserting a spacecraft into a stable SSSB orbit is a major challenge due to the low escape velocity of the SSSB. As the potential future application of the present inversion approach we consider the Deep Interior Scanning CUbesat (DISCUS) concept [14], [15] in which two small spacecraft carrying a bistatic (dual-antenna) radar [16] record penetrating radar data at about a few kilometers distance to a 260–600 m (Itokawa-size [17]) rubble pile near-Earth asteroid (NEA). Using two CubeSats for a bistatic radar measurement was first proposed for the AIM mission [5].

Rubble-pile asteroids are celestial bodies composed of aggregates bound together by gravitation and weak cohesion [18]–[24]. Therefore, they are likely to contain macroporosity, e.g., internal voids or cracks. From the observed rotation period cut-off limit of about >2.2 hours for asteroids with diameters greater than 200–300 m, it has been concluded that these bodies are not monolithic, but in the vast majority rubble pile asteroids [25]. The estimated density for the rubble piles suggests that macroporosity exists [26] but the actual proof is still missing. The radar onboard DISCUS would use a 20–50 MHz center frequency which is advantageous regarding both void detection [27], [28] and also the measurement noise due to the Sun [29]–[31]. As an independent mission, DISCUS would demonstrate a new and affordable mission concept to gain knowledge of the inside of NEAs.

In the numerical experiments, we investigated a three-dimensional asteroid model containing deep interior anomalies and a surface dust layer. The inversion accuracy and reliability were explored for several different noise levels and also for sparse limited-angle data, i.e., a situation in which the trajectory of the spacecraft does not allow measurements from all directions. Full-wave CRT was applied in order to maximize the imaging quality and to allow the sparsity of the measurements which is vital for the many limitations of the space missions, such as low data transfer rates and comparably short instrument lifetime [5], [14], [32], [33]. Volumetric full-wave CRT in a realistic geometry is a computationally challenging imaging technique which requires 3D wave simulation and inversion of a large system of equations. In order to achieve a sufficiently short computation time, a state-of-the-art cluster of graphics processing units (GPUs) was applied in the forward simulation. The waveform data were linearized and inverted using a high-end dual-processor workstation computer.

The results obtained suggest that the proposed mathematical model can be applied to invert full-wave far-field data for realistic asteroid sizes and shapes. Furthermore, based on the results, it seems that the existing background noise in the solar system and the expected level of modeling errors allow detection of macroporosities from the planned orbiting distance. The bistatic and stepped-frequency measurement techniques present in the DISCUS concept were found to be vital for improving the signal-to-noise ratio and for reducing the effects of the measurement noise and modeling errors. A comparison between full- and limited-angle CRT results suggests that the interior structure of the targeted NEA with a typical spin orientation can be reconstructed without requiring an orbital plane that includes shadow phases of the spacecraft and without the need to cover the entire surface of the SSSB.

This paper is organized as follows. Section II briefly describes the DISCUS radar, numerical experiments and the full-wave CRT model for the far-field measurements. Sections III and IV include the results and the discussion.

II. Materials and Methods

A. DISCUS radar

The DISCUS concept comprises two identical CubeSats. Both carry an identical radar instrument capable of a 10 W signal transmission. The CubeSats are equipped with a half-wavelength dipole antenna with a center frequency f_c between 20 and 50 MHz and a bandwidth B of at least 2 MHz. The bistatic measurement approach is used, since the scattering waves can be headed away from the

M. Takala (corresponding author) , M. Kaasalainen and S. Pursiainen are with the Laboratory of Mathematics, Tampere University of Technology, P.O. Box 692, 33101 Tampere, Finland.

M. Takala is with Laboratory of Pervasive Computing, Tampere University of Technology, P.O. Box 553, 33101 Tampere, Finland.

P. Bambach, J. Deller and E. Vilenius are with Max Planck Institute for Solar System Research, Justus-von-Liebig-Weg 3, 37077 Göttingen, Germany.

M. Wittig is with MEW-Aerospace, Hameln, Germany.

H. Lentz and H. M. Braun are with RST Radar Systemtechnik AG, Ebenaustrasse 8, 9413 Oberegg, Switzerland.

transmitter spacecraft (Figure 1). That is, one of the CubeSats both transmits and receives the signal, and the other one serves as an additional receiver.

The stepped-frequency measurement technique is applied [34]–[36]. That is, the signal is a pulse sequence of narrow frequency lines $\psi_1, \psi_2, \ldots, \psi_N$ which allow one to approximate a given function f via the sum

$$f = \sum_{\ell=1}^{N} c_\ell \psi_\ell. \tag{1}$$

If φ_ℓ is the received signal corresponding to frequency line ψ_ℓ, then the data g resulting from a transmission f is approximately given by $g = \sum_{\ell=1}^{N} c_\ell \varphi_\ell$ with $c_1, c_2, \ldots, c_N$ following from (1). Consequently, the data g for any transmission f within the given frequency range can be approximated, if the function pairs ψ_ℓ and φ_ℓ for $\ell = 1, 2, \ldots, N$ are given, i.e., if the stepped-frequency measurement data are available. Recording the frequency lines separately is advantageous with regard to the measurement accuracy, since the signal-to-noise ratio between the received power and the noise power is inversely proportional to the bandwidth of a single line.

The CubeSats follow their target asteroid in a polygonal plane which will be nearly perpendicular to the ecliptic of the solar system. The signals will be transmitted and captured via the two half-wavelength dipole antennas which will be pointed towards the Sun during the measurement to suppress the effect of the solar radiation (Figure 1). In order to optimize the radar performance for the target NEA's interior structure, the spacecraft will be equipped with a camera so that an accurate optical surface model can be created.

B. Numerical Modeling

In this study, we validate the radar concept of DISCUS numerically using the publicly available surface model of the asteroid 1998 KY_{26} scaled to 550 m diameter. The center frequency and bandwidth of the radar measurement are assumed to be $f_c = 20$ MHz (wavelength $\lambda = 15$ m in vacuum) and $B \approx 2.4$ MHz, respectively. The essential model parameters and their values can be found in Table I. In the numerical simulation, we use a scalable unitless parameter presentation. The unitless values can be scaled to SI-units as shown in Table II.

The signal power P_{RX} (dB) received by the radar is estimated via the equation

$$P_{RX} = P_{TX} + G_{TX} + S + G_{RX}, \tag{2}$$

where $P_{TX} = 0$ dB is the power transmitted, $G_{TX} = G_{RX} = 2.15$ dBi (1.64) follows from the gain of the half-wavelength dipole antenna and S is the signal power at the receiver location obtained through an isotropic radiator model, i.e., with an isotropic source and effective antenna aperture $A_{eff} = \lambda^2/(4\pi)$.

In the stepped frequency measurement, the bandwidth of a single frequency line is given approximately by $B_\ell = 1/T_\ell$, where T_ℓ is the pulse duration. We assume that the data is collected at a 5 km distance to the target asteroid. The duration of a single line is set to be $T_\ell = 32$ μs, i.e., 96 % of the signal travel-time, in order to minimize the corresponding bandwidth (here $B_\ell = 31$ kHz) and, thereby, also the relative amplitude of the measurement noise.

1) Permittivity and Conductivity: The present inverse problem of the CRT is to reconstruct the target asteroid's internal dielectric permittivity distribution ε_r which contains, in this study, a 40 m surface layer (e.g. dust or sand) with $\varepsilon_r = 3$ and three 60–100 m interior voids with $\varepsilon_r = 1$ (vacuum), respectively. Otherwise, ε_r is assumed to be 4, which is typical, e.g., for Kaolinite and Dunite [39].

The motivation for using this synthetic and relatively simple permittivity distribution was to enable validating the current far-field inversion approach both for the surface and deep interior structures with an exact measure for the inversion accuracy. The size of the details is mainly determined by the estimated tomography resolution. According to the recent studies, macroporosity structures of the present size and permittivity range can exist in rubble pile asteroids [19], [26].

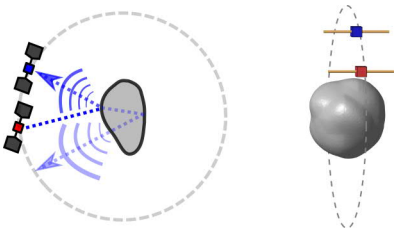

Fig. 1. **Left:** A bistatic measurement approach is used, since the scattering waves can be headed away from the transmitter spacecraft. One spacecraft (red) is utilized to both transmit and receive the signal. The other one (blue) serves as an additional receiver. **Right:** The spacecraft are assumed to orbit their target asteroid in a plane which will be nearly perpendicular to the ecliptic of the solar system. Each spacecraft is equipped with a single half wavelength dipole antenna (yellow) which will be pointed towards the Sun during the measurement in order to suppress the effect of the solar radiation. That is, the Sun is assumed to be located in the direction of the normal of the orbiting plane.

The electrical conductivity distribution inside the asteroid was assumed to be an unknown nuisance parameter, i.e., not of primary interest. It was set to be $\sigma = 5\varepsilon_r$ matching roughly to 3E-5 S/m and a loss rate of around 25 dB/km which is typical, e.g., for porous basalt (pyroxene) [37], [38]. Outside the asteroid the σ was assumed to be zero.

2) Measurements: The data are simulated for 128 measurement points (Figure 2) evenly distributed on an origin centric sphere. The angle ω between the asteroid spin and the normal of the orbiting plane determines the coverage of the measurements. We investigate the following three different cases (A) $\omega = 90^\circ$, (B) $\omega = 30^\circ$ and (C) $\omega = 10^\circ$. In (A), a full-angle dataset can be recorded, meaning that the spacecraft will form a dense network of points enclosing the whole asteroid. The limited-angle cases (B) and (C), include an aperture of $90^\circ - \omega$ around the spin axis.

The following two measurement approaches were compared:

1) *Monostatic measurement*. A single spacecraft both transmits and receives the signal. The measurement is made each time at the point of the transmission. The total number of measurement positions is 128, 64, and 24 for (A), (B) and (C), respectively.
2) *Bistatic measurement*. Two spacecraft are used; one transmits the signal and both record the backscattered wave (Figure 1). Each measurement is made simultaneously at two different positions. The additional measurement is made at the point closest to 25 degrees apart from the transmission location with respect to the asteroid's center of mass. The total number of transmission/measurement points is 128/256, 64/128 and 24/48 for (A), (B) and (C), respectively. In each case, the total number of unique measurement positions in the point set is the same as in the respective monostatic case.

C. Far-Field Forward Model for CRT

The forward problem of CRT is to predict the voltage of the antenna given the computation geometry and the unknown parameters. In this study, we model a sparse set of (simulated) measurements in

TABLE I

THE PRESENT NUMERICAL MODEL IN UNITLESS FORMAT AND SI-UNITS. THE SPATIAL PARAMETERS ARE ALSO GIVEN RELATIVE TO CENTER WAVELENGTH IN VACUUM ($\lambda = 15$ M). THE CONDUCTIVITY VALUE AND LOSS RATE OF POROUS BASALT CAN BE FOUND IN [37], [38]. HERE B IS AN ESTIMATE FOR THE RADAR BANDWIDTH WHICH ALLOWS TRANSMITTING THE SIGNAL PULSE WITH ERRORS BELOW -20 DB. CENTER FREQUENCY f_c IS USED IN THE CALCULATION OF THE ANTENNA APERTURE.

Item	Unitless	SI-units	Relative to λ
Asteroid diameter	0.262	550 m	36.7
Geometry scaling factor s	1	2100 m	140
Conductivity σ	20	2.5E-5 S/m	
Attenuation rate	52.5 dB/(unit length)	25 dB/km	
Orbiting distance	2.4	5 km	330
Void diameter	0.029–0.048	60–100 m	4–6.7
Dust layer thickness	0.019	40 m	2.7
Void ε_r	1	1	
Dust ε_r	3	3	
Body ε_r	4	4	
Final pulse duration after processing T_0	0.12	0.84 μs	
Radar bandwidth $B \approx 2/T_0$	16.7 1/(unit time)	2.4 MHz	
Center frequency f_c	140	20 MHz	
Center wavelength in vacuum λ	7.1E-2	15 m	1
Final data duration after processing T	0.7	5.0 μs	
Frequency line duration T_ℓ	4.5	32 μs	
Frequency line bandwidth B_ℓ	0.217 1/(unit time)	31 kHz	

TABLE II

FORMULAS FOR SCALING BETWEEN THE UNITLESS AND SI-UNIT EXPRESSIONS. IN THESE, THE PERMITTIVITY AND MAGNETIC PERMEABILITY OF THE VACUUM ARE GIVEN BY $\varepsilon_0 = 8.85 \cdot 10^{-12}$ F/M, AND $\mu_0 = 4\pi \cdot 10^{-7}$ H/M, RESPECTIVELY, AND s (METERS) DENOTES THE SPATIAL SCALING FACTOR.

Item	Unitless	SI-units
Dielectric permittitivity	ε_r	ε_r
Electrical conductivity	σ	$(\mu_0/\varepsilon_0)^{-1/2} s^{-1} \sigma$
Position	$\vec{x}$	$s\vec{x}$
Time	t	$(\varepsilon_0\mu_0)^{1/2} st$
Frequency	t^{-1}	$(\varepsilon_0\mu_0)^{-1/2} s^{-1} t^{-1}$
Velocity ($\mathsf{c} = \varepsilon_r$)	c	$(\varepsilon_0\mu_0)^{-1/2}\mathsf{c}$

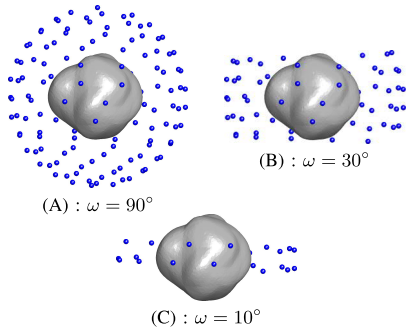

Fig. 2. A schematic (non-scaled) illustration showing the sparse full-angle configuration (A) of 128 measurement points (left) and two sparse limited-angle configurations (B) and (C) of 64 and 24 points (right), respectively. The angle ω between the orbiting plane normal and the asteroid spin is 90, 30 and 15 degrees. The limited-angle configurations results in a pronounced aperture around the polar regions in (C).

the spatio-temporal domain $[0,T]\times\Omega$ applying the wave propagation model presented in Appendix.

1) Weak form: The signal transmission at point $\vec{p}$ is modeled as a point source of the form

$$\frac{\partial \vec{f}}{\partial t}(t,\vec{x}) = \frac{\partial \vec{h}}{\partial t}(t)\,\delta(\vec{x}-\vec{p}) \quad \text{with} \quad h(0) = \frac{\partial \vec{h}}{\partial t}(0) = 0, \tag{3}$$

where $\vec{h}$ denotes the dependence of $\vec{f}$ on time and $\delta(\vec{x}-\vec{p})$ is the Dirac's delta function satisfying $\int q(\vec{x})\delta(\vec{x}-\vec{p})\,dV = q(\vec{p})$ for any sufficiently regular function q. Physically $\vec{f}$ can be interpreted as the current density of the antenna (Appendix).

The i-th component $E = E_i$ electric field $\vec{E} = E_i$ evoked by $\vec{f}$ satisfies the following weak form:

$$a(E, \mathbf{g}; \mathbf{w}; \Omega) = 0, \tag{4}$$

$$b(E, \mathbf{g}; v; \Omega) = -\langle f, v; \Omega\rangle \tag{5}$$

where $\mathbf{g} = (\vec{g}^{(1)}, \vec{g}^{(2)}, \vec{g}^{(3)})$ with $g^{\vec{(j)}} = \int_0^t \nabla E_i(\tau,\vec{x})\,d\tau$ for $j = 1,2,3$ and $\langle f, v; \Omega\rangle = \int_\Omega f v\,\mathrm{d}V$. The bilinear forms a and b correspond to the right-hand sides of the equations (34) and (35), respectively, and $v \in H^1(\Omega)$, $\mathbf{w} = (\vec{w}^{(1)}, \vec{w}^{(2)}, \vec{w}^{(3)})$ with $\vec{w}^{(i)} \in [L_2(\Omega)]^3$ are test functions. Under regular enough initial conditions this weak form [3] has a unique solution $E : [0,T] \to H^1(\Omega)$ [40].

For modeling the far-field, we assume that the domain Ω consists of two sub-domains: an outer part Ω_1 and an enclosed ball Ω_2 containing the target asteroid. The spherical inner boundary is denoted with $\mathcal{S} = \Omega_1 \cap \Omega_2$ (Figure 3). The spacecraft position $\vec{p}$ is assumed to be located outside Ω.

2) Incident and Scattered Field: The total field E is expressed as the sum of the incident and scattered field, i.e., $E = E_\mathrm{I} + E_\mathrm{S}$, where the incident field E_I emanates from the source and vanishes in the interior of Ω_2, that is, in $\Omega_2 \setminus \mathcal{S}$. The scattered field E_S is the total field in Ω_2, and its restriction to the surface $\mathcal{S}$ is utilized in calculating the measured far-field. The incident field E_I satisfies the following weak form in Ω_1:

$$a(E_\mathrm{I}, \mathbf{g}_\mathrm{I}; \mathbf{w}; \Omega_1) = 0, \tag{6}$$

$$b(E_\mathrm{I}, \mathbf{g}_\mathrm{I}; v; \Omega_1) = -\langle f, v; \Omega_1\rangle + \langle \mathbf{g}_\mathrm{I}, v; \mathcal{S}\rangle, \tag{7}$$

in which

$$\langle \mathbf{g}_\mathrm{I}, v; \mathcal{S}\rangle = \int_\mathrm{S} (\vec{g}_\mathrm{I}\cdot\vec{n}) v\,\mathrm{d}S \tag{8}$$

with $\vec{g}_\mathrm{I} = \int_0^t \nabla E_\mathrm{I}(\tau,\vec{x})\,d\tau$. The inner product $\langle \mathbf{g}_\mathrm{I}, v; \mathcal{S}\rangle$ corresponds to the nonzero surface term in the integral

$$\int_{\Omega_i} (\nabla\cdot\vec{g}_\mathrm{I})\,v\,dV = (-1)^i \int_\mathrm{S} (\vec{g}_\mathrm{I}\cdot\vec{n}) v\,\mathrm{d}S - \int_{\Omega_i} \vec{g}_\mathrm{I}\cdot\nabla v\,\mathrm{d}V, \tag{9}$$

where $\vec{n}$ denotes the outward unit normal of $\mathcal{S}$ and $j = 1,2$. For the scattered field E_S, it holds $E_\mathrm{S} = E - E_\mathrm{I}$. Thus, its weak form in Ω_i for $i = 1,2$ can be obtained by subtracting both sides of (6), (7)

from (4), (5) written for Ω_1 and Ω_2, respectively, taking into account that $\langle f, v; \Omega_2\rangle_2 = 0$ and that the incident field vanishes in $\Omega_2 \setminus \mathcal{S}$. It follows that

$$a(E_{\mathtt{S}}, \mathbf{g}_{\mathtt{S}}; \mathbf{w}; \Omega_i) \;=\; 0, \tag{10}$$

$$b(E_{\mathtt{S}}, \mathbf{g}_{\mathtt{S}}; v; \Omega_i) \;=\; -\langle \mathbf{g}_{\mathtt{I}}, v; \mathcal{S}\rangle \tag{11}$$

for $i = 1, 2$. Summing both sides of (10), (11) for Ω_1 and Ω_2 together leads to the following full domain weak form for the scattered field:

$$a(E_{\mathtt{S}}, \mathbf{g}_{\mathtt{S}}; \mathbf{w}; \Omega) \;=\; 0, \tag{12}$$

$$b(E_{\mathtt{S}}, \mathbf{g}_{\mathtt{S}}; v; \Omega) \;=\; -2\,\langle \mathbf{g}_{\mathtt{I}}, v; \mathcal{S}\rangle. \tag{13}$$

This formulation is otherwise similar to (4)–(5), but instead of a single point, the source function $\mathbf{g}_{\mathtt{I}}$ is evaluated on the sphere $\mathcal{S}$.

3) Incident Far-Field: In empty space ($\varepsilon_r = 1$ and $\sigma = 0$), the incident field for a monopolar (isotropic) point source (3) placed at $\vec{p}$ can be expressed as the following convolution:

$$E_{\mathtt{I}} = -\mathcal{G} *_\tau \frac{\partial h}{\partial t} = -\frac{1}{4\pi|\vec{x}-\vec{p}|}\left[\frac{\partial h}{\partial t}\right], \tag{14}$$

where $h *_\tau k(t, \vec{x}) = \int_0^\infty h(t-\tau, \vec{x})k(\tau, \vec{x})\,d\tau$, $[\partial h/\partial t]$ is a retarded signal evaluated at $t - |\vec{x}-\vec{p}|$ and $\mathcal{G} = \delta(t - |\vec{x}-\vec{p}|)/(4\pi|\vec{x}-\vec{p}|)$ is a Green's function with δ denoting the Dirac's delta function defined with respect to time. That is, $h(t, \vec{x}) = \int_0^\infty h(t-\tau, \vec{x})\delta(\tau)\,d\tau$ for any sufficiently regular h. It follows from (14) through a straightforward calculation that

$$\nabla E_{\mathtt{I}} = \frac{(\vec{x}-\vec{p})}{4\pi|\vec{x}-\vec{p}|^3}\left[\frac{\partial h}{\partial t}\right] + \frac{(\vec{x}-\vec{p})}{4\pi|\vec{x}-\vec{p}|^2}\left[\frac{\partial^2 h}{\partial t^2}\right] \tag{15}$$

$$\vec{g}_{\mathtt{I}} = \int_0^t \nabla E_{\mathtt{I}} d\tau = \frac{\vec{x}-\vec{p}}{4\pi|\vec{x}-\vec{p}|^3}[h] + \frac{\vec{x}-\vec{p}}{4\pi|\vec{x}-\vec{p}|^2}\left[\frac{\partial h}{\partial t}\right]. \tag{16}$$

The incident field $E_{\mathtt{I}}$ needs to be evaluated only on its first arrival at $\mathcal{S}$, that is, in the subset $\mathcal{S}^- = \{\vec{x} \in \mathcal{S} \,|\, (\vec{x}-\vec{p})\cdot\vec{n} < 0\}$. In the remaining part $\mathcal{S}^+ = \mathcal{S} \setminus \mathcal{S}^-$, $E_{\mathtt{I}}$ is set to be zero. Hence, it follows that $\langle \vec{g}_{\mathtt{I}}, v; \mathcal{S}^-\rangle = \langle \vec{g}_{\mathtt{I}}, v; \mathcal{S}\rangle$ with

$$\langle \vec{g}_{\mathtt{I}}, v; \mathcal{S}^-\rangle = \int_{\mathcal{S}^-}\left(\frac{(\vec{x}-\vec{p})\cdot\vec{n}}{4\pi|\vec{x}-\vec{p}|^3}[h] + \frac{(\vec{x}-\vec{p})\cdot\vec{n}}{4\pi|\vec{x}-\vec{p}|^2}\left[\frac{\partial h}{\partial t}\right]\right) v\,\mathrm{d}S. \tag{17}$$

This can be verified by extending the surface $\mathcal{S}^-$ with the tangent cone of $\mathcal{S}$ which intersects $\vec{p}$, and further with a $\vec{p}$-centric sphere with a radius larger than T. For the resulting surface $\mathcal{C}$, it holds that $\langle \vec{g}_{\mathtt{I}}, v; \mathcal{C}\rangle = \langle \vec{g}_{\mathtt{I}}, v; \mathcal{S}^-\rangle$. Namely, the integrand in (17) is zero on the tangent cone and within the distance $> T$ from $\vec{p}$ the incident wave is zero for $t \in [0, T]$.

4) Scattered Far-Field: Following from the Green's integral identities [41], the empty space ($\varepsilon_r = 1, \sigma = 0$) wave radiating out of $\mathcal{S}$ satisfies the following Kirchhoff integral equation, which we utilize to extrapolate the scattered far-field (total field) at $\vec{p}$:

$$E(\vec{p}) \;=\; \int_{\mathcal{S}}[E_{\mathcal{S}}]\frac{\partial \mathcal{G}}{\partial \vec{n}}\,\mathrm{d}S - \int_{\mathtt{S}}\mathcal{G}\left[\frac{\partial E_{\mathcal{S}}}{\partial \vec{n}}\right]\mathrm{d}S \tag{18}$$

$$= -\frac{1}{4\pi}\int_{\mathtt{S}}\frac{(\vec{x}-\vec{p})\cdot\vec{n}}{|\vec{x}-\vec{p}|^2}\left(\frac{[E_{\mathcal{S}}]}{|\vec{x}-\vec{p}|} + \left[\frac{\partial E_{\mathcal{S}}}{\partial t}\right]\right)\mathrm{d}S$$

$$-\frac{1}{4\pi}\int_{\mathtt{S}}\frac{1}{|\vec{x}-\vec{p}|}\left[\frac{\partial E_{\mathcal{S}}}{\partial \vec{n}}\right]\mathrm{d}S. \tag{19}$$

D. Linearized Forward Model, Signal and Noise

We use the following linearized forward model [3] in which the point of linearization is a constant background permittivity $\varepsilon_r^{(\mathrm{bg})}$:

$$\mathbf{y} = \mathbf{L}\mathbf{x} + \mathbf{y}^{(\mathrm{bg})} + \mathbf{n}. \tag{20}$$

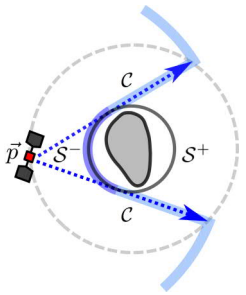

Fig. 3. The incident field needs to be evaluated only on its first arrival at $\mathcal{S}$ (dark gray circle), that is, on the subset $\mathcal{S}^- = \{\vec{x} \in \mathcal{S} \,|\, (\vec{x}-\vec{p})\cdot\vec{n} < 0\}$ (dark blue). On the remaining part $\mathcal{S}^+ = \mathcal{S} \setminus \mathcal{S}^-$, it is set to be zero. Surface $\mathcal{C}$ (dark and light blue) results from extending the surface $\mathcal{S}^-$ with the tangent cone (light blue) of $\mathcal{S}$ which intersects $\vec{p}$, and further with a $\vec{p}$-centric sphere with a radius larger than T. It holds that $\langle \vec{g}_{\mathtt{I}}, v; \mathcal{C}\rangle = \langle \vec{g}_{\mathtt{I}}, v; \mathcal{S}^-\rangle$. Namely, the integrand in (17) is zero on the tangent cone and within the distance $> T$ from $\vec{p}$ the incident wave is zero for $t \in [0, T]$.

The vectors $\mathbf{y}$ and $\mathbf{y}^{(\mathrm{bg})}$ contain the measured and simulated data for ε_r and $\varepsilon_r^{(\mathrm{bg})}$, respectively, $\mathbf{x}$ is the coordinate vector for ε_r, $\mathbf{L}$ denotes the Jacobian matrix resulting from the linearization, and $\mathbf{n}$ contains both the measurement and forward modeling errors.

A single Blackman-Harris window $h(t)$ [42], [43] is used as the signal pulse. That is,

$$h(t) = 0.359 \;-\; 0.488\cos\left(\frac{2\pi t}{T_0}\right) + \;0.141\cos\left(\frac{4\pi t}{T_0}\right) - 0.012\cos\left(\frac{6\pi t}{T_0}\right) \tag{21}$$

for $t \in [0, T_0]$ and $h(t) = 0$, otherwise. We choose $T_0 = 0.12$ as the final (unitless) pulse duration obtained after combining the frequency lines. For each measurement point, the received signal $\mathbf{y}$ is recorded for unitless time values 0.1–0.7, that is, 0.7–5.0 μs. The corresponding sampling rate is 15 MHz.

The present noise estimates are based on the targeted antenna specifications of the DISCUS mission concept. We assume that the measurement errors contained by $\mathbf{n}$ will be mainly caused by the galactic background noise and the Sun. At 20 MHz, the galactic noise can be estimated to be around 5E-20 W/(m^{2}Hz). The radiation from the Sun at a distance of 1 AU and 20 MHz is about 2E-19 W/(m^{2}Hz) and 2E-23 W/(m^{2}Hz) for its active and inactive (quiet) phase of sunspot activity, i.e., for surface temperatures 1E+10 and 1E+6 K, respectively [31], [44]. During the active phase, the Sun emits radio-frequency waves in time scales varying from seconds to hours. As the reference level for modeling inaccuracies, we use the observation that, in CONSERT [6], the peaks related to unpredictable echoes stayed mainly -20 dB below the main signal peak.

The total error $\mathbf{n}$ is assumed to be an independent Gaussian white noise term with standard deviation between -25 and 0 dB with respect to the maximal entry of the difference $|\mathbf{y} - \mathbf{y}^{(\mathrm{bg})}|$ between the measured and simulated signal. A Gaussian noise model is used, since $\mathbf{n}$ is expected to include both unknown forward and measurement errors, and as the sum of different independent and random error sources approaches a Gaussian distribution by the central limit theorem [45]. The measurement errors due to the spectral radiation flux density F [W/(m^{2}Hz)] of the galactic background and the Sun are approximated using this relative scale. We estimate the

relative standard deviation of the measurement noise with the formula

$$\sigma_m = \sqrt{\frac{FA_{\text{eff}}B_\ell}{P_{TX}}}, \tag{22}$$

i.e., it is the square root of the ratio between the absorbed noise and transmitted signal amplitude. With σ_m, the noise will have the desired average power given by F. As the antenna aperture, the standard approximation for the half-wavelength dipole antenna $A_{\text{eff}} = G\lambda^2/(4\pi)$ is used. The antenna of each spacecraft is assumed to be parallel to the orbiting plane normal and pointed towards the Sun during the measurements (Figure 1).

E. Inversion Process

In this study, the process of finding an estimate ε_r^* for the relative permittivity ε_r, the unknown of the inverse problem, consists of the following three stages presented in [3]:

1) *Forward Simulation*. For each transmission and/or measurement position, the signal can be propagated using the leap-frog iteration. A parallel computing cluster can be used, as the iteration is an independent process between different source points. In this study, altogether sixteen Nvidia Tesla P100 GPUs belonging to the *Narvi* cluster of Tampere University of Technology were used. Running the wave simulation for a single source position took about 71 and 184 minutes in the case of the background and exact data, respectively. The matrix–vector products including the inverse of the mass matrix [3] were evaluated using the preconditioned conjugate gradient method with the lumped diagonal preconditioner, i.e., a matrix with row sums on its diagonal. The system matrices required a total of about 4 GB memory of which the mass matrix took 0.62 GB. The total GPU memory consumption during the forward simulation was around 10 GB, since the transposed matrices were stored separately in the memory to speed up the matrix-vector products of the iteration.
2) *Linearization*. The forward model can be linearized in a coarse nested mesh [3] covering the asteroid which allows achieving an invertible system size. To speed up the parsing of the Jacobian matrix, the Tikhonov regularized deconvolution routine applied can be formulated as a pixelwise parallel algorithm. In the linearization stage, we applied a coarse mesh of 80000 tetrahedra. Running a parallelized 32-thread version of the parsing routine took 340 and 720 seconds for the monostatic and bistatic full-angle data in a Lenovo P910 workstation equipped with two Intel Xeon E5 2697A v4 2.6 GHz 16-core processors and 128 GB of RAM. The size of the resulting Jacobian matrix took 4.7 GB and 9.4 GB memory space, respectively.
3) *Reconstruction procedure*. The relative permittivity distribution can be reconstructed via the total variation (TV) regularized iteration presented in [3]. The reconstruction was found via one iteration step using the regularization parameter values $\alpha = 0.1$ and $\beta = 0.001$ [3]. The first one of these controls the overall regularization level and the second one the weighting ratio between the TV and norm-based regularization (the larger the value the more weight on the norm). To invert the regularized system matrix, we applied the conjugate gradient method with the stopping criterion 1E-5 for the relative residual norm. Computing a single reconstruction in the P910 workstation required around 500 and 400 conjugate gradient steps for the monostatic and bistatic full-angle system. The computation time was 100 and 170 seconds, respectively.

1) Inversion Accuracy: The accuracy of the estimate ε_r^* obtained is measured using the relative overlap and value error (ROE and RVE), that is, the percentages

$$\text{ROE} \;=\; 100\left(1 - \frac{\text{Volume}(\mathbf{T}\cap\mathbf{V})}{\text{Volume}(\mathbf{S})}\right) \tag{23}$$

$$\text{RVE} \;=\; 100\left(1 - \left|\frac{\int_{\mathbf{T}}(\varepsilon_r^* - \varepsilon_r^{(\text{bg})})\,\mathrm{d}V}{\int_{\mathbf{T}}(\varepsilon_r - \varepsilon_r^{(\text{bg})})\,\mathrm{d}V}\right|\right). \tag{24}$$

where ε_r denotes the actual permittivity distribution and $\varepsilon_r^{(\text{bg})}$ is the background (initial guess). The set $\mathbf{S}$ is a region of interest (ROI) including both the surface layer and the voids and $\mathbf{V} = \mathbf{S}\cap\mathbf{R}$ denotes the overlap between the ROI and the set $\mathbf{R}$ in which a given reconstruction is smaller than a limit such that $\text{Volume}(\mathbf{R}) = \text{Volume}(\mathbf{S})$. Examples of the set $\mathbf{V}$ are illustrated in Figure 8. The target set $\mathbf{T}$ refers to (1) the full ROI, i.e., $\mathbf{T} = \mathbf{S}$, (2) its surface part or (3) voids.

F. Discretization

The spatial domain was discretized as presented in [3] and Appendix, using an unstructured tetrahedral mesh with accurate interior surfaces for all the modeled structures including the asteroid and the sphere $\mathcal{S}$. The fields $\vec{E}$ and $g^{(i)}$, $i = 1, 2, 3$ were discretized using piecewise linear and (element-wise) constant finite element basis functions, respectively. The temporal interval $[0, T]$ was divided into regular subintervals. The leap-frog based finite element time-domain algorithm (FETD) [46]–[48] presented in [3] was utilized to obtain the fields and their linearizations. The scattered far-field for the source (3) was simulated as follows:

1) Calculate the incident far-field on the surface $\mathcal{S}^-$
2) Solve the weak form (12)–(13).
3) Extrapolate the scattered far-field via the restriction of E_{S} to $\mathcal{S}$.

The surface integral terms of (8) and (18)–(19) were evaluated over the triangulated surface of $\mathcal{S}$ using the one point (barycenter) quadrature rule. In order to prevent numerical noise due to non-smoothness of the incident field at the boundary between $\mathcal{S}^-$ and $\mathcal{S}^+$, the following smoothed approximation for $\langle \vec{g}_{\text{I}}, v; \mathcal{S}\rangle$ was applied:

$$\langle \vec{g}_{\text{I}}, v; \mathcal{S}\rangle \approx \int_{\mathcal{S}^-} (\vec{g}_{\text{I}}\cdot\vec{n})v\,\mathrm{d}S + \int_{\mathcal{S}^+} (\vec{g}_{\text{I}}\cdot\vec{n})v\exp\left(\frac{-\gamma(\vec{x}-\vec{p})\cdot\vec{n}}{1-(\vec{x}-\vec{p})\cdot\vec{n}}\right)\mathrm{d}S \tag{25}$$

with the parameter $\gamma = 10$ determining the decay rate for the second term. The shortest distance between $\vec{p}$ and $\mathcal{S}$ was utilized as a time shift to cancel out the signal travel-time between $\vec{p}$ and $\mathcal{S}$ in the simulated data sequence in a systematic way.

1) Domain: The present test domain $\Omega = \Omega_1 \cup \Omega_2$, is an origin centric cube (Figure 4). The interior of the sphere $\mathcal{S}$ centered at origin formed the subdomain Ω_2 the exterior of which Ω_1 contained a split-field perfectly matched layer [3], [47] to simulate open field scattering. As the target, we utilized the surface model of asteroid 1998 KY_{26} which can be associated through scaling with a rubble pile asteroid (Table I).

Two different conforming tetrahedral finite element meshes were used for simulating background and exact data, i.e., $\mathbf{y}^{(\text{bg})}$ and $\mathbf{y}$, respectively. Each one consisted of a total of 14.9 M elements of which 5.3 M were contained by the asteroid. All the surfaces present in the model were modeled accurately as triangular finite element mesh boundaries. The interior structure was homogeneous in the case of the background. The exact model included the following inhomogeneities to be reconstructed: (i) a surface layer together and (ii) three deep interior anomalies. Two different meshes were applied in order to avoid overly good data fit, i.e., the *inverse crime* [49].

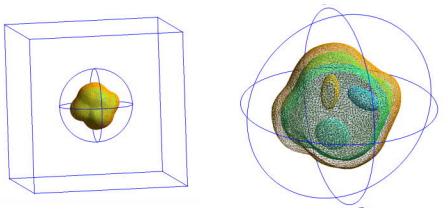

Fig. 4. The present test domain $\Omega = \Omega_1 \cup \Omega_2$ (left) is an origin centric cube. The interior of the sphere $\mathcal{S}$ centered at origin formed the subdomain Ω_2 (right) the exterior of which Ω_1 contained a split-field perfectly matched layer [3], [47] to simulate open field scattering. As the test target, we utilized the surface model (12260 triangles) of asteroid 1998 KY_{26} which can be associated through scaling with a 550 m (36.7 relative to λ) diameter asteroid (Table I). The volumetric finite element discretization used in the reconstruction procedure was created based on the multi-layer surface mesh model illustrated in the pictures.

TABLE III

ROE AND RVE FOR RECONSTRUCTIONS **(i)**, **(ii)** AND **(iii)** OBTAINED WITH BISTATIC DATA, TOTAL NOISE OF -15 DB AND CONFIGURATIONS (A), (B) AND (C), RESPECTIVELY (FIGURE 8). THE VALUES HAVE BEEN CALCULATED SEPARATELY FOR THE TOTAL ROI **S** AND FOR ITS INTERSECTION WITH THE SURFACE LAYER AND VOIDS.

Rec.	Conf.	Measure	Total (%)	Surface (%)	Deep (%)
(i)	(A)	ROE	33	34	21
		RVE	22	5	48
(ii)	(B)	ROE	39	41	20
		RVE	34	27	57
(iii)	(C)	ROE	45	45	46
		RVE	62	55	85

The wave was propagated from zero time to the (unitless) value $T = 0.7$ (5.0 μs) using the FETD method. As the time increment for the background and exact asteroid mesh we employed the (unitless) values $\Delta t =$ 1E-4 and $\Delta t =$ 3.7E-5, respectively.

III. RESULTS

The mathematical far-field model introduced in this paper was found to perform adequately for the test asteroid model with different levels of the total noise. The results have been included in Figures 5–8 and Tables III and IV.

Figures 5, 6 and 7 illustrate the ROE and RVE as a function of the total noise for the full ROI **S**, the surface layer and voids, respectively. At each investigated noise level, a sample of 30 different reconstructions, obtained with independent realizations of the total noise, has been visualized as a box plot bar. The overall error level can be observed to be elevated for the -5 and 0 dB total noise levels. In comparison between the monostatic and bistatic CRT, the latter was found to be more robust with respect to noise and limited-angle data.

Figure 8 visualizes reconstructions **(i)**, **(ii)** and **(iii)** obtained with the total noise level -15 dB, bistatic data and configurations (A), (B) and (C), respectively. The errors of the limited-angle reconstructions **(ii)** and **(iii)**, are particularly concentrated around the z-axis, that is, around the aperture in the limited-angle measurement positions. In **(iii)**, they are also notably more spread than in **(ii)**. Table III includes the ROE and RVE for **(i)**, **(ii)** and **(iii)** calculated separately for the full ROI **S** and for its intersection with the surface layer and the deep part (voids).

Table IV includes the relative signal amplitudes and noise levels for bistatic measurement. Both galactic noise and the upper estimate for the Solar radiation (active Sun) were observed to stay at a tolerable level with median peak levels of -14 dB and -8 dB, respectively. The

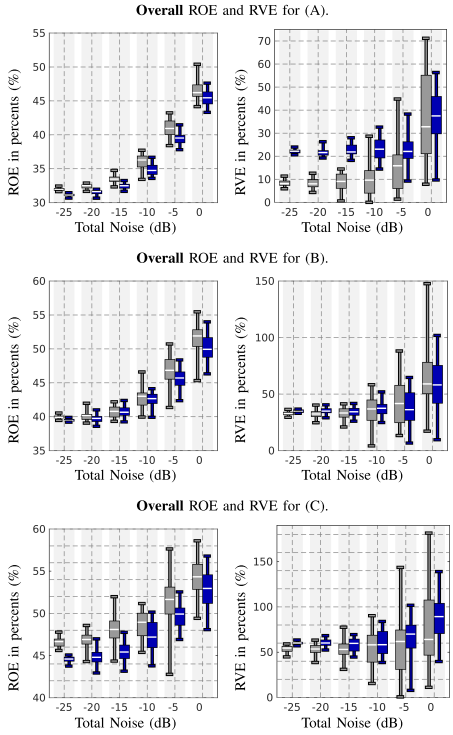

Fig. 5. The **overall** relative overlap and value error (ROE and RVE) in percents (%) in the full ROI **S** for cases A, B and C which are shown in Figure 2. The results for the monostatic and bistatic data correspond to the light grey and dark blue box plot bars, respectively. Each bar is based on a sample of 30 reconstructions obtained with independent realizations of the total noise vector. The narrow part visualizes the interval between the minimum and maximum value in the sample. The thick part is called the interquartile range (IQR) or spread, that is, the interval between the 25 % and 75 % quantile. The white line shows the median.

TABLE IV

THE MINIMUM, MAXIMUM AND MEDIAN VALUES (DB) OF THE RELATIVE SIGNAL AMPLITUDE AND MEASUREMENT NOISE STANDARD WITH RESPECT TO THE TRANSMITTED SIGNAL AND DEVIATION σ_m WITH RESPECT TO THE SIGNAL PEAK INTENSITY ESTIMATED FOR BISTATIC DATA IN THE SET OF THE SIMULATED SIGNALS.

	Source	Min	Max	Median
Relative signal amplitude		-136	-120	-130
Relative noise σ_m	Galactic	-24	-7	-14
	Active Sun	-18	-1	-8
	Quiet Sun	-58	-41	-48

lower Solar radiation estimate (quiet Sun) was below the investigated noise range with the median -48 dB.

IV. DISCUSSION

This paper introduced and validated a mathematical far-field model applicable in the Computed Radar Tomography (CRT) imaging [1], [2] of small solar system bodies (SSSBs). In particular, the Deep Interior Scanning CUbeSat (DISCUS) mission concept [14], [15] was examined as a potential application of this method. The numerical results obtained with the test asteroid model and the relative total noise range of -25–0 dB suggest that a sparse set of full-wave

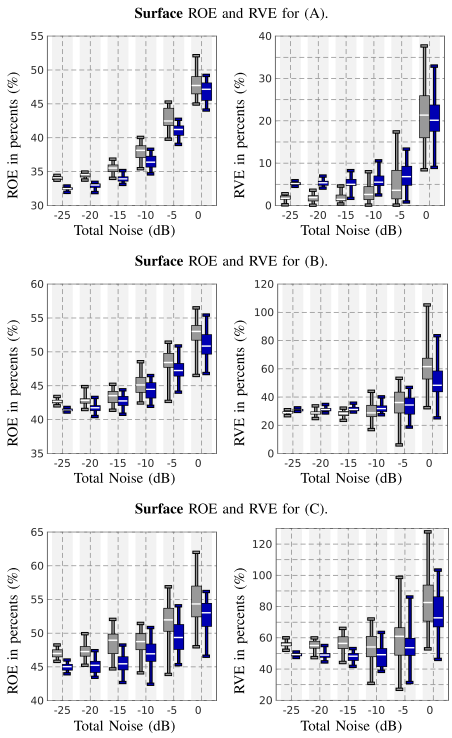

Fig. 6. The relative overlap and value error (ROE and RVE) in percents (%) for the **surface part** of ROI **S**. The results for the monostatic and bistatic data correspond to the light grey and dark blue box plot bars, respectively.

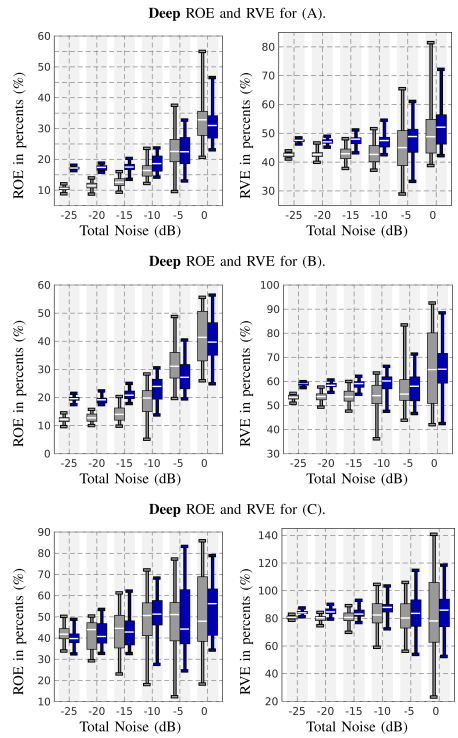

Fig. 7. The relative overlap and value error (ROE and RVE) in percents (%) for the **deep interior** part of ROI **S**. The results for the monostatic and bistatic data correspond to the light grey and dark blue box plot bars, respectively.

measurements can be inverted with the planned DISCUS mission specifications. A sufficient reconstruction accuracy was obtained with sparse full- and limited-angle data. Furthermore, the results suggest that a bistatic (dual spacecraft) measurement technique [16] with a fixed 25 degrees angle between the transmitter and receiver can improve the reliability of the inversion as compared to the monostatic (single spacecraft) approach.

In this study, the simulations were conducted for orbit radius of 5 km. The final orbit is determined by the spacecraft's Δv budget and orbit stability and is currently under investigation. Generally, the closer the approach the better is the signal-to-noise ratio of the measurements. We currently expect that a radius of about 5 km will be achievable by a CubeSat. For comparison, Rosetta orbited at around 10 km distance with its closest approach at about 4.5 km [6] but was limited mostly by the environment of the active comet 67P/Churyumov-Gerasimenko. The present results suggest that a deeper descent is not needed for detecting a surface dust layer and deep interior voids. It is noteworthy that performing close observations of SSSBs is a recent tendency in the planetary research. For example, during Rosetta's final descent its Osiris wide-angle camera took its final image at 20 m altitude [50], [51]. Another example is the ongoing Osiris-REx mission [9], [10] in which the goal is to achieve a 730 m orbiting distance and also to bring a sample of the regolith back to Earth. Moreover, advanced active control strategies for hovering in the vicinity of an SSSB have been developed [52], [53].

The present results suggest that an appropriate reconstruction quality can be achieved, if the standard deviation of the total noise is below -10 dB. Of the investigated sources of measurement errors [31], [44], the Sun's radiation during its active phase seems to exceed this limit for the 5 km orbiting distance which will need to be taken into account in the mission design. A natural way to reduce the noise would be to point the radar antennas towards the Sun. Namely, a dipole antenna is practically insensitive to radiation propagating along its axis. The galactic background noise, which cannot be reduced, seems to remain on an acceptable level with a median of around -14 dB. Other potential noise sources not investigated in this study include for example Jupiter's radiation the magnitude of which depends largely on the target asteroid's position in the solar system. Furthermore, it seems obvious that achieving a feasibly low measurement noise with the 10 W transmitting power applied in this study will, in practice, require applying the stepped-frequency technique [34]–[36] which allows dividing the total radar bandwidth and, thereby, also the noise, into narrow frequency lines.

The errors related to the forward modeling can be significant and require further research. In the CONSERT measurements, the unpredicted noise peaks were observed to stay mainly -20 dB below the actual signal peak, suggesting that also those errors remain tolerable. Akin to [54], the echo reflecting from the surface opposite to the spacecraft was found to be noisy. Achieving the best possible reconstruction quality necessitated excluding this echo from the measurement data. That is, the recorded time interval had to be

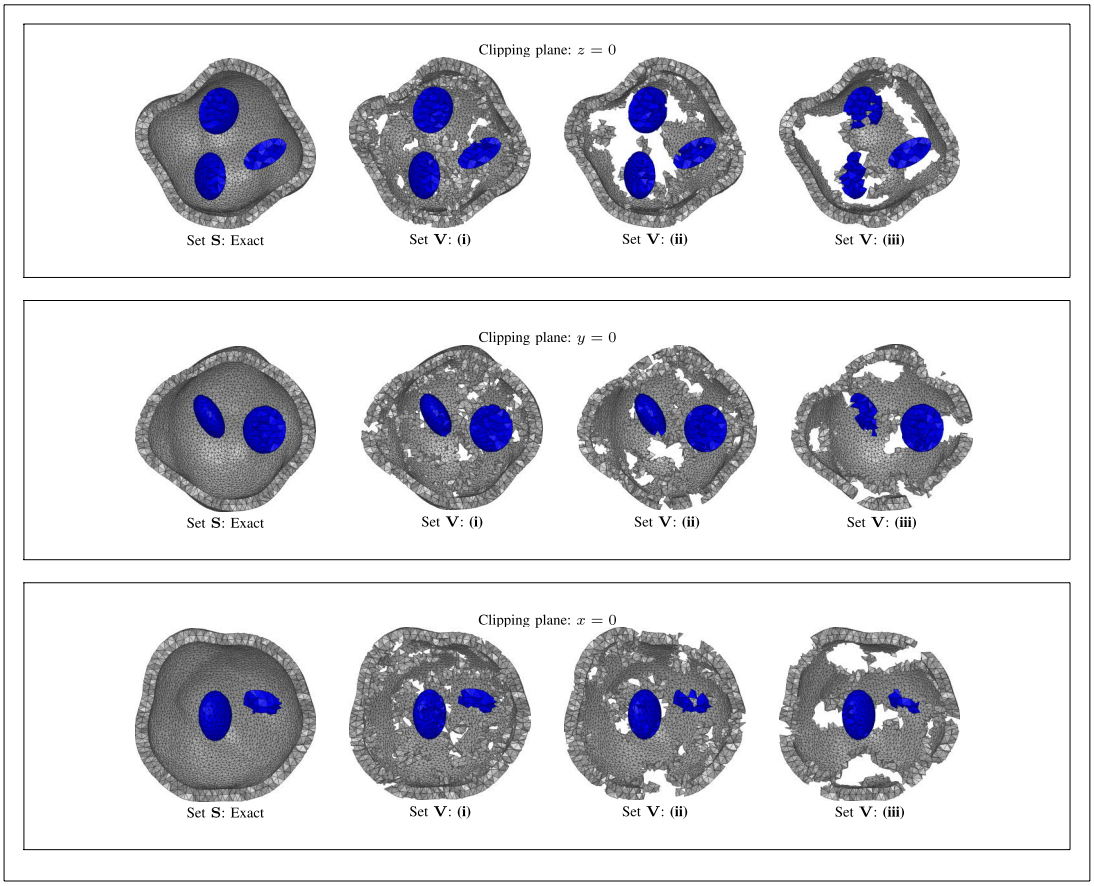

Fig. 8. A visual comparison of the reconstructions **(i)**, **(ii)** and **(iii)** obtained, respectively, with configurations (A), (B) and (C) using bistatic data and total noise with the relative standard deviation of -15 dB. On each row, the left image illustrates the ROI $\mathbf{S}$ (Section II-E1) containing the exact surface dust layer (grey) and voids (blue). That is, the grey and blue area mark the overlap obtained for the dust layer and voids, respectively. The other images present, the overlap set $\mathbf{V}$, i.e., the relative overlap between the exact permittivity distribution and the reconstruction (Section II-E1). The diameter of the asteroid is here 550 m (36.7 relative to λ).

limited to 5.0 μs.

Based on the comparison between the full- and limited-angle tomography results, it seems that the interior structure can be reconstructed, if targeted NEA has a typical spin without the need to alter the orbiting plane of the spacecraft which greatly simplifies operations. Namely, the spin latitude is close to -90 degrees for a large majority of the small NEAs [55], suggesting that a better measurement coverage than in the 30 degrees limited-angle test can be achieved.

The bistatic CRT was found to an essential way to improve the inversion reliability as compared to the monostatic approach. The advantage of the bistatic measurement was observed to be particularly emphasized for a high total noise level and sparse limited-angle observation both of which are potential scenarios for a space mission. Hence, we propose that maximizing the reliability of the data requires measurements between two spacecraft in addition to recording the backscattering data at the point of transmission.

In this study, the smallest (low-noise) ROE and RVE were in some cases obtained with the monostatic approach. This was obviously due to the larger polarization shift in the signal captured by the second spacecraft, following from the non-direct reflection. Consequently, spacecraft positioning can have a major effect on the signal quality. The present choice for the distance between the transmitter and receiver is based on our preliminary numerical tests using the test asteroid model. Further optimization can be done in the future.

The current computational implementation is scalable and allows using any asteroid geometry. In a three-dimensional spatial scaling, the system matrix size is roughly proportional to $(s_1/s_0)^3$, where s_0 and s_1 denote the scaling factors of the original and scaled domain. With the current measurement setting, the system size would be approximately 64 GB, for the diameter of 1100 m, i.e., two times the current one. The 0.62 GB mass matrix of the current system would be of the size 10 GB for the scaled one. A system size of 64 GB is feasible regarding an implementation in a computation cluster. If the cluster nodes are equipped with a GPU with more than 10 GB memory, then the mass matrix can be inverted rapidly in the GPU

which, due to its parallel computing capabilities, may be assumed to provide a faster solution for sparse matrix–vector multiplication than the central processing unit.

Based on the diameter distribution of the NEAs [56], [57], the range of potential target diameters for DISCUS extends to at least 1000 m above which the distribution decays. For a target diameter significantly larger than 1000 m, it might be reasonable to limit the imaging to some *a priori* estimated depth estimated, e.g., based on maximal observed signal penetration. If necessary, it is also possible to compress the memory consumption by replacing some of the matrices with matrix-free functions returning a given matrix–vector product. Also methodological development can be considered. For example, the discontinuous Galerkin time-domain method can be compared to the current finite element time-domain implementation [58], [59] and the leap-frog iteration can be replaced with the well-known Runge-Kutta algorithm.

The reconstruction of interior structures containing less contrast than the structure analyzed in this study might also prove more difficult, and the existence of multiple scattering surfaces in the interior might increase the signal to noise required for a good reconstruction. It is therefore planned to assess the reconstruction of more complex interior structures, as for example an interior filled with spherical monolithic fragments following a power law size distribution as motivated in [23], [24].

An ongoing future work is to verify the current results for a carefully simulated orbit. Additionally, the effect of the polarization and sparse limited-angle data on the reconstruction quality will be studied further. An asteroid flyby can be considered as an alternative way to do tomographic measurements. Based on this study, achieving a sufficient signal-to-noise ratio might be challenging for a flyby, since flybys are usually made in the range of 1000 km. For example, the closest point of Rosetta's flyby at the asteroids Lutetia and Steins was 3170 km and 800 km [60], [61], respectively. On the contrary, CRT seems to require an extremely close 5 km rendezvous. Therefore, to achieve a reasonable signal to noise level during a flyby mission, concepts of very close flyby configurations with low relative velocity have to be developed.

Acknowledgements

MT, MK and SP were supported by the AoF Centre of Excellence in Inverse Problems. MT and SP were funded by the Academy of Finland Key Project number 305055. PB, JD and EV were supported by the Max Planck Institute for Solar System Research. Special thanks to Juha Herrala and Kari Suomela for support in computing resources.

Appendix

The present wave equation and its weak form can be derived from the (unitless) Maxwell's equations

$$\nabla \cdot \varepsilon_r \vec{E} = 0 \tag{26}$$

$$\nabla \cdot \vec{B} = 0 \tag{27}$$

$$\nabla \times \vec{E} = -\frac{\partial \vec{B}}{\partial t} \tag{28}$$

$$\nabla \times \vec{B} = \vec{J} + \varepsilon_r \frac{\partial \vec{E}}{\partial t} \tag{29}$$

in which $\vec{E}$ and $\vec{B}$ denote the electric and magnetic field, respectively, and $\vec{J} = \sigma\vec{E} + \vec{f}$ is the total current density with $\vec{f}$ denoting the current density of the antenna. The curl of the third equation (28) can be written as

$$\nabla \times \nabla \times \vec{E} = \nabla(\nabla \cdot \vec{E}) - \nabla^2 \vec{E} = -\sigma \frac{\partial \vec{E}}{\partial t} - \varepsilon_r \frac{\partial^2 \vec{E}}{\partial t^2} - \frac{\partial \vec{f}}{\partial t}. \tag{30}$$

Expressing the electric field and the position vector in the component-wise form, i.e., $\vec{E} = (E_1, E_2, E_3)$ and $\vec{x} = (x_1, x_2, x_3)$, respectively, one obtains the following general form of the present wave propagation model:

$$\varepsilon_r \frac{\partial^2 E_i}{\partial t^2} + \sigma \frac{\partial E_i}{\partial t} - \sum_{j=1}^{3} \frac{\partial^2 E_i}{\partial x_j^2} + \frac{\partial}{\partial x_i} \sum_{j=1}^{3} \frac{\partial E_j}{\partial x_j} = -\frac{\partial f_i}{\partial t}. \tag{31}$$

The first-order formulation of this equation is given by

$$\frac{\partial g_j^{(i)}}{\partial t} - \frac{\partial E_i}{\partial x_j} = 0, \tag{32}$$

$$\varepsilon_r \frac{\partial E_i}{\partial t} + \sigma E_i - \sum_{j=1}^{3} \frac{\partial g_j^{(i)}}{\partial x_j} + \frac{\partial}{\partial x_i} \sum_{j=1}^{3} g_j^{(j)} = -f_i, \tag{33}$$

in which the first equation holds for $i = 1, 2, 3$ and the second one for $i, j = 1, 2, 3$. The entries of the vectors $\vec{g}^{(1)}, \vec{g}^{(2)}$ and $\vec{g}^{(3)}$ are given by $g_j^{(i)} = \int_0^t \frac{\partial E_i}{\partial x_j}(\tau, \vec{x})\, d\tau$ for $j = 1, 2, 3$. Multiplying the first and the second equation of (32) by the test functions $\vec{w}^{(i)} \in [L_2(\Omega)]^3$ and $v_i \in H^1(\Omega)$, respectively, and integrating by parts yields the system

$$\begin{aligned} 0 = \frac{\partial}{\partial t} \sum_{j=1}^{3} \int_\Omega \vec{g}_j^{(i)} w_j^{(i)}\, \mathrm{d}V \\ - \sum_{j=1}^{3} \int_\Omega w_j^{(i)} \frac{\partial E_i}{\partial x_j}\, \mathrm{d}V, \end{aligned} \tag{34}$$

$$\begin{aligned} -\int_\Omega f_i v_i\, \mathrm{d}V = \frac{\partial}{\partial t} \int_\Omega \varepsilon_r\, E_i\, v_i\, \mathrm{d}V + \int_\Omega \sigma\, E_i\, v_i\, \mathrm{d}V \\ + \sum_{j=1}^{3} \int_\Omega g_j^{(i)} \frac{\partial v_i}{\partial x_j}\, \mathrm{d}V \\ - \sum_{j=1}^{3} \int_\Omega g_j^{(j)} \frac{\partial v_i}{\partial x_i}\, \mathrm{d}V. \end{aligned} \tag{35}$$

This system can be discretized via the approach presented in the two-dimensional study [3]. Using the notation of [3], the last right-hand side term affecting the polarization of the wave, absent in the 2D case, is of the form $-\mathbf{B}^{(i)^T} \sum_{j=1}^{3} \mathbf{q}_k^{(k)}$, where $\mathbf{q}_j^{(i)}$ denotes the coordinate vector of $g_i^{(j)}$.

References

[1] R. Persico, *Introduction to ground penetrating radar: inverse scattering and data processing*. John Wiley & Sons, 2014.

[2] A. J. Devaney, *Mathematical foundations of imaging, tomography and wavefield inversion*. Cambridge University Press, 2012.

[3] S. Pursiainen and M. Kaasalainen, "Orbiter-to-orbiter tomography: a potential approach for small solar system bodies," *IEEE Transactions on Aerospace and Electronic Systems*, vol. 52, no. 6, pp. 2747–2759, 2016.

[4] H. Su, F. Xu, S. Lu, and Y.-Q. Jin, "Iterative ADMM for inverse FE–BI problem: A potential solution to radio tomography of asteroids," *IEEE Transactions on Geoscience and Remote Sensing*, vol. 54, no. 9, pp. 5226–5238, 2016.

[5] A. Herique and V. Ciarletti, "A Direct Observation of the Asteroid's Structure from Deep Interior to Regolith: Two Radars on the AIM Mission," in *47th Lunar and Planetary Science Conference*, 2016, p. 2096.

[6] W. Kofman, A. Herique, Y. Barbin, J.-P. Barriot, V. Ciarletti, S. Clifford, P. Edenhofer, C. Elachi, C. Eyraud, J.-P. Goutail, E. Heggy, L. Jorda, J. Lasue, A.-C. Levasseur-Regourd, E. Nielsen, P. Pasquero, F. Preusker, P. Puget, D. Plettemeier, Y. Rogez, H. Sierks, C. Statz, H. Svedhem, I. Williams, S. Zine, and J. Van Zyl, "Properties of the 67P/Churyumov-Gerasimenko interior revealed by CONSERT radar," *Science*, vol. 349, no. 6247, 2015. [Online]. Available: http://www.sciencemag.org/content/349/6247/aab0639.abstract

[7] E. Asphaug, M. Belton, A. Cangahuala, L. Keith, K. Klaasen, L. McFadden, G. Neumann, S. Ostro, R. Reinert, A. Safaeinili *et al.*, "Exploring asteroid interiors: The Deep Interior mission concept," in *Lunar and Planetary Science Conference*, vol. 34, 2003.

[8] W. Kofman, A. Herique, J.-P. Goutail, T. Hagfors, I. P. Williams, E. Nielsen, J.-P. Barriot, Y. Barbin, C. Elachi, P. Edenhofer, A.-C. Levasseur-Regourd, D. Plettemeier, G. Picardi, R. Seu, and V. Svedhem, "The Comet Nucleus Sounding Experiment by Radiowave Transmission (CONSERT): A short description of the instrument and of the commissioning stages," *Space Science Reviews*, vol. 128, no. 1-4, pp. 413 – 432, 2007.

[9] K. Berry, B. Sutter, A. May, K. Williams, B. W. Barbee, M. Beckman, and B. Williams, "OSIRIS-REx touch-and-go (TAG) mission design and analysis," 2013.

[10] D. S. Lauretta and O.-R. Team, "An overview of the OSIRIS-REx asteroid sample return mission," in *Lunar and Planetary Science Conference*, vol. 43, 2012.

[11] J. Kawaguchi, A. Fujiwara, and T. Uesugi, "Hayabusa—its technology and science accomplishment summary and Hayabusa-2," *Acta Astronautica*, vol. 62, no. 10, pp. 639–647, 2008.

[12] Y. Tsuda, M. Yoshikawa, M. Abe, H. Minamino, and S. Nakazawa, "System design of the Hayabusa 2-asteroid sample return mission to 1999 JU3," *Acta Astronautica*, vol. 91, pp. 356–362, 2013.

[13] P. Michel, M. Kueppers, I. Carnelli, A. Galvez, K. Mellab, and A. Cheng, "Asteroid Impact Mission (AIM): the European component of the AIDA space project," in *Lunar and Planetary Science Conference*, vol. 47, 2016, p. 1204.

[14] P. Bambach, J. Deller, E. Vilenius, S. Pursiainen, M. Takala, H. M. Braun, and H. Lentz, "DISCUS - the Deep Interior Scanning CUbeSat mission to a rubble pile near-earth asteroid," *Advances in Space Research*, 2018, accepted.

[15] P. Bambach, J. Deller, S. Pursiainen, H. Braun, and M. Takala, "2017.A.3.4. What is a rubble pile asteroid? A CubeSat Mission to find out," in *6th Interplanetary CubeSat Workshop, Cambridge, United Kingdom 30-31 May 2017*. iCubeSat, 2017. [Online]. Available: https://icubesat.org/papers/2017-2/2017-a-3-4-what-is-a-rubble-pile-asteroid-a-cubesat-mission-to-find-out/

[16] N. Willis, *Bistatic Radar*, ser. Electromagnetics and Radar. Scitech Publishing Inc, Raleigh, NC, USA, 2005.

[17] S. Abe, T. Mukai, N. Hirata, O. S. Barnouin-Jha, A. F. Cheng, H. Demura, R. W. Gaskell, T. Hashimoto, K. Hiraoka, T. Honda, T. Kubota, M. Matsuoka, T. Mizuno, R. Nakamura, D. J. Scheeres, and M. Yoshikawa, "Mass and Local Topography Measurements of Itokawa by Hayabusa," *Science*, vol. 312, no. 5778, pp. 1344–1347, 2006.

[18] W. Bottke, *Asteroids III*, ser. University of Arizona space science series. University of Arizona Press, 2002.

[19] P. Michel, F. DeMeo, and W. Bottke, *Asteroids IV*, ser. Space Science Series. University of Arizona Press, 2015.

[20] D. C. Richardson, P. Elankumaran, and R. E. Sanderson, "Numerical experiments with rubble piles: equilibrium shapes and spins," *Icarus*, vol. 173, no. 2, pp. 349–361, 2005.

[21] D. Polishook, N. Moskovitz, R. Binzel, B. Burt, F. DeMeo, M. Hinkle, M. Lockhart, M. Mommert, M. Person, A. Thirouin *et al.*, "A 2 km-size asteroid challenging the rubble-pile spin barrier–a case for cohesion," *Icarus*, vol. 267, pp. 243–254, 2016.

[22] P. Sánchez and D. J. Scheeres, "The strength of regolith and rubble pile asteroids," *Meteoritics & Planetary Science*, vol. 49, no. 5, pp. 788–811, 2014.

[23] J. Deller, "Hyper-velocity impacts on rubble pile asteroids," Ph.D. dissertation, University of Kent and International Max Planck Research School for Solar System Science, 2015, https://kar.kent.ac.uk/54352/.

[24] J. Deller, S. Lowry, C. Snodgrass, M. Price, and H. Sierks, "A new approach to modelling impacts on rubble pile asteroid simulants," *Monthly Notices of the Royal Astronomical Society*, vol. 455, no. 4, pp. 3752–3762, 2016.

[25] P. Pravec and A. W. Harris, "Fast and Slow Rotation of Asteroids," *Icarus*, vol. 148, pp. 12–20, Nov. 2000.

[26] B. Carry, "Density of asteroids," *Planetary and Space Science*, vol. 73, no. 1, pp. 98–118, 2012.

[27] R. P. Binzel and W. Kofman, "Internal structure of near-Earth objects," *Comptes Rendus Physique*, vol. 6, no. 3, pp. 321–326, 2005.

[28] D. J. Daniels, *Ground Penetrating Radar (2nd Edition)*. Stevenage: Institution of Engineering and Technology, 2004.

[29] B. F. Burke and F. Graham-Smith, *An introduction to radio astronomy*. Cambridge University Press, 2009.

[30] R. G. Stone, K. W. Weiler, M. L. Goldstein, and J.-L. Bougeret, "Radio astronomy at long wavelengths," *Washington DC American Geophysical Union Geophysical Monograph Series*, vol. 119, 2000.

[31] J. D. Kraus and A. T. Moffet, "Radio astronomy," *American Journal of Physics*, vol. 35, no. 5, pp. 450–450, 1967.

[32] V. Agrawal, *Satellite Technology: Principles and Applications*. Wiley, 2014.

[33] D. Doody, *Deep space craft: an overview of interplanetary flight*. Springer Science & Business Media, 2010.

[34] K. Iizuka, A. P. Freundorfer, K. H. Wu, H. Mori, H. Ogura, and V.-K. Nguyen, "Step-frequency radar," *Journal of Applied physics*, vol. 56, no. 9, pp. 2572–2583, 1984.

[35] G. S. Gill, *Ultra-wideband radar technology*. CRC Press, Boca Raton, Florida, USA, 2001, ch. 11: High-Resolution Step-Frequency Radar, pp. 303–328.

[36] A. Paulose, "High radar range resolution with the step frequency waveform," NAVAL POSTGRADUATE SCHOOL MONTEREY CA, Tech. Rep., 1994.

[37] G. R. Olhoeft, "Electrical properties of rocks," *Physical properties of rocks and minerals*, vol. 2, pp. 257–297, 1981.

[38] W. Kofman, "Radar techniques to study subsurfaces and interiors of the solar system objects," in *19th International Conference on Microwave Radar and Wireless Communications (MIKON)*, vol. 2. IEEE, 2012, pp. 409–412.

[39] A. Herique, J. Gilchrist, W. Kofman, and J. Klinger, "Dielectric properties of comet analog refractory materials," *Planetary and Space Science*, vol. 50, no. 9, pp. 857–863, AUG 2002.

[40] L. Evans, *Partial Differential Equations*, ser. Graduate studies in mathematics. American Mathematical Society, 1998.

[41] J. Jackson, *Classical Electrodynamics*. Wiley, 2007.

[42] F. J. Harris, "On the use of windows for harmonic analysis with the discrete fourier transform," *Proceedings of the IEEE*, vol. 66, no. 1, pp. 51–83, 1978.

[43] A. H. Nuttall, "Some windows with very good sidelobe behavior," *IEEE Transactions on Acoustics, Speech, Signal Processing*, vol. ASSP-29, no. 1, pp. 84–91, 1981.

[44] W. Barron, E. Cliver, J. Cronin, and D. Guidice, "Solar radio emission," *Handbook of geophysics and the space environment*, 1985.

[45] J. Rice, *Mathematical Statistics and Data Analysis*, ser. Advanced series. Cengage Learning, 2006, no. s. 3.

[46] J. Li and Y. Huang, *Time-Domain Finite Element Methods for Maxwell's Equations in Metamaterials*, ser. Springer Series in Computational Mathematics. Springer Berlin Heidelberg, 2012.

[47] J. B. Schneider, *Understanding the FDTD Method*. John B. Schneider, 2016. [Online]. Available: http://www.eecs.wsu.edu/ schneidj/ufdtd/

[48] R. A. Carley and E. Heggy, "Finite difference time domain simulation of radar wave propagation through comet nuclei dielectric models," *Meteoritics & Planetary Science*, vol. 43, no. 6, pp. 1085–1095, 2008.

[49] D. Colton and R. Kress, *Inverse Acoustic and Electromagnetic Scattering Theory*, ser. Applied Mathematical Sciences. Springer, 1998.

[50] C. Barbieri, "Comet 67P/CG seen through Osiris, the eyes of Rosetta," *Rendiconti Lincei*, pp. 1–29, 2017.

[51] D. Clery, "Rosetta ends 2-year comet mission with final descent," *Science*, vol. 353, no. 6307, pp. 1482–1483, 2016. [Online]. Available: http://science.sciencemag.org/content/353/6307/1482

[52] S. B. Broschart and D. J. Scheeres, "Control of hovering spacecraft near small bodies: Application to asteroid 25143 Itokawa," *Journal of Guidance Control and Dynamics*, vol. 28, no. 2, pp. 343–353, 2005.

[53] D. Lee and G. Vukovich, "Adaptive finite-time control for spacecraft hovering over an asteroid," *IEEE Transactions on Aerospace and Electronic Systems*, vol. 52, no. 3, pp. 1183–1196, 2016.

[54] S. Pursiainen and M. Kaasalainen, "Detection of anomalies in radio tomography of asteroids: Source count and forward errors," *Planetary and Space Science*, vol. 99, no. 0, pp. 36 – 47, 2014.

[55] A. La Spina, P. Paolicchi, A. Kryszczynska, and P. Pravec, "Retrograde spins of near-Earth asteroids from the Yarkovsky effect," *Nature*, vol. 428, no. 6981, p. 400, 2004.

[56] D. E. Trilling, F. Valdes, L. Allen, D. James, C. Fuentes, D. Herrera, T. Axelrod, and J. Rajagopal, "The Size Distribution of Near-Earth Objects Larger Than 10 m," *Astronomical Journal*, vol. 154, p. 170, Oct. 2017.

[57] A. Mainzer, T. Grav, J. Bauer, J. Masiero, R. McMillan, R. Cutri, R. Walker, E. Wright, P. Eisenhardt, D. Tholen *et al.*, "NEOWISE observations of near-Earth objects: Preliminary results," *The Astrophysical Journal*, vol. 743, no. 2, p. 156, 2011.

[58] L. Angulo, J. Alvarez, A. Bretones, F. Teixeira, and S. Garcia, "Discontinuous Galerkin methods: An affordable alternative to FDTD," in *Electromagnetics in Advanced Applications (ICEAA), 2014 International Conference on*. IEEE, 2014, pp. 517–520.

[59] T. Lu, W. Cai, and P. Zhang, "Discontinuous Galerkin time-domain method for GPR simulation in dispersive media," *Geoscience and Remote Sensing, IEEE Transactions on*, vol. 43, no. 1, pp. 72–80, 2005.

[60] A. Accomazzo, P. Ferri, A. Hubault, S. Lodiot, J. Pellon-Bailon, and R. Porta, "Rosetta visits asteroid (21) Lutetia," *Acta Astronautica*, vol. 72, pp. 178–184, 2012.

[61] H. Keller, C. Barbieri, D. Koschny, P. Lamy, H. Rickman, R. Rodrigo, H. Sierks, M. A'Hearn, F. Angrilli, M. Barucci *et al.*, "E-type asteroid (2867) Steins as imaged by OSIRIS on board Rosetta," *Science*, vol. 327, no. 5962, pp. 190–193, 2010.

Figure captions

Figure 1

A bistatic measurement approach is used, since the scattering waves can be headed away from the transmitter spacecraft. One spacecraft (red) is utilized to both transmit and receive the signal. The other one (blue) serves as an additional receiver. **Right:** The spacecraft are assumed to orbit their target asteroid in a plane which will be nearly perpendicular to the ecliptic of the solar system. Each spacecraft is equipped with a single half wavelength dipole antenna (yellow) which will be pointed towards the Sun during the measurement in order to suppress the effect of the solar radiation. That is, the Sun is assumed to be located in the direction of the normal of the orbiting plane.

Figure 2

A schematic (non-scaled) illustration showing the sparse full-angle configuration (A) of 128 measurement points (left) and two sparse limited-angle configurations (B) and (C) of 64 and 24 points (right), respectively. The angle ω between the orbiting plane normal and the asteroid spin is 90, 30 and 15 degrees. The limited-angle configurations results in a pronounced aperture around the polar regions in (C).

Figure 3

The incident field needs to be evaluated only on its first arrival at $\mathcal{S}$ (dark gray circle), that is, on the subset $\mathcal{S}^- = \{\vec{x} \in \mathcal{S} \,|\, (\vec{x} - \vec{p}) \cdot \vec{n} < 0\}$ (dark blue). On the remaining part $\mathcal{S}^+ = \mathcal{S} \setminus \mathcal{S}^-$, it is set to be zero. Surface $\mathcal{C}$ (dark and light blue) results from extending the surface $\mathcal{S}^-$ with the tangent cone (light blue) of $\mathcal{S}$ which intersects $\vec{p}$, and further with a $\vec{p}$-centric sphere with a radius larger than T. It holds that $\langle \vec{g}_{\mathrm{I}}, v; \mathcal{C} \rangle = \langle \vec{g}_{\mathrm{I}}, v; \mathcal{S}^- \rangle$. Namely, the integrand in (17) is zero on the tangent cone and within the distance $> T$ from $\vec{p}$ the incident wave is zero for $t \in [0, T]$.

Figure 4

The present test domain $\Omega = \Omega_1 \cup \Omega_2$ (left) is an origin centric cube. The interior of the sphere $\mathcal{S}$ centered at origin formed the subdomain Ω_2 (right) the exterior of which Ω_1 contained a split-field perfectly matched layer [3], [47] to simulate open field scattering. As the test target, we utilized the surface model (12260 triangles) of asteroid 1998 KY_{26} which can be associated through scaling with a 550 m (36.7 relative to λ) diameter asteroid (Table I). The volumetric finite element discretization used in the reconstruction procedure was created based on the multi-layer surface mesh model illustrated in the pictures.

Figure 5

The **overall** relative overlap and value error (ROE and RVE) in percents (%) in the full ROI $\mathbf{S}$ for cases A, B and C which are shown in Figure 2. The results for the monostatic and bistatic data correspond to the light grey and dark blue box plot bars, respectively. Each bar is based on a sample of 30 reconstructions obtained with independent realizations of the total noise vector. The narrow part visualizes the interval between the minimum and maximum value in the sample. The thick part is called the interquartile range (IQR) or spread, that is, the interval between the 25 % and 75 % quantile. The white line shows the median.

Figure 6

The relative overlap and value error (ROE and RVE) in percents (%) for the **surface part** of ROI $\mathbf{S}$. The results for the monostatic and bistatic data correspond to the light grey and dark blue box plot bars, respectively.

Figure 7

The relative overlap and value error (ROE and RVE) in percents (%) for the **deep interior** part of ROI $\mathbf{S}$. The results for the monostatic and bistatic data correspond to the light grey and dark blue box plot bars, respectively.

Figure 8

A visual comparison of the reconstructions **(i)**, **(ii)** and **(iii)** obtained, respectively, with configurations (A), (B) and (C) using bistatic data and total noise with the relative standard deviation of -15 dB. On each row, the left image illustrates the ROI $\mathbf{S}$ (Section II-E1) containing the exact surface dust layer (grey) and voids (blue). That is, the grey and blue area mark the overlap obtained for the dust layer and voids, respectively. The other images present, the overlap set $\mathbf{V}$, i.e., the relative overlap between the exact permittivity distribution and the reconstruction (Section II-E1). The diameter of the asteroid is here 550 m (36.7 relative to λ).

Mika Takala received the B.Sc. degree in electrical engineering from the Tampere University of Technology (TUT), Tampere, Finland in 2015, and the M.Sc.(tech.) degree from TUT in 2016. In 2016 he started working at the Laboratory of Mathematics, TUT, as a PhD student. He currently works on his PhD research, which is closely related to geophysical inversion strategies with a view towards computing aspects and embedded systems.

Patrick Bambach studied aerospace engineering at the University of Stuttgart. He finished his diploma thesis in 2014 at the University of Tokyo. Since 2015, he is working as an engineer at the Max Planck Institute for Solar System Research in Göttingen. He worked on the Solar Orbiter Mission as a thermal and test engineer. Currently he is working on the design, calibration and ground qualification of particle detectors for BepiColombo and the Jupiter Icy Moons Explorer. Since 2016 he is also part of the DISCUS CubeSat team.

Jakob Deller graduated 2012 in astrophysics at the University of Göttingen. During his PhD at the University of Kent in Canterbury, UK, he investigated hypervelocity impacts on rubble pile asteroids in the context of the Rosetta fly-by at asteroid Steins. Since 2015, he supports the science operations of the OSIRIS camera system on board the Rosetta spacecraft, planning and negotiating pointing and imaging sequences during active mission, and preparing the acquired data for public archiving afterwards. He works on understanding possible impact features on comet 67P/Churyumov-Gerasimenko. Since 2016 he is part of the DISCUS study to finally find out what is in the interior of a rubble pile asteroid.

Esa Vilenius received the M.Sc. (Eng.) degree from the Electrical and Communications Engineering Department of the Helsinki University of Technology, Finland, in 2002, the Master of Space Studies degree from the International Space University, France, in 2004, and the Ph.D. degree from the University of Göttingen, Germany, in 2009. He has experience in instrument calibration, data reduction and observation planning in planetary&space observatory missions at near-infrared and far-infrared wavelengths as well as with energetic particle spectrometers. His research interests include Kuiper belt and trans-Neptunian objects. He is currently at Max Planck Institute for Solar System Research, Germany.

Manfred Wittig studied telecommunications engineering at Technical University Berlin and got his PhD from Stuttgart University. He is the founder and CEO of MEW-Aerospace UG, which specialises in the development of microwave and optical communications payloads for CubeSats. He has 25 years of experience in ESA until retirement and he led ESA project managers for advanced communication satellite technology developments for European and Canadian space industry. He has done pioneering work on Ka-band utilization in Europe and has particular competence in the field of on-board processing technology and laser space communication techniques.

Harald Lentz studied electrical engineering at the Technical University of Berlin/Germany with special focus on RF- and microwave technology. Since 1996 he is with RST. He has been involved in system design as well as hardware design of various radar sensors for airborne and spaceborne applications as well as of ground penetration radars.

Hans Martin Braun is an expert in Radar Systems. He received his Dr.-Ing. (PhD) on RF-Engineering in 1982 from the Technical University of Berlin, Germany and became Honorary Professor at the University of Stuttgart in 2008. Today, he is General Director of RST Radar Systemtechnik AG Switzerland, Board Member of RST Raumfahrt Systemtechnik GmbH Germany, and Professor for Radar-Navigation at the University of Stuttgart. Dr. Braun is a sound expert in space-borne Synthetic Aperture Radar covering the wide field of Phased Array SAR to Reflector-based SAR and all variations in between. He is a Senior Member of IEEE Geoscience and Remote Sensing Society, a Member of the St. Petersburg Academy of Navigation and Motion Control, and a Member of the European GPR Association.

Mikko Kaasalainen obtained his PhD at Oxford in 1994, and he has been professor of applied mathematics at Tampere University of Technology since 2009. His main research fields are inverse problems and mathematical modeling, with interdisciplinary application projects ranging from biology to galactic dynamics. He is the vice director of the Centre of Excellence in Inverse Problems funded by the Academy of Finland. The website of his research group at TUT is at math.tut.fi/inversegroup

Sampsa Pursiainen received the M.Sc. (Eng.) and Ph.D. (Eng.) degrees in mathematics from the Helsinki University of Technology (Aalto University since 2010), Espoo, Finland, in 2003 and 2009, respectively. He focuses on various forward and inversion techniques of applied mathematics. In 2010–2015, he worked as a postdoc with the Department of Mathematics, University of Genoa, Italy, with Institute for Biomagnetism and Biosignalanalysis (IBB), University of Münster, Germany, Department of Mathematics and Systems Analysis, Aalto University, and also with the Laboratory of Mathematics, Tampere University of Technology (Tampere University from 2019 on), Tampere, Finland, where he currently holds an Assistant Professor's position.

Received xxxx 20xx; revised xxxx 20xx.

PUBLICATION
IV

DISCUS – The Deep Interior Scanning CubeSat mission to a rubble pile near-Earth asteroid

P. Bambach, J. Deller, E. Vilenius, S. Pursiainen, M. Takala, H. M. Braun, H. Lentz and M. Wittig

Advances in Space Research 62.12 (2018), 3357–3368. Advances in Technologies, Missions and Applications of Small Satellites
DOI: 10.1016/j.asr.2018.06.016

Available online at www.sciencedirect.com

ScienceDirect

Advances in Space Research 62 (2018) 3357–3368

ADVANCES IN SPACE RESEARCH (a COSPAR publication)

www.elsevier.com/locate/asr

DISCUS – The Deep Interior Scanning CubeSat mission to a rubble pile near-Earth asteroid

Patrick Bambach [a,*], Jakob Deller [a], Esa Vilenius [a], Sampsa Pursiainen [b], Mika Takala [b], Hans Martin Braun [c], Harald Lentz [c], Manfred Wittig [d]

[a] Max Planck Institute for Solar System Research, Justus-von-Liebig-Weg 3, 37077 Göttingen, Germany
[b] Tampere University of Technology, PO Box 527, FI-33101 Tampere, Finland
[c] RST Radar Systemtechnik AG, Ebenaustrasse 8, 9413 Oberegg, Switzerland
[d] MEW-Aerospace UG, Diesterwegstrasse 2, 31787 Hameln, Germany

Received 31 May 2017; received in revised form 8 June 2018; accepted 10 June 2018
Available online 19 June 2018

Abstract

We have performed an initial stage conceptual design study for the *Deep Interior Scanning CubeSat* (DISCUS), a tandem 6U CubeSat carrying a bistatic radar as the main payload. DISCUS will be operated either as an independent mission or accompanying a larger one. It is designed to determine the internal macroporosity of a 260–600 m diameter Near Earth Asteroid (NEA) from a few kilometers distance. The main goal will be to achieve a global penetration with a low-frequency signal as well as to analyze the scattering strength for various different penetration depths and measurement positions. Moreover, the measurements will be inverted through a computed radar tomography (CRT) approach. The scientific data provided by DISCUS would bring more knowledge of the internal configuration of rubble pile asteroids and their collisional evolution in the Solar System. It would also advance the design of future asteroid deflection concepts. We aim at a single-unit (1U) radar design equipped with a half-wavelength dipole antenna. The radar will utilize a stepped-frequency modulation technique the baseline of which was developed for ESA's technology projects GINGER and PIRA. The radar measurements will be used for CRT and shape reconstruction. The CubeSat will also be equipped with an optical camera system and laser altimeter to support navigation and shape reconstruction. We provide the details of the measurement methods to be applied along with the requirements derived from the known characteristics of rubble pile asteroids. Additionally, an initial design study of the platform and targets accessible within 20 lunar distances are presented.

Keywords: Deep-space CubeSat; Near earth asteroid; Rubble pile asteroid; Radar; Computed radar tomography

1. Introduction

The goal of this paper is to advance the mission design for recovering the deep interior structure of an asteroid using small spacecraft. We introduce the initial stage mission concept, the *Deep Interior Scanning CubeSat* (DISCUS), in which the goal is to fly two identical six-unit (6U) CubeSats (Fig. 1) as a tandem into the orbit of a small rubble pile asteroid and to resolve its global interior structure via tomographic radar measurements. This is an important scientific objective which has been approached via several mission concepts (Safaeinili et al., 2002; Asphaug et al., 2001; Herique and Ciarletti, 2016; Kofman et al., 2007; Snodgrass et al., 2017). The DISCUS concept could either work as an independent mission or accompanying a larger one. DISCUS CubeSats will be equipped with a bistatic penetrating radar and an optical imaging system. The design is derived from airborne Ground Penetrating Radar (GPR) which is today applied

* Corresponding author.
E-mail address: bambach@mps.mpg.de (P. Bambach).

https://doi.org/10.1016/j.asr.2018.06.016
0273-1177/

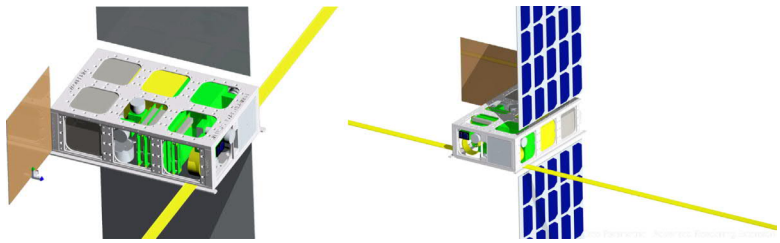

Fig. 1. Conceptual pictures of the 6U DISCUS design containing (a) 1U radar (green), (b) 1U Communication (yellow), (c) 2U BIT-3 propulsion system (gray). Attached to the frame is a linear half-wavelength dipole antenna (yellow line). During the launch, the antenna will be rolled up. The other parts are components of the shelf (COTS). Among others a Pumpkin 6U frame with star trackers, an altimeter, a camera, three reaction wheels and PCB boards for housekeeping and a cold gas thruster. Two solar panels are oriented in a perpendicular direction with respect to the antenna. The radar measurement is performed with the antenna pointed towards the sun in order to minimize the noise caused by solar radiation. It also maximizes the power gain of the solar panels and reduces the need for power storage. (For interpretation of the references to colour in this figure legend, the reader is referred to the web version of this article.)

in mapping subsurface glacier and soil structures, e.g., ice thickness (Gundelach et al., 2010; Eisenburger et al., 2008; Fu et al., 2014).

The first realized tomography attempt for a small Solar System body was the COmet Nucleus Sounding Experiment by Radio-wave Transmission (CONSERT) (Kofman et al., 2007; Kofman et al., 2015) during the European Space Agency's (ESA) *Rosetta* mission in 2014. In CONSERT, a radio-frequency signal was transmitted between the *Rosetta* orbiter and its lander *Philae*. Rosetta was a major scale mission with its total budget of 1.4 Billion Euro with the cost of the lander being 200 Million. Even though the mission has been a success the high cost is a challenge for the realization of a comparable successor. CubeSats cannot replace those missions on their full scale, but by reducing the science payload to less than 2 kg and choosing targets which are more easy to reach they can complement traditional missions. Due to the recent technology advances and high number of commercially available hardware CubeSats would allow rapid missions at a fraction of the costs. For example, the recently published M-ARGO concept aims for a budget of 25 Million Euro for carrying a 1U payload to an NEA (Walker et al., 2017). The interest towards using CubeSats in planetary science is constantly increasing and, therefore, mission design to support this development is needed. Staehle et al. (2013) published an initial report on potential Interplanetary CubeSats with a 2U science payload and a 2U propulsion module. Later on in 2014, NASA announced with NeaScout the first detailed mission design of a 6U CubeSat to fly with a solar sail to an asteroid (McNutt et al., 2014). Recently developed CubeSats capable of operating in deep space include the Lunar IceCube (Clark et al., 2016) and the in 2018 launched[1] Mars Cube One twins (Imken et al., 2017).

In Imken et al. (2017), the current status of 6U Interplanetary CubeSat development at the Jet Propulsion Laboratory (JPL) is given. Critical hardware, such as data handling and communication systems have been developed as standard buses at JPL. Namely, the Sphinx data handling system and the Iris transponder. The volume and weight of this hardware show that the promise of 6U interplanetary CubeSats with around 2U housekeeping, 2U propulsion and almost 2U payload could be kept. An ESA/ESTEC study found the limitations of 6U for a NEA mission to be critical, especially regarding on thermal management and Δv requirements of independent interplanetary missions. Therefore, a 12U based CubeSat concept M-ARGO (Walker et al., 2017) has been investigated and found promising. Besides completely autonomous missions also so-called CubeSat piggy-bag missions can become more common in the future. In the piggy-bag approach, a mothership transports the CubeSats to its target, deploys them and serves as a communication link. The advantage is that the requirements for navigation, communication, propulsion and total ionizing dose (TID) are reduced. For example, the plans of the unrealized Asteroid Impact Mission (AIM) included two CubeSats and the Mascot-2 lander (Michel et al., 2016; Herique and Ciarletti, 2016).

DISCUS (Fig. 1) is designed to detect the internal macroporosity of an Itokawa-size (Abe et al., 2006) 260–600 m diameter *Near Earth Asteroid* (NEA) from a few kilometers distance. The primary goal of DISCUS will be to achieve a global signal penetration as well as to analyze the scattering strength for various different penetration depths and measurement positions. Additionally, forming an actual 3D reconstruction based on the measurements will be attempted. Using the reflected wave, also the shape of the body can be determined. Due to the many limitations of space missions, e.g., the strict payload and energy bounds, our radar design aims at a minimal weight and power consumption. Akin to airborne GPR, we apply the stepped-frequency (SF) measurement technique and a half-wavelength dipole antenna (Fu et al., 2014). Maximizing the detectability of deep structures such as voids necessitates using a signal frequency bellow 100 MHz (Francke and Utsi, 2009; Leucci, 2008; Kofman, 2012). We initially

[1] https://www.jpl.nasa.gov/cubesat/missions/marco.php.

target a 20 MHz center frequency with 2 MHz bandwidth in the radar design. 20 MHz was selected for providing good penetration into asteroid material. A 50 MHz radar based mostly on identical hardware is also considered. The higher frequency would allow a shorter dipole antenna, but reduce the penetration depth of the radar.

This paper is structured as follows. In Section 2, we motivate the mission plan via a brief review of what is known of rubble pile asteroids. Section 3 describes the on-board scientific instruments and their use. We provide the details of the measurement methods to be applied along with the requirements derived from the known characteristics of the rubble pile asteroids. Section 4 sketches the mission layout. An initial design concept of the platform and accessible targets is presented. Section 5 is devoted to the discussion. Finally, Section 6 concludes the paper and summarizes the study.

2. Rubble pile asteroids in the Solar System

When the Solar System was formed 4.6Ga ago, planetesimals constituted the building blocks of protoplanets and eventually the planets themselves. Comets and asteroids are the remainders of this early stage. Exploring their population is a key to understanding the Solar System's history and evolution, although they contain only about 0.002% of its total mass. The asteroids have evolved through several processes; space weathering changed their surface by effects of radiation, internal heating may have altered their chemistry and mineralogy, and collisional events transformed their interior structure and size distribution. According to the present knowledge, most asteroids result from catastrophic disruptions of large parent bodies (Farinella et al., 1982). Namely, modeling of catastrophic disruptions (Michel et al., 2001, 2002) can reproduce the size distribution of the Karin asteroid family, showing that many fragments re-accumulated to form rubble pile asteroids.

The current evidence also shows that these processes have left most of the asteroids in the size range of about 200 m–100 km with an interior that is not monolithic but rather an agglomerate of smaller fragments, bound together mainly by gravity and only weak cohesion (Richardson et al., 2002).

The rough comparisons between the meteoritic materials and the indirect density estimates suggest that many asteroids have a large amount of internal macroporosity, that is, voids larger than the typically micrometer sized cracks in the matrix of meteoritic samples (denoted as microporosity). Recently, Carry (2012) found high percentages of macroporosity by comparing mass and volume of 287 asteroids, and aggregating information about meteoritic samples linked to their taxonomic classes. For example, the estimate $P_{\mathrm{macro}} = 72 \pm 14$ % was obtained for asteroid (854) Frostia. The measurements provided by the recent Hayabusa and Rosetta missions have also shown that the small asteroid Itokawa (Fig. 2a Saito et al., 2006; Abe et al., 2006) as well as the larger one Šteins (Fig. 2b) might have around 40% of macroporosity, respectively. Moreover, simulations of granular flowing material match well with the observed top-like shape of many observed asteroids, e.g., Šteins; simulating the spin-up of rotating asteroids, Walsh et al. (2008) as well as Sánchez and Scheeres (2012) found a material flow towards the equator, forming asteroids with comparable shapes. Analyzing the rotation period as a function of the size has revealed that, for asteroids larger than 200–300 m, there exists a general cut-off at a period of 2.2 hours which only some so-called superfast rotators such as the asteroid 1950 DA[2] surpass (Pravec et al., 2002; Rozitis et al., 2014). This spin barrier (e.g. Pravec and Harris, 2000; Kwiatkowski, 2010) is coinciding with the limit for a cohesionless body before it starts loosing mass at the equator, which indicates that most bodies larger than 200–300 m in diameter are not monolithic in the interior.

While the evidence for a shattered interior of asteroids is strong, the exact configuration of the interior of these objects is unclear, as direct measurements are still missing. Macroporosity can arise from void space inside the asteroid at various different scales. There might be large void fractures at the scale of hundreds of meters in the interior, as shown to be likely for Šteins (Fig. 2b, see details in Deller, 2017), or small scale cavities caused by interlocking of boulders. Moreover, the sorting effects of the granular mechanics suggest that the asteroid Itokawa might be a rubble pile with large constituent fragments, explaining the enhancement of the large boulders on its surface. Namely, the amount of regolith observed on Itokawa's surface is significantly larger than what could be produced by impact events forming the observed number of surface craters (Barnouin-Jha et al., 2008). Itokawa's *rough highlands* terrain is covered with rubbles following a cumulative power law distribution of -3.1 ± 0.1, and the number of large boulders is enhanced compared to models of re-aggregation after a catastrophic impact event, which most likely formed the asteroid (Michikami et al., 2008). Indirect inferences of the macroporosity structures can also be obtained through the simulation of the impact events which allows one to connect the crater structure to the surface features and also to determine the shock wave propagation characteristics inside the asteroid. Deller (2017) demonstrated this method on asteroid Šteins, showing that the catena of pits running from the rim of the crater on Šteins can be interpreted as a sequence of sinkholes into an interior crack, which has opened due to the impact.

The mission proposed here provides the means to finally sample the interior of a rubble pile asteroid directly and to provide direct measurements about the distribution of porosity inside these objects. The knowledge obtained would be vital, for example, for the assessment of the asteroid impact deflection as a possible way to neutralize threats by potentially hazardous earth colliding asteroids. Namely,

[2] https://cneos.jpl.nasa.gov/doc/1950da/.

(a) Image of the asteroid Itokawa taken by the Hayabusa spacecraft. Source: JAXA, http://global.jaxa.jp/article/special/hayabusa_sp3/index_e.html

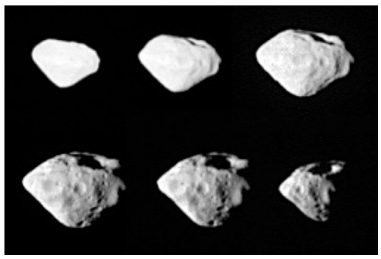

(b) Asteroid Šteins imaged by the OSIRIS camera system on board of Rosetta. Source: ESA © 2008 MPS for OSIRIS Team MPS/UPD/LAM/IAA/RSSD/INTA/UPM/DASP/IDA

Fig. 2. Itokawa and Šteins, two rubble pile asteroids visited by spacecraft.

the internal structure is of crucial importance in this regard, since the scale of the porosity inside asteroids determines the propagation of shock waves and, therefore, the efficiency of energy transfer during impact events. Another important application would, obviously, be the mineralogy of asteroids, since the proposed radar measurement technique would provide first-hand information of the dielectric properties in the interior, see e.g. (Reddy et al., 2015).

NEAs that are easy to reach for space missions have been explored, e.g., in the Mission Accessible Near-Earth Objects Survey (MANOS, Thirouin et al., 2016) focusing on NEAs that have orbital parameters with low Δv, i.e., low relative velocity with respect to the Earth. For a small, but well-described sample of 86 sub-kilometer sized asteroids, it rated seven of these objects as possible targets for manned missions. Using expectations on the number of NEAs from de-biasing studies of the NEA population (Tricarico, 2017), Thirouin et al. (2016) estimate that a total number of approximately 33, 000 NEAs are accessible for space missions in the Thirouin et al. (2016) definition.

3. Scientific instruments and their use

3.1. Stepped-frequency radar

The radar design of DISCUS is based on the stepped-frequency technique which requires a relatively low DC power and low data rate. This is possible since, instead of a single full-bandwidth signal pulse, narrow frequency bands are transmitted and received separately. As the stepped-frequency technique allows measurement of weaker bands, it is generally used in radars with a narrow instantaneous bandwidth as compared to the total bandwidth of the resolution aimed (Lacomme, 2001).

3.1.1. Mathematical concept

The set of transmitted narrow frequency lines $\psi_1, \psi_2, \ldots, \psi_N$ allows one to approximate a given function f via the sum $f = \sum_{\ell=1}^{N} c_\ell \psi_\ell$. If φ_ℓ is the received signal (data) corresponding to frequency line ψ_ℓ, then the data g resulting from a transmission f is approximately given by $g = \sum_{\ell=1}^{N} c_\ell \varphi_\ell$, where the coefficients $c_1, c_2, \ldots, c_N$ follow from the formula for f. Hence, the data g for any transmission f within the given frequency range can be approximated, if the function pairs ψ_ℓ and φ_ℓ for $\ell = 1, 2, \ldots, N$ are given, i.e., if the stepped-frequency measurement data are available. For a mathematical study of the DISCUS radar, please refer to Takala et al. (2017).

3.1.2. Baseline design

The stepped-frequency radar design referred to in this study was originally developed and verified by *RST Radar Systemtechnik AG* within ESA's GINGER (Guidance and Into-the-Ground Exploration Radar) project (Braun et al., 1997b), where a planetary rover was used as the reference platform. The operating frequency of GINGER was around 600 MHz. In a subsequent ESA project PIRA (Planetary Into-the-Ground Radar and Altimeter) this technology was verified under platform movement using a helicopter as the carrier (Braun et al., 1997a). PIRA was designed for deep planetary penetration (~1 km) at a frequency of 10 MHz. In addition to space systems, RST has also previous experience on packing a stepped-frequency radar into a very small volume. For example, HOPE (Handheld Operated Demining System) landmine detector operating at 2–6 GHz has a total radar volume of 900 cm^3 (Fig. 3). RST has developed and operated SF radar GPRs from 1 MHz through 8 GHz up to today. The bandwidth at low frequencies is, however, always limited by the used antenna type and therefore 2 MHz at 20 MHz center frequency seems to be a limit for any kind of dipole. The radar electronics can be built to be programmable for center frequencies between 20 MHz and 50 MHz for different missions, but the antenna and the dedicated balun

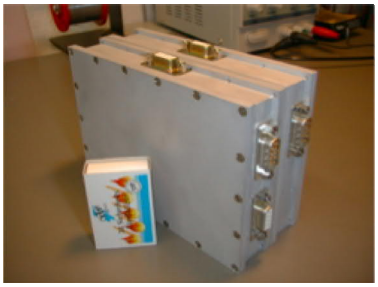

Fig. 3. Stepped-frequency radar for the HOPE (Handheld Operated Demining System) (RST Radar Systemtechnik AG, 2001). The dimensions of the box are 12 cm × 15 cm × 5 cm and its volume is 900 cm^3.

has to be made for the center frequency of the selected mission.

3.1.3. DISCUS radar

In the 6U DISCUS design, the goal is to fit a radar with a 2–5 MHz total signal bandwidth and 20–50 MHz center frequency into a 1U cube (1000 cm^3). The lower end of the targeted frequency interval is advantageous in order to achieve an appropriate signal penetration (Kofman, 2012) and to minimize solar noise. Namely, if the Sun is active, the dominating error source will be the solar radiation which is on a comparably low level at the targeted interval decreasing towards the lower frequencies (Kraus and Tiuri, 1966). The minimum total effect of the active Sun and the galactic background corresponds to about 20 ± 5 MHz, since the galactic noise increases towards the low frequencies. In order to minimize the effect of the Sun, the antenna will be pointed towards it during the measurement. The targeted radar specifications have been listed in Table 1.

In the stepped-frequency measurement, the duration of a single frequency line (single pulse) can be estimated via $\tau = 1/B_\ell$, where $B_\ell = B/N$ is the bandwidth of the pulse. That is, the total bandwidth B covered by the pulse sequence is divided by the number N of the frequency lines. Roughly around 64 lines with pulse duration 32 μs can be transmitted and received separately from a 5 km distance to the asteroid, estimating that the pulse duration is 96% of the total travel-time. Notice that smaller is B_ℓ the longer is the single pulse duration, meaning that the more energy is transmitted.

Table 1
Targeted radar parameters.

• Center frequency:	20–50 MHz
• Antenna length (20–50 MHz):	2 × 3.75 m(20 MHz)–2 × 1.5 m(50 MHz)
• Radar modulation:	32–2048 lines
• Pulse duration (5 km distance):	32 μs
• Pulse repetition time (5 km distance):	150 μs
• Input/Transmitting power:	40 W/10 W
• Receiver bandwidth:	2–5 MHz
• Size:	1 U
• Weight:	1 kg

A sufficient pulse repetition time (PRT) with respect to the signal decay time will be about 150 μs taking into account that several reflections will be received later than the main signal pulse. Consequently, the duration of the complete pulse sequence can be estimated to be about 9.6 ms at 5 km distance. Since the ground speed relative to the asteroid will be negligible (maximally a few meters per second), all frequency lines for one sequence can be assumed to be measured from a single position. For each frequency line, the spectrum of the signal is recorded over a time interval at 5 km distance will start at the first pulse arrival around 34 μs and extend maximally to the 150 μs length of the PRT.

3.1.4. Computed radar tomography

Tomographic analysis of the targeted NEA can be performed akin to ordinary tomographic GPR surveys in which radio frequency signals enable reconstructing subsurface ground layers. Based on the radar specifications, the range resolution ($\delta_r = c/(2B)$ with c denoting the signal velocity and B the bandwidth) determines the minimum distance between two separable details of 20–40 m inside the NEA, assuming that its relative electric permittivity is 3–12 (e.g. solid and pulverized rocks and silica). On ground, the numerical simulations necessary for inverting the radar measurements can be performed using a state-of-the-art computer or computing cluster with sufficient memory for running iterative wave equation solvers within a three-dimensional computation domain. Our recent simulation study demonstrates that a 2 MHz full-wave (full-bandwidth) data can be computed and inverted for the targeted asteroid size range using a high-end workstation computer equipped with up-to-date graphics processing units (GPUs) (Takala et al., 2017).

To record the tomography data, we will use a simple bistatic (two-spacecraft) measurement scenario in which the CubeSats will be placed within a (nearly) constant angle γ from each other as seen from the NEA. One of the CubeSats will both transmit and receive the signal and the other one will serve as an additional receiver. As the instrumentation on both CubeSats is identical the concept is redundant by its design. The reference phase can be transmitted by the master satellite. The flying formation does not necessarily need to be maintained stationary: the mutual distance between the CubeSats can slightly vary during the measurements, since their positions will be tracked independently. At least the following two different choices for γ will be used: (i) $\gamma \leqslant 35^\circ$ and (ii) $\gamma \geqslant 145^\circ$. The first one of these (i) will enable an enhanced backscattering measurement; our numerical results (Takala et al., 2017) suggest that with the choice $\gamma = 25^\circ$ the accuracy and reliability of the bistatic tomography outcome is superior compared to the monostatic (single-spacecraft) case. The second option (ii) will allow a higher signal-to-noise ratio due to one-way signal paths and tomographic travel-time

measurements, performed, e.g., in CONSERT (Takala et al., 2018; Kofman et al., 2015).

3.2. Shape model

The altimeter-based shape model of the asteroid can be reconstructed via a combined use of radar and laser measurements. The laser data will complement the radar measurements in which the first return coming from the surface of the asteroid is detected. In the radar measurement, the topographic (flat surface) height accuracy δ_{th} for a single point is below 20% of the range resolution (Manasse, 1960). Consequently, in empty space, a measurement with the bandwidth of 2 MHz and the range resolution of $\delta_r = 75$ m will have the maximal height accuracy of about $\delta_{th} = 15$ m. This reflects the maximal shape modeling accuracy of the radar assuming that a sufficiently dense distribution of points over the asteroid surface can be covered at the orbit. However, due to the rough surface scattering effects, the practical resolution will be lower (Brown, 1977; Brown, 1978) which is why the optical measurements will be needed to refine the shape.

3.3. Optical imaging

A visual camera system is needed to enhance the accuracy of spacecraft positioning. The images provided by the camera can also be used to optimize the shape model. Because of the limited data transmission rate and the resulting constrains on the data volume, the angular resolution of the camera has to be chosen to provide a surface coverage with a reasonable amount of images in the expected orbit. Without detailed analyses available at this point, we build our estimate on the experience from the Hayabusa mission (Ishiguro et al., 2010). The AMICA imaging system (Nakamura et al., 2001) on the Hayabusa spacecraft took a total of >1400 images of asteroid Itokawa. The camera had a field-of-view (FOV) of $5.83° \times 5.69°$, and a detector with $1024\ \text{px} \times 1000\ \text{px}$. The analog-to-digital converter sampled the signal with 12 bit resolution. This corresponds to an image file size of 1.46 MiB uncompressed. Lossless compression can achieve an estimated factor 2 in file size reduction. Therefore, we expect to need to downlink a total of $\approx 1025\ MiB$ over the course of the mission in order to achieve a shape model for a scenario similar to Hayabusa. Commercial of the shelf camera systems mounted on small satellite platforms achieve a FOV of about 15°. While the lower resolution directly decreases the resolution achievable for the surface shape model, the estimate of the data volume is still applicable.

4. Mission layout

4.1. Overall design

For the 6U design of DISCUS, mostly components of the shelf (COTS) have been selected. The spacecraft is illustrated in Fig. 1. The frame is based on the 6U Supernova Bus of Pumpkin Inc. Electric propulsion will be used. A COTS engine that can provide the required Δv within the power and mass requirements is the Busek BIT-3.[3] The engine is also used for other CubeSat missions such as the Lunar IceCube (Folta et al., 2016). With a wet weight of 3 kg including 1.5 kg of propellant, the BIT-3 delivers a Δv of 3.2 km s^{-1} for a 13 kg CubeSat, when operated at 75 W power.

A Vacco cold-gas thruster and four star trackers complement the COTS attitude determination and control system. For power generation, the solar panel system MMA eHAWK with 96 W beginning-of-Life (BOL) has been chosen. The camera and a military rated JenOptic altimeter are mounted in the front next to the dipole antenna. Additionally 1U is occupied by housekeeping systems such as battery systems and an on-board computer. The green and yellow boxes represent the radar and communication system, respectively. The estimated weight of these systems leads to the total wet mass of the satellite, with 20% margin of non-COTS of around 13.2 kg. The mass budget can be found in Table 2.

Since the bistatic measurement process requires accurate timing, e.g., regarding radar pulse window synchronization, a chip-scale atomic clock (CSAC) will be needed on board in order to minimize all possible clocking differences between the two CubeSats (DeNatale et al., 2008). The synchronization accuracy provided natively by the CSAC will be around 100 ns,[4] that is, the travel-time corresponding to the maximal attainable radar accuracy (20 % of the range resolution, Section 3.2). The precision of the CSAC will allow a several hours' measurement time without re-synchronization, i.e., control pulse exchange.

4.2. Power requirement

In the science phase, the total peak power consumption will be about 50 W. The stepped frequency radar will require 40 W non-continuously in short pulses. The attitude control and housekeeping need together up to 10 W. During the cruise phase, the electric propulsion system requires most of the power. The desired Busek BIT-3 engine can be operated between 55 and 80 W. The efficiency of the engine will decrease along with the power consumption.

The MMA eHAWK is supplying solar arrays in the required scale. The HaWK 112–7058 delivers 96 W BOL peak power.[5] The system consists, hereby, of two triple folded $2\ \text{U} \times 3\ \text{U}$ solar panels each mounted on one gimbaled root hinge. The power consumption estimates have been budgeted in Table 2.

[3] http://www.busek.com/technologies__ion.htm.
[4] https://www.microsemi.com/document-portal/doc_view/133866-low-noise-csac-datasheet.
[5] http://mmadesignllc.com/existing-hawk-configurations/.

Table 2
Mass and power budget for DISCUS. Note that the radar and electric propulsion are not running simultaneously. Power refers to nominal (non-peak) power. The radar power refers to the short stepped-frequency pulse sequences.

Component	Specification	Availability	Mass (kg)	Power (W)
Bus	6U w. shielding	modif. COTS	2.0	
Solar panels	w. pointing	Announced	1.0	96.0
Propulsion	Bit 3	COTS	3.0	56.0–80
Thruster	Cold gas, 50 Ns	COTS	0.6	0.0–10.0
Attitude control	2 mNm	COTS	1.0	0.5–2.0
Housekeeping	Incl. thermal	modif. COTS	1.0	2.0–7.0
Radar		TRL 3	1.0	40.0
Dipole antenna	2×3.75 m	TRL 2	0.4	
Atomic clock	Chip-Sized Atomic Clock	COTS	3.5×10^{-2}	0.12
Nav. camera		modif. COTS	0.5	0.5–2.0
Laser altimeter		modif. COTS	0.05	0.01
Communication		TRL 2	1.5	10.0
Total			12.1 kg	
+ 20% Margin	w/o unmodif. COTS		13.2 kg	

4.3. Antenna

Commercial systems using a motor have already proven the feasibility of a 3 m deployable antenna for Cubesats. For example, Oxford Space ASTROTUBE BOOM has been validated in space, by unfolding to 1.5 m (Reveles et al., 2017). The Oxford system is available for length of up to 3 m and fits into 1U at a weight of 0.6 kg. Our half-length dipole antenna is projected to be built based on a metal strip design, which is widely utilized for antennas in space applications. A self-enrolling strip has been chosen as the design basis instead of a motor in order to reduce mass and volume of the system. The antenna structure is slightly bent to be more stable and to function as a pre-stressed spring when rolled up. A thermal knife releases the tapes, which unwind entirely by rolling of the spacecraft.

4.4. Targets

In addition to the scientific and instrument requirements, the target needs to be reachable for a CubeSat. Based on a lunar transfer orbit, a study for an asteroid encountering mission with a 6U CubeSat has been performed by Landis et al. (2014). Landis argues that at least an initial Δv of 1.6 km s^{-1} into various asteroid orbits could be provided from the lunar transit insertion. Thus, the maximum possible total Δv will be 4.8 km s^{-1}, i.e., the sum of the Δv given by the thruster (3.2 km s^{-1}) and that of the lunar transit. As the detailed orbit analysis is still missing, we assume a margin of 0.8 km s^{-1} and limit our survey to asteroids with a Δv of maximally 4 km s^{-1}. Still, various asteroids fulfill this requirement. Fig. 4 shows targets[6] on their closest approach that are reachable on various launch dates. In our opinion, a good reference candidate for 2021 is the asteroid 65717 (1993 BX3)[7,8] because of its close approach of 18.4 lunar distances (LD), relative Δv of around 3.6 km s^{-1} in January 2021 and diameter between 180 and 410 m.[9] As the current discovery rate in the recent years has been around 1500 NEAs per year, more candidates could show up in the future. The selection of a mission target has to be revisited once the final launch window has been fixed.

4.5. Radar measurement and mapping orbit

The two CubeSats will approach the targeted asteroid to a stable point between 5 km and 10 km altitude and perform their first radar measurements from a static position relative to the target. The moving plane is supposed to avoid shadow phases, which would stress the thermal management and decrease the power generation. If the orbit of the spacecraft is polar, i.e., perpendicular to the spin of the asteroid, a single orbit will be sufficient to record a backscattering dataset for a nearly uniformly distributed set of measurement points enclosing the targeted NEA. We assume that a polar or nearly-polar polygonal orbit can be achieved with an orbiting direction that is perpendicular to the Solar System's ecliptic plane, since most NEAs are known to have a retrograde spin (La Spina et al., 2004), i.e., the spin orientation is nearly normal to the ecliptic. The orbital movement of the spacecraft will be very slow. That is, the relative velocity between the asteroid's surface and the spacecraft will be maximally a few meters per second and mainly determined by the spin period. Consequently, Doppler effects can be omitted. The exact duration of the measurements will mainly

[6] https://cneos.jpl.nasa.gov/ca/.
[7] https://ssd.jpl.nasa.gov/sbdb.cgi?sstr=65717.
[8] http://www.minorplanetcenter.net/db_search/show_object?utf8=œ&object_id=65717.

[9] This size range is based on an assumed geometric albedo p_V of $0.05 < p_V < 0.25$. There is an observation by Spitzer Space Telescope which gives, after radiometric analysis using techniques by Trilling et al. (2016), $D = 91^{+31}_{-15}$ m and $p_V = 0.72 \pm 0.33$ (http://nearearthobjects.nau.edu/). However, this albedo solution is unusually high as largest plausible albedos of NEOs are usually not much larger than 0.5 (Trilling et al., 2010). Therefore, we consider this result as a lower limit to the size of 65 717 (1993 BX_3).

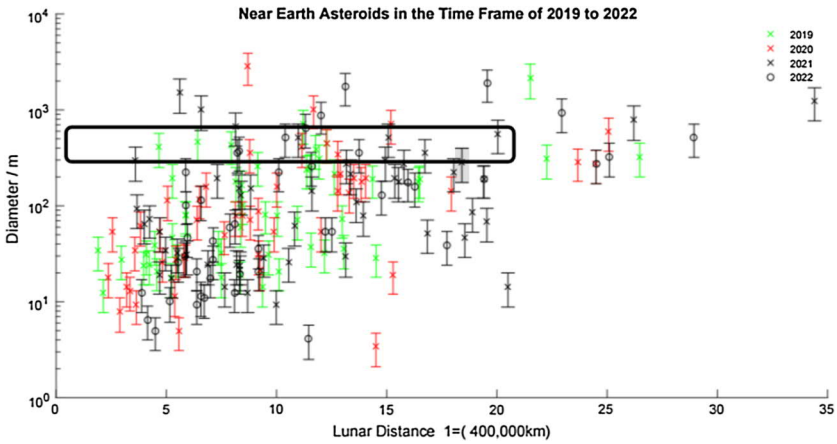

Fig. 4. Potential targets in the 2010–2022 time frame. The black outlined box shows the most interesting target range with respect to the diameter and the distance of the closest approach. The gray box shows the asteroid 65717 (1993 BX3) which is currently regarded as the most promising candidate with respect to the diameter (180–410 m), closest approach distance (18.4 lunar distances) and also Δv (3.6 km s^{-1}). Data taken from: NASA, JPL, https://cneos.jpl.nasa.gov/ca/.

depend on the asteroids spin period and result in a mission duration in the magnitude of some weeks.

For positioning, we will apply the data provided by the radar and laser altimeter, star trackers, and the optical camera. The goal is to obtain an orientation accuracy of at least 3 degrees relative to the target asteroid's surface, which has been suggested to be sufficient for tomography in Takala et al. (2017). The asteroid will be visible in the optical camera. Together with the star trackers providing an accuracy around 0.01 degrees (Enright, 2010), e.g., with BST's iADCS100. The distance to the asteroid can be obtained based on the altimeter data. Using the light-curve inversion, a preliminary estimate for the spin and shape model can be determined during the approach with an estimated couple of degrees accuracy for the spin (Ďurech et al., 2015). As suggested by our present analysis, the shape model can be refined up to an angular accuracy around one degree using the radar (Section 3.2). A further refinement will be attempted via the optical imaging.

In order to ensure that a robust tomographic reconstruction can be produced, we use a 1.5–2.0 spatial oversampling rate with respect to the Nyquist criterion (NC) which was suggested for a monochromatic (travel-time) measurement in Pursiainen and Kaasalainen (2015). This means recording the radar signal for 5000–20 000 measurement positions, when extrapolating the measurement positions to the close proximity of a targeted 260–600 m diameter NEA. The resulting estimated maximal amount of data recorded by a single satellite will be 250–1000 MB, respectively. Two identical CubeSats will be present in the mission. A perpendicular orbit will be used for both satellites. The measurement is bistatic, that is, one CubeSat both transmits and receives the signal and the other one serves as an additional receiver. In the measurements, the spacecraft will be placed within a constant angular distance from each other as seen from the asteroid (Takala et al., 2017).

4.6. Data link

The essential prerequisite for the downlink is the ability to transfer the whole scientific dataset during the visibility to one ground-station on Earth. The size of the dataset is estimated to be about 12–13 GBit, coming from the radar (500 MB), the camera (1025 MB) and an altimeter (50 MB). The size of the antenna is assumed to be 20 cm × 30 cm, the available transmit power is limited by the size of the spacecraft's solar array. Our baseline strategy is to use the 35 m ESA Deep-Space Ground Stations capable to receive in the 31.8–32.3 GHz band. With a 3 W transmitter RF-power we expect that a data rate of about 520 kBit/s can be achieved using the DVB-S2 QPSK 2/3 operations mode. With this transfer rate a dataset of the estimated size can be transmitted to the Earth within less than 7 h.

5. Discussion

In the DISCUS concept, a bistatic (two-spacecraft) low-frequency radar is carried by two CubeSats. The primary goal is to resolve the interior structure of a 260–600 m diameter, i.e., Itokawa-size (Abe et al., 2006), rubble pile asteroid. Based on this study, the most promising target candidate is currently 65 717 (1993 BX3), a potentially hazardous object, which will make its next close Earth approach in 2021 at a Δv of 3.6 km s^{-1} with the closest point being at 18.4 lunar distances from the Earth. More candidates will probably be detected in the near future,

and the final target asteroid can only be selected when a launch opportunity has been found.

Akin to airborne GPR, the radar design is based on the stepped-frequency measurement technique coupled with a linear dipole antenna (Fu et al., 2014). We aim to use a low 20–50 MHz signal frequency in order to maximize the signal penetration depth (Francke and Utsi, 2009; Leucci, 2008; Kofman, 2012) and, thereby, to obtain a global data coverage for the interior part. The main mission objective will be achieved, if the internal macroporosity structures can be detected and mapped. We expect that full or close to full penetration will be achieved, since the level of the signal attenuation in the porous minerals of planetary subsurfaces in the planned low frequency range is known to be low (Kofman, 2012), e.g., 10–30 dB km^{-1} for basalt. Moreover, the estimated data transfer capacity (Section 4.6) allows recording the signal for a sufficiently dense distribution of points within targeted size range (Section 4.5).

Our recent simulation study (Takala et al., 2017) suggests that the tomographic reconstruction of the interior details, such as voids, will be feasible. Based on the results, we expect that the interior can be reconstructed, if the total noise including both measurement and modeling errors is at least 5–10 dB below the signal amplitude. The planned orbiting distance also seems to yield a sufficient signal-to-noise ratio with respect to the cosmic background. The results, furthermore, suggest that also limited-angle measurements following from a non-perpendicular (non-polar) orbit will allow obtaining a reconstruction. That is, also NEAs with an exceptional (non-retrograde) spin (La Spina et al., 2004) are potential targets for tomographic reconstruction. In the numerical simulations, we have assumed a 25 dB km^{-1} signal attenuation level. In practice, the scattering caused by the macroporosity can lead to some additional attenuation.

The targeted 2 MHz total bandwidth for the stepped-frequency measurements would give the resolution of at least 20–40 m inside the target asteroid (Daniels, 2004), if its relative permittivity is 3–12 (e.g. solid and pulverized rocks and silica). This would mean the distinguishability of the details around the size 1/20–1/10 with respect to the asteroid diameter providing an unforeseen reconstruction accuracy for the deep interior structure. Consequently, the current design should be sufficient for the main goal of detecting major variances in the volumetric relative electric permittivity structure. For comparison, the initial maximal resolution estimates for CONSERT and *Deep Interior* were 16 and 20 m, respectively (Kofman et al., 2007; Asphaug et al., 2001). In CONSERT, the carrier frequency and bandwidth of the signal were 90 and 8 MHz, respectively.

We consider the 2 MHz bandwidth advantageous from both computational and measurement viewpoints, as we currently can invert a full set of data for the targeted asteroid size (Takala et al., 2017) and sufficient measurement accuracy seems achievable. A wider bandwidth would, however, allow distinguishing smaller details. Techniques to increase the bandwidth can, in principle, include adding transmission channels and modifying the antenna folding, loading and increasing the width (Fu et al., 2014; Poggio and Mayes, 1971; Balanis, 2012; Alexander et al., 2002). Nevertheless, each of these adjustments would increase the complexity, total weight and power consumption of the system and, therefore, those are not suggested for the initial design.

Our initial hardware design relies on optimizing the weight and size of the spacecraft in order to minimize the mission costs. Therefore, the 6U frame is used as the reference design. Based on this study, the Busek BIT-3 thruster will be able to provide the 6U CubeSat a Δv of 3.2 km s^{-1} which together with an initial Δv obtained from a lunar transfer orbit (Landis et al., 2014) will result in a total Δv of approximately 4 km s^{-1}. This would be enough to reach, e.g., the asteroid 65717 (1993 BX3) in 2021. Depending on the eccentricity of the transfer orbit the targeted 75 W cannot be achieved for the entire transfer. Yet, we expect that including the initial Δv, the required power for the thruster will have enough margins to compensate these phases. In the current design the total Δv is limited mainly by the power provided by the solar cells, as they degrade over time and produce less power at sun distances beyond 1 AU. The number of reachable targets would increase if solar cells with 120 W are used, as the potential of the propulsion system could then be used to the full extend. With currently available solar panels this would increase the mass by 0.8 kg.

A larger 12U size can also be considered, even if all components would fit in the 6U bus and other authors have described the envelope as feasible (McNutt et al., 2014; Staehle et al., 2013). Namely, the margins are small and could be eaten up by any insertion in the radar, communication system or thermal management. Nevertheless, a 12U bus would lead to a higher total weight and, consequently, require a much larger orbit control system. As the power would not necessarily scale with size, a completely different propulsion system would be needed. One possibility to overcome these possible issues would be a piggy-bag ride to an asteroid. This would reduce the need of Δv and communication capability and might lead to an extra 3/2 U of scientific payload, for instance, a more advanced camera system.

The proposed self-rolled half-wavelength dipole antenna design is beneficial with respect to the mass and volume. We emphasize that the present antenna specifications have been designed for Itokawa-size bodies for which a well-penetrating signal frequency is necessary. Nevertheless, the radar and the spacecraft can also operate with higher frequencies and shorter antenna lengths, which might be preferable for smaller bodies or shallower subsurface structures. We consider that the goal to fit the radar in a 1U (1000 cm^3) space is feasible based on RST's earlier experience of the compact 900 cm^3 HOPE radar design at higher frequencies (RST Radar Systemtechnik AG, 2001). The next development stage aims to build a 20 MHz radar

demonstrator to validate the proposed instrumentation in an on-ground test. RST has previous experience of a low-frequency radar designed for a planetary orbiter from ESA's project PIRA (Braun et al., 1997b) in which a stepped-frequency radar equipped with a 10 MHz antenna system was successfully tested under motion.

Compared to more frequently used microwave CubeSat radars, for example, Raincube's 4U and 10 W Ka-band radar (Peral et al., 2017), the planned low-frequency band allows a more simple design. Attaining a considerably better synchronization than what is natively provided by the CSAC, e.g., due to a wider bandwidth, might necessitate extra arrangements. For example, in the recent microwave-range interferometry measurements of the TandDEM-X mission, obtaining a picosecond-level synchronization required relative phase referencing via six dedicated synchronization horn antennas in each spacecraft (Krieger et al., 2007).

Future work will include construction of a demonstrator prototype to validate the radar. Numerical simulations concerning the stepped-frequency measurement technique, shape modeling, and also orbit calculations around the asteroid will be performed. We will also examine the capability of the planned instrumentation, e.g., regarding flyby measurements, to reconstruct the interior of a comet and also in mapping of the recently discovered Moon caves. Several details will need to be refined in the final design stage.

6. Conclusion

DISCUS - The Deep Interior Scanning CubeSat mission is designed with the aim to characterize the interior structure of rubble pile asteroids. Computed radar tomography and a bistatic configuration of two identical CubeSats will be used to reconstruct internal electric permittivity heterogeneities. While deep-space missions for CubeSat sized spacecraft are still a challenge from an engineering point of view, we found that our radar is compatible with the limitations of a CubeSat mission to a near-Earth asteroid. The baseline design of the DISCUS spacecraft provides a Δv of 3.2 km s^{-1}. A launch to a lunar transfer orbit provides an additional Δv so that asteroids with a Δv of approximately 4 km s^{-1} are reachable. The most prominent target candidate among the currently known NEAs is 65 717 (1993 BX3).

The main scientific result that could be accomplished with DISCUS mission is mapping the distribution of porosity within a rubble pile asteroid. This would be on the one hand of great value to formation models of the Solar System, but also of great importance to deflection scenarios for potentially hazardous asteroids imposing an impact threat to earth. Additionally, crucial knowledge of the internal permittivity structures and, thereby, also the mineral content of the asteroids would be obtained.

Acknowledgments

MT and SP were supported by the Academy of Finland Key Project 305055 and AoF Centre of Excellence in Inverse Problems.

PB, JD and EV were supported by the Max Planck Institute for Solar System Research.

References

Abe, S., Mukai, T., Hirata, N., Barnouin-Jha, O.S., Cheng, A.F., Demura, H., Gaskell, R.W., Hashimoto, T., Hiraoka, K., Honda, T., Kubota, T., Matsuoka, M., Mizuno, T., Nakamura, R., Scheeres, D.J., Yoshikawa, M., 2006. Mass and local topography measurements of Itokawa by Hayabusa. Science 312 (5778), 1344–1347.

Alexander, M., Salter, M., Loader, B., Knight, D., 2002. Broadband calculable dipole reference antennas. IEEE Trans. Electromagn. Comp. 44 (1), 45–58.

Asphaug, E., Belton, M.J.S., Kakuda, R.Y., 2001. Geophysical exploration of asteroids: the deep interior mission concept. In: 32nd Annual Lunar and Planetary Science Conference, 12–16 March 2001. Abstract #1867. Lunar and Planetary Institute, Houston, Texas (CD-ROM).

Balanis, C., 2012. Antenna Theory: Analysis and Design. Wiley.

Barnouin-Jha, O.S., Cheng, A.F., Mukai, T., Abe, S., Hirata, N., Nakamura, R., Gaskell, R.W., Saito, J., Clark, B.E., 2008. Small-scale topography of 25143 Itokawa from the Hayabusa laser altimeter. Icarus 198 (1), 108–124.

Braun, H., Lentz, H., Borisch, W., Putz, P., 1997a. A Novel Radar Instrument for Sub-surface Exploration and Planetary Rover Piloting (GINGER). In: Proceedings of the Twelfth International Conference, Applied Geologic Remote Sensing: Practical Solutions for Real-world Problems, Denver, Colorado, 17–19 November 1997, Project: Stepped Frequency Radar Technology. vol. 1. ERIM International, Ann Arbor, MI, pp. I–506 – I–513, full text available at ResearchGate: <https://www.researchgate.net/publication/325170473>.

Braun, H., Lentz, H., Woode, A., 1997b. A Planetary Into-the-Ground Radar and Altimeter (PIRA). In: Proceedings of the Twelfth International Conference, Applied Geologic Remote Sensing: Practical Solutions for Real-world Problems, Denver, Colorado, 17–19 November 1997, Project: Stepped Frequency Radar Technology. vol. 1. ERIM International, Ann Arbor, MI, pp. I–498 – I–505, full text available at ResearchGate: <https://www.researchgate.net/publication/325170557>.

Brown, G., 1977. The average impulse response of a rough surface and its applications. IEEE Trans. Antennas Prop. 25 (1), 67–74.

Brown, G.S., 1978. Backscattering from a gaussian-distributed perfectly conducting rough surface. IEEE Trans. Antennas Prop. 26 (3), 472–482.

Carry, B., 2012. Density of asteroids. Planet. Space Sci. 73 (1), 98–118.

Clark, P., Malphrus, B., Brown, K., Reuter, D., MacDowall, R., Folta, D., Mandell, A., Hurford, T., Brambora, C., Patel, D., et al., 2016. Lunar ice cube mission: determining lunar water dynamics with a first generation deep space CubeSat. Science 330, 463–468.

Daniels, D.J., 2004. Ground penetrating radar, second ed., The Institution of Engineering and Technology, London, United Kingdom.

Deller, J.F., 2017. Hyper-Velocity Impacts on Rubble Pile Asteroids (Ph. D. thesis). School of Physical Sciences University of Kent Canterbury U.K. and International Max Planck Research School for Solar System Science Göttingen Germany.

DeNatale, J., Borwick, R., Tsai, C., Stupar, P., Lin, Y., Newgard, R., Berquist, R., Zhu, M., 2008. Compact, low-power chip-scale atomic clock. In: Position. Position, Location and Navigation Symposium, 2008 IEEE/ION. IEEE, pp. 67–70.

Ďurech, J., Carry, B., Delbo, M., Kaasalainen, M., Viikinkoski, M., 2015. Asteroid models from multiple data sources. In: Michel, P., Demeo, F.

E., Bottke, W.F. (Eds.), Asteroids IV. University of Arizona Press, Tucson, Arizona, pp. 183–202.
Eisenburger, D., Lentz, H., Jenett, M., 2008. Helicopter-borne GPR systems: a way from ice thickness measurements to geological applications. In: IEEE International Conference on Ultra-Wideband, 10–12 September 2008, Hannover, Germany. vol. 3. IEEE, pp. 161–165.
Enright, J., 2010. Moon-tracking modes for star trackers. J. Guid. Control Dyn. 33 (1), 171–185.
Farinella, P., Paolicchi, P., Zappalá, V., 1982. The asteroids as outcomes of catastrophic collisions. Icarus 52, 409–433.
Folta, D.C., Bosanac, N., Cox, A., Howell, K. C., 2016. The Lunar IceCube mission design: construction of feasible transfer trajectories with a constrained departure. NASA Technical Reports Server (AAS 16-285), available online: <https://ntrs.nasa.gov/archive/nasa/casi.ntrs.nasa.gov/20170001470.pdf>.
Francke, J., Utsi, V., 2009. Advances in long-range GPR systems and their applications to mineral exploration, geotechnical and static correction problems. First Break 27 (7), available online: <http://www.novatest.it/wp-content/uploads/2017/04/RealTimeSampling-described.pdf>.
Fu, L., Liu, S., Liu, L., Lei, L., 2014. Development of an airborne ground penetrating radar system: antenna design, laboratory experiment, and numerical simulation. IEEE J. Sel. Top. Appl. Earth Observ. Remote Sens. 7 (3), 761–766.
Gundelach, V., Blindow, N., Buschmann, U., Salat, C., Krellmann, Y., 2010. Exploration of geological structures with GPR from helicopter and on the ground in the Letzlinger Heide (Germany). In: Proceedings of the XIII Internarional Conference on Ground Penetrating Radar. pp. 1–6.
Herique, A., Ciarletti, V., 2016. A direct observation of the asteroids structure from deep interior to regolith: two radars on the AIM mission. In: 47th Lunar and Planetary Science Conference, LPSC 2016, Conference abstract 2096, 2 pages. Topic 315: Planetary Mission Concepts: Small Bodies. Available online: <https://hal-insu.archives-ouvertes.fr/insu-01282911/>.
Imken, T., Castillo-Rogez, J., He, Y., Baker, J., Marinan, A., 2017. Cubesat flight system development for enabling deep space science. 14 pages. In: IEEE Aerospace Conference, 4–11 March 2017, Big Sky, MT. DOI 10.1109/AERO.2017.7943885. Available online: <https://ieeexplore.ieee.org/document/7943885/>.
Ishiguro, M., Nakamura, R., Tholen, D.J., Hirata, N., Demura, H., Nemoto, E., Nakamura, A.M., Higuchi, Y., Sogame, A., Yamamoto, A., Kitazato, K., Yokota, Y., Kubota, T., Hashimoto, T., Saito, J., 2010. The Hayabusa Spacecraft Asteroid Multi-band Imaging Camera (AMICA). Icarus 207, 714–731.
Kofman, W., 2012. Radar techniques to study subsurfaces and interiors of the solar system objects. Proceedings of the 19th International Conference on Microwave Radar and Wireless Communications (MIKON), vol. 2. IEEE, pp. 409–412.
Kofman, W., Herique, A., Barbin, Y., Barriot, J.-P., Ciarletti, V., Clifford, S., Edenhofer, P., Elachi, C., Eyraud, C., Goutail, J.-P., Heggy, E., Jorda, L., Lasue, J., Levasseur-Regourd, A.-C., Nielsen, E., Pasquero, P., Preusker, F., Puget, P., Plettemeier, D., Rogez, Y., Sierks, H., Statz, C., Svedhem, H., Williams, I., Zine, S., Van Zyl, J., 2015. Properties of the 67P/Churyumov-Gerasimenko interior revealed by CONSERT radar. Science 349 (6247), aab0639-1aab0639–6.
Kofman, W., Herique, A., Goutail, J.-P., Hagfors, T., Williams, I.P., Nielsen, E., Barriot, J.-P., Barbin, Y., Elachi, C., Edenhofer, P., Levasseur-Regourd, A.-C., Plettemeier, D., Picardi, G., Seu, R., Svedhem, V., 2007. The comet nucleus sounding experiment by radiowave transmission (CONSERT): a short description of the instrument and of the commissioning stages. Space Sci. Rev. 128 (1), 413–432.
Kraus, J.D., Tiuri, M., 1966. Radio Astronomy. McGraw-Hill, New York.
Krieger, G., Moreira, A., Fiedler, H., Hajnsek, I., Werner, M., Younis, M., Zink, M., 2007. TanDEM-X: A satellite formation for high-resolution SAR interferometry. IEEE Trans. Geosci. Remote Sens. 45 (11), 3317–3341.
Kwiatkowski, T., 2010. Photometric survey of the very small near-Earth asteroids with the SALT telescope. Astron. Astrophys. 509, A95.
La Spina, A., Paolicchi, P., Kryszczynska, A., Pravec, P., 2004. Retrograde spins of near-Earth asteroids from the Yarkovsky effect. Nature 428 (6981), 400–401.
Lacomme, P., 2001. Air and Spaceborne Radar Systems: An Introduction. Electronics & Electrical. William Andrew Publishing LLC, New York.
Landis, G.A., Oleson, S.R., McGuire, M.L., Burke, L.M., Martini, M.C., Fittje, J.E., Packard, T.W., 2014. A cubesat asteroid mission: Propulsion trade-offs. In: 50th AIAA/ASME/SAE/ASEE Joint Propulsion Conference, 28–30 July 2014, Cleveland, OH, paper AIAA 2014-3755, 9 pages. AIAA Propulsion and Energy Forum. American Institute of Aeronautics and Astronautics, Reston, VA.
Leucci, G., 2008. Ground Penetrating Radar: The Electromagnetic Signal Attenuation and Maximum Penetration Depth. Schol. Res. Exchange 2008 (2008). Article ID 926091.
Manasse, R., 1960. Summary of maximum theoretical accuracy of radar measurements. Tech. Rep. 2, Mitre Corp, Bedford, MA.
McNutt, L., Johnson, L., Clardy, D., Castillo-Rogez, J., Frick, A., Jones, L., 2014. Near-Earth asteroid scout. In: AIAA SPACE 2014 Conference and Exposition, 4–7 August 2014, paper AIAA 2014-4435, 9p. AIAA Space Forum. American Institute of Aeronautics and Astronautics, Reston, VA.
Michel, P., Kueppers, M., Carnelli, I., Galvez, A., Mellab, K., Cheng, A., 2016. Asteroid Impact Mission (AIM): the European component of the AIDA space project. In: 47th Lunar and Planetary Science Conference, LPSC 2016, Conference abstract 1204, 2p. Topic 315: Planetary Mission Concepts: Small Bodies. Available online: <https://www.hou.usra.edu/meetings/lpsc2016/pdf/1204.pdf>.
Michel, P.P., Benz, W.W., Tanga, P., Richardson, D.C., 2001. Collisions and gravitational reaccumulation: forming asteroid families and satellites. Science 294 (5547), 1696–1700.
Michel, P.P., Benz, W.W., Tanga, P., Richardson, D.C., 2002. Formation of asteroid families by catastrophic disruption: simulations with fragmentation and gravitational reaccumulation. Icarus 160 (1), 10–23.
Michikami, T., Nakamura, A. M., Hirata, N., Gaskell, R.W., Nakamura, R., Honda, T., Honda, C., Hiraoka, K., Saito, J., Demura, H., Ishiguro, M., Miyamoto, H., 2008. Size-frequency statistics of boulders on global surface of asteroid 25143 Itokawa. In: Earth Planets and Space. Fukushima Natl Coll Technol, Iwaki, Fukushima 9708034, Japan, pp. 13–20.
Nakamura, T., Nakamura, A.M., Saito, J., Sasaki, S., Nakamura, R., Demura, H., Akiyama, H., Tholen, D., et al., 2001. Multi-band imaging camera and its sciences for the Japanese Near-Earth asteroid mission MUSES-C. Earth Planets Space 53 (11), 1047–1063.
Peral, E., Statham, S., Taneli, S., Imken, T., Williams, A., Price, D., Sauder, J., Chahat, N., 2017. RainCube, a Ka-band Precipitation Radar in a 6U CubeSat. In: Presentation SSC17-VII-80 at the 31st Annual AIAA/USU Conference on Small Satellites, 5–10 August 2017, Logan, UT. Available online: <https://digitalcommons.usu.edu/smallsat/2017/all2017/80/>.
Poggio, A., Mayes, P., 1971. Bandwidth extension for dipole antennas by conjugate reactance loading. IEEE Trans. Antennas Prop. 19 (4), 544–547.
Pravec, P., Harris, A.W., 2000. Fast and slow rotation of asteroids. Icarus 148, 12–20.
Pravec, P., Harris, A.W., Michalowski, T., 2002. Asteroid rotations. In: Bottke, W., Cellino, A., Paolicchi, P., Binzel, R. P. (Eds.), Asteroids III. University of Arizona, Tucson, Arizona, pp. 113–122.
Pursiainen, S., Kaasalainen, M., 2015. Electromagnetic 3D subsurface imaging with source sparsity for a synthetic object. Inverse Prob. 31 (12), 125004.
Reddy, V., Dunn, T.L., Thomas, C.A., Moskovitz, N.A., Burbine, T.H., 2015. Mineralogy and surface composition of asteroids. In: Michel, P., Demeo, F.E., Bottke, W.F. (Eds.), Asteroids IV. University of Arizona Press, Tucson, Arizona, pp. 43–63.

Reveles, J., Lawton, M., Fraux, V., Gurusamy, V., Parry, V., 2017. In-orbit performance of astrotube: Alsat nano's low mass deployable composite boom payload. In: Proceedings of the 31st Annual AIAA/USU Conference on Small Satellites, paper SSC17-II-08. Available online: <https://digitalcommons.usu.edu/smallsat/2017/all2017/76/>.

Richardson, D.C., Leinhardt, Z.M., Melosh, H.J., Bottke, W.F., Asphaug, E., 2002. Gravitational aggregates: evidence and evolution. In: Bottke, W.F., Cellino, A., Paolicchi, P., Binzel, R.P. (Eds.), Asteroids III. University of Arizona Press, Tucson, Arizona, pp. 501–515.

Rozitis, B., MacLennan, E., Emery, J.P., 2014. Cohesive forces prevent the rotational breakup of rubble-pile asteroid (29075) 1950 DA. Nature 512 (7513), 174–176.

RST Radar Systemtechnik AG, 2001. HOPE (Handheld Operated Demining System). <http://www.rst-group.biz/index.php?id=113&no_cache=1> (accessed: 2017-10-05).

Safaeinili, A., Gulkis, S., Hofstadter, M.D., Jordan, R.L., 2002. Probing the interior of asteroids and comets using radio reflection tomography. Meteorit. Planet. Sci. 37, 1953–1963.

Saito, J., Miyamoto, H., Nakamura, R., Ishiguro, M., Michikami, T., Nakamura, A.M., Demura, H., Sasaki, S., Hirata, N., Honda, C., Yamamoto, A., Yokota, Y., Fuse, T., Yoshida, F., Tholen, D.J., Gaskell, R.W., Hashimoto, T., Kubota, T., Higuchi, Y., Nakamura, T., Smith, P., Hiraoka, K., Honda, T., Kobayashi, S., Furuya, M., Matsumoto, N., Nemoto, E., Yukishita, A., Kitazato, K., Dermawan, B., Sogame, A., Terazono, J., Shinohara, C., Akiyama, H., 2006. Detailed images of asteroid 25143 Itokawa from Hayabusa. Science 312 (5778), 1341–1344.

Sánchez, P., Scheeres, D.J., 2012. DEM simulation of rotation-induced reshaping and disruption of rubble-pile asteroids. Icarus 218 (2), 876–894.

Snodgrass, C., Jones, G., Boehnhardt, H., Gibbings, A., Homeister, M., Andre, N., Beck, P., Bentley, M., Bertini, I., Bowles, N., Capria, M., Carr, C., Ceriotti, M., Coates, A., Corte, V. D., Hanna, K. D., Fitzsimmons, A., Gutirrez, P., Hainaut, O., Herique, A., Hilchenbach, M., Hsieh, H., Jehin, E., Karatekin, O., Kofman, W., Lara, L., Laudan, K., Licandro, J., Lowry, S., Marzari, F., Masters, A., Meech, K., Moreno, F., Morse, A., Orosei, R., Pack, A., Plettemeier, D., Prialnik, D., Rotundi, A., Rubin, M., Snchez, J., Sheridan, S., Trieloff, M., Winterboer, A., 2017. The Castalia mission to Main Belt Comet 133P/Elst-Pizarro. Adv. Space Res.

Staehle, R., Blaney, D., Hemmati, H., Lo, M., Mouroulis, P., Pingree, P., Wilson, T., Puig-Suari, J., Williams, A., Betts, B., et al., 2013. Interplanetary CubeSats: opening the solar system to a broad community at lower cost. J. Small Satellites 2 (1), 161–186.

Takala, M., Bambach, P., Deller, J., Vilenus, E., Wittig, M., Lentz, H., Braun, H.M., Kaasalainen, M., Pursiainen, S., 2017. A far-field inversion approach for the deep interior scanning cubesat. Available from: arXiv preprint arXiv:<1709.04309v2>.

Takala, M., Us, D., Pursiainen, S., 2018. Multigrid-based inversion for volumetric radar imaging with asteroid interior reconstruction as a potential application. IEEE Trans. Comput. Imaging 4 (2), 228–240.

Thirouin, A., Moskovitz, N., Binzel, R.P., Christensen, E., DeMeo, F.E., Person, M.J., Polishook, D., Thomas, C.A., Trilling, D., Willman, M., Hinkle, M., Burt, B., Avner, D., Aceituno, F.J., 2016. The mission accessible Near-Earth Objects survey (MANOS): first photometric results. Astron. J. 152 (6), 163.

Tricarico, P., 2017. The near-Earth asteroid population from two decades of observations. Icarus 284, 416–423.

Trilling, D.E., Mommert, M., Hora, J., Chesley, S., Emery, J., Fazio, G., Harris, A., Mueller, M., Smith, H., 2016. NEOSurvey 1: Initial Results from the Warm Spitzer Exploration Science Survey of Near-Earth Object Properties. Astron. J. 152, 172.

Trilling, D.E., Mueller, M., Hora, J.L., Harris, A.W., Bhattacharya, B., Bottke, W.F., Chesley, S., Delbo, M., Emery, J.P., Fazio, G., Mainzer, A., Penprase, B., Smith, H.A., Spahr, T.B., Stansberry, J.A., Thomas, C.A., 2010. ExploreNEOs. I. Description and First Results from the Warm Spitzer Near-Earth Object Survey. Astron. J. 140, 770–784.

Walker, R., Koschny, D., Bramati, C., Carnelli, I., ESA, C.S.T., 2017. Miniaturised Asteroid Remote Geophysical Observer (M-ARGO): a stand-alone deep space CubeSat system for low-cost science and exploration missions. In: iCubeSat 7 abstracts.

Walsh, K.J., Richardson, D.C., Michel, P.P., 2008. Rotational breakup as the origin of small binary asteroids. Nature 454 (7201), 188–191.